UNIVERSITY OF SOUTHAMPTON

Faculty of Engineering and Physical Sciences
School of Physics and Astronomy

The Effect of Environment on Type Ia Supernovae in the Dark Energy Survey

by

Lisa Grace Kelsey

BSc, MSc

ORCiD: 0000-0003-0313-0487

A thesis for the degree of
Doctor of Philosophy

November 2021

University of Southampton

Abstract

Faculty of Engineering and Physical Sciences
School of Physics and Astronomy

Doctor of Philosophy

The Effect of Environment on Type Ia Supernovae in the Dark Energy Survey

by Lisa Grace Kelsey

Analyses of type Ia supernovae (SNe Ia) have found puzzling correlations between their standardised luminosities and host galaxy properties: SNe Ia in high-mass, passive hosts appear brighter than those in lower-mass, star-forming hosts. As key cosmological probes, it is vital to understand galaxy-SN correlations, to ensure they do not bias measurements of cosmological parameters.

In this thesis, I examine the host galaxies of SNe Ia in the Dark Energy Survey (DES). I use both spectroscopically- and photometrically-confirmed SN Ia samples (the DES3YR and DES5YR samples, respectively), measuring *griz* photometry of their host galaxies in both 'local' apertures centred on each SN, and for the entire 'global' host galaxy. I study the differences in the properties of these environments, such as stellar mass and rest-frame optical $U - R$ colours, and their correlations with SN Ia parameters including Hubble residuals.

For both DES3YR and DES5YR, all environmental property correlations with Hubble residual are significant at $> 3\sigma$, with the majority significant at $> 5\sigma$ for DES5YR, for both local and global environment properties. $U - R$ correlations are larger than for traditional global host mass, indicating that colour may better account for environmental effects. By analysing the scatter in the Hubble residuals, I also show that SNe Ia in redder, high-mass environments have higher scatter than SNe in bluer, low-mass environments, with a noticeably small scatter for blue SNe Ia in blue/low-mass environments. Such a sample currently presents the most homogeneous sample for use in cosmology.

I find that redder SNe Ia also have larger Hubble residual steps than the bluer SNe, suggesting that they drive the overall step size. Investigating this further, I find suggestion that the global host galaxy stellar mass has the strongest relationship with SN colour, and by fitting for a two-component colour-dependent Hubble residual relationship (a simple approximation of a dust model), I am able to remove the mass step from the data. However, a statistically significant (2.9σ) step in local $U - R$ remains, indicating

that multiple environmental corrections may be needed to account for the dispersion in SN Ia luminosity.

Finally, I investigate the differences in local properties for SN Ia siblings (SNe Ia occurring in the same host galaxy) in DES. In all cases, the larger the difference in local environment properties between SNe Ia in the same galaxy, the larger the differences in their Hubble residuals, and SN light-curve shape and colour. This emphasises the importance of local environmental corrections for SNe Ia standardisation.

Contents

List of Figures

List of Tables

Definitions and Abbreviations

c	SALT2 **c**olour
CCSNe	**C**ore-**C**ollapse **S**uper**N**ova**e**
CCD	**C**harged **C**oupled **D**evice
CfA	Harvard-Smithsonian **C**enter **f**or **A**strophysics
CO-WD	**C**arbon-**O**xygen **W**hite **D**warf
CSM	**C**ircum**S**tellar **M**edium
CSP	**C**arnegie **S**upernova **P**roject
CMB	**C**osmic **M**icrowave **B**ackground
DD	**D**ouble-**D**egenerate
DES	**D**ark **E**nergy **S**urvey
DES3YR	The **three-year** spectroscopically-confirmed SNe Ia sample from **DES**
DES5YR	The **five-year** photometrically-confirmed SNe Ia sample from **DES**
DES-SN	The **DES** **S**uper**N**ova transient survey
DLR	**D**irectional **L**ight **R**adius
DP	**D**ivision **P**oint
FWHM	**F**ull **W**idth at **H**alf **M**aximum
Global	For the entire SN host galaxy
$\mathbf{H_0}$	**H**ubble Constant
IFS	**I**ntegral **F**ield **S**pectroscopy
IMF	**I**nitial **M**ass **F**unction
IR	**I**nfra**R**ed
JLA	**J**oint **L**ight-curve **A**nalysis
Local	Within a local aperture centred on each SN location
$M_{\mathbf{stellar}}$	**Stellar M**ass
MY	**M**inus **Y**ear stacks
PÉGASE	**P**rogramme d'**É**tude des **GA**laxies par **S**ynthèse **É**volutive
PSF	**P**oint **S**pread **F**unction
r.m.s.	**R**oot **M**ean **S**quare
SALT(2)	**S**pectral **A**daptive **L**ight-curve **T**emplate (v**2**)
SD	**S**ingle-**D**egenerate
SDSS	**S**loan **D**igital **S**ky **S**urvey
SED	**S**pectral **E**nergy **D**istribution

SFH	**S**tar **F**ormation **H**istory
SFR	**S**tar **F**ormation **R**ate
SLSNe	**S**uper **L**uminous **S**uper**N**ova**e**
sSFR	**s**pecific **S**tar **F**ormation **R**ate
SN(e)	**S**uper**N**ova**e**
SN(e) Ia	Type **Ia** **S**uper**N**ova**e**
SNLS	**S**uper**N**ova **L**egacy **S**urvey
SPS	**S**tellar **P**opulation **S**ynthesis
SSP	**S**imple **S**tellar **P**opulation
U-R	Rest-frame ***U-R*** colour
UV	**U**ltra**V**iolet
WD	**W**hite **D**warf
x_1	SALT2 stretch
z	Redshift

Declaration of Authorship

I declare that this thesis and the work presented in it is my own and has been generated by me as the result of my own original research.

I confirm that:

1. This work was done wholly or mainly while in candidature for a research degree at this University;
2. Where any part of this thesis has previously been submitted for a degree or any other qualification at this University or any other institution, this has been clearly stated;
3. Where I have consulted the published work of others, this is always clearly attributed;
4. Where I have quoted from the work of others, the source is always given. With the exception of such quotations, this thesis is entirely my own work;
5. I have acknowledged all main sources of help;
6. Where the thesis is based on work done by myself jointly with others, I have made clear exactly what was done by others and what I have contributed myself;
7. Parts of this work have been published as: Kelsey et al. (2021)

Signed:..... Date:.....

Acknowledgements

Firstly, to my supervisor, Mark Sullivan. These past few years have not been easy, but you always made time for me and gave me the guidance to make my way through my PhD. Thank you for always being so enthusiastic about my work and for all of the advice you have given me over the years.

To Mat, Phil and Chris. You were always there with help, support, encouragement and unwavering belief in my abilities. I don't know how I would have made it through this PhD without your support and motivation. You are wonderful people and outstanding scientists - academia is a better place with people like you in it.

To the rest of the Southampton Supernova Group in my time here: Charlotte, Claudia, Cosimo, Miika, Tomás, Matt G, Marcus, Zoe; and our adopted members from Portsmouth: Lizi and Maria; you have been a fantastic team to work with and I look forward to seeing all the amazing things that you continue to do in the years to come. To Matt Middleton, you may not have been my second supervisor long, but you came in at a time when I was feeling lost and your encouragement helped set me back on track.

Office 4053, thank you for being such great officemates, and to you and to my other friends in the department, thank you for making my time here so enjoyable. My particular thanks go to: Pip, Matt G, Marta, Ella, Dave, Bella, Arianna, Claire, John C, John P, Ed, Dale, Jamie, and Rory. You have all shaped my PhD experience, and I can't imagine what it would have been like without you. To Rob, you've been alongside me for all of this PhD journey, thank you for all of your encouragement and support.

To my mum, thank you for always believing that I can do whatever I set my mind to, and for always supporting me and encouraging me to do my best. You are there for me when I need you, no matter what, and for that I am always grateful.

To my dad, I know you find this sort of thing awkward (I wonder where I get it from!), so I will keep it brief. You are my best friend, my constant champion, and are always ready with advice, encouraging words of wisdom or a well-timed joke. I would simply not be where I am or who I am today without you.

Thank you.

Chapter 1

Introduction

"Low down and near the horizon hung a great, red sun, far bigger than our sun. Digory felt at once that it was also older than ours: a sun near the end of its life, weary of looking down upon that world. To the left of the sun, and higher up, there was a single star, big and bright."

— C.S. Lewis, *The Magician's Nephew*

For thousands of years, we have looked to the night sky for the purposes of navigation, artistic inspiration, spiritual guidance and simple human curiosity. On the scale of a lifetime, much of what can be seen by eye might be considered constant, however ancient astronomers noticed that this was not entirely correct. Some sources of light were moving across the sky with recorded regularity, whilst others were appearing and fading away more sporadically. Nowadays, we understand that such events are likely a mixture of comets, variable stars, novae and supernovae; but astronomers in ancient China termed them 'guest stars'.

Debated and incomplete evidence puts the first written record of these guest stars in the BC era, with tentative records for later events in 185, 386 and 393 AD. However, the first recorded evidence of an event that we would now confidently confirm as a supernova came in 1006 AD (SN1006), recorded by many independent observers across the world (Stephenson, 2017). This event is the brightest supernova on record, with numerous reports that it was visible for approximately three months, including in the day (Winkler et al., 2003b).

Over time, more of these events were observed, including SN1054 (whose remnant is the Crab Nebula), SN1572 (Tycho's Supernova) and SN1604 (Kepler's Supernova). The latter two resulted in a paradigm shift in European astronomy, as measurements by Tycho, Kepler and Galileo of their unchanging parallax indicated that they were located further away than expected, contradicting the established Aristotelian belief of

the time (Green, 2017). This was the theory that space consisted of multiple layers of a sphere, with the outermost layer being fixed, unchanging stars, whilst only the inner layers consisting of the Sun, Moon and planets could change.

The nature of supernovae remained elusive for considerable time, due to the rarity of events that were visible by eye or by the telescopes of the time. Observations of distant galaxies by Zwicky in the 1930s, using an early method of difference imaging (comparing new photographic plates to reference images of the region by eye) provided the first sizeable sample, allowing for more detailed study of their properties. This also established the name 'Supernova' to describe these events (Baade & Zwicky, 1934), originating from the Latin *nova* 'new' indicating the relatively sudden nature of the increase in luminosity of the star, and 'super' to indicate the strength of the luminosity compared to classical novae.

Supernovae are vitally important in the history and ongoing evolution of our universe. They are a key source of chemical enrichment in the cosmos, particularly through the formation of heavy elements in their explosions. The subsequent expanding shock wave of a supernova remnant distributes these elements and dust through their surroundings, enriching the interstellar medium and any nearby molecular clouds. This shock wave can trigger nearby star formation, creating a new population of stars with differing chemical signatures to those formed in the same generation as the progenitor of the supernova. However, the force of this shock wave can also suppress star formation, and destroy dust grains. This turbulent trigger and suppression means that they are one of the main factors regulating star formation in the universe.

1.1 Supernova Classification

Supernovae (SNe) are classified into a range of different types, dependent on their spectra and light-curve properties, as summarised in Figure 1.1; an outline from Turatto (2003), displaying the classification criteria for the major SN types. Initially, SNe are divided into two main groups; type I and type II, based on the absence or presence respectively of hydrogen lines in their early spectra (Minkowski, 1941, but see also Popper (1937)).

After this initial division, type I and II are further subdivided by spectral features and light-curve properties (for a review see Filippenko, 1997).

1.1.1 Type I Supernovae

Type I SNe do not contain hydrogen lines in their spectra, and are subdivided by the presence or lack of blue-shifted silicon absorption features, in particular the SiII

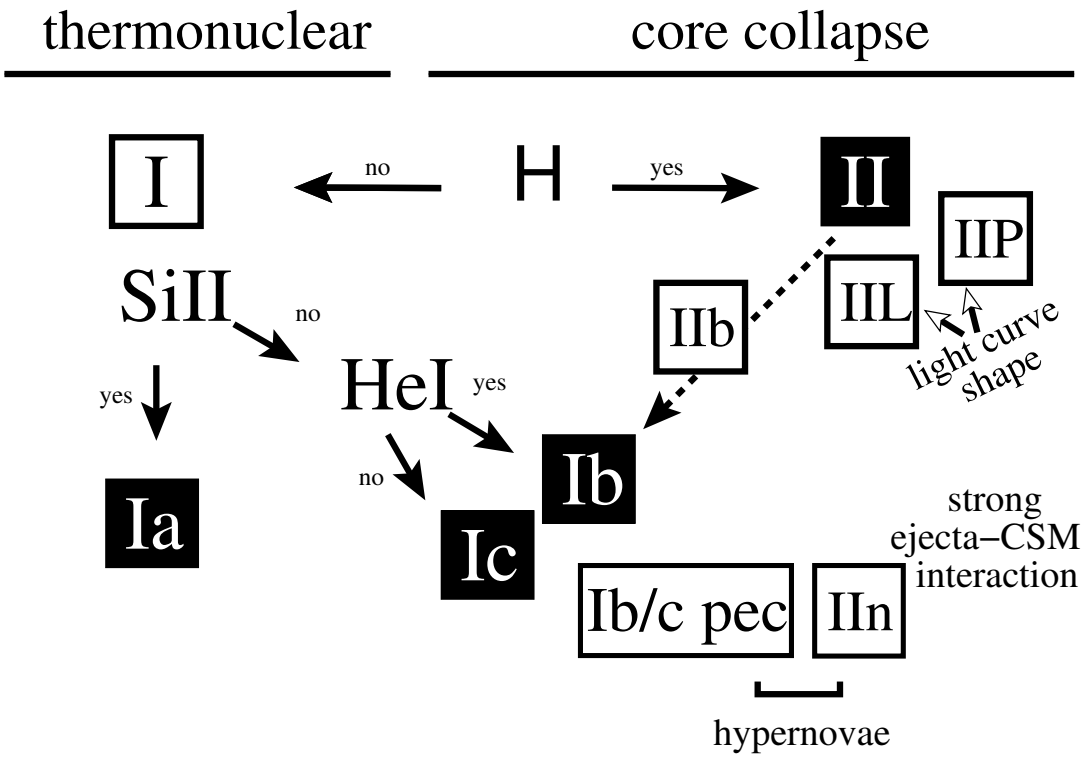

FIGURE 1.1: Supernova classification scheme; Figure 1 from Turatto (2003).

λ6347,6371Å doublet ('6150Å feature'). If this is contained within the spectra, the SN is classified as a SNe Ia, which will be discussed in detail in Section 1.2. SNe Ia are 'thermonuclear' supernovae, due to their explosion being mainly powered by thermonuclear fusion, unlike the other SNe types which mainly fall into the category of core-collapse supernovae (CCSNe). If no Si features are observed then further subdivision is made dependent on the presence of helium lines. Those containing HeI are classified as SNe Ib, and those without are Ic. These two subtypes are difficult to distinguish, and are typically grouped together as SNe Ibc. Their progenitor systems are ambiguous, but the lack of hydrogen in their spectra suggests that they result from the deaths of massive stars which have stripped envelopes due to the presence of strong stellar winds.

1.1.2 Type II Supernovae

The subclassification of type II SNe is slightly more complex, as the subtypes are dependent on the dominance of elements in spectra at later times and on the overall shape of their light-curves.

Type IIb SNe exhibit unusual behaviour, in which their spectra follow classic type II hydrogen features at the initial maximum luminosity soon after explosion, however strong helium lines, characteristic of type Ib supernovae, appear and dominate at later

times, with a secondary maximum light feature in their light-curves. This is suggestive of the progenitors undergoing a large mass loss prior to explosion, leaving an unusually thin layer of hydrogen around the helium-rich core compared to more typical type II progenitors, perhaps due to stellar winds, circumstellar interaction or the presence of a binary companion. Such objects are often considered as a transition class between type II and the stripped-envelope type Ib supernovae.

The majority of type II supernovae do not have this helium dominance at late times, and remain hydrogen dominated. These are further classified by the shape of their light-curves after maximum light, in which type IIL have a linearly decaying light-curve, whilst the type IIP show a plateauing light-curve. These are often classed together as 'normal' SN II, and appear as more of a continuum due to a number of intermediate cases with short plateaus before a linear decline. Alongside these, there are type IIn supernovae, which exhibit strong narrow emission lines in their spectra instead of the broad absorption features seen in the other types.

1.1.3 Superluminous Supernovae

In addition to these two main types, a new class of rare supernovae has been discovered: Superluminous Supernovae (SLSNe). These SNe are extremely bright ($\sim$ 100 brighter than classic SNe types), with magnitudes ≤ -21, and are considered likely to be powered by magnetar spin-down. At early times, their spectra resemble a blue continuum, but cool into a spectra resembling that of a SN Ic (see Inserra, 2019, for a review).

1.2 Type Ia Supernovae

SNe Ia are vital for use in cosmology as standardisable candles or distance indicators, and have most famously been used to reveal the accelerating expansion of the universe (Riess et al., 1998; Schmidt et al., 1998; Perlmutter et al., 1999). Thus it is important to discuss their main light-curve and spectral properties to gain understanding on why they are so important. I will expand in Section 1.3 to discuss their potential progenitor scenarios and explosion mechanisms, and detail their use in cosmology in Section 1.4.

1.2.1 Light-curves

SNe Ia are the result of the runaway thermonuclear explosion of a carbon-oxygen (CO) white dwarf (WD) (CO-WD; more on this in Section 1.3), which releases large amounts of energy ($\sim 10^{51}$erg) through the radioactive decay chain of nickel-56 (^{56}Ni). Following

Arnett's rule, the peak luminosity of the SN is proportional to the ^{56}Ni mass produced in the explosion (Arnett, 1979, 1982), corresponding to a peak absolute magnitude of ~ -19 to -20. The decay chain is as follows (Diehl et al., 2014), where τ represents the mean lifetime of the particle before decay:

$$^{56}\mathrm{Ni} \xrightarrow{\tau\sim 8.8 \text{ days}} {}^{56}\mathrm{Co} \xrightarrow{\tau\sim 111.3 \text{ days}} {}^{56}\mathrm{Fe} \tag{1.1}$$

This radioactive decay generates gamma-rays and positrons at each stage, which are reprocessed in the expanding ejecta, absorbed and re-radiated powerfully in the optical (Churazov et al., 2014; Diehl et al., 2014). As the SN ejecta expands and decreases in density, gamma rays and positrons are able to escape, and dominate at 80-200d after maximum (Maguire, 2017). This decay chain has been confirmed by studies by Churazov et al. (2014); Diehl et al. (2014) using the International GammaRay Astrophysics Laboratory (INTEGRAL; Winkler et al., 2003a), finding ^{56}Co and ^{56}Ni gamma-ray signals which agree with classic thermonuclear explosion models. Such studies also allow for analysis of the distribution of ^{56}Ni, which may help constrain SNe Ia progenitor scenarios.

Peak B-band[1] brightness is typically reached at $\sim$ 19 days from first light (Firth et al., 2015), with a slow decline after maximum light that is dependent on the absolute peak brightness and the wavelength of the observation. Bluer bands decline faster than the redder bands, which show more of a plateau before declining, i.e. the SNe reddens in optical colour over time. An example light-curve of a typical SN Ia (SN2011fe) is displayed in Figure 1.2, Figure 2 from Pereira et al. (2013).

Given that the light-curve is powered by ^{56}Ni, there is a limited range of potential luminosities due to the constraints on this process. This narrow luminosity range, combined with the observed correlations between light-curve shape and peak luminosity is key to their use as standardisable candles. I discuss this in detail in Section 1.4.

1.2.2 Spectra

As a type I SN, initial classification is made upon the lack of hydrogen in their early optical spectra. SNe Ia are then distinguished by the presence of blue-shifted and Doppler broadened absorption features at maximum light, such as for the intermediate-mass elements: calcium, oxygen, silicon and sulphur. Most noticeable are the Si II absorption lines: Si II 4130Å, Si II 5972Å, and SI II 6355Å, which can be seen in the example spectra of SN2011fe shown in Figure 1.3, Figure 8 from Pereira et al. (2013). This blue-shifting and line broadening is due to the high expansion velocities of the SN ejecta of

[1] With central wavelength $\lambda_{\text{eff}} = 445$nm, and filter full width at half maximum (FWHM) $\Delta\lambda = 94$nm (Binney & Merrifield, 1998).

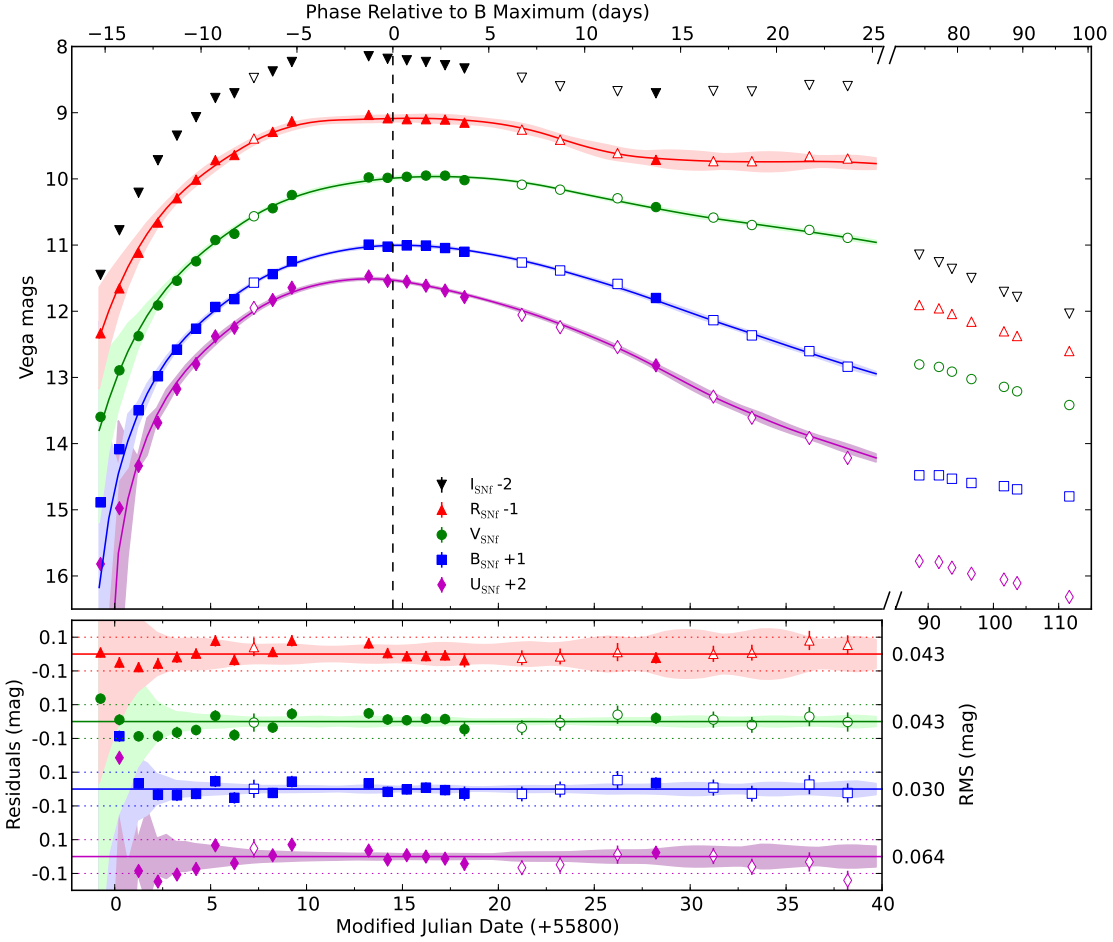

FIGURE 1.2: $UBVRI$ light-curves of SN2011fe $UBVRI$, an example of a typical SNe Ia; Figure 2 from Pereira et al. (2013).

$\sim 10^4 \mathrm{km} s^{-1}$. As the time from maximum increases, iron-group elements dominate the spectra due to the expanding ejecta and the outer layers of the ejecta begin to become optically thin at $\sim$ 150 days post-maximum, meaning that more of the ejecta core can be observed (Maguire, 2017).

1.2.3 SN Ia Sub-types

Alongside the 'normal' SNe Ia, there are some that do not follow the rest of the typical population, and are further classified and named after the archetypal example. Two of the more well-known are '91bg-like' and '91T-like' SNe (Jha et al., 2019). The first of these, the '91bg-like' SNe Ia, are fast-declining, cool, subluminous and are most commonly found in old, passive (low star formation) stellar populations. '91T-like' SNe Ia are the opposite: slow declining, hot, over-luminous SNe typically found in more star forming regions.

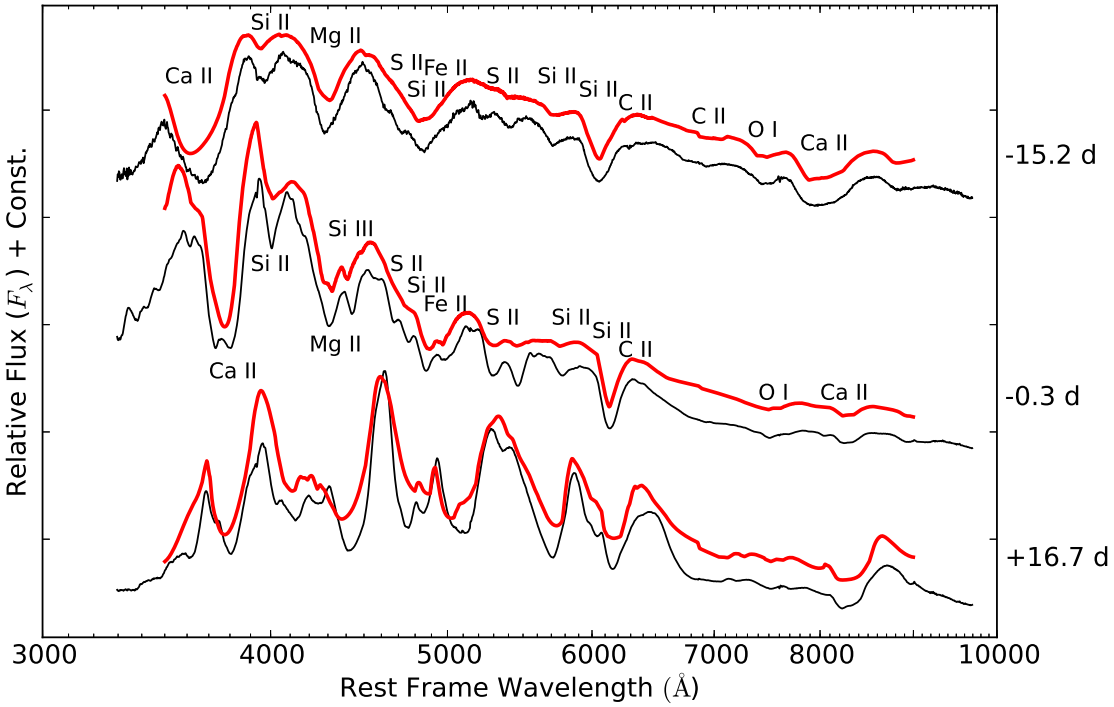

FIGURE 1.3: Early, peak, and post-peak fits to SN2011fe spectra, an example of a typical SN Ia; Figure 8 from Pereira et al. (2013). Key chemical signatures are displayed in the first two spectra.

1.3 Type Ia Progenitors

Although the explosion mechanism of SNe Ia is not fully understood, the established consensus is that it is the thermonuclear runaway of a CO-WD which has gained mass from a binary companion. By gaining mass, the WD approaches the Chandrasekhar mass ($M_{Ch} \sim 1.4 M_{\odot}$; Chandrasekhar, 1931). At this critical mass, electron density pressure can no longer support the WD, which would cause it to collapse to a neutron star. However, models suggest that a CO-WD that reaches close to this limit will begin to fuse carbon in its core, and eventually oxygen, both of which contribute to powering a subsonic deflagration flame front. This increases the temperature of the WD, igniting heavier elements, causing the runaway ^{56}Ni chain outlined above (Equation 1.1), and the release of energy as a supersonic shock wave detonation. However, changing ionisation values, temperature differences, etc. in the explosion could cause differing SNe Ia evolution and alter their observed properties.

In what is sometimes termed 'the progenitor problem', there are a range of possibilities for the nature of the progenitor, or even for multiple progenitors, which could result in such an explosion. The two historically most favoured are the single-degenerate (SD) and double-degenerate (DD) models.

1.3.1 Single Degenerate

For the SD scenario, a CO-WD accretes material from a non-degenerate binary companion star which is likely to be either a main sequence star or a red giant. Accretion continues until the CO-WD nears the Chandrasekhar mass and thermonuclear runaway is triggered (Whelan & Iben, 1973). There are two main ways for this mass-transfer accretion to occur. One is via Roche lobe overflow, in which the expanding material from the companion exceeds its gravitational capture equilibrium point (Roche lobe) and is no longer gravitationally bound, essentially 'falling' into the WD's Roche lobe and forming an accretion disk. Another way is by stellar winds from the companion star simply blowing material towards the WD, which becomes gravitationally captured, causing the WD to grow in mass.

Given that this model relies on the WD reaching the Chandrasekhar mass, the resulting explosion energy and ^{56}Ni mass should be very similar in each case. Hence, this may explain the observed relative consistency in luminosity for SNe Ia.

1.3.2 Double Degenerate

In the DD scenario, the binary system consists of two CO-WDs. This system emits gravitational waves, which causes the WDs to lose energy through angular momentum and so they spiral inwards, and eventually collide and merge, potentially exceeding the Chandrasekhar mass (Iben & Tutukov, 1984). Alternatively, there may also be accretion from one WD to the other, causing carbon detonation or even 'double-detonation' in which a shock wave from helium fusion on the surface of a WD triggers carbon detonation in the core (Woosley & Weaver, 1994).

In this case, the masses of the two merging WDs can vary significantly. Combined with the range of possibilities for the double-detonation scenario, this means that there may be more variety in the luminosities and properties of the resulting SNe Ia. This variation raises worrisome questions about the validity of SNe Ia with such progenitors as standardisable candles.

1.3.3 Uncertainties

Both of these potential scenarios result in the thermonuclear runaway required for a SNe Ia through modelling. However, there is ongoing analysis and debate over which progenitor is more likely, or if it is a combination of multiple different scenarios. As SNe Ia are found in all galaxy types (Childress et al., 2013), progenitors must be able to be formed in all galaxy types and thus over a range of timescales. Alternatively, this fact may be an indication that SN Ia come from a range of progenitors, such as a

combination of SD and DD scenarios. Without direct observation of progenitors, it is difficult to disentangle what is truly causing the SNe Ia that we observe.

1.4 Cosmology with SNe Ia

SNe Ia are most well known for their important role as distance indicators, and so are vitally important cosmological probes to understand the nature of the universe and for precision measurements of cosmological parameters.

1.4.1 The Expanding Universe

The use of SNe Ia in cosmology has as its origin the discovery that our universe is expanding. In 1915, Einstein proposed his theory of General Relativity (Einstein, 1915), with a field equation suggesting that the universe must be expanding or collapsing. However, in what he later termed his "greatest blunder," he added a cosmological constant term which forced the solution to be a static universe.

The disprovement of this static universe theory came in 1929, through the measurement of distances to galaxies using Cepheid variables by Hubble (1929). In the outer layers of Cepheid variable stars, ionised helium is opaque and increases in temperature, causing the layer to expand and cool. As the layer cools, the helium becomes less ionised and radiation escapes. At this point, gravity dominates over the expansion pressure and the star contracts; this process can then begin again. The period of this radial pulsation is well studied, and found to be proportional to the Cepheid intrinsic luminosity (the period-luminosity relationship; Leavitt & Pickering, 1912). This means that they can be used as standard candles by comparing the observed brightness to the intrinsic luminosity calculated from the pulsation. By making a comparison of the radial velocity and distance in the original 'Hubble diagram' (shown in Figure 1.4), Hubble showed that the galaxies were receding away from us, with velocities that increase proportionally with distance; i.e. more distant galaxies are receding quicker than those closest to us, indicating that the space between galaxies is increasing with time. This provided the key evidence that the universe is expanding, and the relationship became known as the 'Hubble Law'.

However, whilst Hubble (1929) is perhaps the most historically celebrated for the discovery, and his was the analysis that caused the general acceptance of the expanding universe, it was not the first indication of this. The works of Slipher (1913, 1915, 1917, 1921) provided the first empirical basis. By measuring the Doppler redshifts of spectral features from high signal-to-noise galaxy spectra, he discovered that the galaxies were receding away from one another. At the time, the implications of this discovery were

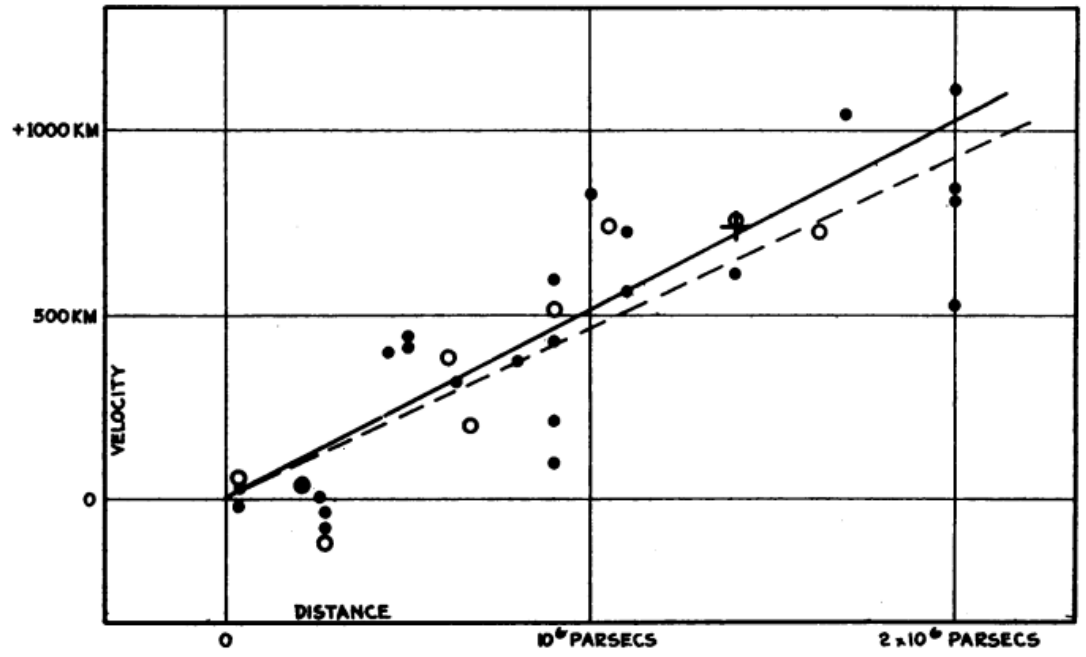

FIGURE 1.4: The first Hubble diagram; Figure 1 from Hubble (1929).

not understood. Hubble later went on to combine some of these measurements of the redshifts with his own in his 1929 work. In addition to Slipher's observations, theoretical evidence was growing, with Friedmann (1922) and Lemaître (1927) independently solving Einstein's field equations and finding a solution that requires the universe to be expanding. Further to this, Lemaître was the first to link his expanding universe solution to the redshift measurements from observations of the time, therefore providing the first real indication of the relationship between velocity and distance. However, his work was not widely known at the time, so went largely unnoticed. To honour the discovery and scientific contribution of Lemaître, in 2018 the members of the International Astronomical Union (IAU) voted in favour of renaming the 'Hubble law' as the 'Hubble-Lemaître' law.

This law follows the simple equation:

$$v = H_0 d \tag{1.2}$$

Where v is the velocity, d is distance, and H_0 is the 'Hubble constant', measured in km s^{-1} Mpc^{-1}. Hubble originally measured this value at $\sim$ 500 km s^{-1} Mpc^{-1}, but this has changed dramatically over the years as cosmological surveys have improved, with measurements today putting the value of H_0 at $\sim 70(\pm 2)$ km s^{-1} Mpc^{-1}. There is some tension between current measurements using different probes, with Planck Cosmic Microwave Background (CMB) measurements finding a value of $\sim$ 67 km s^{-1} Mpc^{-1} (Planck Collaboration et al., 2020), and Supernova H_0 for the Equation of State

(SH0ES) measurements of SNe Ia finding ~ 74 km s^{-1} Mpc^{-1} (Riess et al., 2019). However, considering how far we have come in a century since the original measurement of H_0, this is a small discrepancy that will be the subject of detailed analysis using multiple different probes over the coming years.

In modern analyses, the use of the recession velocity has been replaced by measurements of the redshift (z) of the object, as it is a more accurate measure. In its simplest terms, redshift is defined as the relative difference between the observed ($\lambda_{\text{observed}}$) and emitted ($\lambda_{\text{emitted}}$) wavelengths of chemical signatures in the spectra of the object being studied:

$$z = \frac{\lambda_{\text{observed}}}{\lambda_{\text{emitted}}} - 1 \tag{1.3}$$

The principle of standard candles relies upon the fact that their intrinsic luminosities are well-defined, thus Cepheid variables and SNe Ia are cosmologically useful for this purpose. Their luminosity distance (d_L) can be calculated through use of the inverse-square law, a rearrangement of the flux-luminosity relationship:

$$d_L = \sqrt{\frac{L}{4\pi F}} \tag{1.4}$$

Where L is the luminosity and F is the observed flux. Typically, the distance modulus (μ) is used as the distance measure in modern Hubble diagrams, which is defined as the difference between apparent (m; brightness observed from Earth)and absolute (M; the apparent magnitude if located 10 parsecs away) magnitudes, and is related to the luminosity distance measured in parsecs as follows:

$$\mu = m - M = 5 \log d_L - 5 \tag{1.5}$$

The distance modulus is particularly important in SNe Ia standardisation for use in cosmology, see Section 1.4.4. A recent example of a Hubble diagram is displayed in Figure 1.5; Figure 1 from Abbott et al. (2019), the Hubble diagram for the DES3YR SNe Ia sample, clearly showing the established relationship between distance modulus and redshift.

1.4.2 The Accelerating Expansion of the Universe

Of the uses for SNe Ia, of particular importance to cosmology was their use in the pivotal discovery that the expansion of the universe is accelerating. This culminated

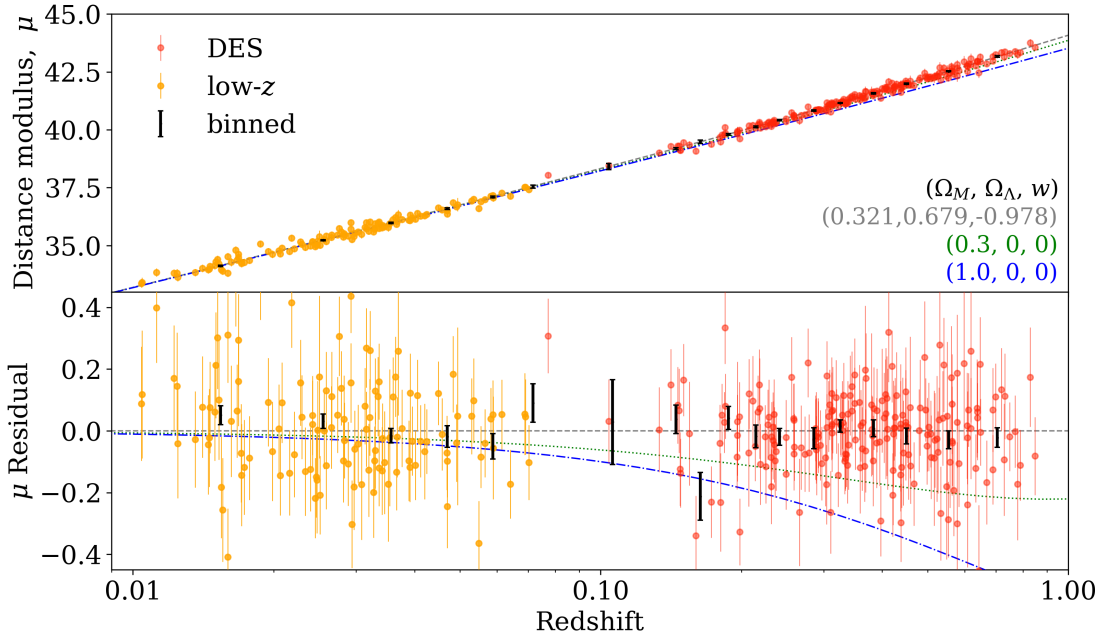

FIGURE 1.5: An example Hubble diagram for the DES3YR SNe Ia sample; Figure 1 from Abbott et al. (2019). Yellow markers indicate the addition of the supplemental low-redshift sample. The top panel is the classically-defined Hubble diagram showing the relationship between distance modulus and redshift, with cosmological fits from the BBC method (see Section 2.4.2), where the grey markers are the best-fit, and green and blue show models with no dark energy and alternate matter densities Ω_m. The lower panel illustrates the residuals to the best-fit model.

in the award of the 2011 Nobel Prize in Physics to the leads of the two independent research teams involved: Saul Perlmutter, Brian Schmidt and Adam Riess.

In the late 1990s, two independent groups: the Supernova Cosmology Project (SCP; Perlmutter et al., 1997) and the High-Z Supernova Search Team (HZT; Schmidt et al., 1998) observed samples of high-redshift SNe Ia in order to measure the expected deceleration of the universe expansion due to gravitational interaction. Contrary to their expectations, they found that the high-redshift SNe were fainter than should be expected in a matter-dominated universe, suggesting that the universe must be accelerating (Riess et al., 1998; Perlmutter et al., 1999). The distances of the high redshift SNe Ia were too large when compared to nearby objects, meaning that not only are more distant galaxies receding quicker than those closest to us, but they are accelerating faster too. This result also implied that there must be something causing this acceleration, such as a cosmological constant or the presence of dark energy which dominates over

matter (Garnavich, 2017). The measurement of the accelerating expansion of the universe was later confirmed by complementary analyses of the CMB and of large-scale galaxy distributions.

1.4.3 Extracting H_0 and ω from SNe Ia data

To obtain the Hubble constant (H_0) from SNe Ia data, the direct distance-ladder method is used (e.g. Freedman & Madore, 2010, for an overview). In this method, distances to nearby SNe Ia host galaxies are typically determined through measurements of Cepheid variable stars. By measuring the periods of the Cepheids, luminosities can be obtained following the period-luminosity relationship (Leavitt & Pickering, 1912) outlined in Section 1.4.1. Comparing the observed brightness of each Cepheid to their intrinsic luminosities enables distances to their host galaxies to be obtained. By choosing a sample of host galaxies that contain both a Cepheid and a SNe Ia, Cepheid distances can be used as an anchor to calibrate SNe Ia distances. After calibration, the SNe Ia themselves can then be used to measure the distances out into the Hubble flow, at higher redshifts than possible with the Cepheids, by using them as 'standardisable candles' given their intrinsic luminosities are known.

For each SNe, the light-curves are standardised following the techniques outlined in the following section, Section 1.4.4. As intrinsic luminosity is known, and apparent luminosity can be measured, the difference can provide the luminosity-distance of the supernova. The resulting luminosity distances (or the distance modulus) and redshifts can then be plotted in a Hubble diagram (see Figure 1.5), and cosmological parameters (such as H_0 and ω, the dark energy equation of state) derived by fitting to the data.

However, Cepheid variable stars are typically found in star-forming, face-on spiral galaxies, whilst SNe Ia are found in all galaxies, meaning that there is a selection effect. Thus the fraction of SNe Ia in star-forming environments is higher in the Cepheid calibration sample than in the Hubble flow. If the calibration sample is not representative of the main sample, it could cause a potential bias in the measurement of cosmological parameters. As discussed in detail in Section 1.5, there are known correlations between host galaxy parameters and SN Ia luminosities, which will affect the Cepheid sample differently to the Hubble flow sample. This means that light-curve standardisation may be different between the two samples and thus may not be accurate, biasing the fit of H_0. As mentioned in Section 1.6, by measuring the local star formation (a proxy for age) around a sample of SNe Ia, Rigault et al. (2020) found that SNe Ia in younger environments were fainter than those in older environments. Given that the average age of stellar populations, i.e. the fraction of young stars, evolves with redshift, this indicates an age bias when comparing the lower redshift Cepheid sample to the higher redshift Hubble flow sample. If the measured brightness offset between young and old environments is consistent with redshift, and the fraction of young SNe changes between

samples or as a function of redshift, the SNe Ia magnitudes will not be standard and so will bias the cosmology. This effect has been shown to bias ω and H_0 by approximately 3% (Rigault et al., 2020). Accounting for this bias can reduce the Hubble tension (Section 1.4.1) from $\sim 4\sigma$ to 2σ.[2]

1.4.4 Standardisation

SNe Ia have characteristically low intrinsic peak absolute magnitude dispersion, ~ 0.35 mag (e.g. Riess et al., 1996), even considering the potential differences in progenitors and explosion mechanisms outlined. However, in the realm of precision cosmology, this dispersion is too large and thus additional corrections need to be made to their light-curves to improve their standardisation.

As illustrated in the left-hand panel of Figure 1.6, a plot showing a range of B-band light-curves for a typical sample of SNe Ia, it can be seen that there are correlations between the maximum intrinsic brightness and the light-curve shape. The brightest SNe Ia decline slower, shown by the wider light-curves (or larger 'stretch'), defined as the 'brighter-slower' relation (Phillips, 1993). This was found by calculating the difference in B-band magnitude at maximum light and 15 days after maximum light ($\Delta m(B)_{15}$). In addition, the maximum B-band brightness correlates with the SN intrinsic B-V colour at maximum light, with the redder SNe Ia being dimmer. This is defined as the 'brighter-bluer' (Riess et al., 1996; Tripp, 1998) relation, and has been found to be the dominant correction. Correcting for these two relationships can achieve a remaining $\sim$0.14 mag dispersion in SNe Ia luminosities (Scolnic et al., 2018). This is illustrated by the right-hand panel of Figure 1.6.

The cause of the 'brighter-slower' relation is likely due to factors relating to the decay chain of ^{56}Ni. The ^{56}Ni mass governs the peak luminosity of the light-curve, but it is thought that the light-curve width is dependent on the amount of time it takes photons to escape the SN ejecta (the diffusion time), which is related to the amount of ^{56}Co and ^{56}Fe formed, and the temperature of the ejecta (Hoeflich et al., 1996; Kasen & Woosley, 2007). If more ^{56}Co and ^{56}Fe are formed, the opacity will be higher causing the diffusion time to be longer, and so the light-curve will be wider.

There are two main potential causes of the 'brighter-bluer' relation. One possibility is that it is due to dust attenuation causing reddening and dimming of the light-curves. Alternatively, it may be something intrinsic to the SNe themselves, such as differing progenitor scenarios or explosion characteristics. Of course, one must also consider the possibility of a combination of these effects causing the relationship that we observe.

[2] M. Rigault, 'Environmental Bias and The H_0 Tension', SNIa Cosmology Analysis Meeting, slides available at: https://kicp-workshops.uchicago.edu/2019-SCAM/depot/talk-rigault-mickael.pdf

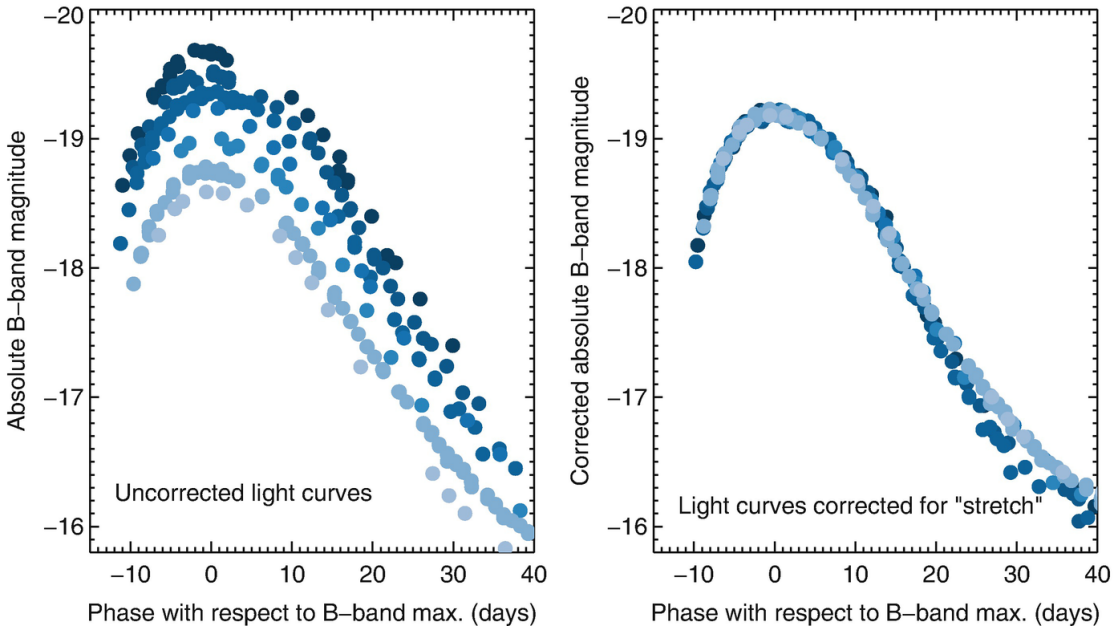

FIGURE 1.6: *B*-band light-curves of a sample of SNe Ia, showing the differences in scatter before and after light-curve corrections; Figure 2 from Maguire (2017). Data taken from the CfA (Hicken et al., 2009b) and CSP (Stritzinger et al., 2011) surveys.

Of the resulting $\sim$ 0.14 mag dispersion, $\sim$ 0.08–0.10 mag remains that cannot be explained by observational uncertainties (Brout et al., 2019b) which are dependent on the individual surveys. This indicates either the limit to which SNe Ia are standardisable, or that there are further brightness corrections required. This latter possibility could arise from astrophysical uncertainties in the SN Ia progenitor mechanisms, explosion physics, and/or environment (Maoz et al., 2014; Maguire, 2017; Livio & Mazzali, 2018). This is a key motivator behind studies, such as this thesis, of environmental effects in SNe Ia cosmology.

1.4.4.1 The Tripp Equation

In cosmological analyses, light-curve fitters, such as SALT2 (see Section 2.4) are used to account for these corrections. This allows for the estimation of the observed distance modulus (μ_{obs}) as follows:

$$\mu_{obs} = m_B - M_0 + \alpha x_1 - \beta c \tag{1.6}$$

Where 'stretch' (x_1), 'colour' (c) and the observed apparent magnitude (m_B) are for each SN Ia event. The terms α, β and M_0 are global nuisance parameters describing the overall SN sample population determined in the cosmological fit, found by minimising the residuals in the Hubble diagram.

In SNe Ia cosmology, it is typical to analyse the 'Hubble residual'. This is defined as the difference between the measured distance modulus ($\mu_{\rm obs}$) to each event, and the distance modulus calculated from the best-fit cosmology to the SN sample ($\mu_{\rm cosmo}$), i.e.:

$$\Delta\mu = \mu_{\rm obs} - \mu_{\rm cosmo}, \tag{1.7}$$

1.5 Host Properties

As discussed above, despite corrections for the light-curve properties x_1 and c, and for observational uncertainties, there remains a $\sim$ 0.08–0.10 mag dispersion in the luminosities of SNe Ia, which is believed to be due to uncertainties in the progenitors, explosion physics, and environments. The desire for an improved standardisation has motivated decades of work searching for correlations between the properties of SNe Ia and the closest proxy we have for their progenitor stellar populations: their host galaxies.

Given that SNe Ia are found in all galaxy types, early studies of their host galaxies searched for potential trends between SN properties and host galaxy morphological types. Filippenko (1989) found that elliptical galaxies host SNe Ia with a smaller dispersion in the decline rate, which they suggest is unlikely to be due to the role of dust or gas in the galaxy. This was confirmed by Hamuy et al. (1996) who found that SNe Ia in spiral galaxies have a wide range of potential decline rates, with no slow-declining SNe Ia in elliptical galaxies in their sample, again even with dust reddening. They also found that the brightest SNe preferentially occur in late-type galaxies (spiral and irregular). Similarly, by measuring the blueshifts in the Si II feature for a sample of SNe Ia, Branch & van den Bergh (1993) observed that SN Ia with low expansion velocities ($< 9500 {\rm km s}^{-1}$) all occurred in early-type galaxies (elliptical). These studies speculated that their findings indicate a link between SNe Ia brightness, decline rate, expansion velocity and progenitor age, suggesting differences in stellar populations could produce the observed relationships. Filippenko (1989) in particular advised that narrow-band Hα imaging should be obtained to measure the distribution of HII regions close to each SN, to study the immediate stellar population environments of SNe Ia, which has been taken on board by the analyses in Section 1.6.

More recently, strong evidence has been found that the c- and x_1-corrected brightness, and thus Hubble residual, correlates with the stellar mass ($M_{\rm stellar}$) of the SN Ia host galaxy: SNe Ia in high-mass hosts standardise to brighter luminosities than those in lower-mass hosts (e.g. Kelly et al., 2010; Lampeitl et al., 2010; Sullivan et al., 2010), in a relationship that has become known as 'The Mass Step'. This empirical dependence of the corrected Hubble residuals on the SN Ia host galaxy $M_{\rm stellar}$ has now been studied extensively (e.g., Gupta et al., 2011; Childress et al., 2013; Johansson et al., 2013; Rigault

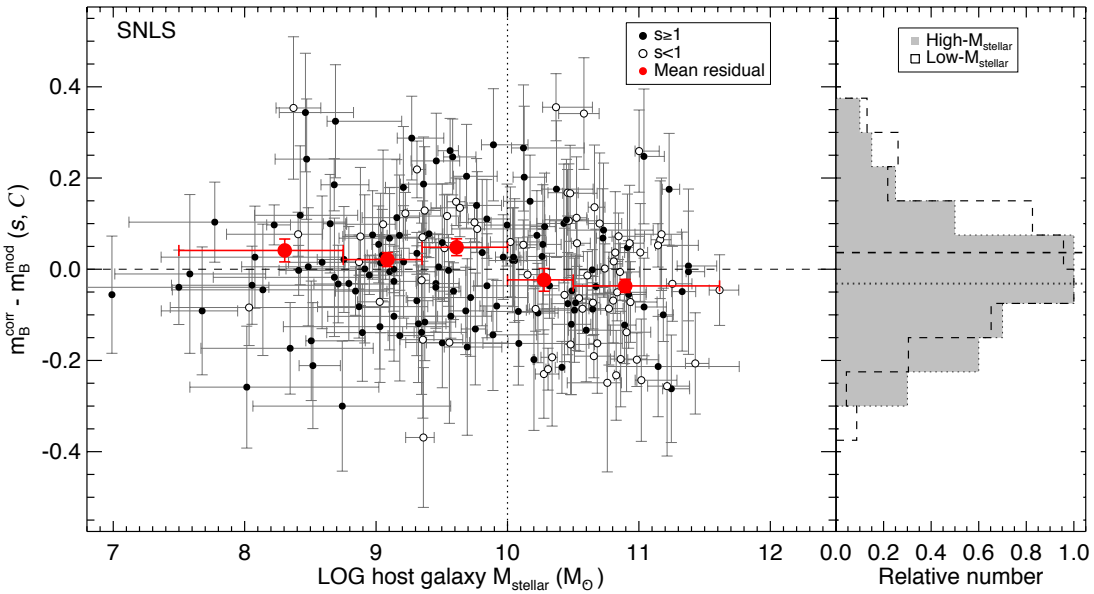

FIGURE 1.7: An example of the host galaxy mass step; Figure 4 from Sullivan et al. (2010). The red markers represent the bin mean Hubble residuals.

et al., 2013; Betoule et al., 2014; Pan et al., 2014; Scolnic et al., 2014; Campbell et al., 2016; Wolf et al., 2016; Uddin et al., 2017; Jones et al., 2018a,b; Roman et al., 2018; Scolnic et al., 2018; Brout et al., 2019b; Kim et al., 2019; Rigault et al., 2020; Smith et al., 2020b), with modern samples finding a step in calibrated SN Ia magnitude of ~ 0.06 mag at around $\log(M_{\rm stellar}/M_{\odot}) \simeq 10$. An example mass step is presented in Figure 1.7, Figure 4 from Sullivan et al. (2010), where a clear difference in bin mean Hubble residuals of 4σ is observed between low and high mass galaxies. Sullivan et al. (2010) suggested that this should be corrected for in SNe Ia cosmological analyses by including a host galaxy correction term in the cosmological fit, and in applying two different corrections for high and low mass hosts, they improved the cosmological fits at $\sim 4\sigma$, removing this host $M_{\rm stellar}$ dependency in their data.

The astrophysical reason(s) for this effect is unclear, however it is known that the $M_{\rm stellar}$ of a galaxy correlates with the stellar ages, gas-phase and stellar metallicities, and dust content of its stellar populations (Tremonti et al., 2004; Gallazzi et al., 2005; Garn & Best, 2010a; Bravo & Badenes, 2011; Zahid et al., 2013), suggesting that the trends between corrected SN Ia brightness and host stellar mass could be due to differences in intrinsic SN progenitor properties (e.g., age or metallicity; Timmes et al., 2003; Röpke & Hillebrandt, 2004; Kasen et al., 2009; Bravo et al., 2010) or dust (e.g., Brout & Scolnic, 2021). The physical nature of the dominant underlying effect remains controversial.

As one of the key potential causes of this mass effect is thought to be dust, studies of host galaxy environments in the NIR may provide important insights. The NIR ($1 < \lambda < 2.5\mu m$) is less prone to extinction from dust than measurements in the optical, so the presence of a mass step in such wavelengths could rule out or constrain a dust-based explanation. Currently, analysis on this is inconclusive, with different teams (Ponder et al., 2020; Uddin et al., 2020; Thorp et al., 2021; Johansson et al., 2021) finding contradictory results, with some finding a mass step in the NIR, and some not. This is an important avenue for further research, especially as we move to the next generation of large-scale SNe surveys, and particularly those such as the VISTA Extragalactic Infrared Legacy Survey (VEILS[3]) and those with the Nancy Grace Roman Space Telescope (Hounsell et al., 2018) which are primed for NIR observations.

In addition to looking at the M_{stellar} of the galaxy, some studies (e.g. Lampeitl et al., 2010; Sullivan et al., 2010; D'Andrea et al., 2011; Childress et al., 2013; Pan et al., 2014; Wolf et al., 2016; Uddin et al., 2017; Kim et al., 2019) also consider other environmental properties such as the star formation rate (SFR) or more typically the specific star formation rate (sSFR; SFR per unit M_{stellar}). These are correlated with M_{stellar}; the most massive galaxies tend to be more passive, with the lowest sSFR, whilst the lower mass galaxies tend have more recent or ongoing star formation, but this parameter provides another, complementary, way to probe the stellar populations of the SN host galaxies, and may also provide insight into potential ages of the host stellar populations. Similarly sized steps to the mass step have been found for global host galaxy sSFR, with evidence that SNe Ia in low sSFR galaxies are brighter on average than those in higher sSFR galaxies after corrections at $> 3\sigma$.

The result of these SNe Ia host galaxy environment analyses is the addition of an extra standardisation term in Equation 1.6 for typical cosmological analyses, γG_{host}, where $G_{\text{host}} = \pm 1/2$ and the sign depends on the value of a SN Ia host galaxy property, and γ is analogous to α and β. This step function changes sign at some value of the SN host global property, which we label as the 'division point'. For example, when using M_{stellar}:

$$G_{\text{host}} = \begin{cases} +1/2, & \text{if } \log(M_{\text{stellar}}/M_{\odot}) > M_{\text{step}} \\ -1/2, & \text{if } M_{\text{step}} < \log(M_{\text{stellar}}/M_{\odot}) \end{cases} \tag{1.8}$$

where M_{step} is the division point.

Thus for many cosmological analyses, Equation 1.6 becomes:

$$\mu_{obs} = m_B - M_0 + \alpha x_1 - \beta c + \gamma G_{\text{host}} \tag{1.9}$$

[3]https://people.ast.cam.ac.uk/ mbanerji/VEILS/index.html

In this thesis I do not fit for γ, instead I calculate $\mu_{\rm obs}$ without the mass step to test physics and the potential cause of the SN Ia residual dispersion by studying environmental properties in order to infer γ.

1.5.1 Searching for host galaxy steps

In most SNe Ia host galaxy cosmological analyses, a single step is normally fitted at the $M_{\rm step}$ division point instead of a continuous trend function. In Childress et al. (2013), a step function was found to better fit the data than a continuous linear trend, driving the use of such steps in later analyses. Additionally, by using a step function, host galaxy analyses assume that environmental dependencies are caused by two different populations of SNe Ia in differing environments. As discussed in detail in Briday et al. (2021), this assumption is outlined as follows:

- There are two populations of SNe Ia, which differ on average in intrinsic properties, such as magnitude or Hubble residual.
- A host galaxy environmental property can act as a tracer to differentiate between these two populations.

This means that the size of the step will depend on the intrinsic property measured and how well the tracer can differentiate between the two populations.

Typically, SNe host galaxy analyses will split into the two populations at the sample median of the environmental property being measured. However, for host galaxy $M_{\rm stellar}$ many use $M_{\rm step} = 10^{10} M_{\odot}$ to be consistent with Sullivan et al. (2010). The use of this division point is discussed in Section 3.2.3.1 and Section 4.2.4, with a potential explanation of why such a step location for $M_{\rm stellar}$ could differentiate between SNe populations and tests of a range of division points.

When analysing the magnitude of the steps, SNe Ia host galaxy studies typically regard any steps below 1σ in significance as clearly 'not a step', with statistically significant steps being $\geq 3\sigma$. Those that fall between 1 and 3σ are more tentative and are open to discussion and interpretation.

1.6 Local Properties

Focusing on the 'local' host galaxy properties close to the SNe position, rather than the global properties of the host galaxy, perhaps provides a more immediate census of the stellar populations from which the progenitor was drawn (Rigault et al., 2013, 2015, 2020; Galbany et al., 2018; Jones et al., 2015, 2018b; Kim et al., 2018, 2019; Roman

et al., 2018; Rose et al., 2019). Global galaxy properties are weighted by surface brightness, meaning that global measurements are most representative of the properties of the brightest galactic regions, and thus may not be accurate measurements of the true environment of the progenitor and resulting SN (Rigault et al., 2013). For example, a SNe Ia may be located within a locally star forming region within a globally passive galaxy, or vice versa. On the other hand, any correlations with local host properties are diluted if the birth place of the progenitor differs from the region the SN explodes, an effect that becomes larger with longer delay times. Methods to obtain local environmental properties are survey and redshift dependent, as they rely upon the resolution and quality of the environmental data available. Such analyses are typically undertaken using local aperture photometry (such as that used in this thesis) within a specified radius dependent upon survey imaging, or through Integral Field Spectroscopy (IFS), where a spectrum is obtained by the survey for each pixel in the field.

By using a sample of low redshift ($z < 0.08$) SNe data from the Nearby Supernova Factory (Aldering et al., 2002) to measure nebular Hα emission from HII regions (as a tracer of SFR), Rigault et al. (2013) found correlations between the local SFR within a 1 kpc radius around each SN and the SN Ia corrected magnitude, in which SNe Ia in locally star-forming environments are fainter than those in locally passive environments by ~ 0.094 mag. This relationship was later confirmed using the 'Constitution' SN sample (Hicken et al., 2009b) combined with Far Ultra-Violet (FUV) flux measured by the Galaxy Evolution Explorer satellite (GALEX), an indicator of star formation local to the SN (Rigault et al., 2015). Curiously, Jones et al. (2015) also used FUV and Hα measurements, but found no step in star formation from a sample of hosts in JLA and HST, suggesting that sample selection may have an effect on trends for local environments. However, subsequent results have confirmed local steps using different probes of the environment.

Roman et al. (2018) analysed to higher redshift ($z < 1$) using the local rest-frame $U - V$ colour from photometry of the host galaxy within a 3 kpc radius aperture at the SN Ia position in place of Hα, using a compilation of Supernova Legacy Survey (SNLS; Astier et al., 2006) 5-year data, the Sloan Digital Sky Survey (SDSS; Sako et al., 2018) SN survey, and various low-redshift surveys. $U - V$ is an excellent probe for such analyses as it is an indicator of the luminosity-weighted age of the stellar population, and the use of photometry-based measurements allows for measurements of local properties spanning the redshift range of the SNe Ia Hubble diagram. The step in corrected magnitude from blue to red environments was 0.091 ± 0.013 mag, comparable to the global galaxy mass step found by Childress et al. (2013), and is shown as an example of a local step in Figure 1.8. This step persists when a correction for the mass step is performed first, although decreases to 0.057 ± 0.012 mag. Using a larger low-redshift SN Ia sample (including SNe Ia from the 'Foundation' sample; Foley et al., 2018), Jones et al. (2018b) found similar-sized steps to Roman et al. (2018) using local stellar mass

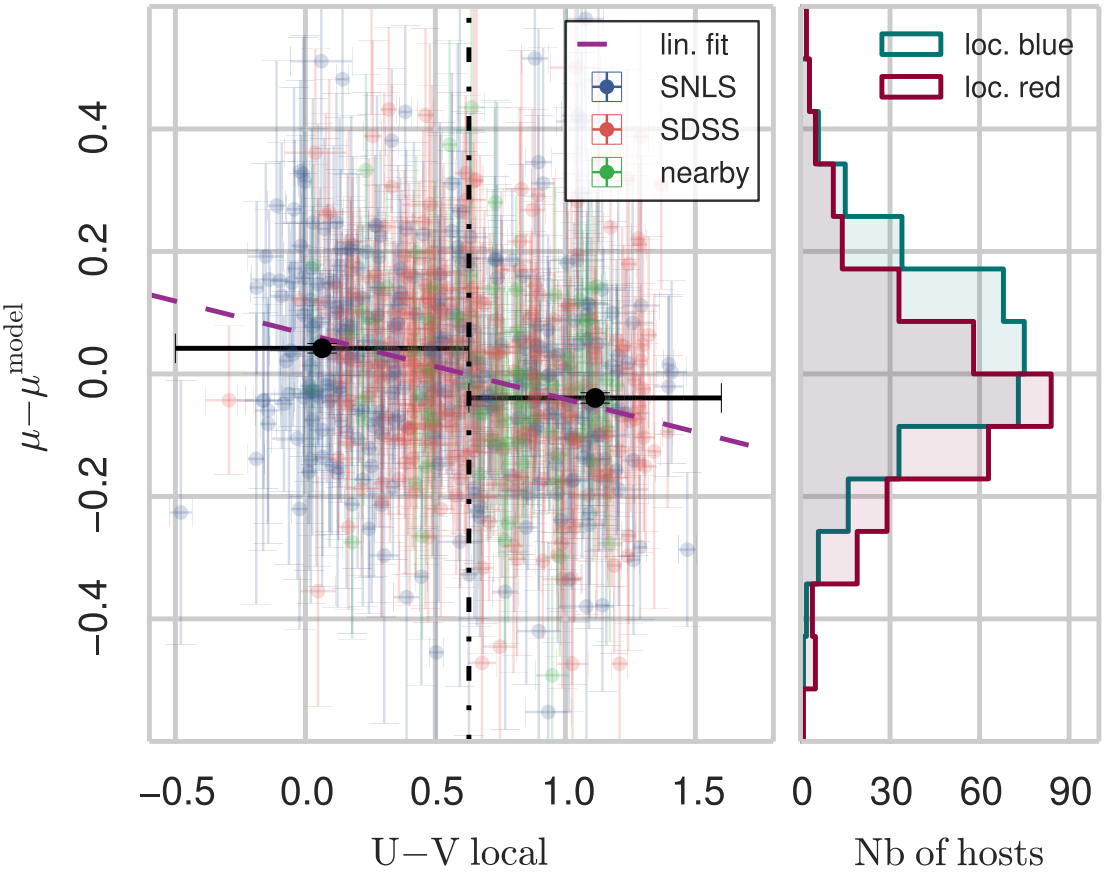

FIGURE 1.8: An example of a local $U - V$ step; Figure 13 from Roman et al. (2018). The black markers indicate the bin mean Hubble residuals.

and local $u - g$ colour, although at lower significance. A further nuance was that low-redshift SNe Ia discovered in targeted galaxy surveys showed no local stellar mass or colour steps, while SNe Ia located in the 'rolling' Foundation survey similar to SNLS or SDSS showed a significant local step. Kim et al. (2018, 2019) also found a similar bias using local SFR for a sample of SNe Ia from the YOnsei Nearby Supernova Evolution Investigation (YONSEI) SN Catalog (Kang et al., 2016).

Rigault et al. (2020) developed these ideas further by statistically classifying a sample of SNe Ia from the Nearby Supernova Factory into younger or older environments based on the local specific star formation rate (LsSFR) measured within a distance of 1 kpc from each SN. They found that SNe in younger environments are fainter at 5.7σ significance than those in older environments after light-curve corrections. As the average age of stellar populations evolve with redshift, this could create a bias in cosmological analysis, including on the measurement of the Hubble constant, H_0. Understanding and accounting for environmental biases may help to resolve the current Hubble Tension.

Rose et al. (2019) estimated the stellar population age of the host and local environments of a sample from SDSS, finding a step in local stellar age of 0.114 ± 0.039 mag at ~ 8 Gyr. Recently, expanding on this analysis, Rose et al. (2021a) suggest that combining corrections based on host galaxy stellar mass and local stellar age provides the best improvement to SNe Ia standardisation at $> 3\sigma$, reducing the unexplained scatter by $\sim 10\%$. Larger upcoming surveys will be able to provide further data to better constrain this result.

Regardless of whether corrections should be global, local or a combination of the two; whether they should be for mass, SFR, colour, age or something else; it is evident from these prior analyses that corrections based on host galaxy environments are an important avenue of research for improving the standardisation of SNe Ia for use in cosmology.

1.7 Thesis Outline

In this thesis, I study the effects of the environments of SNe Ia on their cosmological parameters, focusing particularly on their Hubble residuals. This allows for greater understanding of their remaining magnitude dispersion after current standardisation, and suggests further relationships to account for when using them as cosmological distance indicators. This analysis uses data from the Dark Energy Survey, which provides excellent photometric calibration, redshift coverage, and large sample size, meaning that it acts as a fantastic testing ground for the next generation of large supernova surveys.

In Chapter 2, I discuss the Dark Energy Survey samples which were used for my analysis, the DES-SN survey and spectroscopic follow-up, light-curve fits, image stacking, and discuss the difference between the spectroscopically-confirmed (DES3YR) and photometrically-confirmed (DES5YR) samples. This chapter also presents the method used in the analysis, split into two key sections, the first covering the aperture photometry used for both global and local host galaxy measurements, and the other discussing the SED fitting technique used to obtain the environmental properties.

In Chapter 3, the results of applying the method to the Dark Energy Survey Three-Year spectroscopically-confirmed sample are presented. I discuss the photometry from this sample and the selection requirements that were used, and present the results from the analysis of environmental dependence of SN Ia luminosites, covering global vs. local measurements, SN properties vs. environments, and Hubble residuals. I explain the systematic tests applied of changing the local aperture radius, applying different cosmological corrections, and using different environmental properties such as the sSFR.

I discuss the use of different rest-frame colours, and splitting the sample into subsamples based on SN x_1 and c, or environmental properties. I conclude this section by explaining the cosmological implications of this analysis.

In Chapter 4 I present the results of applying the same method to the larger Dark Energy Survey Five-Year photometrically-confirmed sample. Similarly to Chapter 3, I discuss the photometry and selection requirements for this photometric sample, and present the results from analysing the environmental dependence of SN Ia luminosities. In this chapter, I also investigate changing the local aperture radius, and looking at different environmental properties.

In Chapter 5 I continue the DES5YR analysis from the previous chapter, but dedicate the entire chapter to investigating the SN c, and the relationship it has with environmental properties, based on the findings in Chapter 3.

In Chapter 6 I introduce the concept of SNe Ia Siblings (multiple SNe Ia hosted in the same galaxy), and investigate why they are important and how they can be used to test global vs. local environments in cosmological standardisation. I give an overview of the DES siblings, and analyse the differences in sibling local properties compared to their cosmological parameters.

Finally in Chapter 7 I conclude by wrapping up the major findings from my analysis before making final closing remarks on the thesis as a whole, and presenting my thoughts on the future of such analyses.

Chapter 2

Data and Methods

In this chapter I describe the data used for this thesis, and the methods that were used to obtain my results. I begin by describing the Dark Energy Survey, with particular focus on the supernova survey, and go on to describe the image stacking used to obtain host galaxy photometry. I continue by discussing the differences between the spectroscopic three-year supernova sample, and the photometric five-year supernova sample, before presenting the cosmology fitting used to obtain supernova cosmological parameters. I then describe the two different techniques used in this analysis to obtain photometry for the SNe host galaxies and for local regions centred on the SNe locations. I then discuss how these photometric measurements are used to measure environmental properties through the use of spectral energy distribution (SED) fitting.

2.1 The Dark Energy Survey

The Dark Energy Survey (DES; Dark Energy Survey Collaboration et al., 2016), was a six-year optical imaging survey which covered $\sim 5100\,\mathrm{deg}^2$ of the southern hemisphere with the aim of constraining the measurements of cosmological parameters, such as the dark energy equation of state parameter ω, through the combination of surveys of weak gravitational lensing, large scale structure, galaxy clusters and SNe Ia. The data was obtained using the 4-m Blanco telescope at the Cerro Tololo Inter-American Observatory (CTIO), equipped with the 520 megapixel wide-field Dark Energy Camera (DECam; Flaugher et al., 2015) with a $0.263''$ per pixel resolution and a $3\,\mathrm{deg}^2$ field of view.

2.1.1 DES-SN

The five-year transient survey within DES ('DES-SN'), optimised for the detection and measurement of SNe Ia for cosmology, was designed to obtain several thousand SN

Ia light-curves over $0.2 < z < 1.2$ (Bernstein et al., 2012; Brout et al., 2019a). In *griz* filters and with a mean cadence (interval between observations) of $\simeq 7$ days over the five annual, ~ 5.5 month observing seasons (Smith et al., 2020a), DES-SN observed ten $2.7\,\mathrm{deg}^2$ pointings consisting of eight 'shallow' fields (E1, E2, S1, S2, C1, C2, X1, X2; with an average single-epoch depth of $23.5\,\mathrm{mag}$[1]) and two 'deep' fields (C3 and X3; with an average single-epoch depth of $24.5\,\mathrm{mag}$[2]), where each observation consisted of a single DECam pointing. The survey found SNe Ia at a range of intermediate and high redshifts.

DES-SN has two key features that are of great advantage for cosmology, and for the host environment analysis undertaken in this thesis. The first is that the z-band response of DECam means that it has a wide redshift coverage, allowing for high redshift ($z \sim 1$) rest-frame optical light-curves. This provides a range of environments with SN candidates identified and targeted using algorithms principally agnostic to environment (Kessler et al., 2015; Smith et al., 2020a), and enables it to act as a testing-ground for the next generation of large scale supernova surveys. Secondly, as the largest systematic uncertainty in SN Ia cosmology (Scolnic et al., 2018), having good calibration is of vital importance. DES-SN is very well calibrated, with a 'DES Science Requirement' ensuring that the absolute calibrations and colours are at 0.5% (Smith et al., 2020a).

The SN data were processed by the DES Data Management team (DESDM; Morganson et al., 2018) for routine image detrending, such as: bias-subtraction, flat-fielding, masking bad pixels, correcting crosstalk, and masking the effects of cosmic rays, satellites etc. Transient events were then identified from the resulting images using the DES-SN Difference Imaging Pipeline (DIFFIMG; Kessler et al., 2015). DIFFIMG compares a coadded image of new observations in a given filter to previous reference images to create a 'difference image' from which new sources are identified. These detected sources are analysed by AUTOSCAN (Goldstein et al., 2015), a supervised machine-learning algorithm, which assigns a likelihood to each object of being a real transient, thereby removing a large fraction of artefacts from the data.

2.1.2 Spectroscopic Follow-up

Using the Photometric Supernova IDentification software (PSNID; Sako et al., 2011), each candidate was photometrically classified to prioritise their follow-up spectroscopy. By comparing each candidate light-curve to a variety of common SN templates, the probability that they are a SN Ia was obtained. This was done in real-time, adding each new epoch of photometry as it was taken, and running both with and without knowledge of the photometric redshift of the host galaxy (see Section 2.1.3)[3].

[1] Where depth refers to the magnitude at which 50% of artificially injected point sources are recovered, see Kessler et al. (2015).

[2] See Smith et al. (2020a) for a list of field centres and overlapping data.

[3] See Bonnett et al. (2016) for photometric redshift estimators used during the survey.

It was not possible to get spectroscopic time for each SN, and some were too faint, meaning that SN spectroscopy was obtained for only a subset of the data. This created the three-year spectroscopically-confirmed sample 'DES3YR', which acts as a complementary probe to the larger photometric sample 'DES5YR', enabling greater understanding and constraint of biases and systematics, and a testing-ground for analyses. The differences between the two samples are discussed in detail in Section 2.3.

A variety of telescopes were used for live spectroscopic follow up (see Smith et al., 2020a, for full details) including: the 4-metre Anglo-Australian Telescope (AAT), the European Southern Observatory Very Large Telescope (VLT), Gemini, Gran Telescopio Canarias (GTC), Keck, Magellan, Multiple Mirror Telescope (MMT), and South African Large Telescope (SALT). This enabled redshift measurements, classifications, and host galaxy information directly from the SN spectroscopy.

Additionally, the OzDES programme (Yuan et al., 2015; Childress et al., 2017; Lidman et al., 2020) measured the spectroscopic redshift for thousands of DES-SN host galaxies using the AAT. This provides the majority of spectroscopic redshifts for the DES photometric sample (DES5YR). A subset of host galaxy redshifts are obtained from external catalogues of prior surveys that overlapped with the DES-SN fields.

2.1.3 Host Galaxy Matching

To match transients to host galaxies, the directional light radius method (DLR; Sullivan et al., 2006; Gupta et al., 2016) is used to identify the most likely host. The DLR is a measure of the separation distance between the SN and each galaxy, normalised by the apparent size of the galaxy light profile (obtained from high-quality depth-optimised coadded images; Wiseman et al., 2020) being considered, in terms of the elliptical radius along a line connecting the SN to the host center. An example illustrating the difficulty with matching the SN to its host galaxy is presented in Figure 2.1. As can be seen in the figure, a SN is located between two galaxies, and it is not clear by eye which is the host. Whilst the center of the smaller, right-hand galaxy is closer in angular separation, it is not clear if it is at the same redshift, so may be in the background. On the other hand, the center of the larger galaxy is further away, but the galaxy light profile extends out closer to the observed SN location. Using the DLR method, this larger galaxy would be designated as the host.

The DLR is calculated for all galaxies within a radius of 15″ of the SN, and the galaxy with the lowest DLR is assigned as the host. However, it is additionally required that $DLR \leq 4$, otherwise the SN is classified as hostless (Smith et al., 2020a; Wiseman et al., 2020). The choice of this value minimises the contamination of false associations while maximising the completeness of true hosts (Gupta et al., 2016; Sako et al., 2018).

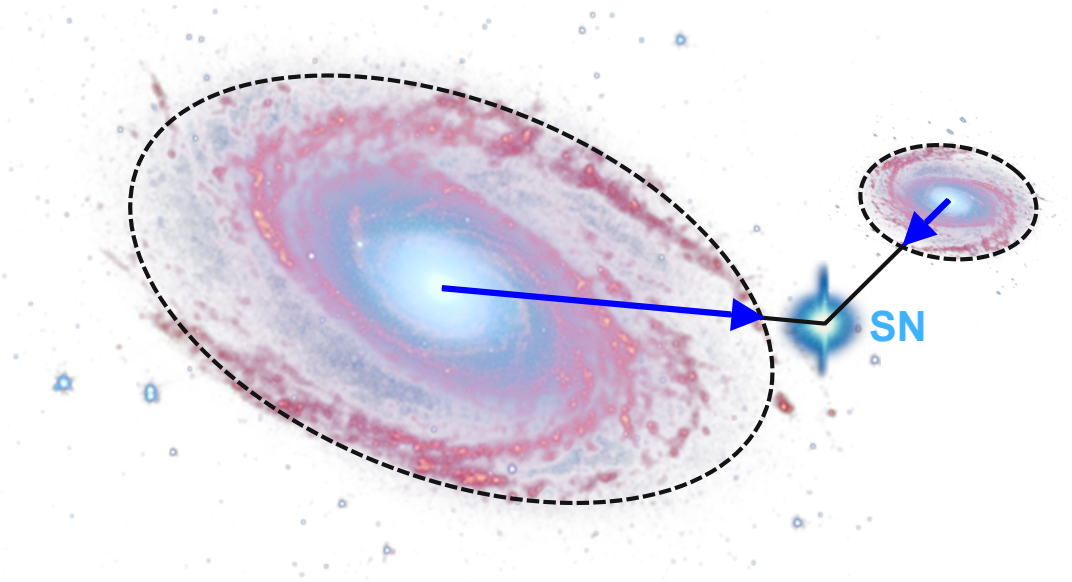

FIGURE 2.1: An illustrative example demonstrating the difficulties with matching SNe to their host galaxy; Figure 1 from Gupta et al. (2016). The SN is labelled, with black dashed ellipses representing the extent of each galaxy light profile, and blue arrows showing the light radii of each galaxy. The black solid line between each arrow and the SN location is a measure of the separation between the SN and galaxy center.

2.2 Image Stacks

To analyse the environmental properties of SN host galaxies and thus study their relationships with SN cosmological parameters, it is important to have high quality, accurate and precise photometry to reduce statistical uncertainties.

In order to obtain this high quality *griz* photometry over a wide range of redshifts, DES-SN relies upon coadding individual single-epoch DES-SN images, selected based on their sky and atmospheric conditions, to create 'stacked' images. These resulting stacks are of superior quality to the single-epoch images, and by altering the coadd image selection, can be optimised for depth (Section 2.2.1) or seeing (Section 2.2.2).

All stacked images used in this thesis have been created by Southampton and DES-SN collaborator Dr Phil Wiseman.

2.2.1 Deep Stacks

The procedure for obtaining DES-SN deep stacks is described in detail in Wiseman et al. (2020), but for completeness I outline it briefly here.

2.2.1.1 Image Selection

It is important for SN host galaxy studies that stacked images do not include exposures contaminated by light from the SN. It is computationally expensive to create individual stacks for each SN, and has the added difficulty of requiring that the date the SN faded below the detection threshold be well-defined. To counter these difficulties, a series of 4-season[4] coadds are created for each CCD in each filter, which exclude all exposures from the remaining season that the SN is associated with. These are designated as minus-year (MY) coadds, so that MY1 indicates the coadd that does not include the first season of DES-SN.

Additionally, it is required that the individual exposures that make up each stack be of suitable quality, so there is a first initial cut on those affected by instrumental noise and atmospheric conditions, and a cut requiring high image quality. Single exposures are then subject to additional selection requirements (cuts) which much be passed before they are added to the coadd.

The first of these selection cuts is τ (Neilsen et al., 2016, 2019; Morganson et al., 2018), the ratio between effective exposure time due to the conditions ($t_{\rm eff}$) and the true exposure time ($t_{\rm exp}$); which is given by:

$$\tau = \eta^2 \left(\frac{\rm FWHM}{0.9''}\right)^{-2} \left(\frac{b}{b_{\rm dark}}\right)^{-1} \tag{2.1}$$

where η corresponds to atmospheric transmission, FWHM is the full-width half-maximum of the point spread function (PSF) of stars measured in the original single-epoch DES images, b is sky brightness, and $b_{\rm dark}$ is the dark sky background at zenith. In this formulation, $\tau = 1$ is considered to be good, with lower values corresponding to worse exposures. To eliminate these from the deep stacks and optimise the limiting magnitude of the final images, threshold values ($\tau_{\rm cut}$) are implemented. After a series of test optimisations, individual images must have τ values higher than the following cuts to make it into the final coadd:

- For the shallow fields: $\tau_{\rm cut} = 0.26, 0.2, 0.2, 0.3$ for g, r, i, z respectively
- For the deep fields: $\tau_{\rm cut} = 0.06, 0.2, 0.4$ and 0.5 for g, r, i, and z respectively

A cut was also applied to the PSF, requiring that single-epoch images have a value below a $\rm PSF_{cut}$ of $2.4''$ for g and $2.2''$ for r, i, and z in all fields.

[4]DES-SN was active for only 5 of the 6 years of DES, hence the use of 4-season coadds instead of 5-season.

2.2.1.2 Coaddition

When combining the images, the 59 DECam science CCDs are treated independently, and individual exposures are stacked using SWARP (Bertin, 2010) after being detrended with the Dark Energy Survey Image Processing Pipeline (Morganson et al., 2018). Images which pass the described selection cuts are grouped by chip, field, band and MY combination, and are resampled and coadded using a clipped mean stacking method (Gruen et al., 2014). This clipping detects and masks outlier pixels in individual exposures thereby reducing artefacts in the data. These are then stacked through a weighted average procedure, using weight maps of inverse variance.

By calibrating photometric zeropoints, this optimisation of exposure selection and coaddition technique results in deep stacked images with limiting magnitudes of ~ 26 mag, reaching ~ 27 mag in g-band (Wiseman et al., 2020). The deep stacks also improve the host matching procedure, enabling the resolution of previous host mismatching, and finding hosts for objects that had been designated as hostless.

2.2.2 Seeing-optimised Stacks

When analysing host galaxy properties of type Ia supernovae, deep imaging is required in order to reduce statistical uncertainties on the photometry. However, as in this analysis I am interested in comparing global and local galaxy properties at each supernova location, I require stacks that have been optimised for the best seeing, which is measured by the FWHM of the PSF of stars measured in the original single-epoch DES images. This ensures better resolution of sub-galactic regions to obtain improved measurements of the environmental properties of local regions. These seeing-optimised stacks are created following the same techniques as the Wiseman et al. (2020) deep stacks described in Section 2.2.1, but with differing selection requirements to improve the resolution at the cost of depth.

By testing various combinations of τ_{cut} and PSF_{cut} for the seeing-optimised stacks it was found that the τ_{cut} is relatively unimportant and so to remove clear outliers in image quality, a minimum limiting value of $\tau_{\text{cut}} = 0.02$ is used. To provide a balance between depth, image quality and redshift coverage, the PSF_{cut} was set at $1.3''$ in all filters, considerably lower than those for the deep stacks. This results in stacks which have limiting magnitudes of ~ 25 mag. Histograms showing the average seeing across all DES-SN exposures and in the seeing-optimised stacked images are shown in Figure 2.2, and corresponding stack parameters for the seeing-optimised stacks are available in Table 2.1. As can be seen for Figure 2.2a, the distributions share similar shapes with long, high-seeing tails, which are all excluded from the seeing-optimised stacks (Figure 2.2b) by the additional selection cut. The distributions peak at increasingly smaller values as the filter wavelength increases.

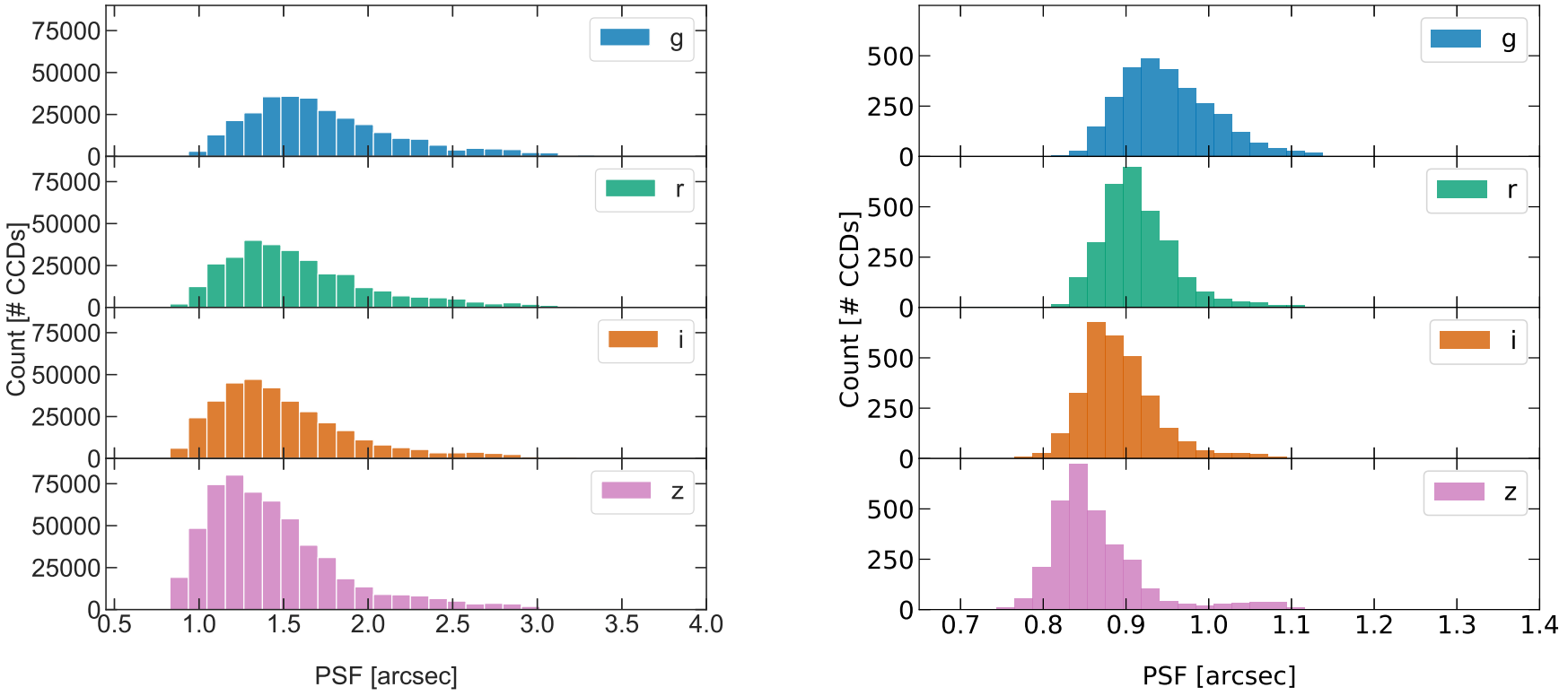

(A) Histograms for the distribution of the PSF FWHM across all DES-SN exposures.

(B) Histograms of the average seeing in the seeing-optimised stacks.

FIGURE 2.2: Histograms of the average seeing across all DES-SN exposures and in the seeing-optimised stacked images. Figure 2.2a displays the distribution of the PSF FWHM across all DES-SN exposures, with data used with permission from Wiseman et al. (2020). Figure 2.2b shows the average seeing in the resulting seeing-optimised stacks. Each histogram contains the 59 working DECam science CCDs across the 10 DES-SN fields for the 5 years of the SN survey.

TABLE 2.1: Seeing-optimised image stack parameters.

Field[1]	Band[2]	MY[3]	N_{exp}[4]	$t_{exp;tot}$[5]	m_{lim}[6]
SN-E1	g	1	7	0.34	26.25
SN-E1	g	2	3	0.15	25.06
SN-E1	g	3	6	0.29	26.24
SN-E1	g	4	5	0.24	26.17
SN-E1	g	5	7	0.34	26.25
Full data presented in Table A.1					

[1] SN field.
[2] Filter band.
[3] 'Minus Year' missing season, subtracted to remove contamination from SN light.
[4] Number of single exposures in each coadd.
[5] Total exposure time given in hours.
[6] Limiting magnitude determined from the sky background.

2.3 Spectroscopic and Photometric Samples

In this thesis, two different DES-SN samples are used: the spectroscopically-confirmed three-year sample (DES3YR), and the photometrically-confirmed five-year sample (DES5YR).

2.3.1 DES3YR

The first of the samples is the DES3YR spectroscopically-confirmed SNe Ia cosmology sample. Data from the full data release[5] of DES3YR are freely available and can be found as follows: photometry in Brout et al. (2019a), cosmology sample and systematics in Brout et al. (2019b), spectroscopy in Smith et al. (2020a).

707 transients candidates discovered during the first three seasons of DES-SN were spectroscopically followed-up (Smith et al., 2020a) as described in Section 2.1.2. After reducing the spectra, they were classified using the software packages SNID (SuperNova IDentification; v5.0; Blondin & Tonry, 2007) and SUPERFIT (v3.5; Howell et al., 2005), with a variety of spectral templates (Silverman et al., 2012; Liu et al., 2016; Modjaz et al., 2016; Gutiérrez et al., 2017; Quimby et al., 2018; Williamson et al., 2019). Where possible, these fits were measured using the spectroscopic redshift from host galaxy emission lines in the spectra. By making a rank-ordered list of best-fitting templates for each spectrum using either cross-correlation techniques (SNID) or chi-squared minimisation (SUPERFIT), classifications were determined by visual inspection of the fits by DES-SN collaboration members. From the total of 707, 251 were classified as 'certain' or 'likely' to be a SNe Ia, with redshifts of $0.02 < z < 0.85$ (Smith et al., 2020a). The SNe Ia light-curves are fitted (see Section 2.4), and additional quality requirements on

[5] https://des.ncsa.illinois.edu/releases/sn

signal-to-noise and light-curve parameters are implemented to generate the cosmology subset, resulting in 206 'cosmologically useful' SNe Ia (Brout et al., 2019b). In this cosmological analysis, I refer to this cosmology subset as DES3YR.

A particular benefit of this well-defined DES3YR sample is the opportunity to establish key analysis techniques and build greater understanding of underlying systematics that will be valuable for the much larger DES5YR sample.

2.3.2 DES5YR

The second of the samples used in this analysis is based on the developing DES5YR SNe Ia sample. This will include both spectroscopically-confirmed and photometrically-confirmed SNe Ia, and will be approximately ten times larger than DES3YR. This dramatically increased size, whilst having additional complications due to the systematic uncertainty of the photometric classification and host galaxy redshift measurements, will be of significant statistical importance and act as a testing-ground for the next generation of large-scale photometric supernova surveys, where it is not realistically possible to spectroscopically classify all of the transients, such as the Rubin Observatory Legacy Survey of Space and Time (LSST; Ivezić et al., 2019).

The final version of this sample has not been released publicly to date, and is undergoing additional photometric classification quality checks and revisions within the collaboration to reach a final consensus. Thus, when I refer to DES5YR in this thesis, I mean our current preliminary version of the sample[6]. I expect a few additional SNe Ia to be present in the final data release when compared to this sample, but this will not affect the conclusions of this work.

2.3.2.1 Photometric Classification

For photometric classification, DES-SN uses SuperNNova (Möller & de Boissière, 2020), an open-source light-curve classifier that uses a recurrent neural network, with an optional host galaxy redshift input allowing for improved classification. Inputting this valuable redshift information can improve the accuracy of the classification from 97% to over 99%.

The training sample for SuperNNova is created from a representative sample of simulated multi-band SN light-curves based on templates, so it is vital to obtain high quality, accurate templates, both for the SNe Ia that we want to obtain for cosmology, and for transient objects that may appear as contamination, e.g. core-collapse supernovae. Simulated SNe Ia are obtained from the Joint Lightcurve Analysis (JLA) data set (Betoule et al., 2014); and the core-collapse SNe from the templates of Vincenzi et al. (2019),

[6]Similar preliminary samples are explored in Vincenzi et al. (2021) and Wiseman et al. (2021)

which were found to provide low core-collapse SNe contamination in the DES5YR data set (Vincenzi et al., 2021).

Candidates that have been flagged by SUPERNNOVA as having a high probability of being a SNe Ia undergo light-curve fitting in the same way as DES3YR (see Section 2.4), and also are subject to further quality selection requirements which are currently dependent on the nature of the individual analyses in DES-SN. For this analysis, full details of the cuts and resulting sample sizes are given in the individual chapters, however I consistently require that the SNe have a probability of $P(Ia) > 0.5$, and apply typical light-curve correction cuts to x_1, c, and their associated uncertainties as outlined in Section 2.4.1.

2.4 Light-curve fits

To standardise their luminosities for use in cosmology, each *griz* SNe Ia light-curve is fit to measure SN parameters m_B, x_1, c and calculate the distance moduli (μ). In DES-SN the Spectral Adaptive Lightcurve Template model (SALT2; Guy et al., 2007, 2010) using training parameters from Betoule et al. (2014) was used with the SNANA (Kessler et al., 2009) light-curve fitting programme. This method uses a χ^2 minimisation to estimate the best-fit SN parameters and their uncertainties, and calculates a light-curve fit probability $P_{\rm fit}$ (a measure of the quality of the fit by estimating the likelihood of finding as large a χ^2 assuming Gaussian flux uncertainties; Brout et al., 2019b). From these cosmological parameters, μ can be calculated (see Section 1.4.4.1).

As a reminder from Section 1.4.4, when SNe Ia light-curves are standardised, corrections are made for the parameters 'stretch' (x_1) and 'colour' (c) based on the 'brighter-slower' (Phillips, 1993) and 'brighter-bluer' (Riess et al., 1996; Tripp, 1998) relations. The x_1 stretch parameter is a measure of the width of the light-curve, with the 'brighter-slower' relation indicating that more luminous SNe Ia have broader light curves than fainter SNe Ia, which was first found by measuring the difference in B-band magnitude at maximum light and 15 days after maximum light. Modern fitters, such as SALT2, additionally incorporate information from other bands and the overall shape of the light-curve when best-fitting for this parameter. The c colour parameter refers to the SN B-V colour at maximum light, with the 'brighter-bluer' relation being the correlation between SN B-V colour at maximum and B-band luminosity, and is the dominant correction for SNe Ia cosmology (Maguire, 2017). In SALT2, c is considered to vary independent of time, and be either intrinsic or due to extinction by host galaxy dust, or a combination of both. It is implemented in the model as a colour offset with respect to the average at the date of the maximum B-band luminosity (Guy et al., 2007):

$$c = (B - V)_{max} - \langle B - V \rangle \tag{2.2}$$

The SALT2 model describes the spectral flux density (F) for a SN Ia at phase (p) and wavelength (λ) as the following:

$$F(SN, p, \lambda) = x_0 \times [M_0(p, \lambda) + x_1 M_1(p, \lambda) + ...] \times exp[cCL(\lambda)] \tag{2.3}$$

In this equation, x_0 is the SN amplitude, x_1 and c are stretch and colour as defined above, M_0 is the average spectral sequence or SED of a SN Ia, M_1 is the deviation around this SED, and CL is the average phase-independent SALT2 colour law (Guy et al., 2007; Taylor et al., 2021). It is important to note that the x_0, x_1 and c terms are for each individual SN and therefore will vary, whilst the other parameters are global for the SALT2 model and therefore are used for every SN in the sample.

2.4.1 Cosmology Selection Requirements

Within DES-SN, there are a variety of selection cuts that must be applied to each SN to ensure that they are of high-quality for cosmological analysis and obtain reliable measurements. Thus they are subject to the following light-curve selection requirements as outlined in Brout et al. (2019b):

- $z > 0.01$
- converging light-curve fits
- an observation before peak brightness and an observation at least 10 days after peak brightness
- an observation with signal-to-noise > 5 in at least two bands
- $-3 < x_1 < 3$
- $-0.3 < c < 0.3$
- $\sigma_{x_1} < 1$
- $P_{\text{fit}} > 0.01$ (see above definition)
- valid simulated BBC bias correction (outlined in Section 2.4.2)

These cuts result in 1606 SNe Ia for the current version of the DES5YR sample (Vincenzi et al., 2021).

2.4.2 BEAMS with Bias Corrections (BBC)

To convert the best-fit light-curve cosmological parameters m_B, x_1 and c into bias-corrected distance moduli μ and determine the nuisance parameters α and β for use in the Tripp Equation (Equation 1.6, Section 1.4.4.1), DES-SN uses the 'BBC' BEAMS with Bias Corrections method (Kessler & Scolnic, 2017) with the simulations of Kessler et al. (2019) to account for various survey selection effects and intrinsic scatter. Simply, this results in the modification of the Tripp Equation (Equation 1.6, and Equation 1.9 for the version including environmental corrections) to contain a bias term μ_{bias} as follows:

$$\mu_{obs} = m_B - M + \alpha x_1 - \beta c + \gamma G_{\text{host}} + \mu_{\text{bias}} \tag{2.4}$$

This μ_{bias} term is either simply a function of redshift, known as a '1D correction' (BBC1D), or a '5D correction' (BBC5D) as a function of $\{z, x_1, c, \alpha, \beta\}$ in a 5-dimensional parameter space. Based on the findings of Smith et al. (2020b), who found that the mass-step calculated with BBC5D was biased due to unresolved correlations between c/x_1 and host galaxy M_{stellar}, BBC7D has been developed (Popovic et al., 2021) to introduce two new dimensions in the bias corrections to account for these additional correlations. Additionally, Popovic et al. (2021) have developed an adaptation of the BBC formalism to address the Brout & Scolnic (2021) dust-based explanation for the mass step, BBC-BS20.

The majority of this analysis utilises the BBC1D redshift-dependent correction as I am focused on understanding the observed relationships between environment properties and cosmological parameters such as x_1, c and Hubble residual $\Delta\mu$. Using BBC5D, BBC7D or BBC-BS20 may blur the effect of these relationships, artificially suppressing the correlations therefore reducing their value and limiting the understanding of the underlying astrophysical causes of the correlations.

2.5 Host Galaxy Photometry

To obtain environmental properties for the host galaxies of SNe Ia, it is important to have good photometric measurements from the stacked images discussed in Section 2.2. I use two different methods in this analysis, one to obtain photometry for the entire host galaxy ('global') and the other for a local aperture centred on the supernova location ('local').

2.5.1 Global Photometry

To obtain photometry for the entire host galaxy or 'global' photometry within DES-SN, SOURCE EXTRACTOR (Bertin & Arnouts, 1996) is used with the stacked images (Smith et al., 2020b; Wiseman et al., 2020).

To create a catalogue of host photometry, SOURCE EXTRACTOR is run in dual-image mode, in which elliptical Kron (1980) measurement apertures for each host galaxy are defined on single detection images consisting of a combination of $r + i + z$, and then used for `FLUX_AUTO` measurements in each *griz* filter. `FLUX_AUTO` is a measure of the summed pixel values within the Kron aperture, subtracted from the local background.

The resulting photometry is corrected for foreground Milky Way dust extinction using Schlegel et al. (1998) dust maps with a Fitzpatrick (1999) reddening law and the ratios of total to selective extinction (multiplicative coefficients) from the DES data release: $R_g = 3.186$, $R_r = 2.140$, $R_i = 1.569$, and $R_z = 1.196$ (Abbott et al., 2018).

2.5.2 Local Aperture Photometry

In order to obtain local environmental properties, I require local aperture photometry within a defined region centred on each SN location. To get the most representative photometry of the stellar population local to the SN, I require the smallest possible aperture, however this is limited by the effects of the atmosphere, telescope PSF size and coadding procedure on the stacked images.

Using the seeing-optimised stacks outlined in Section 2.2.2, I assume a maximum FWHM of 1.3″, and by using a Gaussian PSF with FWHM $= 2\sqrt{2\ln 2} \approx 2.355\sigma$, I obtain the smallest useful aperture radius (σ) of 0.55″. This is coincidentally approximately equal to the best PSF that can be achieved by DECam in near perfect sky, telescope and atmospheric conditions (Abbot et al., 2009). This value dictates the common physical aperture size used in this analysis.

Displayed in Figure 2.3 is the apparent size of 3, 4, and 5 kpc physical apertures as a function of redshift, with a dashed horizontal line indicating the 1σ seeing of the DES seeing-optimised stacks. As can be seen, at $z \approx 0.7$, the 4 kpc aperture becomes smaller than a 0.55″ radius, therefore to be conservative I select $z = 0.6$ as a redshift cut for all DES data in this analysis, and use a 4 kpc radius local aperture size as the standard value throughout. By applying tighter redshift cuts, smaller apertures could be used, but I require a balance between redshift coverage, sample size and resolution. The redshift cut of $z = 0.6$ additionally minimises selection bias in the sample (1D $\mu_{\rm bias} \sim -0.06$ mag at $z = 0.6$; for 5D, see Kessler et al., 2019).

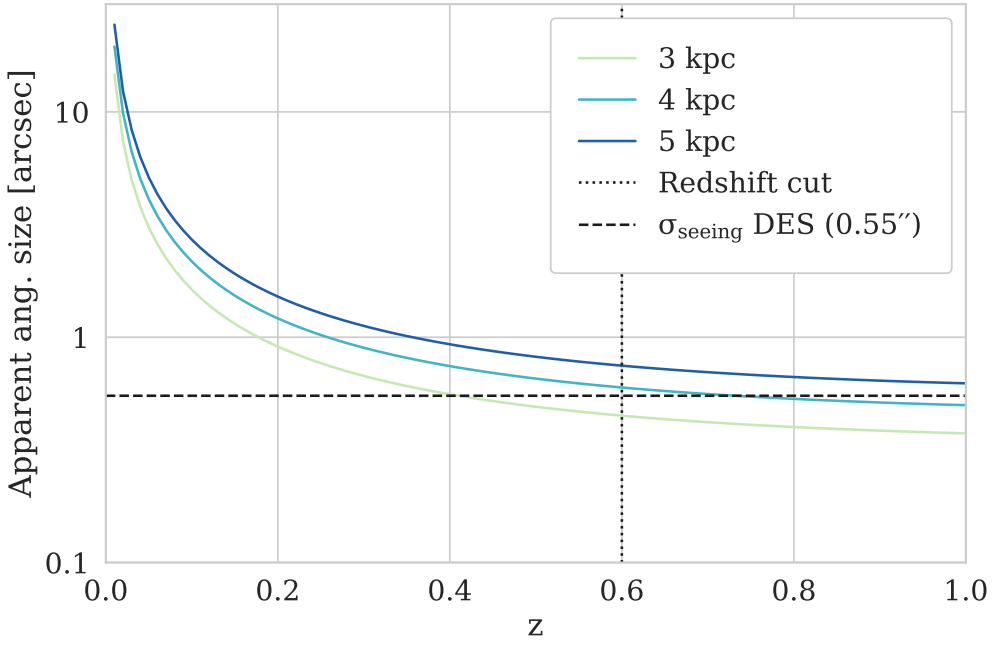

FIGURE 2.3: The evolution of the apparent angular size in arcseconds with redshift for 3, 4, and 5 kpc local aperture radii. The dashed horizontal line indicates the 1σ seeing of the DES seeing-optimised stacks, and the dotted line the $z < 0.6$ redshift cut.

Through a custom pipeline which identifies the redshift, coordinates, season and ccd for each SN Ia, a circular aperture of the correct radius centred on the SN location is defined for each, and matched with the correct stacked image and associated weight map in each of the *griz* filters. The local aperture photometry is then performed within the defined aperture for each SN in all filters, computed using the APERTURE_PHOTOMETRY tool from the PHOTUTILS ASTROPY module (Bradley et al., 2019). This procedure allows for the exact intersection of circular apertures with imaging pixels to be calculated, therefore enabling the use of fractional pixels for more accurate photometric measurements. Example images displaying the aperture regions probed in relation to galaxy size and redshift are presented in Figure 2.4. I calculate photometric uncertainties using the weight maps associated with each stack. In the same way as for the global photometry, the measured local photometry is corrected for foreground Milky Way dust extinction.

2.6 SED fitting

To estimate galaxy properties from the photometry, I use spectral energy distribution (SED) fitting techniques, a method of stellar population synthesis (SPS). The SED of a galaxy is a function of the emitted energy from the galaxy measured against frequency

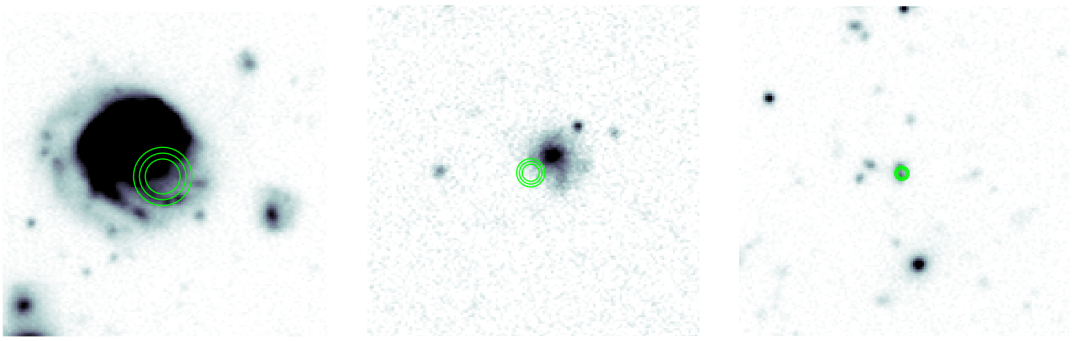

(A) DES15C3efn : $z = 0.078$ (B) DES13E1sae : $z = 0.185$ (C) DES15C3nym : $z = 0.496$

FIGURE 2.4: Three g-band images of DES SN Ia host galaxies at $z < 0.6$. The green circles represent the local region within a 3 kpc, 4 kpc and 5 kpc aperture radius centred on the SN location. All images are set with the same image intensity scaling parameters, and are of the same angular scale.

or wavelength, and therefore is imprinted with the effect of different galactic properties, such as: star formation history, stellar properties such as age, mass and metallicity, galaxy gas content, and the properties of the interstellar medium. Thus SED fitting the individual galaxies allows the determination of these properties from fitting models to the observed data.

In the simplest terms, SED fitting consists of two key stages. The first, the creation of SED templates to predict the flux in the observed photometric filters, and the second the actual fitting process to determine which model template fits the observed data best.

2.6.1 Templates

To create galaxy SED templates, models combine simulated SEDs for stars of the same age and a range of masses determined by a defined initial mass function (IMF) to create a SED for a simple stellar population (SSP). By convolving a variety of these SSP SEDs with a model star-formation history (SFH), composite stellar populations (CSP) that describe entire galaxies are created.

In the galaxy literature, a range of different SPS models are used to create the SSPs but one of the most prevalent for SN Ia host galaxy analyses is PÉGASE (Fioc & Rocca-Volmerange, 1997, 2019), which is used in this analysis. Other popular models are: Bruzual & Charlot (2003) and Maraston (2005), but I note that their galaxy property results have been shown to be consistent when the same IMF is used (e.g. Kelly et al., 2010; Smith et al., 2020b).

Following Smith et al. (2020b), within PÉGASE I use 9 smooth, exponentially declining SFHs to calculate the SED as a function of time. Each takes the form:

$$\mathrm{SFR}(t) = \frac{\exp^{-t/\tau}}{\tau} \tag{2.5}$$

Where t is the galaxy age from the onset of star formation, and τ is the e-folding time (the time for the SFR to decrease by $1/e$), measured at 102 timesteps between 0 and 14 Gyr, and each SFH is normalised to produce $1M_{\odot}$. I implement the default PÉGASE modelling of nebular emission, and evolve the metallicity consistently from an initial value of 0.004, with formed stars having the same metallicity as the surrounding interstellar medium.

In SPS models, the IMF provides a distribution of the initial masses of stars. It determines the normalisation of the stellar mass-to-light ratio, the rate of evolution in luminosity, and alters the SED of stellar populations (Conroy, 2013). Similarly to the SPS models, there are a range of different IMFs in common use in SN Ia host galaxy analyses. To be consistent with prior DES-SN host galaxy analyses (e.g. Smith et al., 2020b), I use a Kroupa (2001) IMF. This is a broken power law of the form:

$$\xi(m) = m^{-\alpha} \tag{2.6}$$

Where:

$$\alpha = \begin{cases} 0.3, & \text{if } m < 0.08 \\ 1.3, & \text{if } 0.08 < m < 0.5 \\ 2.3, & \text{if } m > 0.5 \end{cases} \tag{2.7}$$

There is a slight systematic offset (Sullivan et al., 2010; Speagle et al., 2014; Smith et al., 2020b) in final mean environmental property values (e.g. M_{stellar}, SFR, etc.) when using different IMFs, for example: the simple Salpeter (1955), Rana & Basu (1992), Chabrier (2003) or Baldry & Glazebrook (2003), however these differences are not as a function of the environmental properties or redshift, therefore do not alter the conclusions of such analyses. To illustrate this, I present in Figure 2.5 example distributions of host galaxy M_{stellar} using a range of different models and IMFs for the host galaxies in the full DES3YR cosmology sample. As can be seen, the IMF has the most noticeable effect on the mass distribution, with a few SNe changing side of the traditional mass step location at $\log(M_{\mathrm{stellar}}/M_{\odot})_{\mathrm{global}} = 10$, whilst the SPS model seems to make little difference.

This technique provides a range of template galaxy SEDs, with M_{stellar} at each point in time. For consistency, to fit the local photometry I use the same range of templates as for the global photometry; in essence treating each local region as a small galaxy.

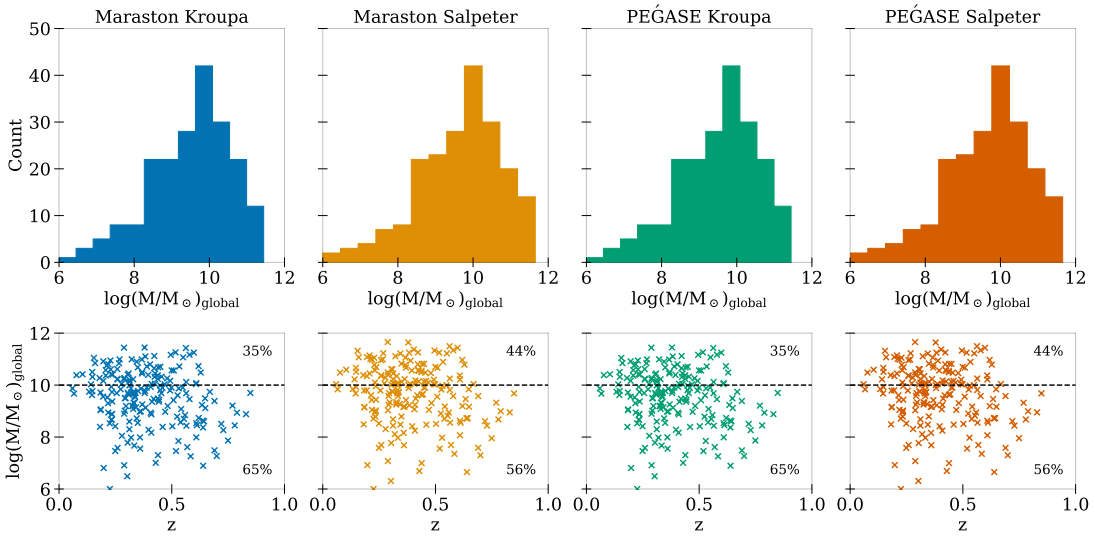

FIGURE 2.5: Distributions of host galaxy M_{stellar} using different models and IMFs for the DES3YR cosmology sample. Top: Histograms displaying the M_{stellar} distribution of the host galaxies in the DES3YR sample of 207 SNe Ia using Maraston and PEGASE templates, with Kroupa and Salpeter IMFs. Bottom: Scatter plots displaying the spread of the M_{stellar} calculated above and below the traditional mass step location $10^{10} M_{\odot}$ (indicated by the black dashed line) for the different templates. Numerical values indicating the percentage of the sample either side of this split are indicated in the plots.

2.6.2 Fitting Technique

I then fit the created template SEDs to the broadband fluxes for each environmental region using SEDFIT, developed in Sullivan et al. (2006, 2010), to find the best fitting template through χ^2 minimisation.

I do not make use of the built-in PÉGASE dust implementation, instead applying foreground dust screens to the template SEDs with a colour excess $E(B-V) = 0$ to 0.3 mag in steps of 0.05 mag. By combining this with the PÉGASE templates, there are thousands of unique SED templates to fit. All fitting is done in flux space, and I only consider solutions which are younger than the age of the universe at each SN redshift.

The flux in DES *griz* filters is calculated for each template SED (F_{template}) at the SN redshift for each observed environmental region. For each, I calculate the χ^2:

$$\chi^2 = \sum_{x \in griz} \left(\frac{A F_{\text{template;x}} - F_{\text{obs;x}}}{\sigma_{\text{obs;x}}} \right)^2 \tag{2.8}$$

Where A is a scale factor determined from a global χ^2 minimisation (Smith et al., 2020b). This allows the determination of the best-fitting SED template for each environmental region, and thus the identification of the M_{stellar} and SFR. An example best-fitting SED is displayed in panel (A) of Figure 2.6.

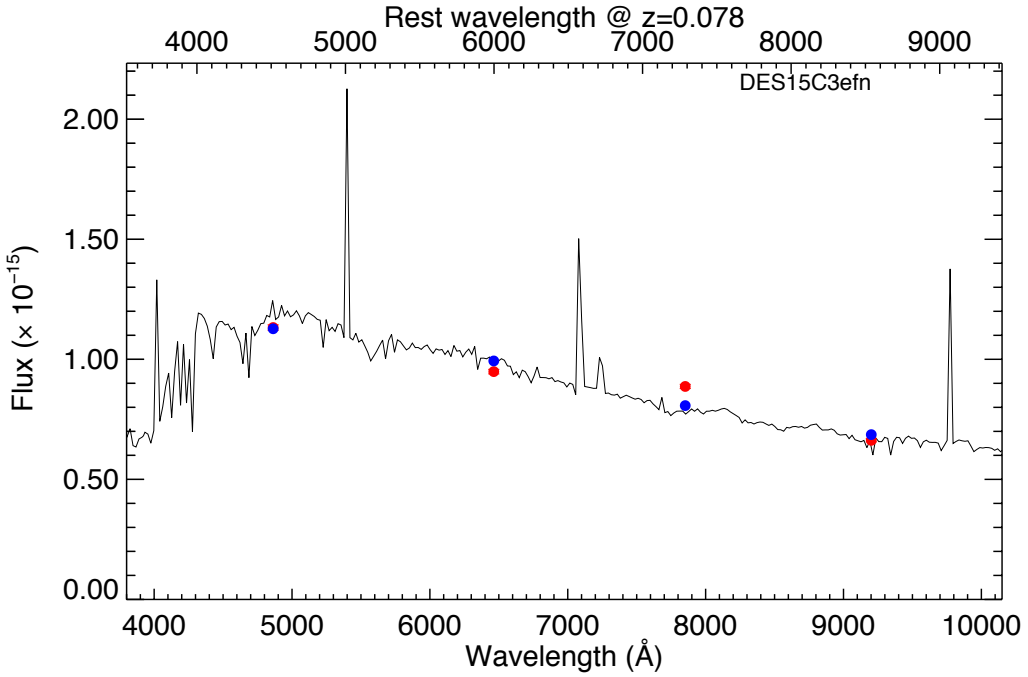

(A) Best-fitting template.

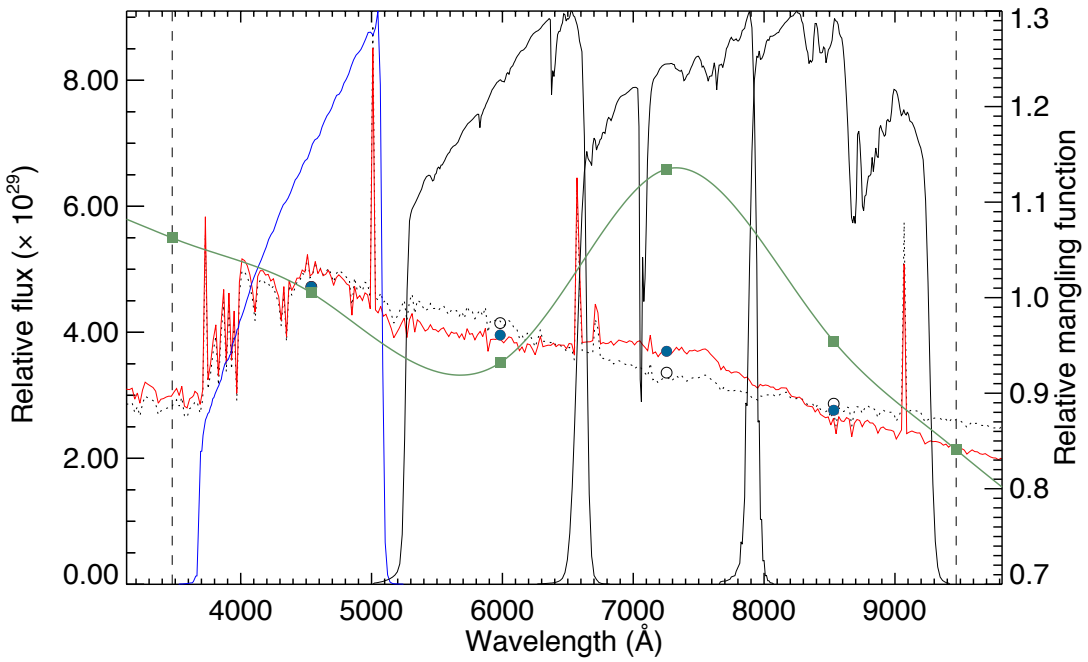

(B) Example of a mangled best-fitting template.

FIGURE 2.6: Example SED fits for the host of DES15C3efn. Figure 2.6a shows the best-fitting template spectrum in black, with *griz* markers shown for the template in blue, and for the data in red. Figure 2.6b shows the filter responses for each *griz* measurement, and the associated relative mangling function in green. The red spectrum is the result of applying the mangling function to the best-fitting template spectrum.

The reliability of SED fitting can be improved by adding photometry from a wider range of bands, for example expanding out of the optical and into the UV or IR. In particular, expanding into the mid or far IR may provide valuable insights into the dust content of host galaxies, but here I am limited by the rest-frame wavelength range of the DES *griz* filters.

From the best-fitting PÉGASE template, I obtain the current M_{stellar}. The SFR is defined as the mean SFR over the last 0.25 Gyr of SFH for the best-fitting template, therefore correcting for the UV light from older stars (Sullivan et al., 2006). The specific SFR (sSFR) is simply $\text{sSFR} = \text{SFR}/M_{\text{stellar}}$.

For this analysis I require rest-frame colours, so a new feature has been implemented into SEDFIT to estimate the rest-frame $UBVR$ magnitudes, from which colours can be determined (e.g. $U - R$). I adjust the best-fitting SED for each SN Ia environmental region (local and global) using a wavelength-dependent multiplicative function to exactly match the observed *griz* photometry, in a process known as 'mangling' (Hsiao et al., 2007; Conley et al., 2008). This colour-correcting procedure uses the best-fitting splines (identified through non-linear least-squares fitting), anchored at the edges of the effective wavelengths of the DES filter responses, to smoothly scale the best-fitting SED template. An example of the best-fitting SED and the corresponding mangled SED is presented in Figure 2.6. In this analysis, the colour that I focus on is rest-frame $U - R$, as it spans the largest wavelength range covered by our observer-frame (*griz*) photometry. $U - R$ has also been found to correlate with galaxy morphology (as seen in the correlation with $u - r$; Lintott et al., 2008), is a complementary tracer of the SFR, and carries information related to the SN host galaxy age. This is due to the domination of different emission types in different filter responses, i.e. older stars or more passive galaxies are at the redder end of the spectrum, and the bluer end contains the younger, hotter stars or more star-forming galaxies (Trayford et al., 2016).

To estimate the uncertainties in these environmental parameters, a Monte Carlo method is used, repeating the χ^2 fitting, M_{stellar} and SFR measurements, $UBVR$ estimation through mangling for 1000 random realisations of F_{template}. Each Monte Carlo realisation is drawn randomly from a Normal distribution with mean $= F_{\text{obs}}$ and $\sigma = \sigma_{\text{obs}}$. Final uncertainties are then defined as the standard deviation of the best-fit parameters over all 1000 realisations.

2.7 Summary

In this chapter, I have introduced DES and the data that will be used throughout this thesis, giving an overview of the DES-SN survey and outlining the spectroscopically-confirmed DES3YR and photometrically-confirmed DES5YR samples. I have discussed the light-curve fitting procedure employed by DES-SN to obtain cosmology, and the

image stacking procedure used for DES-SN host analyses. I then moved on to present the method used to obtain photometry for the entire host galaxy ('global' photometry) and the 'local' photometry within a 4 kpc region around each SN location, and the SED fitting procedure used to obtain environmental properties.

In the next chapter, I begin my analysis by applying my method to the spectroscopically-confirmed DES3YR SN Ia sample to obtain global and local environmental properties. By comparing these environmental properties to SN parameters and Hubble residuals, the effect of environment on SNIa can be analysed.

Chapter 3

Environmental Effects in DES3YR

As discussed in depth in Chapter 1, it is of vital importance to analyse the effects of host galaxies and local environments on SN Ia, both for their cosmological implications and to understand more about the astrophysics behind these important transient events. As we approach the era of large-scale high-redshift coverage surveys, many thousands of new SN Ia will be discovered for use in cosmology. The two data samples of DES-SN (DES3YR and DES5YR) provide an excellent testing-ground to gain a solid understanding of the impact of environmental properties and to establish the analysis techniques to take into account these systematics.

I begin with the spectroscopically-confirmed DES3YR sample, introduced in Section 2.3.1, as this well-established SN Ia sample has been analysed in detail by a number of authors for the use in cosmology (e.g. Brout et al., 2019a,b; Smith et al., 2020a). There has been a prior analysis of the host M_{stellar} step in this data (Smith et al., 2020b), which allows for comparison, and for the importance of looking at the local environment and at other environmental properties such as colour to be established. In this chapter I present the results of studying the host galaxy and local environmental properties of this DES3YR sample, which has been published as Kelsey et al. (2021).

3.1 Photometric Measurements

From the DES3YR spectroscopically-confirmed sample, as described in Section 2.3.1, I have a total of 206 cosmologically-useful SNe Ia. Following the techniques outlined in Section 2.5, I obtain photometric measurements for both the SNe host galaxy, and for a 4 kpc radius local aperture around the SN locations. From SED-fitting these photometric measurements using the method described in Section 2.6, I obtain the star formation rate (SFR, in $\mathrm{M_{\odot}yr^{-1}}$, averaged over the last 0.25 Gyr before the best-fitting time step), M_{stellar}, the sSFR (in $\mathrm{yr^{-1}}$), and $UBVR$ magnitudes (which we convert to colours, such

TABLE 3.1: Sample selection cuts used for my DES3YR analysis.

Cut	Number of SNe Ia
Cosmology Sample	206
$z < 0.6$	177
$\sigma_{(U-R)} < 1$	164

as $U - R$), and their associated uncertainties, for each environmental region, both local and global.

3.1.1 Selection Requirements

In addition to the typical light-curve correction cuts already implemented within the DES3YR cosmological sample, I implement two additional cuts to improve the data quality for the host galaxy and local environment analysis. As motivated in Section 2.5.2, it is necessary for $z < 0.6$ to obtain relevant local photometry from the seeing optimised stacks. Additionally, to ensure that the rest-frame $U - R$ colour is well-measured, I implement a selection cut on the $U - R$ uncertainty: $\sigma_{(U-R)} < 1$ mag for both global and local measurements. Given that the $U - R$ is derived from observed photometry, this selection requirement additionally removes SN with large uncertainties in M_{stellar} and SFR.

These selection requirements remove 42 SNe from the sample, resulting in 164 SNe for use in my analysis ($\sim$ 80% of the original sample), as outlined in Table 3.1. As illustrated in Figure 3.1, the selection cuts have only a minor effect on the overall distributions of x_1, c, M_{stellar}, and the local $U - R$ colour. As can be seen from the p-values (p) of a two-sample Kolmogorov–Smirnov (KS) test, presented in the figure, the lowest p-values correspond to those distributions where a selection cut has been made in comparison the the cosmological sample, as seen in Table 3.1. In other words, the redshift of the sample for this analysis is cut at $z = 0.6$, so I do not expect the distributions in redshift between the two samples to be consistent. Additionally, I constrain $\sigma_{(U-R)} < 1$ mag to ensure that environmental properties are well-measured, therefore I do not expect that distribution to be consistent either. Note that the lower right panel of the figure has been limited to only display $\sigma_{(U-R)} < 1$ mag, as the cosmology sample extends out in the x-axis with a few SNe having $\sigma_{(U-R)}$ of up to 36 mag. The p-value presented is for the full range of data, hence has a low value. The minor changes in the distributions of the other parameters are consequences of the changing distributions of the parameters that have had cuts applied.

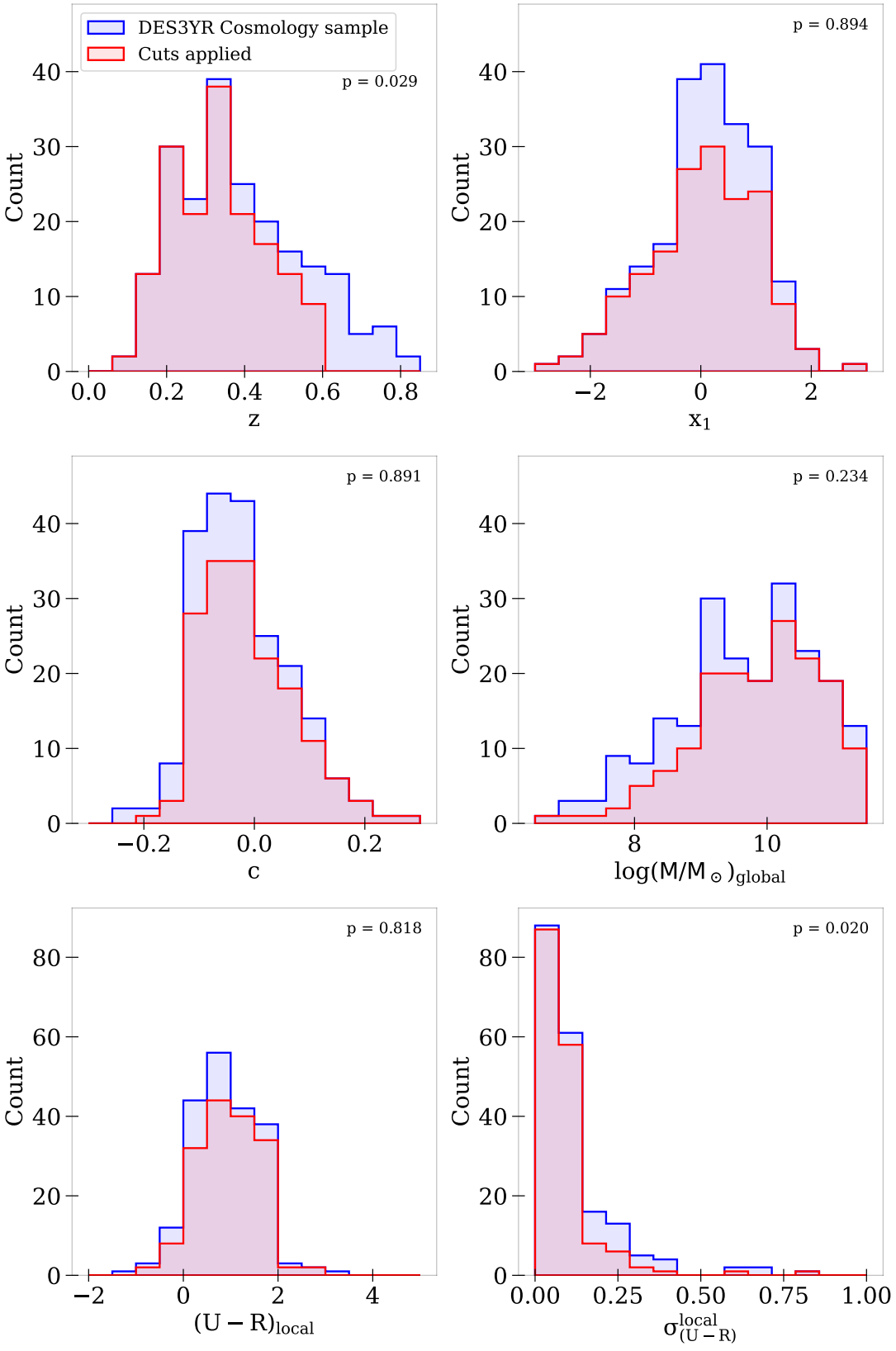

FIGURE 3.1: Histograms of the distributions of SN and environmental properties: redshift (z), SN stretch (x_1), SN colour (c), host $M_{stellar}$, local rest-frame $U-R$ colour (in a 4 kpc aperture radius), and local $U-R$ colour uncertainty ($\sigma^{local}_{(U-R)} < 1$) for DES3YR. The blue-shaded histogram represents the entire DES3YR cosmology sample, and the red histogram is after cuts in Table 3.1. P-values (p) from KS testing is displayed in the top right corner of each panel.

3.2 Environmental Dependence of SN Ia Luminosities

From the global and local photometry of SN Ia host galaxies, I have measured a range of physical properties of the stellar populations within these environmental regions. I now progress by analysing this data for use in improving the standardisation of SN Ia for use in cosmology.

3.2.1 Global vs. Local Measurements

I begin by comparing the local and global environmental properties of the SN Ia host galaxy sample, and the 'global minus local' differences as a function of redshift, as displayed in Figure 3.2. As expected, the local apertures typically have smaller M_{stellar} than the global regions, with no strong trend with redshift. There are a few hosts with a higher local M_{stellar} but these regions have large uncertainty bringing many across the $M_{\text{stellar; local}} = M_{\text{stellar; global}}$ line, or may also represent regions where the local aperture is probing an area larger than the host galaxy.

Looking to $U - R$, the colour difference is slightly positive, indicating that SNe Ia have a slight preference for locally bluer, presumably stronger star-forming environments than their host galaxy average. This preference for bluer regions is consistent with earlier studies (Anderson et al., 2015).

Both comparisons of M_{stellar} and $U - R$ have significant scatter, indicating that local and global measurements provide different information reflecting the properties of the local stellar populations. This scatter is slightly larger for M_{stellar} than for $U - R$.

3.2.2 SN Properties vs. Environments

When studying the host galaxies of SNe Ia, it is important to understand the relationships between environmental properties and the SN properties x_1 and c, used in standardising their light curves. Displayed in Figure 3.3, with corresponding numerical values in Table 3.2, I present the relationships between SN x_1 and c, and the rest-frame $U - R$ colour and M_{stellar}, for both the global host galaxy and the local SN environment within a 4 kpc radius.

Clear trends are evident in the x_1 comparisons, with brighter-slower SNe Ia in bluer, less massive environments, corresponding to bin-mean differences of up to 6.5σ for the global $x_1 - M_{\text{stellar}}$ relationship across a boundary at the environmental property sample median. This recovers the known relationship between x_1 and host galaxy M_{stellar} (Smith et al., 2020b).

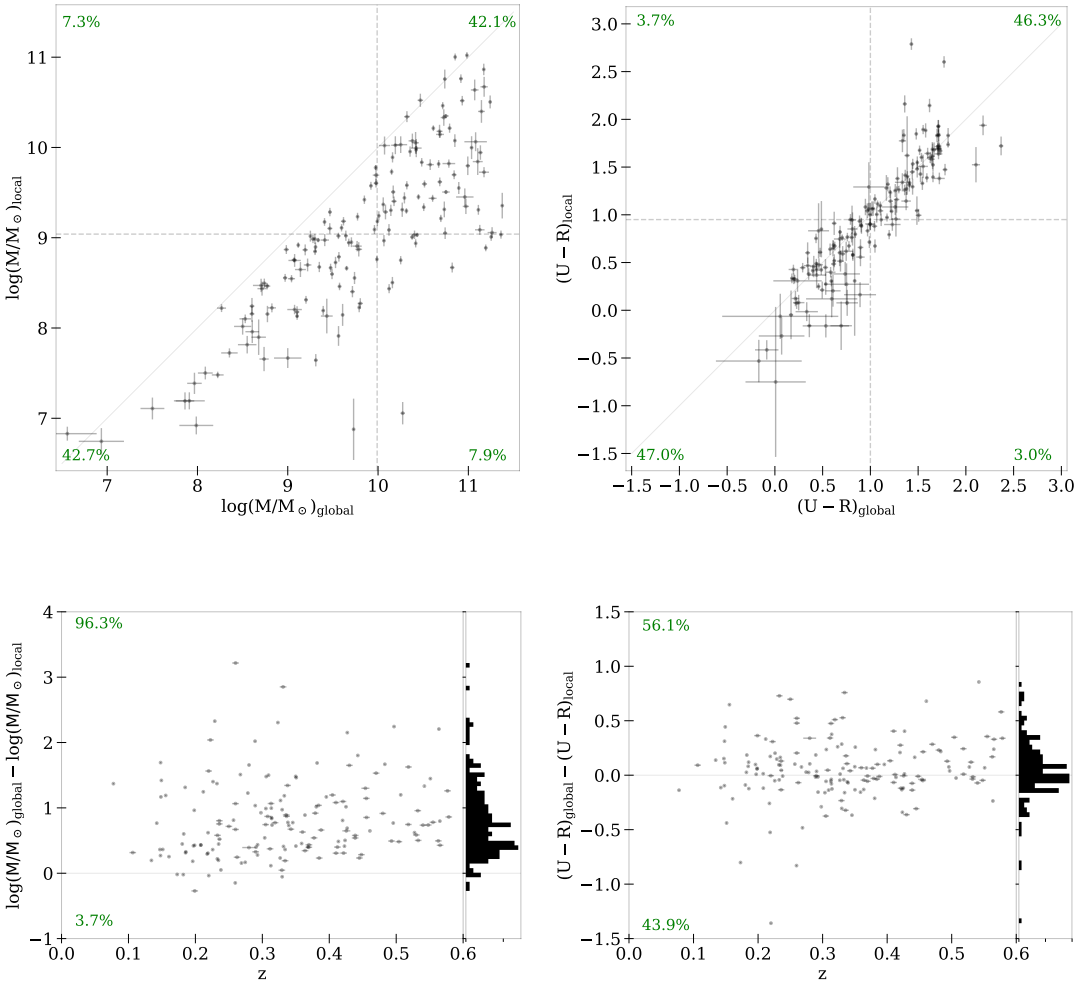

FIGURE 3.2: Left: The difference between the global stellar mass of the host galaxy and the local stellar mass in the 4 kpc radius aperture around the SN location. Right: The difference between the global rest-frame $U - R$ colour and the local rest-frame $U - R$ colour. The solid line shows the 1:1 line (matching the zero difference line in the lower panel), dashed lines indicate the environmental property median points of the sample, and green percentages represent the numbers of agreement in each quadrant (e.g., what percentage of the sample are both high local colour and high global colour, etc.). For stellar mass the Pearson correlation coefficient, $r = 0.801$, and for rest-frame $U - R$: $r = 0.895$. In the lower panels, the difference in properties versus redshift is shown. Green percentages represent the proportions of the sample above and below the zero difference line. Error bars throughout represent the statistical uncertainty in the data.

There are mild trends in the c comparisons, with redder SNe Ia found in more massive or redder galaxies. Additionally, as can be seen in the top panel corresponding to global M_{stellar}, there is an absence of fast evolving and red SNe in low-mass galaxies. Bin-mean differences for c are less significant than for x_1, but there is still $\sim 2\sigma$ difference for both local and global M_{stellar}, whilst only $\sim 1\sigma$ (therefore not significant) for $U-R$. It is also of interest in these c comparison plots that there seems to be a lower limit at $c = -0.1$, particularly for the top right panel with global M_{stellar}, below which where very few SNe Ia are located. In Brout & Scolnic (2021), a value of $c \sim -0.1$ is suggested to indicate 'dust-free'or 'unreddened' SNe Ia. Furthermore, this plot follows an almost triangular distribution, with bluer SNe spanning the global M_{stellar} range, whilst redder SNe have more spread in c and are predominately located at higher M_{stellar}. This could be indicative of the role of dust and different progenitor paths. As blue, unreddened SNe are found in galaxies spanning the full M_{stellar} range of the DES sample, they may represent one progenitor path, whilst the redder SNe are comprised of a mixture of blue SNe that have been reddened by dust (with typically more dust extinction in high mass galaxies (Garn & Best, 2010b)) and SNe that are intrinsically redder, that may have followed a different progenitor path found mainly in higher mass galaxies.

I additionally calculated the Hubble residual r.m.s values of each bin, presented in Table 3.2, to understand the scatter in the residuals around the average in each bin. I find that SNe Ia in more massive galaxies or local environments have higher r.m.s scatter in the SN x_1 and c populations than for lower mass. This is also the case for the redder environments (larger $U-R$ values). SNe Ia in the lower mass, more star-forming, bluer regions present a more homogeneous sample.

Similar relationships were explored in previous work by Roman et al. (2018) for local M_{stellar} and rest-frame $U-V$ colour within a 3 kpc radius, and I find consistent results. As in previous work, I find a significant dependency of the SN x_1 (Sullivan et al., 2006; Howell et al., 2009; Neill et al., 2009) and c (Sullivan et al., 2010; Childress et al., 2013) on environment.

3.2.3 Hubble Residuals

Next, I investigate the dependence of SN Ia Hubble residuals on M_{stellar} and the rest-frame $U-R$ colour, both for the entire SN host galaxy and for the local region. As in prior literature, I plot the Hubble residual vs. my chosen host or local property split into two bins at the division point, and measure the mean and dispersion in Hubble residual for environments either side of the division point. Thus the magnitude of the 'step' is measured as the difference between these two means. In Figure 3.4 I display these relationships, indicating division points split both at the sample environmental property median (as in prior literature) and at the location that gives the step of maximal significance (as defined by Figure 3.5, see Section 3.2.3.1). I present the corresponding

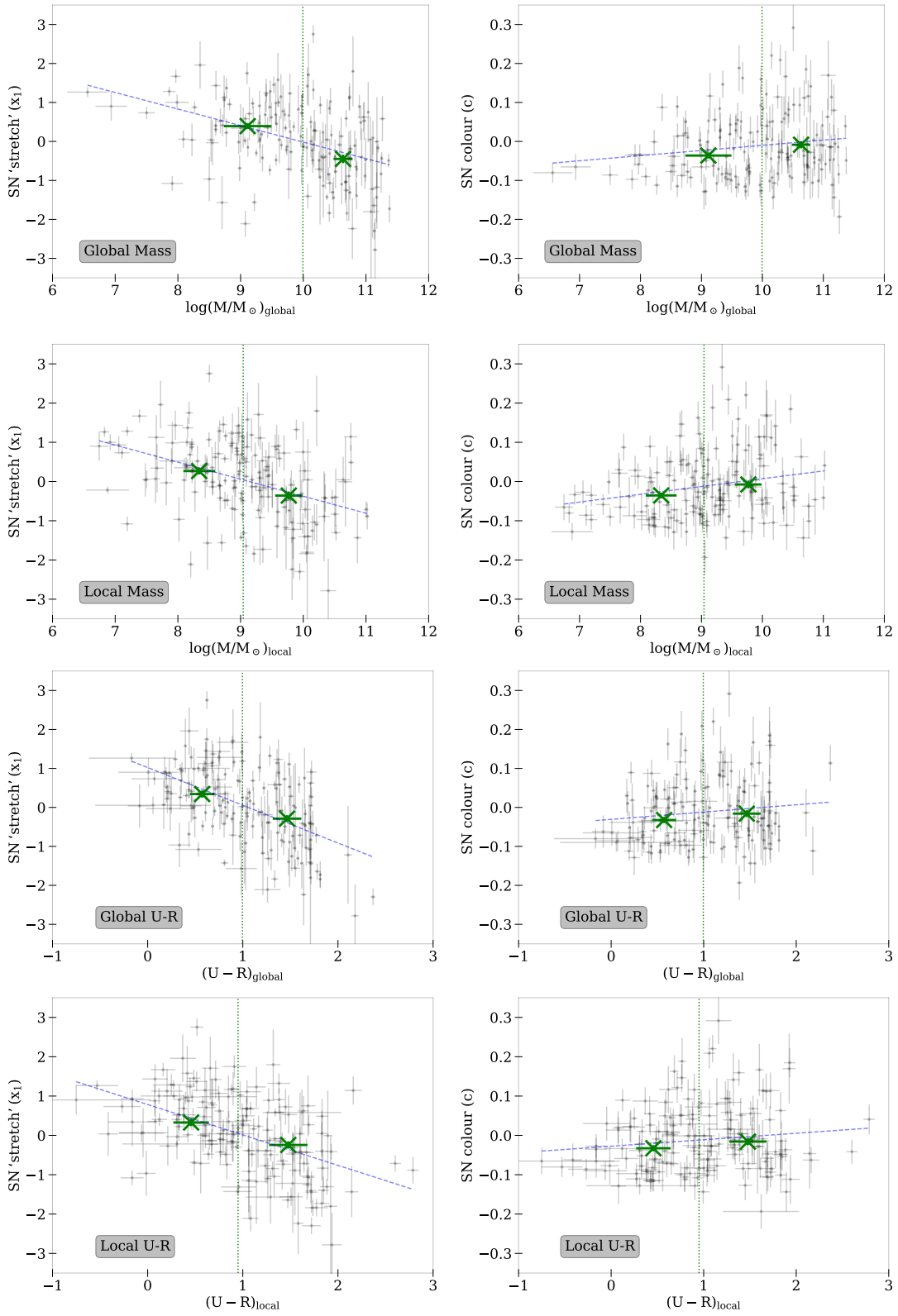

FIGURE 3.3: Correlations between SN stretch (x_1, left column) and colour (c, right column) as a function of: global $M_{stellar}$ (first row), local $M_{stellar}$ within a 4 kpc radius aperture (second row), global $U-R$ (third row) and local $U-R$ (fourth row). Bins are split at the median of the sample, with weighted mean values shown as crosses, x-axis bin-mean error bars showing the dispersion divided by the square root of the number of objects in the bin, and least squares linear fits of the data shown as dashed lines to aid the eye. Corresponding r.m.s. values can be found in Table 3.2.

TABLE 3.2: x_1 and c variation with host galaxy stellar mass and $U-R$ colour (Fig. 3.3).

Property	Division Point[1]	x_1 Sig. (σ)[2]	x_1 Magnitude[3]	x_1 r.m.s. $<$ DP[4]	x_1 r.m.s. $>$ DP	c Sig. (σ)	c Magnitude	c r.m.s. $<$ DP	c r.m.s. $>$ DP
Global Mass	9.99	6.50	0.842 ± 0.130	0.875 ± 0.137	1.066 ± 0.169	2.32	0.028 ± 0.012	0.079 ± 0.012	0.091 ± 0.014
Local Mass	9.04	4.71	0.626 ± 0.133	0.924 ± 0.144	1.023 ± 0.162	2.30	0.028 ± 0.012	0.075 ± 0.012	0.094 ± 0.015
Global U-R	1.00	4.94	0.632 ± 0.128	0.918 ± 0.146	1.025 ± 0.159	1.37	0.016 ± 0.012	0.080 ± 0.013	0.090 ± 0.014
Local U-R	0.95	4.42	0.571 ± 0.129	0.893 ± 0.140	1.049 ± 0.165	1.42	0.017 ± 0.012	0.078 ± 0.012	0.091 ± 0.014

[1] Splitting at the sample median.
[2] Significance of the difference in σ.
[3] Magnitude difference.
[4] Division Point.

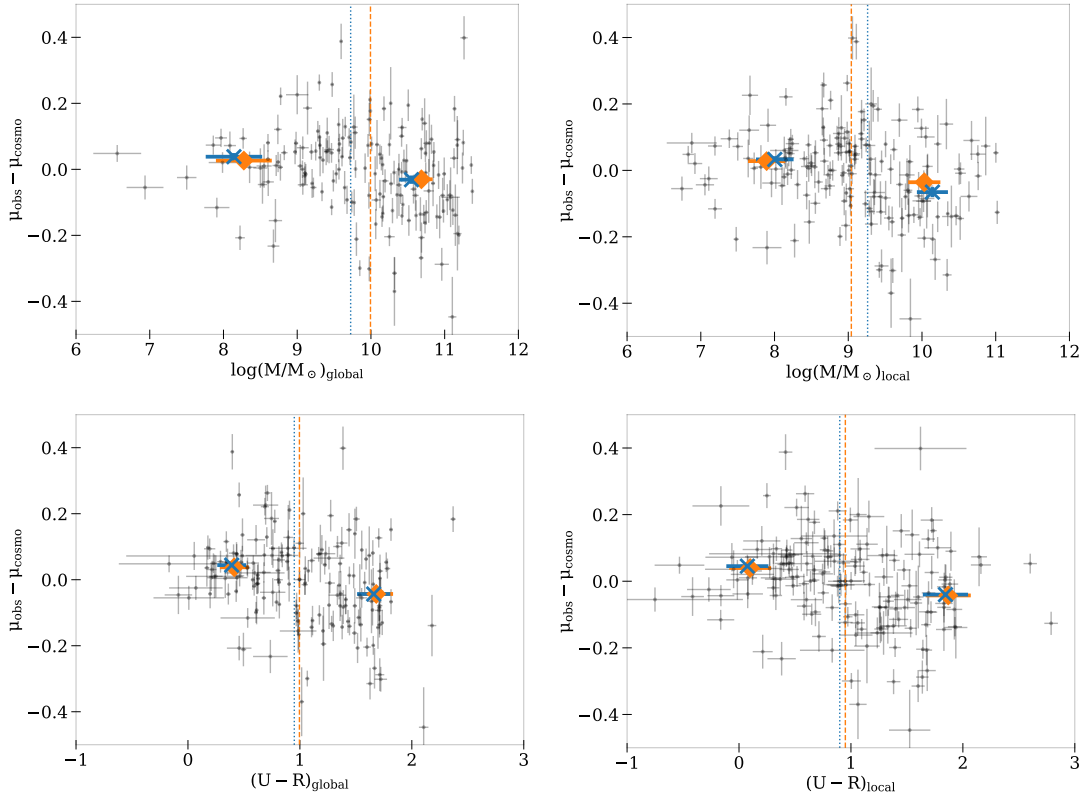

FIGURE 3.4: Hubble residual plots as a function of (from top to bottom and left to right): global M_{stellar}, local M_{stellar} within the 4 kpc radius aperture, global rest-frame $U-R$ colour and local rest-frame $U-R$ colour. The orange-dashed lines represent the sample environmental property medians, and the blue-dotted lines the division point giving the maximum step sizes. These lines correspond with the orange diamond and blue cross bin mean markers, with x-axis error bars showing the dispersion divided by the square root of the number of objects in the bin (as in Figure 3.3). See Table 3.3 for numerical values.

magnitudes and significances of these steps, and r.m.s. values of the Hubble residuals on either side of the steps in Table 3.3.

All the measured steps are significant at $> 3\sigma$, whether using local or global measures, or using M_{stellar} or $U-R$ colour. The local M_{stellar} step is more significant than the global M_{stellar} step, with a maximum step of 0.098 ± 0.018 mag. This is around 0.03 mag larger than the largest global M_{stellar} step in my sample. I note that the local and global step uncertainties quoted here and in the tables are statistical only, and the complicated positive covariance between the local and global M_{stellar} and local and global $U-R$ colour measures (see Fig. 3.2) will likely increase the significance of the difference in the step size between local and global samples, beyond that obtained with a naive quadratic sum.

I find a local $U-R$ step of 0.082 ± 0.017 mag (4.8σ) at the median $U-R$ of the sample, similar in magnitude to that found by Rigault et al. (2020) of 0.091 ± 0.013 mag (7σ)

TABLE 3.3: Hubble residual steps for stellar mass and $U - R$ using a 1D bias correction; shown in Fig. 3.4.

Property	Sample Median/ Max Significance[1]	Division Point	Hubble Residual Step Sig. (σ)	Hubble Residual Step Magnitude	Hubble Residual r.m.s. $<$ DP	Hubble Residual r.m.s. $>$ DP
Global Mass	Median	9.99	3.25	0.057 ± 0.017	0.118 ± 0.019	0.142 ± 0.022
Global Mass	Max	9.73	4.14	0.070 ± 0.017	0.108 ± 0.019	0.145 ± 0.021
Local Mass	Median	9.04	3.57	0.064 ± 0.018	0.102 ± 0.016	0.154 ± 0.024
Local Mass	Max	9.28	5.47	0.098 ± 0.018	0.115 ± 0.017	0.150 ± 0.026
Global U-R	Median	1.00	4.73	0.081 ± 0.017	0.110 ± 0.017	0.149 ± 0.023
Global U-R	Max	0.95	5.29	0.088 ± 0.017	0.110 ± 0.018	0.146 ± 0.022
Local U-R	Median	0.95	4.84	0.082 ± 0.017	0.109 ± 0.017	0.149 ± 0.023
Local U-R	Max	0.90	5.15	0.085 ± 0.017	0.111 ± 0.018	0.146 ± 0.022

[1] The difference between median locations/max significance locations is explained in Section 3.2.3 and in Figure 3.5.

within a 3 kpc radius aperture for a larger sample size. At the step with the maximum significance, my $U-R$ step is similar (0.085 ± 0.017 mag; 5.2σ).

From Table 3.3 I also note that the r.m.s. values for the Hubble residuals are smaller in bluer galaxies/environments and lower mass galaxies/environments (cf. Section 3.2.2) by an average of 1.3σ, suggesting that they represent a more homogeneous sample than the redder, higher mass regions, agreeing with our findings for x_1 and c r.m.s. values.

3.2.3.1 Changing Step Location

In most previous host galaxy mass analyses, the step division point was chosen to be at the median or mean $M_{\rm stellar}$ of the SN Ia sample, or arbitrarily chosen (e.g., 10^{10} M$_\odot$; Sullivan et al., 2010). There is little physical motivation for this choice, although I note that 10^{10} M$_\odot$ lies just below the knee in the galaxy-mass/halo-mass relation ($\sim 3x10^{10}$ M$_\odot$ at low redshift, Kauffmann et al., 2003), the point at which galaxies transform from 'star-formation-dominated SN-regulated', to 'accretion-dominated AGN-regulated' growth (Silk, 2011, 2013; Taylor et al., 2017; Grylls et al., 2020), as also noticed by (Johansson et al., 2013). This galaxy–halo connection is known to have effects on galaxy properties, such as $M_{\rm stellar}$, galaxy size and SFR (for a review, see Wechsler & Tinker, 2018). To study this, I explore the SN/host connection across a range of division points in Figure 3.5, showing the step locations, significances and magnitudes for the global and local $M_{\rm stellar}$ and $U-R$ steps.

For local and global $M_{\rm stellar}$, the maximum step location and environmental property median are quite separate, with relatively large differences in significances and magnitudes of the corresponding steps as a result of the prominent peaks in the curves shown in the top panels of the figure. This is particularly noticable for the local $M_{\rm stellar}$, with almost a 2σ difference in step size depending on whether you choose to use the traditional sample median or the location giving the most significant step. The maximum step location and environmental property median step location for the rest-frame $U-R$ colour for both the global and local measurements are located close together, at just below a $U-R$ value of 1.0, while the $M_{\rm stellar}$ step locations are more than 1 dex different. The local $U-R$ measurement has a relatively broad peak in the property-step significance space (Fig. 3.5; i.e., the step size is insensitive to the split point), suggesting that the local $U-R$ step is more stable – but perhaps also less discriminating – than the local $M_{\rm stellar}$ step. This is consistent with Roman et al. (2018), who found similar magnitude steps for global and local rest-frame $U-V$ colour (their table 7).

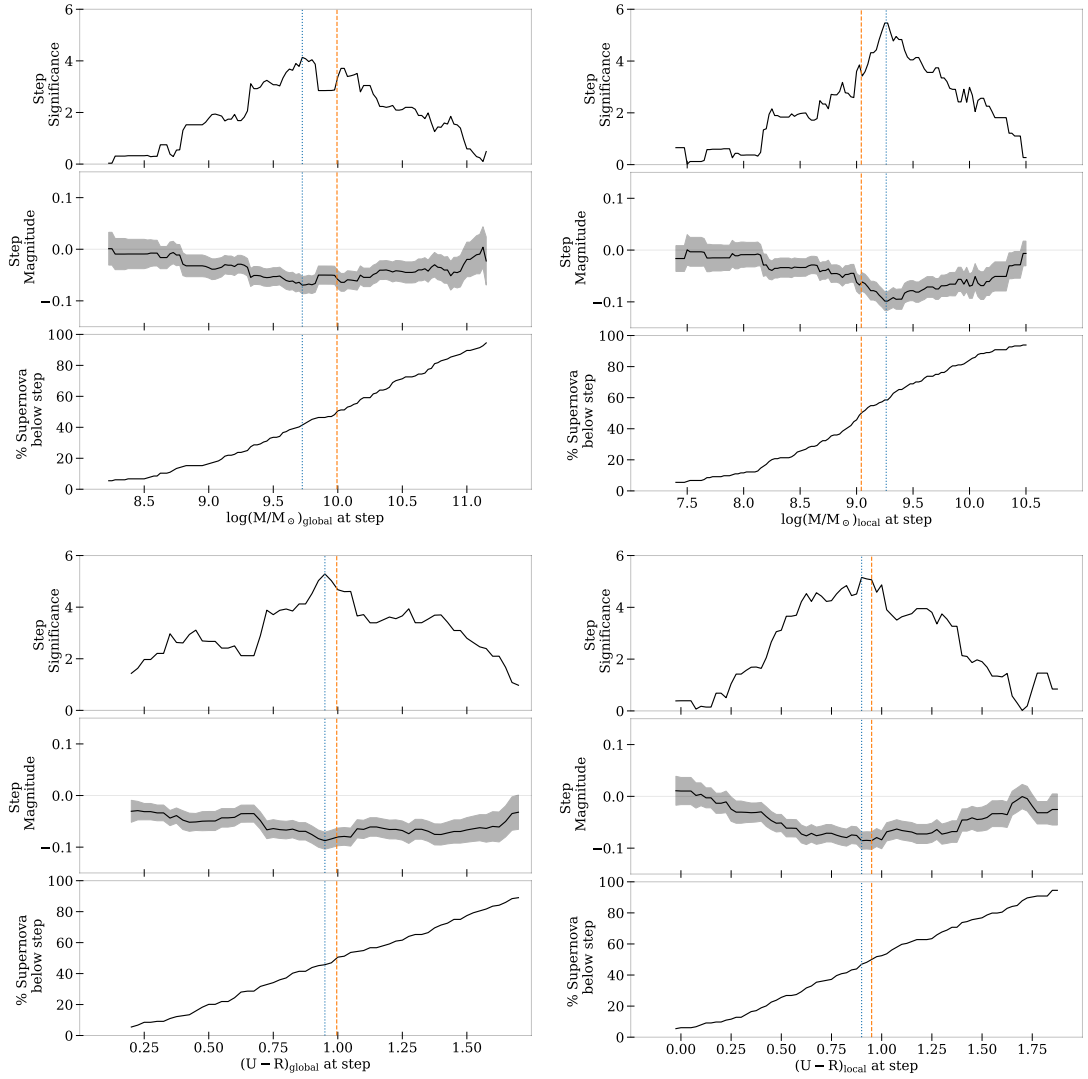

FIGURE 3.5: Plots comparing the significance, magnitude and location of the steps for each parameter. From top to bottom, and left to right: global M_{stellar}, local M_{stellar} within a 4 kpc radius, global rest-frame $U - R$ colour, and local rest-frame $U - R$ colour. In each plot, the lower panel shows the percentage of SNe Ia in the sample in the bin below the step location as the location of the step is varied; the middle panel is the magnitude of the step at each location with the grey shaded region showing the uncertainty; and the top panel shows the significance of the step in σ. The orange-dashed line indicates the location of the environmental property median of the sample, and the blue-dotted line shows the step that gives the maximum significance.

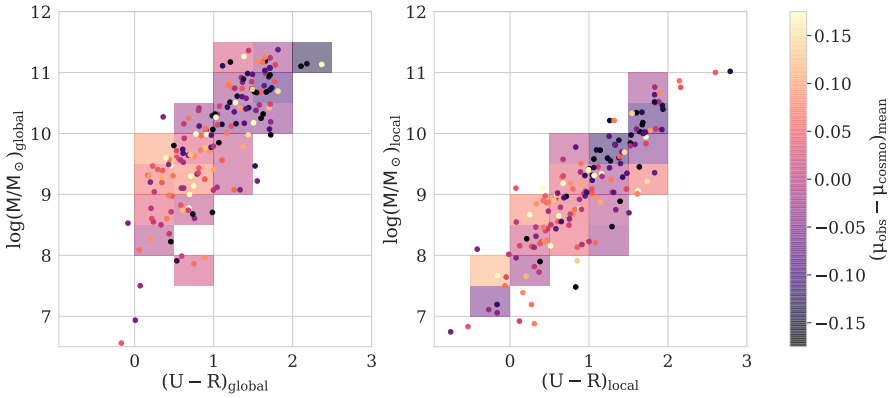

FIGURE 3.6: Heatmaps displaying correlations between rest-frame $U - R$ and stellar mass, with bins weighted by mean Hubble residual, for both global (left plot) and local (right plot) environments. Bins containing two or fewer SN are not displayed. Overplotted with scatter plot displaying raw, unbinned data. To give an indication of the uncertainty in the colour coding, we quote the median uncertainty in the bin mean Hubble residuals as 0.037 mag.

3.2.3.2 Comparing M_{stellar} and $U - R$

To understand how host properties relate to one another with regards to Hubble residuals, I present in Figure 3.6 a complementary visualisation of my data using two-dimensional heatmaps in the parameter space of rest-frame $U - R$ and M_{stellar}, with bins coloured by mean Hubble residual. This enables me to study the trends in Hubble residual with a given host galaxy property at a fixed value of another. For example, the variation in Hubble residual with $U - R$ colour at fixed M_{stellar} and vice versa.

Any variation in Hubble residual at fixed environmental property is quite minimal, but as an example, if I keep global M_{stellar} constant just below $10^{10}\,\text{M}_{\odot}$, a very slight decrease in Hubble residual with increasing global $U - R$ can be seen. This tentative finding suggests that better standardisation may be obtained by combining the effects of multiple environmental properties.

3.3 Systematics

To explore some of my key analysis choices and their impact on the results, I perform additional tests. These include changing the size of the local aperture photometry radius, changing the cosmological bias correction from BBC1D to BBC5D, using different environmental properties such as sSFR and other restframe colours instead of $U - R$. I also explore the effects of splitting the sample into subsamples based on SN properties x_1 and c, or environmental properties.

3.3.1 Changing Local Radius

Throughout this thesis, I define a local physical radius of 4 kpc as motivated by the quality of the stacked images. However, to understand the effect of this choice on my results, I vary here the size of this local radius, choosing radii of size from 2.5 to 10 kpc in 0.5 kpc steps, and from 10 to 30 kpc in 5 kpc steps. This range allows me to probe from very small apertures to those of galactic size.

I study all apertures independently and follow the original method from the beginning, remeasuring all photometry and rederiving all environmental properties using SED fitting. Due to this, the number of objects in each sample varies slightly as objects near the boundaries of the cuts discussed in Section 3.1.1 may no longer pass the quality requirements with the new aperture. As an example, for the smallest radii there are fewer photons entering the aperture, leading to larger statistical uncertainties in the measurements of properties, so more objects are likely to be rejected. On the other end of the scale, or the largest radii studied, satellite, companion, or background galaxies may enter the aperture if it extends over the edge of the galaxy as measured by SOURCE EXTRACTOR. This may introduce background flux not associated with the host which may introduce additional scatter in the overall colour measurement of the region, and thus affect the Hubble residual dependence. This effect is redshift dependent: a 30 kpc aperture at $z = 0.1$ is likely to have more background sources than one at $z = 0.5$.

In Figure 3.7, I present the local $U - R$ and local M_{stellar} steps as a function of aperture radius size. As can be seen, as the aperture size increases, the magnitude of the step decreases. However, I note that, particularly for $U - R$, the global measurements are not following this trend; the global result is not the asymptotic limit. There are two reasons for this. Firstly, different aperture types were used for local and global, i.e. circular apertures were used for local measurements whereas the global measurements used a Kron aperture. Second, these measurements may never converge as global measurements of the properties of galaxies are centred on the galaxy centre and local measurements are centred on the individual SN locations. These locations may be close together if the SN is at the centre of the galaxy, or the SN may be located at the very outer edge of a galaxy, on a spiral arm, so apertures of identical sizes and shapes simply will not measure the same area.

For visualisation purposes, I present the global step sizes in Figure 3.7 at the 'average global radius'. This is defined using the SOURCE EXTRACTOR output values to obtain an area for each measured ellipse, equating this area to the area of a circle to obtain an effective circular aperture radius for each host galaxy, by taking the mean for the sample we find that the average circular galaxy radius is 16.45 ± 6.08 kpc. which can be compared to the circular aperture radii used in our local analysis instead of semi-major and semi-minor axes of ellipses.

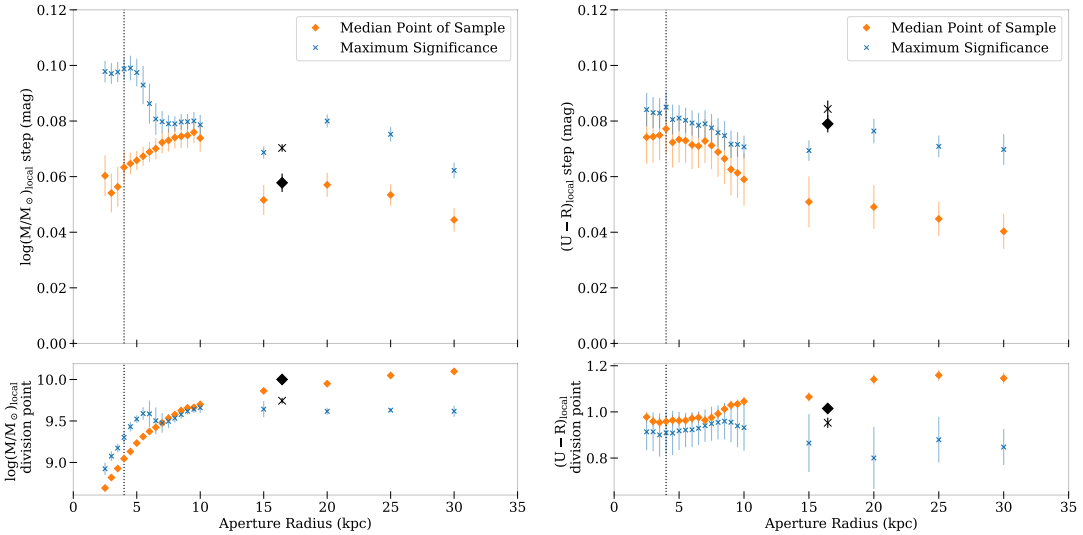

FIGURE 3.7: Top panels: variation of the local M_{stellar} step and the rest-frame $U - R$ colour step as functions of the local aperture radius. Lower panels: evolution of the division points of the step as a function of the local aperture radius. Error bars in all panels are the standard deviations of the sample, however we acknowledge that there will be correlations between the different aperture sizes. The global measurements for both M_{stellar} and $U - R$ are represented by the black symbols (diamond for median, cross for point of maximum significance) placed at the average sized aperture radius for the sample used of 16.45 ± 6.08 kpc. The black dotted line in all panels indicates the fiducial 4 kpc aperture sized used in our analysis. This additionally is the minimum size that includes all data points, results below this aperture are potentially biased by the PSF size.

From the shapes of the curves in the upper panels of Figure 3.7, the local $U - R$ measurement is be more consistent than the local M_{stellar}, with less of a difference between the magnitudes of the steps when dividing at the environmental property median or maximum step significance point of the sample, particularly in the $2.5 - 10$ kpc region. For the $U - R$, the step size also gets consistently larger as the aperture gets smaller, for both split point location options, whereas for the M_{stellar}, the step sizes diverge at the lower aperture sizes, with the size of the step for the median step location being dramatically different than the size of the most significant step. In the lower panels of Figure 3.7, as expected the local mass displays a decreasing division point as smaller apertures are used and thus each aperture contains less mass. For the local $U - R$ however, the division points are consistent at ~ 1 for all apertures below 15 kpc in radius. This indicates a stability to $U - R$ over M_{stellar} which suggests that using $U - R$ to probe local environment characteristics is simpler than M_{stellar} as it is less dependent on the local aperture size.

TABLE 3.4: As Table 3.3, but for a 5D bias correction.

Property	Sample Median/ Max Significance	Division Point	Hubble Residual Step Sig. (σ)	Hubble Residual Step Magnitude
Global Mass	Median	9.99	1.06	0.019 ± 0.018
Global Mass	Max	9.73	2.17	0.037 ± 0.017
Local Mass	Median	9.04	2.36	0.042 ± 0.018
Local Mass	Max	9.26	4.34	0.076 ± 0.017
Global U-R	Median	1.00	3.37	0.058 ± 0.017
Global U-R	Max	0.95	3.77	0.064 ± 0.017
Local U-R	Median	0.95	3.82	0.065 ± 0.017
Local U-R	Max	0.95	3.82	0.065 ± 0.017

3.3.2 5D or 1D Cosmological Corrections

As discussed in Section 2.4.2, for my baseline analysis I use the BBC1D μ_{bias} correction. This is because an aim of this analysis is to understand the relationships between environmental properties and the cosmological parameters x_1 and c that more complicated μ_{bias} corrections such as BBC5D, BBC7D or BBC-BS20 attempt to correct for.

However, for completeness, if I use the BBC5D μ_{bias} correction, the magnitudes of Hubble residual steps are found to be smaller than with the BBC1D baseline analysis by an average of ~ 0.026 mag across M_{stellar} and $U - R$, as shown in Table 3.4. This difference most strongly impacts the global M_{stellar} (a difference of 0.038 mag), and is likely a result of the underlying simulated x_1-M_{stellar} correlation that is not modelled in existing BBC5D corrections, with Smith et al. (2020b) finding a similar difference of 0.026 ± 0.009 mag for global M_{stellar} in their analysis. To address this, DES-SN developed BBC7D and BBC-BS20, which is currently being tested for use in future DES-SN cosmological analyses (Popovic et al., 2021).

3.3.3 Other Environmental Properties

In this thesis, I focus my analysis on M_{stellar} and rest-frame $U - R$ colour, however the SED fitting procedure described in Section 2.6 provides additional galaxy properties. M_{stellar} is the most well-studied SN host galaxy property, with the discovery of the of the 'mass step' relationship kick-starting the discussion for environmental property corrections in SN cosmology, so is an excellent baseline for any SN host analyses. I chose rest-frame $U - R$ as it covers the largest wavelength range for our DES dataset, therefore traces both the red and blue ends of the spectrum so carries information about both M_{stellar} and SFR (and thus age) of the stellar populations, and has been found to correlate with galaxy morphology (Lintott et al., 2008). However, these are not the only

environmental properties that can be studied, and I present a brief overview of the other environmental properties in the following sections:

3.3.3.1 sSFR

From measurements of the M_{stellar} and SFR, the sSFR can be determined. Numerous previous analyses of the host galaxies of Type Ia SNe have used this parameter, as (particularly when measured locally to the SN location) the star formation activity is well-correlated with the fraction of old and young progenitor systems, and is only weakly affected by dust (Rigault et al., 2020).

As presented in Table 3.5, I find that the local sSFR step is of similar magnitude and significance to the local $U - R$ step measurements, with the local sSFR step found at the sample median sSFR location being 0.064 ± 0.017 mag (3.7σ) for the 4 kpc radius aperture between star-forming and passive regions. This is consistent with the 0.081 ± 0.018 mag step found by Kim et al. (2019), but considerably smaller than the 0.163 ± 0.029 mag step found by Rigault et al. (2020), although I note that my measure of sSFR is less direct (based on template fitting), and Rigault et al. (2020) is at low z, where the step is expected to be larger; see Rigault et al. (2013) Figure 11, also Childress et al. (2014) and Kim et al. (2018).

Interestingly, the global and local values of the sSFR step at the sample median are equal. Additionally, the division points for local and global are equal at -9.28 when using the step size of maximum significance. This may simply be coincidental, but may also point to interesting physics suggesting that the overall distributions of sSFR is consistent in local and global regions for SNe host galaxies at the redshifts I measure in the DES analysis.

3.3.3.2 Other Rest-frame Colours

Using the rest-frame $UBVR$ magnitudes calculated in Section 2.6 for each global host galaxy and local region, I can measure a variety of rest-frame colours and their corresponding step sizes, which are presented in Table 3.5.

Consistent with my main analysis, all step sizes are significant to $> 3\sigma$, and vary in size from ~ 0.058 mag to 0.99 mag. Of particular note is the local $U - V$ value of 0.087 ± 0.016 mag, very similar to the value of 0.091 ± 0.013 mag found for local $U - V$ colour within a 3 kpc radius by Roman et al. (2018). Interestingly, I find that the largest local rest-frame colour step of 0.099 ± 0.016 mag (6σ) for the 4 kpc radius aperture is found when using $V - R$ colour, representing two neighbouring filter responses in our $UBVR$ estimates.

TABLE 3.5: Hubble residual steps for sSFR, and a variety of rest-frame colours using a 1D bias correction.

Property	Sample Median/ Max Significance	Division Point	Hubble Residual Step Sig. (σ)	Magnitude
Global sSFR	Median	-9.65	3.70	0.064±0.017
Global sSFR	Max	-9.28	4.81	0.080±0.017
Local sSFR	Median	-9.43	3.70	0.064±0.017
Local sSFR	Max	-9.28	5.04	0.084±0.017
Global U-B	Median	-0.04	3.55	0.062±0.017
Global U-B	Max	-0.05	4.33	0.074±0.017
Local U-B	Median	-0.05	3.36	0.058±0.017
Local U-B	Max	-0.17	4.72	0.078±0.017
Global U-V	Median	0.52	4.52	0.078±0.017
Global U-V	Max	0.55	4.58	0.080±0.017
Local U-V	Median	0.48	4.74	0.081±0.017
Local U-V	Max	0.45	5.25	0.087±0.016
Global B-V	Median	0.58	4.19	0.072±0.017
Global B-V	Max	0.55	4.96	0.083±0.017
Local B-V	Median	0.53	4.53	0.078±0.017
Local B-V	Max	0.47	4.68	0.077±0.017
Global B-R	Median	1.09	4.63	0.079±0.017
Global B-R	Max	1.03	5.36	0.089±0.017
Local B-R	Median	0.99	5.08	0.086±0.017
Local B-R	Max	1.00	5.25	0.089±0.017
Global V-R	Median	0.49	4.89	0.084±0.017
Global V-R	Max	0.48	5.15	0.085±0.016
Local V-R	Median	0.46	6.00	0.099±0.017
Local V-R	Max	0.45	6.01	0.099±0.016

Further investigation is needed with a larger dataset to determine which colour is the most stable and effective for use in cosmological analysis.

3.3.4 Splitting the Sample by Stretch and Colour

Although the DES3YR sample is of modest size, I perform a preliminary investigation of splitting the sample by SN x_1 and c: $x_1 > 0$ and $x_1 \leq 0$, and $c > 0$ and $c \leq 0$, following Sullivan et al. (2010) and Rigault et al. (2020). This tests if the steps in SN Ia luminosity could be driven by underlying relationships between SN properties x_1/c and host galaxy properties. Based on my findings from this work, I explore this relationship in depth in Chapter 5 for the DES5YR sample.

For each subsample I repeat the analysis of the environmental properties using my default 4 kpc radius local aperture and BBC1D cosmological bias correction throughout.

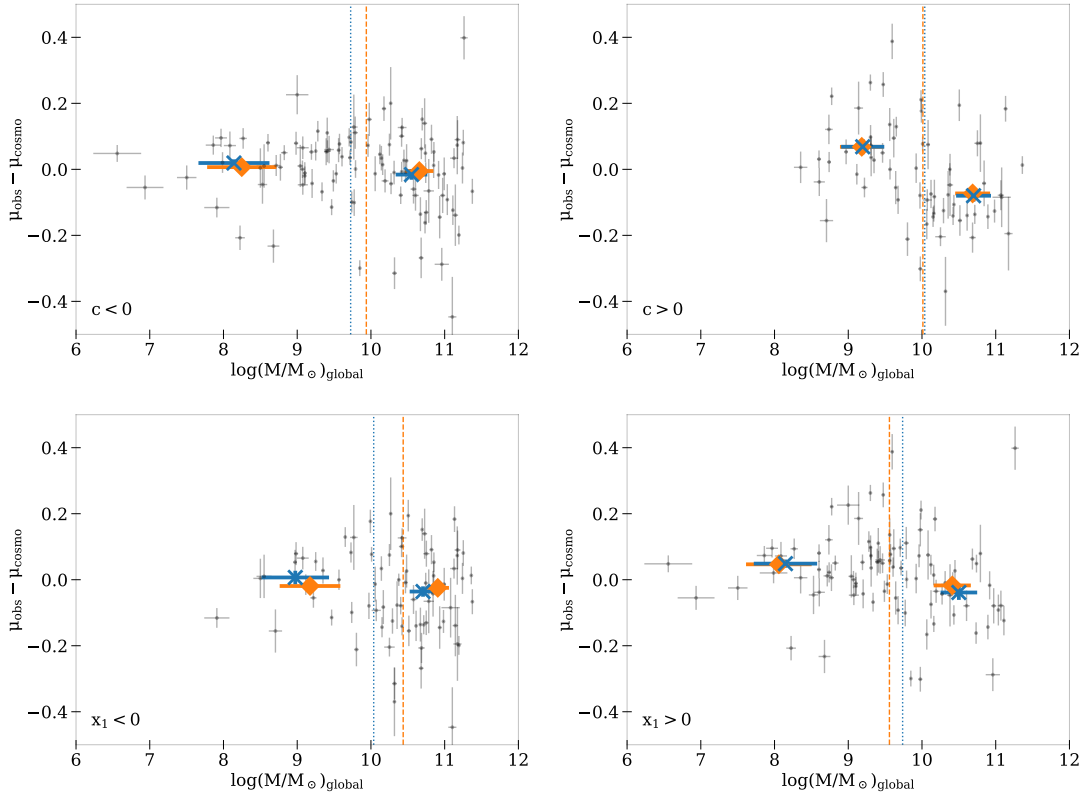

FIGURE 3.8: Hubble residual plots as a function of global M_{stellar}, for subsamples split by c and x_1, where α and β have been fixed as in the main analysis. As in Figure 3.4, the orange-dashed line represent the sample environmental property median, and the blue-dotted line the location of the maximum step. These correspond with the orange diamond and blue cross bin mean markers. See Table 3.6 for the numerical values for the steps when split at the environmental property median of the subsamples. r.m.s. values are displayed in Table 3.7.

In Table 3.6 I present the step magnitudes and uncertainties for steps at the median environmental property ($U - R$ and M_{stellar}) division point of the sample.

I begin by fixing α and β at the values derived from the full DES3YR sample ($\alpha = 0.156 \pm 0.012$, $\beta = 3.201 \pm 0.131$), displaying the resulting Hubble residual steps in the top section of Table 3.6, and corresponding r.m.s. values in Table 3.7. As examples, I present in Figure 3.8 and Figure 3.9 the global mass and local $U - R$ Hubble residual plots for the different subsamples.

As can be clearly seen in Table 3.6 and illustrated in both Figures 3.8 and 3.9, I find significant differences in step sizes ($\sim 3\sigma$) when splitting the sample based on c. The bluer $c < 0$ have smaller steps than for $c > 0$, for all environmental properties, both globally and locally, indicating that the bluer subset is more homogeneous. The redder $c > 0$ have higher dispersion and larger steps (~ 0.14 mag), similar to in Smith et al. (2020b). The scale of this difference is not consistent with Rigault et al. (2020) who

TABLE 3.6: Subsample data when splitting the sample based on on x_1 and c.

Property	c split			x_1 split		
	$c < 0$	$c > 0$	Difference (σ)[1]	$x_1 < 0$	$x_1 > 0$	Difference (σ)
Number of Supernovae	102	62		74	90	
Keeping α and β fixed ($\alpha = 0.156 \pm 0.012$, $\beta = 3.201 \pm 0.131$)						
Global Mass Step[2]	0.012 ± 0.020	0.141 ± 0.029	3.66	0.006 ± 0.026	0.064 ± 0.024	1.64
Local Mass Step	0.034 ± 0.020	0.125 ± 0.031	2.47	0.069 ± 0.025	0.041 ± 0.025	0.79
Global U-R Step	0.045 ± 0.020	0.154 ± 0.029	3.09	0.065 ± 0.024	0.070 ± 0.024	0.14
Local U-R Step	0.046 ± 0.020	0.148 ± 0.029	2.89	0.058 ± 0.025	0.085 ± 0.023	0.79
α and β free to best-fit for each sub-sample						
α	0.158 ± 0.017	0.094 ± 0.028	1.95	0.254 ± 0.028	0.228 ± 0.031	0.62
β	4.487 ± 0.619	3.894 ± 0.481	0.76	3.273 ± 0.195	3.585 ± 0.211	1.09
Global Mass Step	0.033 ± 0.026	0.123 ± 0.033	2.14	0.030 ± 0.027	0.069 ± 0.027	1.02
Local Mass Step	0.049 ± 0.026	0.126 ± 0.034	1.79	0.088 ± 0.025	0.066 ± 0.027	0.60
Global U-R Step	0.071 ± 0.026	0.143 ± 0.032	1.75	0.094 ± 0.025	0.079 ± 0.026	0.42
Local U-R Step	0.077 ± 0.025	0.118 ± 0.034	0.97	0.097 ± 0.025	0.103 ± 0.025	0.17

[1] Significance is quadrature sum.
[2] Step division point at the subsample environmental property ($U - R$ and M_{stellar}) median.

TABLE 3.7: r.m.s. values for the split subsamples, corresponding to Table. 3.6.

Property	Sub-sample r.m.s.[1]			
	$c < 0$		$c > 0$	
	$<$ DP[2]	$>$ DP	$<$ DP	$>$ DP
Global Mass	0.095 ± 0.019	0.141 ± 0.028	0.147 ± 0.038	0.144 ± 0.037
Local Mass	0.086 ± 0.017	0.147 ± 0.029	0.134 ± 0.035	0.156 ± 0.040
Global U-R	0.084 ± 0.017	0.149 ± 0.030	0.142 ± 0.037	0.150 ± 0.039
Local U-R	0.084 ± 0.017	0.148 ± 0.030	0.141 ± 0.037	0.150 ± 0.039
	$x_1 < 0$		$x_1 < 0$	
	$<$ DP[2]	$>$ DP	$<$ DP	$>$ DP
Global Mass	0.131 ± 0.031	0.141 ± 0.033	0.106 ± 0.023	0.144 ± 0.031
Local Mass	0.104 ± 0.024	0.162 ± 0.038	0.101 ± 0.022	0.147 ± 0.031
Global U-R	0.124 ± 0.029	0.147 ± 0.035	0.116 ± 0.025	0.136 ± 0.029
Local U-R	0.123 ± 0.029	0.147 ± 0.035	0.116 ± 0.025	0.136 ± 0.029

[1] Subsamples where α and β were kept fixed ($\alpha = 0.156 \pm 0.012$, $\beta = 3.201 \pm 0.131$).
[2] Division point at subsample median.

found no significant difference between the size of the Local sSFR bias in subsamples split for high and low c (0.45σ).

There are two broad interpretations of this c dependency: redder and bluer objects may represent different progenitor paths, i.e. bluer objects represent one distinct set of progenitors (hence no step), whilst redder objects are a combination of different progenitors (hence show a step); or alternatively, the bluer $c < 0$ objects may suffer less dust extinction (Brout & Scolnic, 2021) and thus less event-to-event scatter. These interpretations suggest that the Hubble residual steps that we see in the main sample may be driven by physics that affects the colour of the SNe, and could be a source for the origin of the remaining ~ 0.14 mag (Scolnic et al., 2018) Hubble residual dispersion in the general SN Ia population. Additionally, as bluer objects are observationally brighter than redder objects and so have lower uncertainties, they drive the fit of α and β so they may in turn drive the size of the step.

I find no significant difference between the step sizes for the subsamples split into high and low x_1, consistent with Sullivan et al. (2010), who found no significant difference between the size of the global stellar mass step in subsamples split for high and low x_1, with an average difference between subsamples of 0.60σ; and with Rigault et al. (2020) who found a difference of 0.84σ. My largest difference for x_1 subsamples is 1.64σ for the global mass step, indicative of the known $x_1 - M_{\text{stellar}}$ relationship (Smith et al., 2020b).

The Hubble residual r.m.s. values are similar to my main analysis, with SNe Ia in the bluer, low mass galaxies being more homogeneous. This homogeneity is most pronounced when the sample is split by c, with a particularly low r.m.s. of $0.084 \pm$

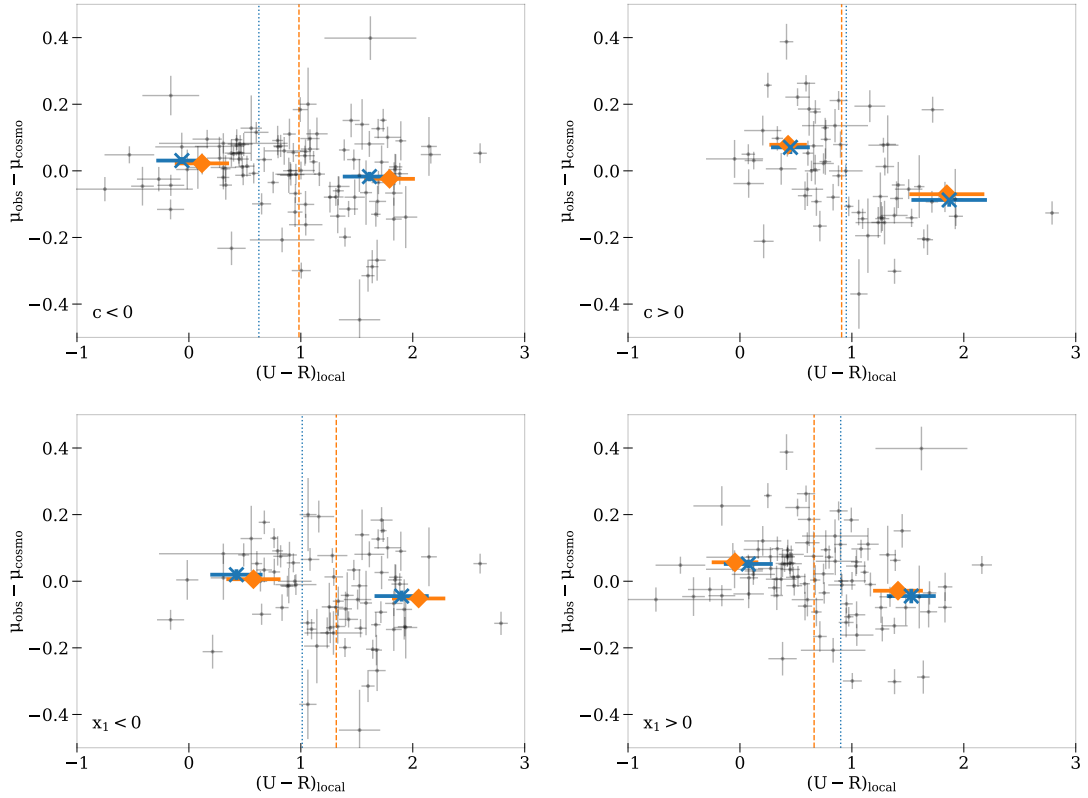

FIGURE 3.9: Hubble residual plots as a function of local $U - R$ within the 4 kpc radius aperture, for subsamples split by c and x_1, where α and β have been fixed as in the main analysis. As in Figure 3.4, the orange-dashed line represent the sample environmental property median, and the blue-dotted line the location of the maximum step. These correspond with the orange diamond and blue cross bin mean markers. See Table 3.6 for the numerical values for the steps when split at the environmental property median of the subsamples. r.m.s. values are displayed in Table 3.7.

0.017 mag for blue SNe Ia in blue local galaxy regions, with a consistent value for globally blue galaxies.

When I refit α and β to best fit for the x_1 and c subsamples, my findings are consistent but the differences in step sizes between subsamples decrease slightly, as shown in the lower half of Table 3.6, indicating that the effects have been absorbed by the changing α and β parameters. However, by modifying α and β in this way, I am no longer recovering the underlying effect of the x_1 and c parameters on the main sample, so this may not be the best representative of the fundamental cause of the steps seen.

3.3.5 Splitting the Sample by Environmental Properties

As a final test of my analysis, I refit the α and β correction terms for subsamples based on splitting by the environmental properties of stellar mass and rest-frame $U - R$ at the sample median, for example using different α and β values for high and low global

M_{stellar}. In a similar way to the previous section where I split the sample by c and x_1, this test also investigates whether the steps in SN Ia luminosity could be driven by underlying relationships between x_1/c and host galaxy properties.

Presented in Table 3.8, I find a small, but interesting, $\sim 2\sigma$ difference in both α and β values on each side of the environmental property division point, for all properties measured. Brout & Scolnic (2021) suggest that SNe found in high mass galaxies follow a different colour law to those in lower mass systems, thus it is expected that they would have a lower β. I see evidence of this expectation with smaller β values found in higher mass, redder regions; also agreeing with Sullivan et al. (2011). I additionally see a smaller α for low mass, bluer regions, suggestive of the relationship between host galaxy stellar mass and x_1, and the prediction of Childress et al. (2014): that the most cosmologically uniform sample is located in actively star-forming, lower-mass galaxies. The lower α value means that there is less need for a correction for these SNe, therefore they have lower scatter and thus they are considered to be better standard candles.

3.4 Summary and Discussion

In this chapter, I have used my framework to investigate the effects of host galaxy properties on SNe Ia from the DES3YR sample. From the DES-SN image stacks, free from SN light, and by measuring the fluxes for SN host galaxies and local apertures at the SN position, I estimated environment properties and compared them to SN Ia light curve properties and luminosities. In this section, I outline those findings and put them into context with previous work.

First, I find that all the measured steps are significant at $> 3\sigma$ (range of 3.3–5.5σ), whether using local or global measures, or using stellar mass or $U-R$ colour, or splitting at the environmental property sample median or maximal step point. This is also the case when I expand my analysis to consider other rest-frame colours and the sSFR. This agrees with prior studies and further emphasises the need for light-curve corrections based on SN environmental properties when using SNe Ia in cosmology.

Focusing on the differences between local and global properties, I find that local stellar mass steps are larger than global stellar mass steps by up to 0.03 mag, and thus may recover more residual SN Ia magnitude dispersion. For $U-R$, both global $U-R$ (0.081 ± 0.017 mag) and local $U-R$ (0.082 ± 0.017 mag) steps are larger than the global mass step (0.057 ± 0.017 mag). Although the difference between global and local $U-R$ steps is small, the size of the local $U-R$ step is more stable when considering different values to divide the SN sample, and thus may be less susceptible to analysis choices. This agrees with the findings of Roman et al. (2018) who found similar steps for global and local rest-frame $U-V$ colour when using a local aperture of 3 kpc radius over a similar redshift range to my analysis. It is likely that to find clear differences between

TABLE 3.8: Subsample data when splitting the sample based on on environmental properties.

Property	α			β		
	$<$ DP[2]	$>$ DP	Difference (σ)[1]	$<$ DP	$>$ DP	Difference (σ)
Global Mass	0.140 ± 0.020	0.198 ± 0.015	2.32	3.65 ± 0.22	3.16 ± 0.19	1.69
Local Mass	0.156 ± 0.017	0.206 ± 0.020	1.90	3.65 ± 0.19	3.07 ± 0.20	2.10
Global U-R	0.154 ± 0.021	0.219 ± 0.018	2.35	3.71 ± 0.18	3.08 ± 0.20	2.34
Local U-R	0.157 ± 0.023	0.218 ± 0.017	2.13	3.62 ± 0.22	2.99 ± 0.18	2.21

[1] Significance is quadrature sum.
[2] Division point at the sample median.

local and global measurements, much smaller apertures need to be explored, but this is limited by the seeing of the images when using photometric measures of properties.

As a test of my analysis, I split my SN Ia sample into subsamples based on the SN properties x_1 and c. When I split my SN Ia sample by c, I find results that do not agree with earlier studies (e.g., Sullivan et al., 2010; Rigault et al., 2020). I find the redder objects ($c > 0$) have larger steps for both M_{stellar} and $U - R$, for both global and local, of ~ 0.14 mag, with a $\sim 3\sigma$ difference in step size between red and blue SNe. This suggests that the overall step size is dominated by the redder objects.

In another test of my analysis, I divide my sample by environmental properties and refit the nuisance parameters α and β. In this scenario, I find mild tension ($\sim 2\sigma$ difference) in α and β across the division point. Smaller β values are observed in higher mass, redder regions (or galaxies), agreeing with the prediction of Brout & Scolnic (2021). I also find a smaller α for low mass, bluer regions, suggesting that the most cosmologically-uniform sample is in actively star-forming, lower-mass galaxies.

By analysing the r.m.s. scatter in Hubble residuals, I find that SNe Ia in redder (and presumably passive or duster) galaxies or local regions have a higher r.m.s., suggesting that SNe Ia in bluer environments provide a more homogeneous sample. This homogeneity is most pronounced when splitting into sub-samples based on c, with an r.m.s. scatter of 0.084 ± 0.017 mag for SNe Ia in bluer local environments when $c < 0$. This finding suggests that the most uniform SNe Ia sample for use in cosmology is blue SNe in blue environments. This conclusion agrees with literature findings. For example, Rigault et al. (2013) postulate that SNe Ia from locally passive environments are the cause of the biases they observed, through their higher scatter, and they suggest adding a selection cut to only include those in locally star forming (i.e. blue) environments for cosmology. This is emphasised by Childress et al. (2014), Kelly et al. (2015), Henne et al. (2017) and Kim et al. (2018) who all find consistent results, and make the same conclusions about selecting star forming galaxies. Kim et al. (2018) also suggest that the scatter is further constrained by limiting to low-mass ($\leq 10^{10} M_{\odot}$) globally star-forming host galaxies. In another test, through the analysis of ejecta velocities, Wang et al. (2009), Foley & Kasen (2011) and Siebert et al. (2020) all find that the SN scatter can be reduced by using lower-velocity, bluer supernovae. Additionally, from the simulations of Kessler & Scolnic (2017), there is a smaller bias correction for blue supernovae than there is for red, across all redshifts.

These results have implications for using SNe Ia as cosmological probes. However, the DES3YR sample that I consider here, despite its exquisite photometric calibration and the spectroscopic confirmation of all SNe in the sample, remains modest in size, particularly after splitting the sample by SN light-curve parameters. The upcoming DES5YR sample of SNe Ia will be significantly larger, and thus provide further insight

in understanding the effect of environment on SNe Ia. Environmental effects using a preliminary DES5YR sample will be explored in the following chapter.

Chapter 4

Environmental Effects in DES5YR

Having established my analysis using the spectroscopically-confirmed DES3YR sample, I can now turn to analysing the effect of environment on SNe Ia in the photometrically-confirmed DES5YR sample. As discussed in Section 2.3, DES5YR will be considerably larger than DES3YR, allowing for greater statistical importance, and for the testing of key analysis techniques for the next generation of large-scale photometric supernova surveys. However, there are additional complications due to the uncertainty of photometric classification and redshift measurements.

4.1 Sample Selection

As the final DES5YR sample is still undergoing development in the collaboration before release, I use a preliminary sample in this analysis, which has been kindly provided by DES-SN collaborator Maria Vincenzi. This sample was created by applying the SuperNNova (Möller & de Boissière, 2020) photometric classifier trained on core-collapse SN templates from Vincenzi et al. (2019) to the potential candidates from Vincenzi et al. (2021) ($\sim$ 1600 objects after JLA-like light-curve cuts), and contains the SALT2 outputs for each SNe that passes the inputted selection requirements. In this sample, it is required that each object has a probability of being a SN Ia of $P(Ia) > 0.5$, and typical JLA-like light-curve quality requirements in x_1 and c and their associated uncertainties were applied, see Section 2.4.1. For this analysis, I require a number of additional cuts on colour and stretch uncertainties, following Brout & Scolnic (2021), and to obtain relevant local information from the stacked images I require a redshift cut in the same way as for Chapter 3 of $z < 0.6$. Additionally, once environmental properties have been calculated for the sample (see Section 4.1.1), I apply a cut on $\sigma_{(U-R)} < 1$ mag for both the global and local measurements to have well-constrained rest-frame $U - R$ colours (this also removes objects with large uncertainties in M_{stellar} and SFR). Building on the work in Chapter 3, I also require that the global host galaxy M_{stellar} is greater than

TABLE 4.1: Sample selection cuts used for my DES5YR analysis.

Cut	Number of SNe Ia
$z < 0.6$ & $P(Ia) > 0.5$[1]	1045
$\sigma_{(U-R)} < 1$	903
Global $M_{\text{stellar}} >$ local M_{stellar}	878
$\sigma_c < 0.05$	681
$\sigma_{x_1} < 1$	677

[1] Data provided already cut with both of these requirements.

the local environment M_{stellar}. A summary of all the selection requirements applied is as follows and is outlined in Table 4.1:

- Before cuts specific to this analysis:
  - Colour $|c| < 0.3$,
  - Stretch $|x_1| < 3$,
  - $\chi^2 < 16$ to remove 4σ outliers in the Hubble residual,
- Requirements for this analysis:
  - $P(Ia) > 0.5$,
  - Redshift $z < 0.6$,
  - $\sigma_{(U-R)} < 1$ mag,
  - Global $M_{\text{stellar}} >$ local M_{stellar},
  - Colour uncertainty $\sigma_c < 0.05$,
  - Stretch uncertainty $\sigma_{x_1} < 1$,

After selection cuts, there are a total of 677 objects in my sample, with values of $\alpha = 0.172 \pm 0.007$ and $\beta = 3.07 \pm 0.07$. Throughout this chapter, I use a BBC1D bias correction.

4.1.1 Photometric Measurements

As in Chapter 3, I follow the techniques outlined in Section 2.5 to obtain photometric measurements for each SNe host galaxy and 4 kpc radius local aperture around each SN. The environmental properties, including M_{stellar} and rest-frame $U - R$, and their associated uncertainties, are obtained through the SED-fitting procedure outlined in Section 2.6 for each of these environments.

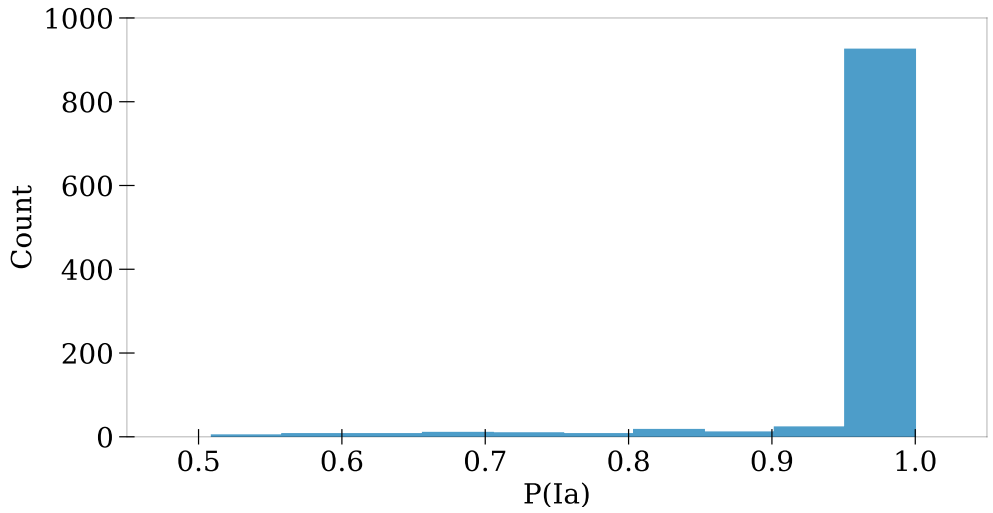

FIGURE 4.1: Histogram displaying the distribution of $P(Ia)$ in the DES5YR sample before analysis-specific selection cuts. $P(Ia)$ values presented here are defined using SNN trained on Vincenzi et al. (2019) templates, for $P(Ia) > 0.5$.

4.1.2 Different Classifiers and Training Sets

For this analysis, I have focused on using the SUPERNNOVA (SNN) (Möller & de Boissière, 2020) photometric classifier trained on core-collapse templates from Vincenzi et al. (2019), as this is currently the preferred choice for the final DES5YR sample within the DES-SN collaboration. However, I repeated this analysis using various combinations of classifier, templates and probability cuts. These are defined as follows:

1. SNN trained on Vincenzi et al. (2019) templates, $P(Ia) > 0.5$
2. SNN trained on Vincenzi et al. (2019) templates, $P(Ia) > 0.8$
3. SNN trained on Vincenzi et al. (2019) templates, $P(Ia) > 0.95$
4. SNN trained on Jones et al. (2017) templates, $P(Ia) > 0.5$
5. SNN trained on Hounsell & Sako (in prep) templates, $P(Ia) > 0.5$
6. Supernova Identification with Random Forest (SNIRF; an extension of Dai et al., 2018) trained on Vincenzi et al. (2019) templates, $P(Ia) > 0.5$
7. SNIRF trained on Jones et al. (2017) templates, $P(Ia) > 0.5$

As can be seen in Figure 4.1, the overwhelming majority of objects have a high probability of being a SNe Ia of $P(Ia) > 0.95$. When the different $P(Ia)$ samples undergo the additional quality cuts that are specific to this analysis outlined in Section 4.1, the final sample sizes were comparable, and there was no real difference in results for each

sample. In other words, the objects that had a low $P(Ia)$ typically also had the largest uncertainties in x_1, c, and environmental properties, meaning that they were removed in each case.

4.2 Environmental Dependence of SN Ia Luminosities

With the measurements of the environmental properties completed, I can turn to comparing them, both for local vs. global properties, and comparing with SN properties such as x_1, c and Hubble residual. I can also explore how these results differ from those found in Chapter 3 for the spectroscopically-confirmed DES3YR data, given the increase in sample size contrasted with the added complications of the photometric sample.

4.2.1 Comparing Properties to DES3YR

Given that the DES5YR sample is photometric, it is prudent to investigate how the overall properties, both for the environments and for the SN properties themselves, differ from those found for the SNe in the DES3YR spectroscopically-confirmed sample.

4.2.1.1 Environmental Properties

I begin by looking at the properties of the SN environments. I present histograms showing the distributions in both global and local M_{stellar} and rest-frame $U - R$ in Figure 4.2 for the DES3YR and DES5YR samples used in this analysis.

For the global host galaxy M_{stellar}, the most obvious difference is the skewed distribution towards the high mass for DES5YR compared to DES3YR. DES3YR is quite uniformly distributed between approximately $8.5 - 11.5$, whereas the distribution for DES5YR rises continuously, before falling off at ~ 11.5. To quantify the difference between the two distributions, I perform a two-sample Kolmogorov–Smirnov (KS) test, the p-values of which are displayed in Figure 4.2. For global host galaxy M_{stellar}, the p-value (p) obtained through the KS test is 0.008, thus corresponding to almost a 3σ likelihood of coming from different distributions. This is likely due to the differences in the survey types for DES3YR and DES5YR. It is difficult to obtain SN spectra for SNe in high mass galaxies, meaning that they may not be present in the DES3YR spectroscopically-classified sample. A photometric survey such as DES5YR does not have this limitation. However, a photometric survey requires host galaxy spectroscopic redshift, which is easier to obtain for brighter or more massive galaxies. Thus this is a potential selection effect of DES5YR and may be the reason for the skewed global

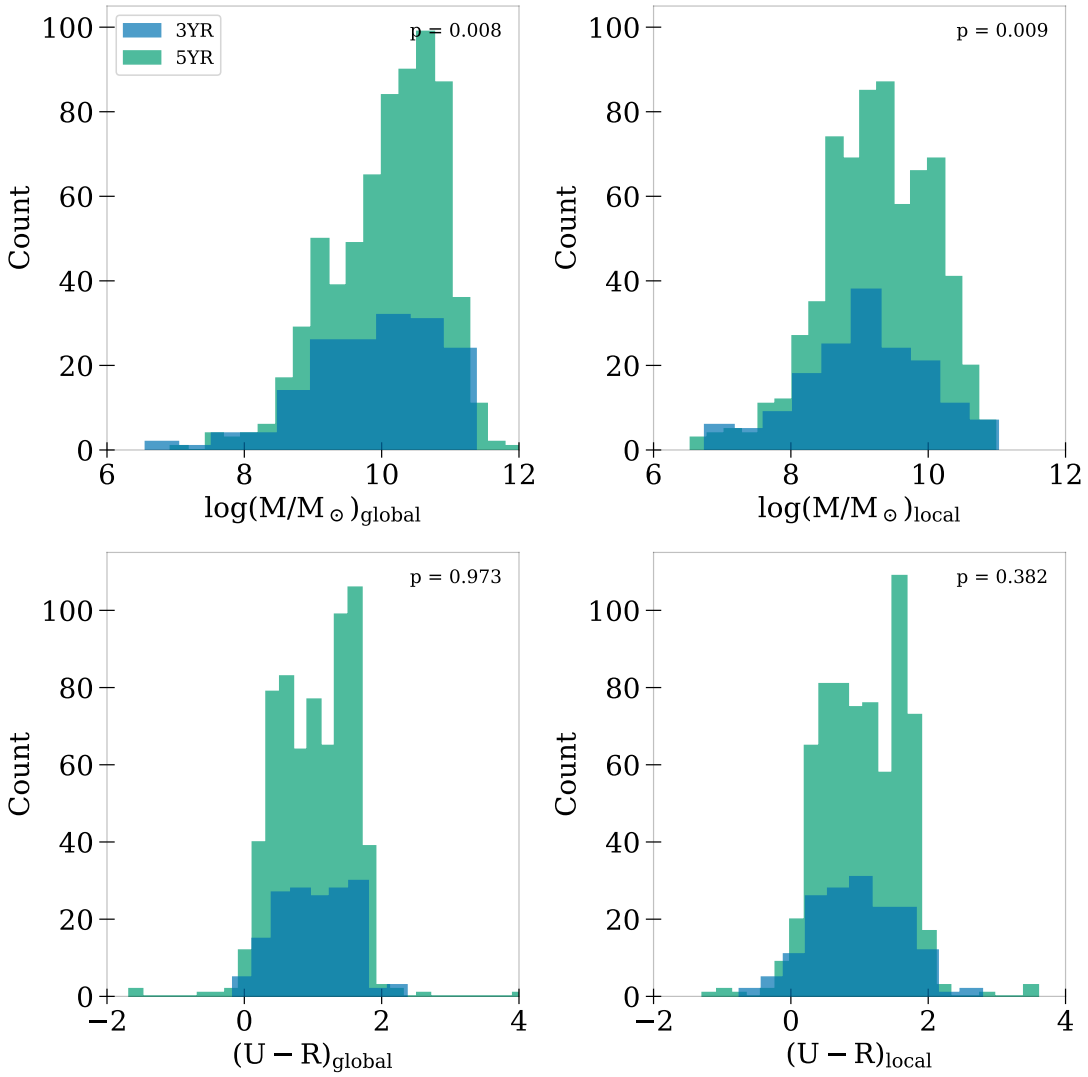

FIGURE 4.2: Histograms displaying the distributions in environmental properties to illustrate differences between the three-year spectroscopically-confirmed sample and the five-year photometric sample used in this analysis. Data presented here is after selection requirements have been implemented, meaning that the 3YR sample consists of the 164 objects studied in Chapter 3, and 5YR is the 677 objects outlined in Section 4.1. P-values (p) from KS testing is displayed in the top right corner of each panel.

M_{stellar} distribution that is seen. The distributions for local M_{stellar} are more similar by eye, with a smooth, almost Gaussian distribution for DES3YR, and a tentative suggestion for a bimodal distribution for DES5YR, with a dip just below 10. This feature remains regardless of the binning used. However, from KS testing, the p-value corresponds to 0.009, thus as for the global M_{stellar}, there is just under 3σ likelihood that samples from DES3YR and DES5YR follow different distributions.

The distributions for global and local $U - R$ are consistent for DES3YR and DES5YR, with the majority of the samples having rest-frame colours of $0 - 2$. For global $U - R$, the KS test gives a p-value of 0.973, rejecting the null hypothesis that they are from

different distributions, clearly indicating that it is likely the distributions are consistent. Again, by eye there is a dip towards the redder end of the local $U - R$, similar to the local M_{stellar}, which remains with binning, and may be suggestive of a bimodal distribution, however there is variation with higher counts towards the red end of the global $U - R$ so the feature in local may simply be reflecting that. This varying increase in count towards the red end of the distribution is not present in the DES3YR sample, which is much more uniform between $0 - 2$. This may be reflective of the increase in high mass galaxies in the DES5YR sample, meaning there are more red galaxies present in the sample, an indication of the underlying selection effects of the photometric sample. The p-value from the KS test for local $U - R$ is considerably lower than for global $U - R$ at 0.382, however as $p > 0.05$, there is little evidence to suggest that the distributions are different.

4.2.1.2 SN Properties

I display in Figure 4.3 distributions of the SN x_1 and c for the DES3YR and DES5YR samples used in this thesis. By eye, it appears that the distributions for DES5YR follow those of DES3YR, for both x_1 and c, however, by using a KS test it can be seen that this is not entirely the case. The distributions for x_1 are the more consistent of the SN properties, with a p-value of 0.122, indicating that there is no evidence to say that they are different. The c distribution extends slightly redder for DES5YR than for DES3YR. This is likely resulting from the increase in high mass galaxies in the DES5YR photometric sample, as from Figure 3.3 in Chapter 3 and from Figure 4.4 in Section 4.2.3, there is a trend for redder SNe Ia in more massive or redder galaxies or local environments. Considering a KS test, a p-value of 0.003 is obtained for c, indicating that the distributions are different to a 3σ confidence level.

4.2.2 Global vs. Local Measurements

Next, I turn to comparing the local and global environmental properties of the DES5YR SNe sample, and the differences between these properties as a function of redshift. As displayed in Figure 4.4, the differences between global and local properties agree well with Figure 3.2 in Chapter 3 for the DES3YR sample, but with a larger spread in the differences and lower Pearson correlation values (M_{stellar} $r = 0.726$, $U - R$: $r = 0.800$) than for DES3YR. This emphasises that local and global measurements provide different environmental information reflecting the importance of local measurements of the stellar populations close to the SNe locations. The larger spread may simply be due to the larger sample size, but it may also be a result of the increase in high mass galaxies for the DES5YR photometric sample. Similarly to Figure 3.2, there is no clear trend with these differences and redshift in the lower panels of Figure 4.4.

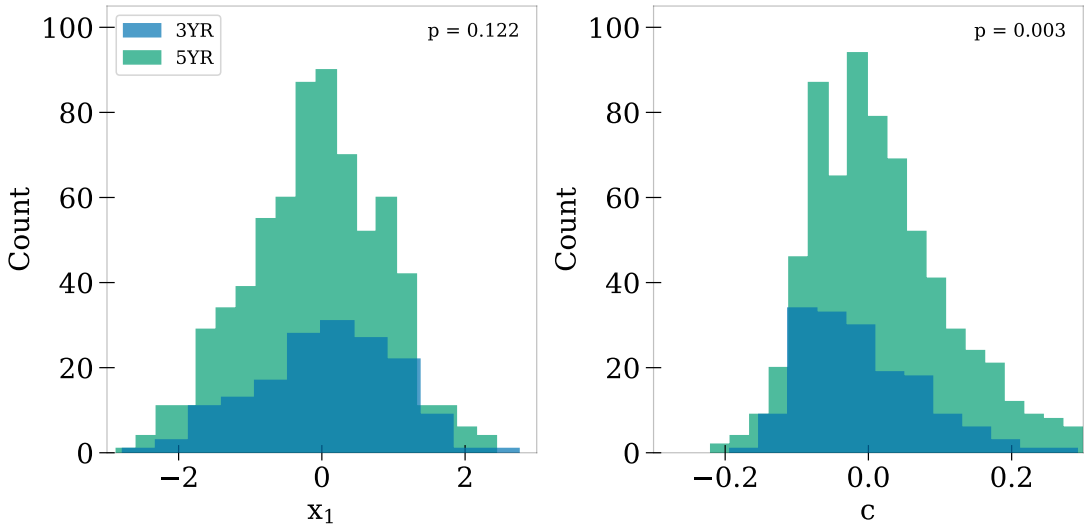

FIGURE 4.3: Histograms displaying the distributions in SN x_1 and c to illustrate differences between the three-year spectroscopically-confirmed sample and the five-year photometric sample used in this analysis. As in Figure 4.2, data presented is after selection requirements. P-values (p) from KS testing is displayed in the top right corner of each panel.

Interestingly, Figure 4.4 reveals that the majority (58.5%) of SNe Ia in the DES5YR sample are located in regions that are locally redder than their host galaxy, the opposite to that in Chapter 3. The relationship is not redshift dependent, so may be due to increased dust in the local SNe regions or may be indicative that the SNe are located in older stellar population regions within their hosts. Alternatively, it may be a feature of types of galaxies that are found to host SNe Ia in a photometric survey. As I know from Figure 4.2 that DES5YR has more SNe in high mass hosts than DES3YR, I investigate the M_{stellar} global minus local difference compared to the $U - R$ difference to see if there is a trend. As displayed in Figure 4.5, the majority of the points with redder local regions than the global colour are those where local and and global M_{stellar} are most similar. Looking at global and local M_{stellar} individually in Figure 4.6, when comparing to global M_{stellar} the majority of the locally redder regions are located in high mass galaxies that would be situated on the right-hand-side of the mass step. For local M_{stellar} the locally redder regions are uniformly distributed, however as one might expect, there is a lack of locally bluer regions for SNe in high local mass regions. As can be seen from Figure 4.7, there are no noticable trends with x_1 or c. Combining this knowledge with the correlation between global and local masses, it is likely the majority of SNe being in regions locally redder than their host galaxy is due to the increase in high mass galaxies in DES5YR. Additionally, this may suggest that the global and local regions are of similar size for these SNe, given the local and global masses are similar. This may be due to the range of different morphology and orientation of galaxies in the survey. To combat this issue, future local property analyses should consider utilising

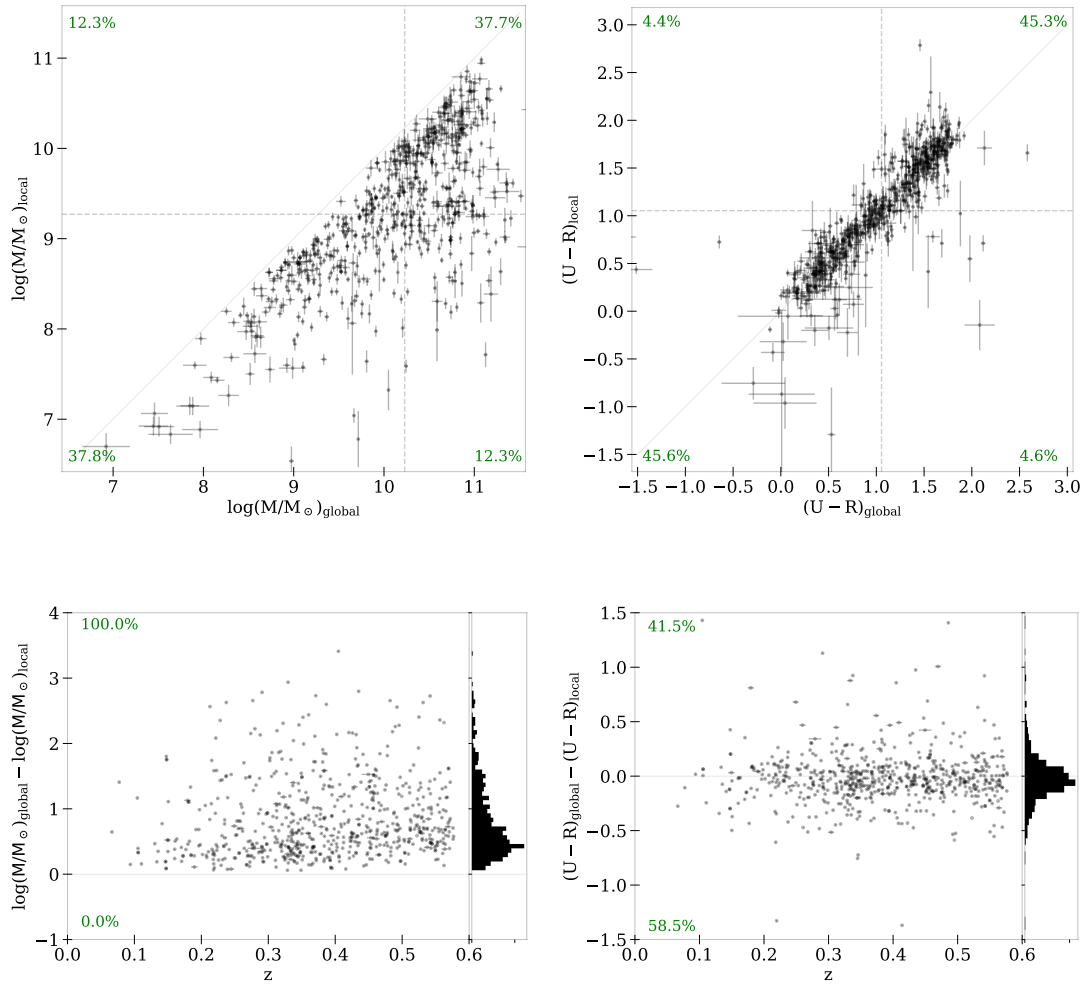

FIGURE 4.4: Left: The difference between the global stellar mass of the host galaxy and the local stellar mass in the 4 kpc radius aperture around the SN location. Right: The difference between the global rest-frame $U - R$ colour and the local rest-frame $U - R$ colour. The solid line shows the 1:1 line (matching the zero difference line in the lower panel), dashed lines indicate the environmental property median points of the sample, and green percentages represent the numbers of agreement in each quadrant (e.g., what percentage of the sample are both high local colour and high global colour, etc.). For stellar mass the Pearson correlation coefficient, $r = 0.726$, and for rest-frame $U - R$: $r = 0.800$. In the lower panels, the difference in properties versus redshift is shown. Green percentages represent the proportions of the sample above and below the zero difference line. Error bars represent the statistical uncertainty in the data.

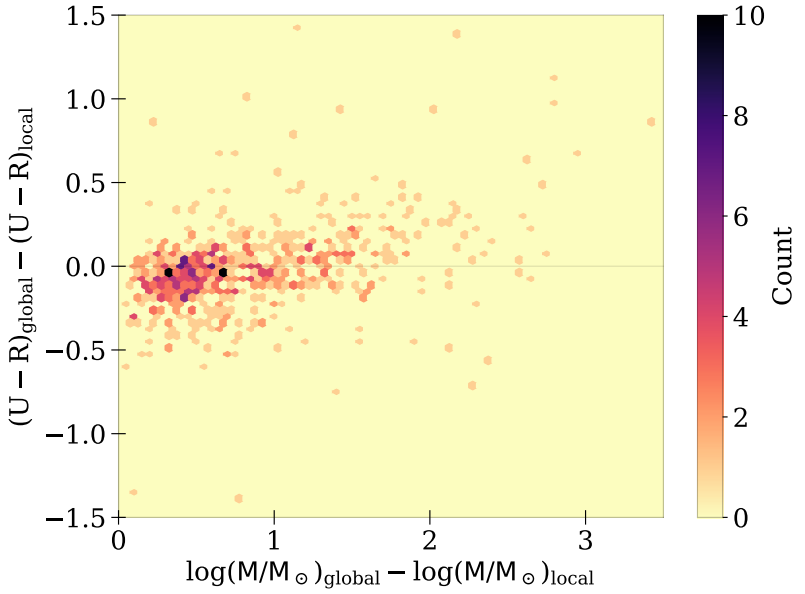

FIGURE 4.5: Differences between global and local M_{stellar} compared to differences between global and local $U - R$. Hexbins are coloured according to the number of objects in each bin, corresponding to the colourbar on the right of the figure.

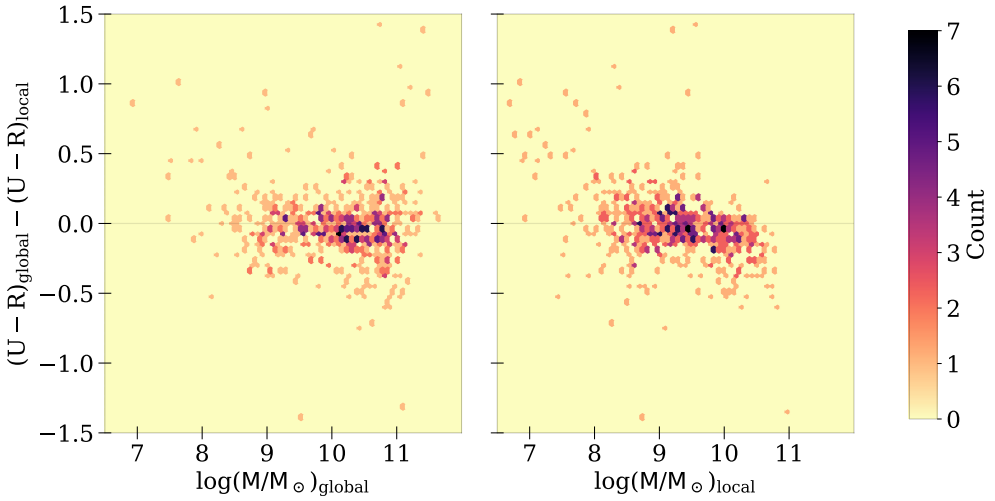

FIGURE 4.6: Global and local M_{stellar} compared to differences between global and local $U - R$. Hexbins are coloured according to the number of objects in each bin, corresponding to the colourbar on the right of the figure.

a selection requirement on the maximum fractional area of a galaxy covered by a local region.

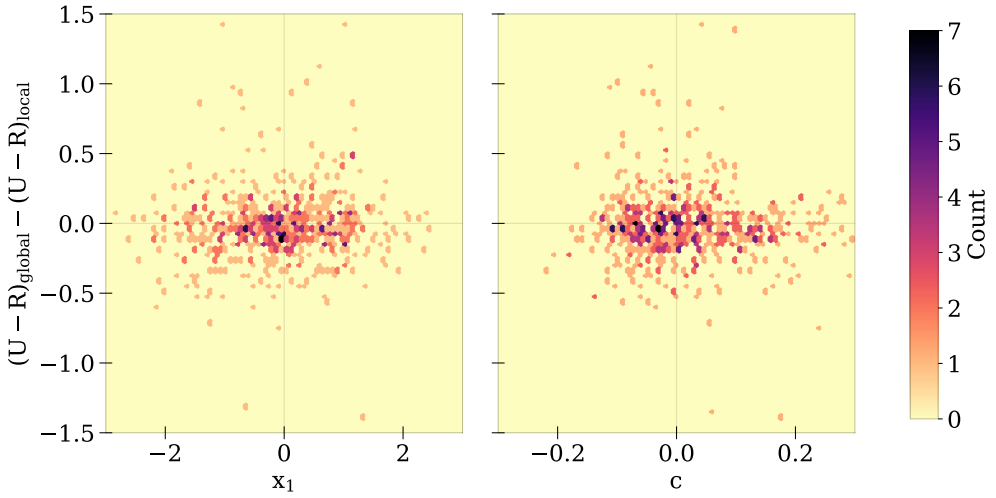

FIGURE 4.7: SN x_1 and c compared to differences between global and local $U - R$. Hexbins are coloured according to the number of objects in each bin, corresponding to the colourbar on the right of the figure.

4.2.2.1 Comparison with DLR

To explore the differences in $U - R$ colour distribution between DES3YR and DES5YR further, I analyse it as a function of radial distance from the centre of the host galaxy in DLR units. As a reminder, DLR (defined in Section 2.1.3) is a measure of the separation distance between the SN and the host galaxy, normalised by the apparent size of the galaxy light profile.

As illustrated in Figure 4.8, the overall distributions in DLR between the two samples are different, with a p-value (p) from KS testing of 0.511. As can be seen, DES5YR contains many more SNe with particularly low values of DLR. For DES3YR, which was spectroscopically-confirmed, SNe spectra were required. These are more difficult to obtain for SNe near the centre of their host galaxies, meaning that there was a bias in the sample, and the numbers of SNe with a DLR between 0 and 1 are relatively consistent. For DES5YR, which was photometrically-confirmed, spectra from the SNe themselves were not needed, so more SNe in the sample are located closer to the centre of their hosts.

Comparing the DLR values for DES3YR and DES5YR to their differences between global and local rest-frame $U - R$, as shown in Figure 4.9, it can be seen that this DLR distribution difference carries forward to differences in the U-R distributions. As reported in Chapter 3, for DES3YR the majority of SNe Ia are located in regions that are locally bluer than their host galaxy average, corresponding to positive y-axis values in the left-hand panel of Figure 4.9. From this panel, it can now be seen that those

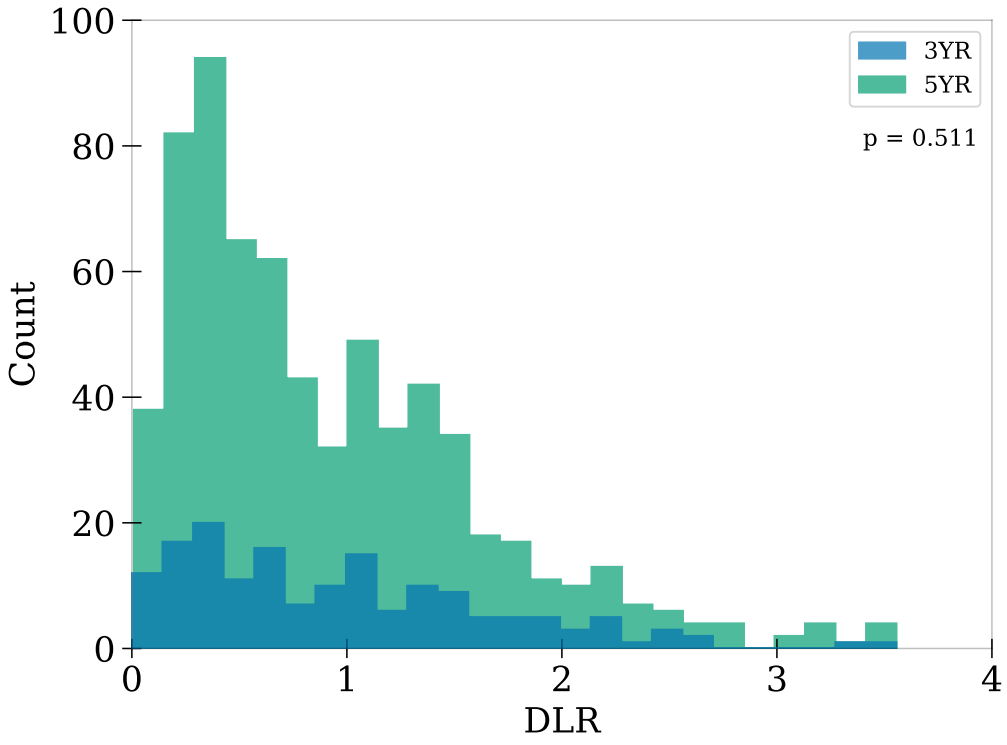

FIGURE 4.8: Distribution of DLR values for DES3YR and DES5YR. P-value (p) = 0.511 from KS testing is displayed in the top right corner.

SNe that are in local regions that are the reddest when compared to their host galaxy average (i.e. most negative on the y-axis) are closer to the centre of their hosts.

Looking to the DES5YR sample in the right-hand panel of Figure 4.9, there are more SNe Ia which are located in local regions that are redder than their host galaxy average (more negative on the y-axis), with the majority clustered with low DLR values. In other words, the majority of SNe Ia that are in locally redder regions than their host galaxy average are located closer to the centre of their host galaxy. This is likely due to the colour gradients in galaxies in which elliptical and spiral galaxies are redder in the centre, getting progressively bluer outwards (e.g. Tortora et al., 2010). This effect is thought to be predominantly driven by metallicity, in which the galaxy centre is more metal-rich than outer regions. This colour gradient means that the average colour of a galaxy may be bluer than the colour of their central region. Without the need for SN spectra in DES5YR, more SNe Ia in the centres of galaxies are present in the sample, meaning that the effect of this colour gradient is more noticeable than for DES3YR.

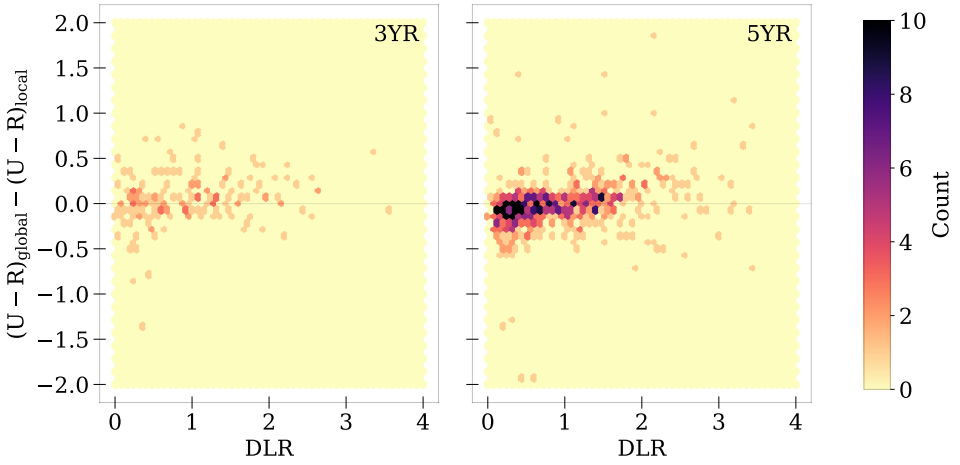

FIGURE 4.9: DLR compared to differences between global and local $U - R$ for DES3YR and DES5YR. Hexbins are coloured according to the number of objects in each bin, corresponding to the colourbar on the right of the figure.

4.2.3 SN Properties vs. Environments

I next explore the relationships between the SN properties x_1 and c, and environmental properties. It is important to understand any potential relationships as they affect the quality of the standardisation of SNe Ia light-curves in cosmological analyses. Presented in Figure 4.10 with corresponding numerical values in Table 4.2, are the relationships between SN properties x_1 and c compared with M_{stellar} and rest-frame $U - R$ colour for the global host galaxy and the local SNe environments.

As in Chapter 3, strong trends are evident for the relationships with SN x_1, indicating that the brighter-slower SNe are in bluer, less massive environments, corresponding with bin-mean differences with a significance of $\simeq 10\sigma$ for global M_{stellar}, recovering the known relationship between x_1 and host galaxy M_{stellar}. There are similar steps of $> 8\sigma$ for $U - R$, indicative of a link between x_1 and stellar age, see Rigault et al. (2013, 2020); Rose et al. (2019); Nicolas et al. (2021); Wiseman et al. (2021).

There is a weaker trend with c, with redder SNe Ia found in more massive, redder galaxies or local environments. This significance is typically $\simeq 2\sigma$, but is $< 1\sigma$ for global M_{stellar}. By moving the location of the split point to 10.18 (the point which gives the maximum Hubble residual difference - see Section 4.2.4) this increases to 2σ. By comparing this figure to Figure 3.3 in Chapter 3, it can be seen that, not only does DES5YR have an increased number of high mass galaxies in general, it also has an increase in high mass galaxies with blue SNe compared to DES3YR, which is pulling the right hand side of the distribution downwards, whilst having more spread in the low mass galaxies with redder SNe which is also pulling the left hand side of the distribution upwards.

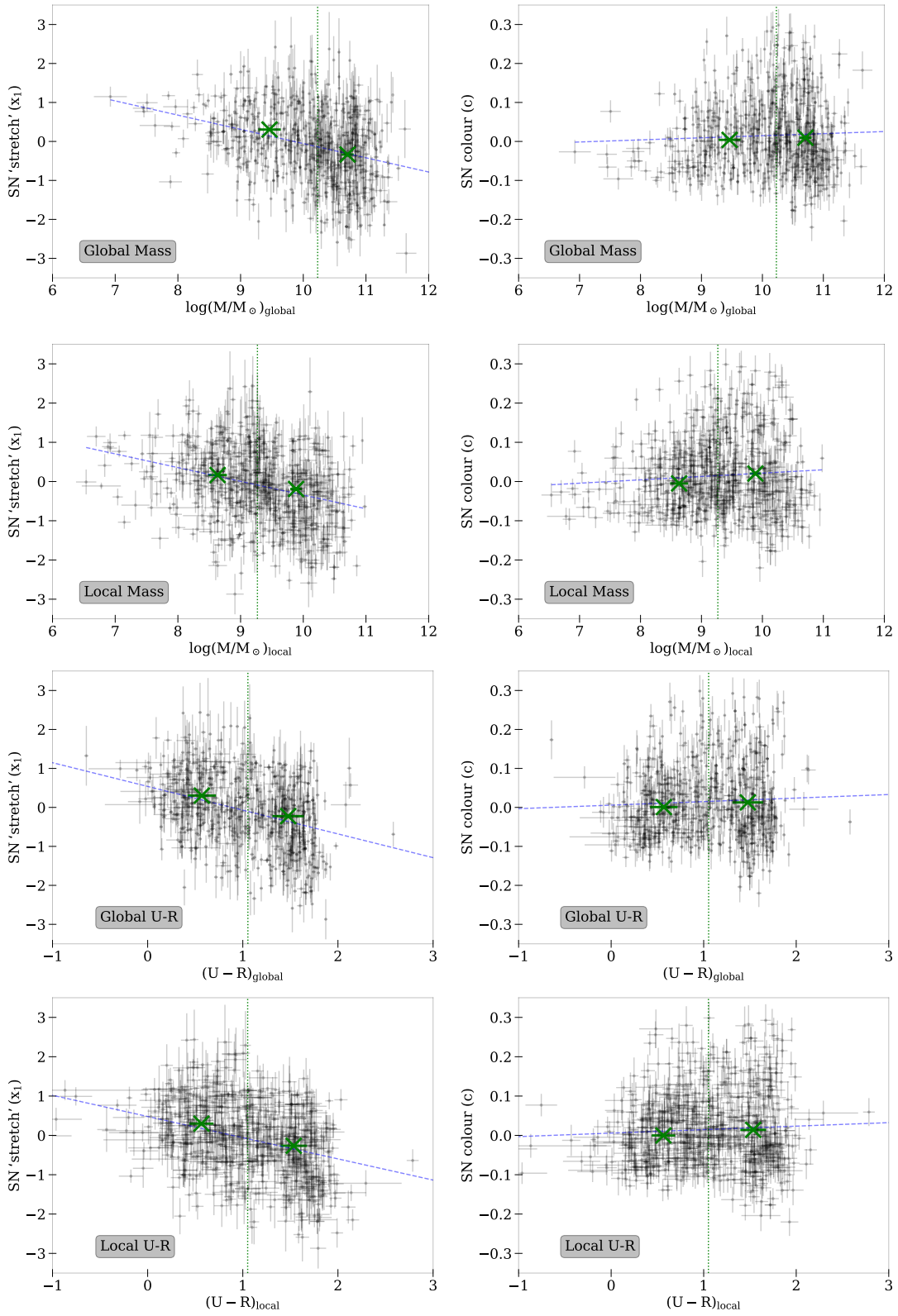

FIGURE 4.10: Correlations between SN stretch (x_1, left column) and colour (c, right column for the DES5YR sample) as a function of: global $M_{stellar}$ (first row), local $M_{stellar}$ within a 4 kpc radius aperture (second row), global $U-R$ (third row) and local $U-R$ (fourth row). Bins are split at the median of the sample, with weighted mean values shown as crosses, x-axis bin-mean error bars showing the dispersion divided by the square root of the number of objects in the bin, and least squares linear fits of the data shown as dashed lines to aid the eye.

TABLE 4.2: x_1 and c variation with host galaxy stellar mass and $U - R$ colour for DES5YR (Fig. 4.10).

Property	Division Point[1]	x_1 Sig. (σ)[2]	x_1 Magnitude[3]	x_1 r.m.s. $<$ DP[4]	x_1 r.m.s. $>$ DP	c Sig. (σ)	c Magnitude	c r.m.s. $<$ DP	c r.m.s. $>$ DP
Global Mass	10.23	10.05	0.640 ± 0.064	0.850 ± 0.065	1.005 ± 0.077	0.80	0.005 ± 0.007	0.088 ± 0.007	0.100 ± 0.008
Local Mass	9.27	5.50	0.356 ± 0.065	0.911 ± 0.070	0.949 ± 0.073	3.68	0.025 ± 0.007	0.081 ± 0.006	0.106 ± 0.008
Global U-R	1.05	8.37	0.527 ± 0.063	0.860 ± 0.066	0.995 ± 0.076	1.75	0.012 ± 0.007	0.085 ± 0.007	0.103 ± 0.008
Local U-R	1.05	8.92	0.563 ± 0.063	0.879 ± 0.068	0.979 ± 0.075	2.10	0.014 ± 0.007	0.083 ± 0.006	0.104 ± 0.008

[1] Splitting at the sample median.
[2] Significance of the difference in σ.
[3] Magnitude difference.
[4] Division Point.

Despite the increase in the number of SNe hosted in high M_{stellar} galaxies in DES5YR when compared to DES3YR, the overall trends with SN properties are consistent across the two data sets. However, it is interesting that the sample medians for local and global $U-R$ are located at the same point (1.05), which is noticeably redder than the median for both local and global $U-R$ in DES3YR. This may be resulting from the increase in high M_{stellar} galaxies in this sample.

Looking at the r.m.s. values in Table 4.2, SNe Ia in more massive regions or redder environments have higher r.m.s in x_1 and c than those in less massive or bluer environments. These lower r.m.s., less massive, blue regions present a more homogeneous sample, agreeing with the findings in Chapter 3 for DES3YR, although the differences are smaller for this analysis.

4.2.4 Hubble Residuals

I now turn to investigating the relationships between SN Ia Hubble residuals with M_{stellar} and rest-frame $U-R$ colour, both globally and locally, for DES5YR. As in Chapter 3, I plot the Hubble residual vs. the chosen environmental property split into two bins at a chosen division point, and measure the mean and dispersion in Hubble residual either side of this division. The magnitude of the 'step' is simply the difference between the two means.

To illustrate the differences in step sizes when changing the location of the division point, I present in Figure 4.11 the evolution in steps over different division points for all environmental properties. As found in Chapter 3, the size of the step can change dramatically depending on where the sample is split. This has also been found by other analyses, such as Ponder et al. (2020), who determine the best location for the step using an updated Akaike Information Criterion (AIC Akaike, 1974; Sugiura, 1978), finding a best step location for global M_{stellar} at 10.44 for their sample. AIC estimates the quality of statistical models for data, by finding a balance between χ^2 and the number of fit parameters. If there had been more time remaining in my PhD, I would have liked to update my simple iteration over different division points with an AIC method to allow for more rigorous statistical analysis, but I do not expect that it would change the results or conclusions of this analysis.

To cover the most common choices of division point, I split the sample at the median, the location that gives the step of maximum significance, and at a value that I define as the 'literature' value, based on findings of prior analyses and outlined as follows:

- $\log(M_{\text{stellar}}/M_{\odot})_{\text{global}} = 10.0$ (e.g., Sullivan et al., 2010; Childress et al., 2013; Smith et al., 2020b; Brout & Scolnic, 2021)
- $\log(M_{\text{stellar}}/M_{\odot})_{\text{local}} = 9.0$ (Kelsey et al., 2021)

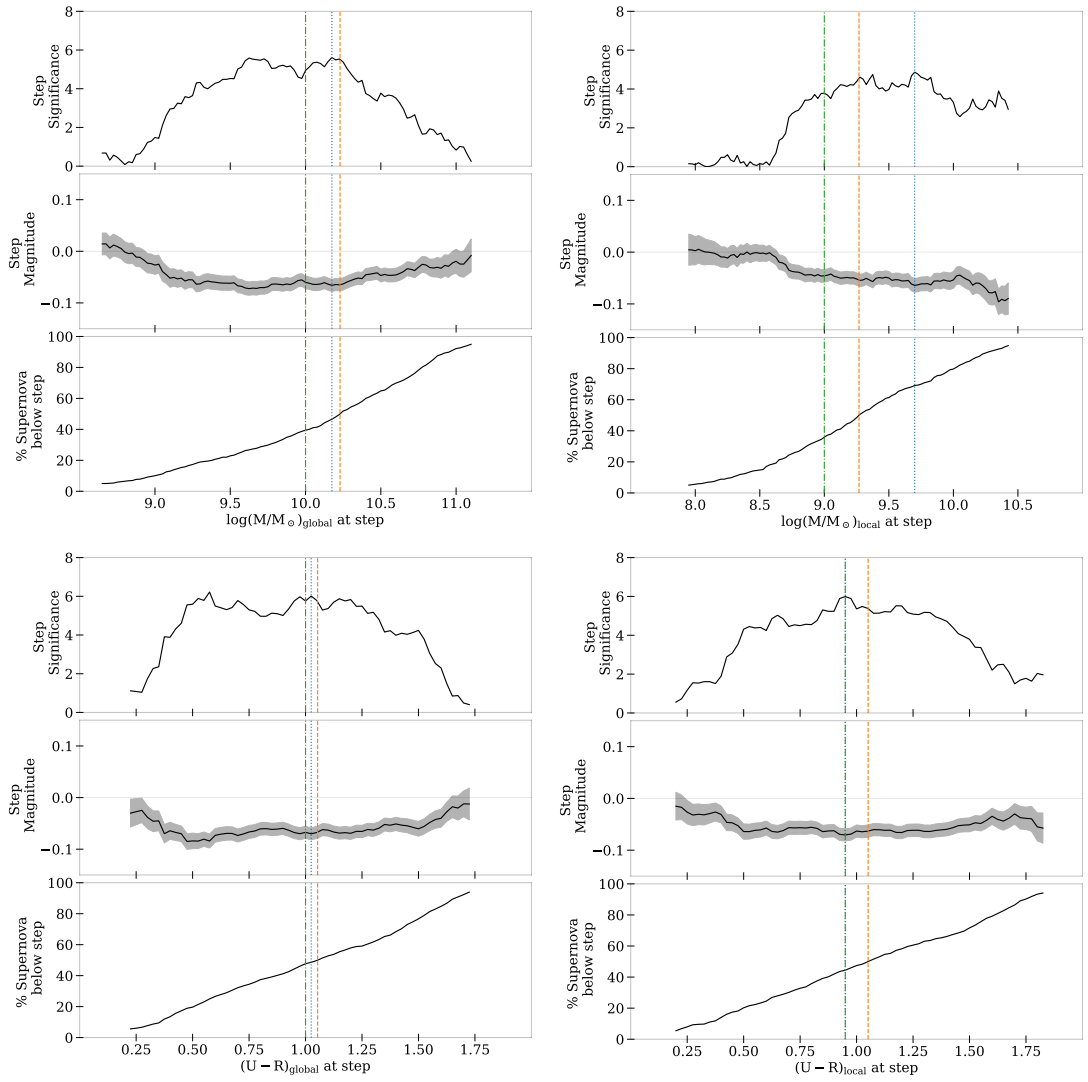

FIGURE 4.11: Plots comparing the significance, magnitude and location of the steps for each environmental property in DES5YR. From top to bottom, and left to right: global M_{stellar}, local M_{stellar} within a 4 kpc radius, global rest-frame $U - R$ colour, and local rest-frame $U - R$ colour. In each plot, the lower panel shows the percentage of SNe Ia in the sample in the bin below the step location as the location of the step is varied; the middle panel is the magnitude of the step at each location with the grey shaded region showing the uncertainty; and the top panel shows the significance of the step in σ. The orange-dashed line indicates the location of the environmental property median of the sample, the blue-dotted line shows the step that gives the maximum significance, and the green dash-dot line shows the 'literature' division point.

- $(U-R)_{\rm global} = 1.0$ (Kelsey et al., 2021)
- $(U-R)_{\rm local} = 0.95$ (Kelsey et al., 2021)

For global $M_{\rm stellar}$, this is simply the standard value used in the literature, and I use this to be consistent with other studies, and for the analysis presented in Chapter 5. As the use of $U-R$ and local mass is not as well established as global mass, and may also depend on the definition of 'local' used, to determine 'literature' values for these properties, I round the median division points from Chapter 3 (Kelsey et al., 2021), mirroring how the classic host mass split was found. This allows the steps to be easily compared with DES3YR and put into context with other analyses. However, a benefit of figures such as Figure 4.11 is that any division point can be chosen, and the corresponding step magnitude and significance simply read off of the graph.

All numerical values for the Hubble residual steps at each of the chosen division points are presented in Table 4.3.

As can be seen in Figure 4.11, the overall distributions in step significance with step location is more uniform than it was for DES3YR in Figure 3.5, with wider and flatter peaks. This suggests that in the larger photometric sample the choice of step location is less important than it was for DES3YR. In each plot, the orange-dashed line indicates the location of the environmental property median of the sample, the blue-dotted line shows the step that gives the maximum significance, and the green dash-dot line shows the 'literature' division point.

I present in Figure 4.12 the Hubble residual steps for DES5YR as a function of $M_{\rm stellar}$ and rest-frame $U-R$ colour, both globally and locally, measured at the literature division points. As in Chapter 3, uncertainties on the steps are statistical only, and the complicated positive covariance between local and global properties will likely increase the significance of these steps. Combining all the information from Table 4.3, Figure 4.11 and Figure 4.12, I turn to understanding the results for $M_{\rm stellar}$ and $U-R$.

4.2.4.1 $M_{\rm stellar}$

Focusing first on global $M_{\rm stellar}$, the Hubble residual steps are consistent in magnitude and significance at $0.060-0.066$ mag ($4.94-5.61\sigma$), despite some variation in the division point, agreeing with prior analyses (e.g. Sullivan et al., 2010; Childress et al., 2013; Smith et al., 2020b). In all cases, the r.m.s. value for the Hubble residuals in the lower mass galaxies is smaller than for the higher mass galaxies. This is least pronounced for the split at the classic literature division point of $\log(M_{\rm stellar}/M_\odot) \simeq 10$, which may be why such a result has not been found in other analyses.

TABLE 4.3: Hubble residual steps for stellar mass and $U - R$ for the DES5YR data using a 1D bias correction.

Property	Sample Median/ Max Significance[1]	Division Point	Hubble Residual Sig. (σ)	Hubble Residual Magnitude	Hubble Residual r.m.s. $<$ DP	Hubble Residual r.m.s. $>$ DP
Global Mass	Median	10.23	5.51	0.065±0.012	0.164 ± 0.013	0.177 ± 0.014
Global Mass	Max	10.18	5.61	0.066±0.012	0.166 ± 0.013	0.175 ± 0.013
Global Mass	Literature	10.00	4.94	0.060±0.012	0.170 ± 0.015	0.171 ± 0.012
Local Mass	Median	9.29	4.55	0.054±0.012	0.162 ± 0.012	0.179 ± 0.014
Local Mass	Max	9.70	4.87	0.064±0.013	0.163 ± 0.011	0.186 ± 0.018
Local Mass	Literature	9.00	3.78	0.046±0.012	0.156 ± 0.014	0.178 ± 0.012
Global U-R	Median	1.05	5.72	0.067±0.012	0.168 ± 0.013	0.174 ± 0.013
Global U-R	Max	1.02	6.01	0.070±0.012	0.166 ± 0.013	0.175 ± 0.013
Global U-R	Literature	1.00	5.76	0.067±0.012	0.165 ± 0.013	0.175 ± 0.013
Local U-R	Median	1.05	5.37	0.063±0.012	0.173 ± 0.013	0.168 ± 0.013
Local U-R	Max	0.95	5.99	0.070±0.012	0.169 ± 0.014	0.172 ± 0.013
Local U-R	Literature	0.95	5.99	0.070±0.012	0.169 ± 0.014	0.172 ± 0.013

[1] The difference between median locations/max significance locations, and the literature split point is explained in Section 4.2.4.

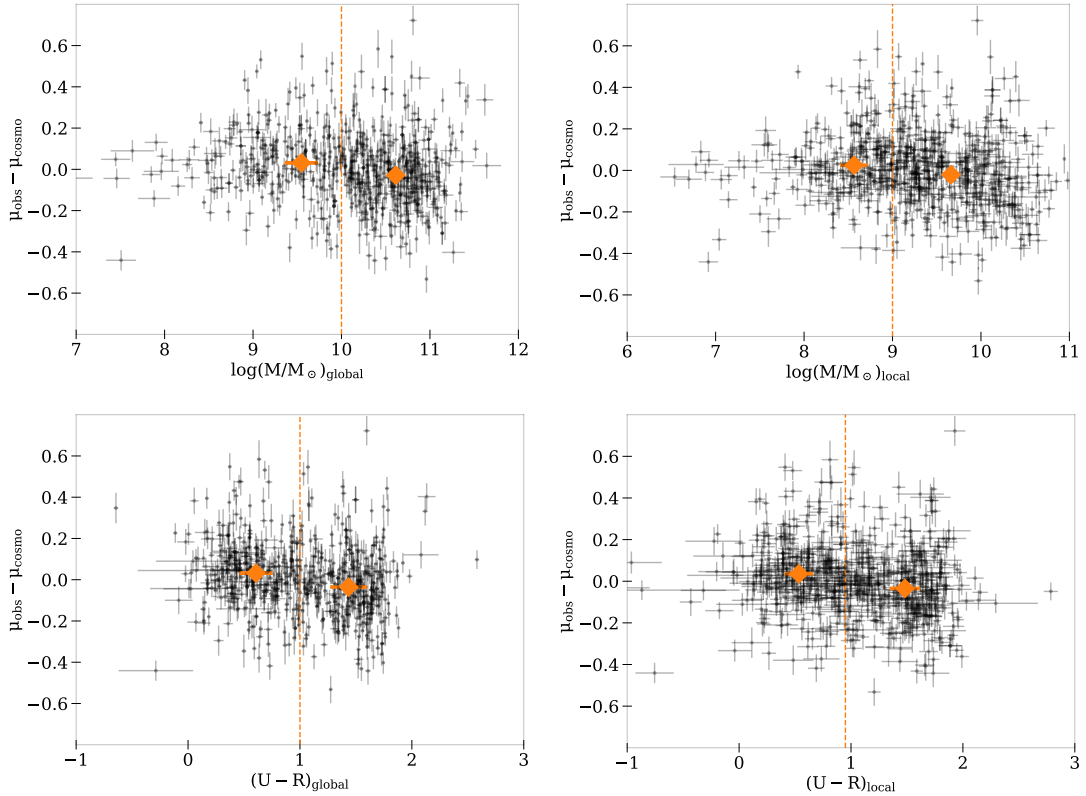

FIGURE 4.12: Hubble residual plots for DES5YR as a function of (from top to bottom and left to right): global M_{stellar}, local M_{stellar} within the 4 kpc radius aperture, global rest-frame $U-R$ colour and local rest-frame $U-R$ colour. In this figure, I present the data split at the 'literature' division points.

For local M_{stellar}, things are more varied, both for the division points and for the Hubble residuals, ranging from $0.046-0.064$ mag ($3.78-4.87\sigma$), mirroring the $\sim 2\sigma$ difference in step size for local mass in Chapter 3. The local M_{stellar} is sensitive to the choice of division point. As with global M_{stellar}, the r.m.s. values are smaller in the lower local mass regions.

For both global and local M_{stellar}, the sample median and the division point of maximum significance are at higher masses than were found for DES3YR, suggestive of the overall higher global mass sample found for DES5YR, which has also meant that average local masses have shifted higher. Unlike DES3YR, the local mass steps are slightly smaller than the steps for global mass, but this difference is small ($< 1\sigma$).

4.2.4.2 $U-R$

Moving to $U-R$, it is noticeable that all the steps, for both local and global, are consistent and the split points are all at similar locations. The magnitudes of the steps $0.063-0.070$ mag ($5.37-6.01\sigma$) are slightly smaller than, but consistent with, DES3YR,

and the findings of Roman et al. (2018) and Rigault et al. (2020). Interestingly, the sample medians for both global and local $U-R$ are located at the same point (1.05), slightly redder than for DES3YR and likely linked to the higher M_{stellar} in DES5YR. In addition, for local $U-R$, the 'literature' division point (based on the sample median from Chapter 3) is identical to the location that gives the step of maximum significance. This agrees with the finding in Chapter 3 that, even if the global and local environment colours are different for individual SNe, the overall $U-R$ colour steps (and $U-V$, Roman et al., 2018) are consistent whether measured globally or locally, likely due to the strong correlations between global and local $U-R$ as illustrated in Figure 4.4.

Again, as in DES3YR and as for M_{stellar}, the Hubble residual r.m.s. values are lower in the bluer regions than for the redder regions. Curiously, there is one situation where this is not the case: at the median local mass division point, the r.m.s is higher for the bluer region. The values for each side of the division point are within each-others uncertainties, but this may be indicative of the overall distribution of local $U-R$. In Section 4.2.2, I found that the majority of SNe Ia in DES5YR are located in regions that are locally redder than their host galaxy. As illustrated in Figure 4.2, there is a dip then sudden peak in the distribution at just above local $U-R = 1.05$ which is not present in DES3YR. If the majority of the SNe in this region are coming from a similar population in terms of x_1, c and Hubble residuals, this could be what is causing this r.m.s. difference when the sample is split close to this point.

4.3 Systematics

The increased sample size of DES5YR over DES3YR means that I can perform more tests of some of the systematics investigated in Chapter 3. Here, I investigate the effect of changing the size of the local aperture, and the use of different environmental properties. I consider splitting the sample using SN properties in Chapter 5.

4.3.1 Changing Local Radius and Redshift Cuts

In Chapter 3, I briefly investigated changing the radius of the local apertures to understand the effect of the choice of aperture size on the analysis. Overall, I found that step magnitudes became progressively larger as the aperture size decreased, but I was limited by the small sample size, and wanted to investigate this more rigorously in the larger DES5YR sample, and add in further redshift constraints to reduce any bias from the PSF size.

I also found in Chapter 3 that very large apertures showed little difference in Hubble residual steps, so for this analysis I only consider local radii of size from 1.25 to 6 kpc,

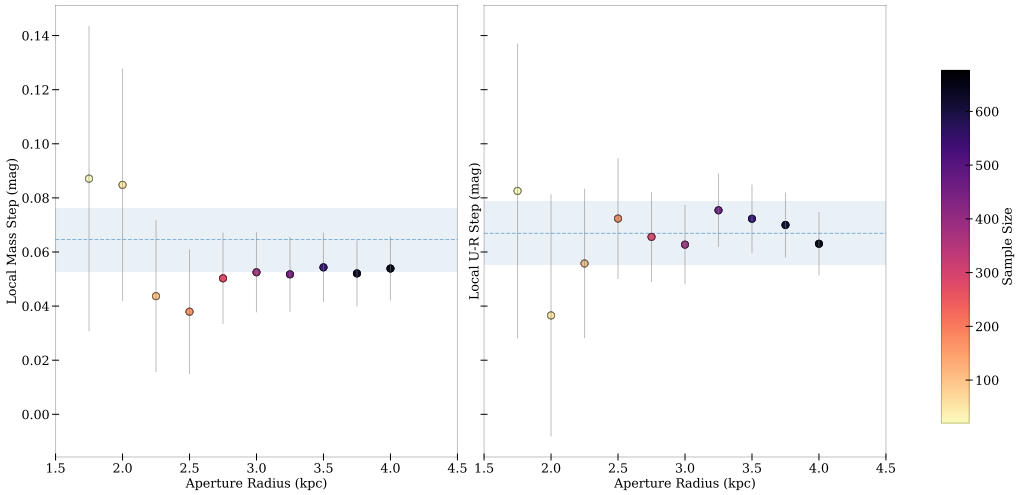

FIGURE 4.13: Variation of step magnitude as a function of local aperture radius for DES5YR, coloured by the number of objects in the sample. Global measurements of step sizes for M_{stellar} and $U - R$ are presented by the horizontal dotted lines, with shaded regions indicating the uncertainties. All measurements on this figure are for a splitting into the steps at the sample median.

using smaller 0.25 kpc steps. Again, I study all apertures independently and follow the original method, remeasuring all photometry and rederiving all environmental properties using SED fitting. In my baseline analysis, for a 4 kpc aperture size, I use a redshift cut of $z < 0.6$, which minimises selection bias in the sample (see Section 2.5.2). To obtain the most relevant photometry within smaller apertures, I require tighter redshift cuts. I first calculate the maximum possible redshift for each aperture size, then cut to slightly less than this value in each case to account for selection bias effects as I did with the original baseline analysis. This results in the steps presented in Table 4.4.

In this table, I simply present the values obtained when dividing at the sample median. Given the sample sizes become quite small, splitting at the locations of maximum significance may not be best representative of the overall trends. I also only consider steps for samples consisting of greater than 5 objects. As can be seen, the step sizes in local M_{stellar} at the sample medians are remarkably similar to each other at ~ 0.052, except when apertures < 2 kpc are used. There is slightly more variation within local $U - R$, with the biggest differences again found for apertures < 2 kpc, but generally they are all within the uncertainties. The significances of the steps for local M_{stellar} increase as the apertures get larger (ignoring < 2 kpc), following the increasing sample sizes. However, the significances for local $U - R$ steps are more varied, mirroring the variation in step magnitudes.

In Figure 4.13 I present plots of the variation of step magnitude as a function of local aperture radius, with the corresponding global step presented as a dotted horizontal line, all of which are for dividing at the sample median. The majority of the points for both local M_{stellar} and $U - R$ are contained within the global step uncertainties (shaded

TABLE 4.4: Aperture radii, redshift cuts and resulting sample sizes.

Aperture			Local M_{stellar} Step[1]		Local $U-R$ Step	
(kpc)	z Cut	Sample Size[2]	Sig. (σ)	Magnitude	Sig. (σ)	Magnitude
1.25	0.05	0	-	-	-	-
1.50	0.10	3	-	-	-	-
1.75	0.15	20	1.54	0.087±0.056	1.56	0.083±0.054
2.00	0.20	49	1.97	0.085±0.043	0.82	0.037±0.045
2.25	0.25	99	1.56	0.044±0.028	2.02	0.056±0.028
2.50	0.30	165	1.65	0.038±0.023	3.24	0.072±0.022
2.75	0.35	275	2.97	0.050±0.017	3.93	0.066±0.017
3.00	0.40	371	3.55	0.053±0.015	4.28	0.063±0.015
3.25	0.45	450	3.74	0.052±0.014	5.56	0.075±0.014
3.50	0.50	547	4.23	0.054±0.013	5.72	0.072±0.013
3.75	0.55	632	4.27	0.052±0.012	5.83	0.070±0.012
4.00	0.60	677	4.55	0.054±0.012	5.37	0.063±0.012

[1] All step sizes are measured at the median local M_{stellar} or $U-R$ for each sample.
[2] I do not consider steps for sample consisting of fewer than 5 objects.

TABLE 4.5: Hubble residual steps for sSFR, and a variety of rest-frame colours using a 1D bias correction for DES5YR.

Property	Sample Median/ Max Significance	Division Point	Hubble Residual Sig. (σ)	Hubble Residual Magnitude
Global sSFR	Median	-9.68	4.75	0.056±0.012
Global sSFR	Max	-9.28	5.76	0.069±0.012
Local sSFR	Median	-9.65	4.68	0.055±0.012
Local sSFR	Max	-9.23	5.15	0.062±0.012
Global U-B	Median	-0.06	5.83	0.068±0.012
Global U-B	Max	-0.03	6.30	0.073±0.012
Local U-B	Median	-0.03	6.00	0.070±0.012
Local U-B	Max	-0.05	6.29	0.073±0.012
Global U-V	Median	0.53	5.45	0.064±0.012
Global U-V	Max	0.68	5.99	0.071±0.012
Local U-V	Median	0.55	5.23	0.061±0.012
Local U-V	Max	0.62	6.09	0.071±0.012
Global B-V	Median	0.60	5.40	0.063±0.012
Global B-V	Max	0.65	5.94	0.070±0.012
Local B-V	Median	0.59	5.53	0.065±0.012
Local B-V	Max	0.60	5.60	0.066±0.012
Global B-R	Median	1.12	5.37	0.063±0.012
Global B-R	Max	0.82	6.12	0.082±0.013
Local B-R	Median	1.08	4.99	0.059±0.012
Local B-R	Max	1.03	5.49	0.065±0.012
Global V-R	Median	0.49	4.34	0.052±0.012
Global V-R	Max	0.45	5.30	0.065±0.012
Local V-R	Median	0.49	4.19	0.050±0.012
Local V-R	Max	0.45	5.19	0.062±0.012

region). As in this aperture range for DES3YR (see Figure 3.7), the median local M_{stellar} step is smaller in magnitude than the corresponding global step, however the $U-R$ is more consistent. If the maximum significance steps are used instead, all the local steps are > 0.06 mag and are larger than the maximum significance global steps, but still within the global uncertainties for those in apertures > 2 kpc.

4.3.2 Other Environmental Properties

Throughout this thesis, the analysis is focused on M_{stellar} and $U-R$ measurements. However, for consistency, I present in Table 4.5 the results from looking at sSFR and a variety of other rest-frame colours, and outline the findings in the following sections. For simplicity, I simply consider division points at the sample median, and at the location that gives the step of maximum significance.

4.3.2.1 sSFR

In DES3YR, the steps with sSFR were consistent with my $U-R$ steps, and with the sSFR steps found by Kim et al. (2019) (0.081 ± 0.018 mag), but were smaller than that found by Rigault et al. (2020) (0.163 ± 0.029 mag). This was thought to be due to differences in the methods used to measure sSFR, and the differences in redshift coverage of the samples. As Rigault et al. (2020) is at low z, we expect the step to be larger (Rigault et al., 2013; Childress et al., 2014; Kim et al., 2018).

As can be seen in Table 4.5, in this DES5YR sample, the step significances are larger than for DES3YR, indicative of the larger sample size, however the magnitudes of the steps are all slightly lower ($\sim 0.055 - 0.069$), similar to the findings for M_{stellar} and $U-R$.

4.3.2.2 Other Rest-frame Colours

In the DES3YR analysis, I found that the largest rest-frame colour step was found when using $V-R$ colour (Table 3.5). To see if this was physical or a result of the sample size, I calculate the Hubble residual steps for the full range of rest-frame colours from $UBVR$ magnitudes in the DES5YR sample.

As displayed in Table 4.5, the steps for $U-B$ are comparable between DES3YR and DES5YR, but the other rest-frame colours have smaller step magnitudes for DES5YR. Interestingly, in DES5YR the largest steps are not found using $V-R$ colour so I predict that the finding in 3YR was a random fluctuation. The steps are all similar in magnitude for this sample. Further analysis is needed to determine which is best to use in cosmology.

4.4 Summary and Discussion

In this chapter, I have expanded my analysis to investigate the effects of host galaxy properties on SNe Ia from a preliminary DES5YR sample of 677 objects after selection requirements. By following the method established by the DES3YR local and global environments analysis in Chapter 3, I measure environmental properties and compare them to SN Ia light curve properties and Hubble residuals. Here, I outline my key results.

Firstly, when comparing the properties of DES5YR to DES3YR, it was found that DES5YR has global host galaxy M_{stellar} distributions that are skewed more towards high mass, which is likely due to the difficulties in obtaining spectra for the spectroscopically-confirmed DES3YR sample for SN in high mass galaxies. This is also due to the requirement of host galaxy spectroscopic redshift for the photometrically-confirmed SNe

in DES5YR, which is easier to obtain for brighter or more massive galaxies. These selection effects mean that the median global and local $M_{\rm stellar}$ values for the DES5YR sample shift to about 0.2 dex larger than they were for DES3YR. This carries through to an increase in the number of $c > 0$ (red) SNe in DES5YR as redder SNe preferentially explode in more massive galaxies. Additionally, unlike DES3YR, the majority of SNe Ia in the DES5YR sample are located in environments that are locally redder than their host galaxy.

Despite this increase in high $M_{\rm stellar}$ host galaxies for DES5YR, the trends with environmental properties when compared with SN properties x_1 and c are consistent with DES3YR. This consistency also holds for r.m.s. values of these SN properties, with the low mass, bluer regions being a more homogeneous sample.

Moving to environmental relationships with Hubble residuals, I find that all of the steps measured for global and local $M_{\rm stellar}$ and rest-frame $U-R$ colour are significant at $> 3\sigma$, with the majority significant to $> 5\sigma$. This significance is robust when the analysis is expanded to consider sSFR and the other rest-frame colours available with the measurements of $UBVR$ magnitudes.

Comparing the global and local $M_{\rm stellar}$ steps, it is interesting that, unlike DES3YR, the steps for local mass ($0.046 - 0.064$ mag) are slightly smaller ($< 1\sigma$) than for global mass ($0.060 - 0.066$ mag). The difference is very small, and is likely to be resulting from the large numbers of high global $M_{\rm stellar}$ objects. As in DES3YR, Hubble residual r.m.s. values are smaller for the lower mass regions, both locally and globally, suggesting that they present a more homogeneous sample.

As found in DES3YR and by Roman et al. (2018) for $U-V$, the Hubble residual steps for $U-R$ are larger than the steps for $M_{\rm stellar}$ and are consistent whether measured locally ($0.063 - 0.070$ mag) or globally ($0.067 - 0.070$ mag). As for $M_{\rm stellar}$, the Hubble residual r.m.s. values are lower in bluer regions than for redder regions.

By altering the size of the local apertures and adding more restrictive redshift cuts, I found that local step magnitudes, particularly for $M_{\rm stellar}$, were remarkably similar to one another. It is simply the significance that is changing as the sample size changes in this analysis. By comparing to global steps, each different aperture measurement mirrored the findings for the main 4 kpc measurement, that global and local steps are consistent using this data, with a slight tendency for smaller steps for local $M_{\rm stellar}$.

In the next chapter, I will expand on this DES5YR environmental property analysis by focusing particularly on how these properties relate to SN c, given the finding of Chapter 3 that the overall Hubble residual steps are dominated by the redder ($c > 0$) objects.

Chapter 5

Concerning Colour

Motivated by my findings in Chapter 3 which suggested that the environmental 'steps' in SN luminosity may be driven by underlying relationships between SN c and galaxy properties, I now turn to investigating this further using the larger, photometrically-confirmed DES5YR sample. This allows me to determine if the effect is physical, or if it was a feature of the relatively small sample size of DES3YR.

Analyses of the underlying relationships with SN colour c have grown over the past year, with suggestion that the differing Hubble residuals are caused by differences in dust properties for SNe with different c values (Brout & Scolnic, 2021). Bluer SNe will suffer less dust extinction (Jha et al., 2007) and therefore less scatter from event-to-event. The presence of dust along the line of sight reddens the SN by differing amounts dependent on the dust properties, and may not be the same for all SNe Ia (Gonzalez-Gaitan et al., 2020; Thorp et al., 2021). There is known variation in the extinction factor (R_V) along different lines of sight in the Milky Way (e.g. Schlafly et al., 2016), so logically it should vary between, and even within, different SNe host galaxies.

Alternatively, as suggested in Chapter 3, red and blue SNe Ia may represent differing progenitor paths (e.g. Milne et al., 2013; Stritzinger et al., 2018; Gonzalez-Gaitan et al., 2020). Simply, blue objects are considered to be comprised of one distinct set of progenitors (hence displaying no significant step in Hubble residual), whilst red objects are likely a combination of different progenitors or explosion mechanisms (including the blue SNe that have been reddened by dust), causing a step in Hubble residual to be observed. Environmental studies may find evidence for this by analysis of the stellar population age of the region surrounding the SNe.

Throughout this chapter, I use the SN properties and environmental properties from the 677 SNe Ia defined and analysed in Chapter 4. I also keep α and β fixed at $\alpha = 0.172 \pm 0.007$, $\beta = 3.07 \pm 0.07$.

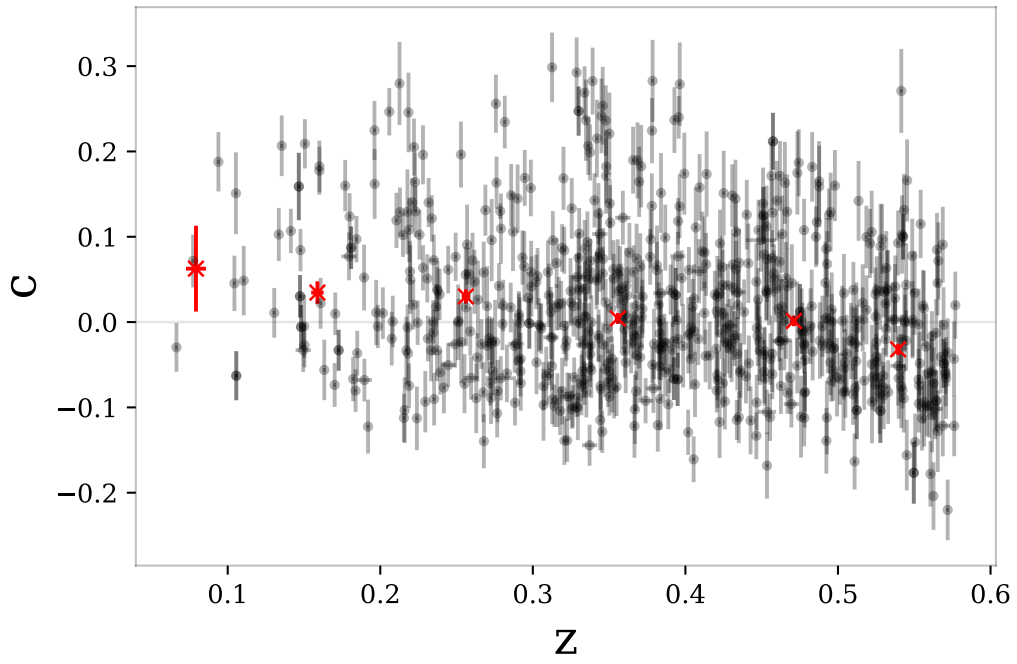

FIGURE 5.1: The relationship between SN c and redshift z for the preliminary DES5YR SN Ia sample. The red points show the weighted mean colour in redshift bins.

5.1 Relationships with c

From the measurements of environmental properties, and the knowledge of SN parameters in the DES5YR sample obtained through light-curve fitting, I can compare and study relationships between these measurements, focusing on the potential relationships with SN c.

5.1.1 Redshift and c

I begin by considering the relationship between c and redshift z (Figure 5.1), to enable understanding of if the results are being biased by underlying evolution with redshift. By binning the data in the c-z parameter space, a slight trend with bluer SNe Ia found at higher redshift is observed, consistent with previous analyses (e.g. Brout & Scolnic, 2021). This slight trend is likely due to selection effects - bluer SNe are brighter, so they are more likely to be observed at higher redshift than the fainter objects.

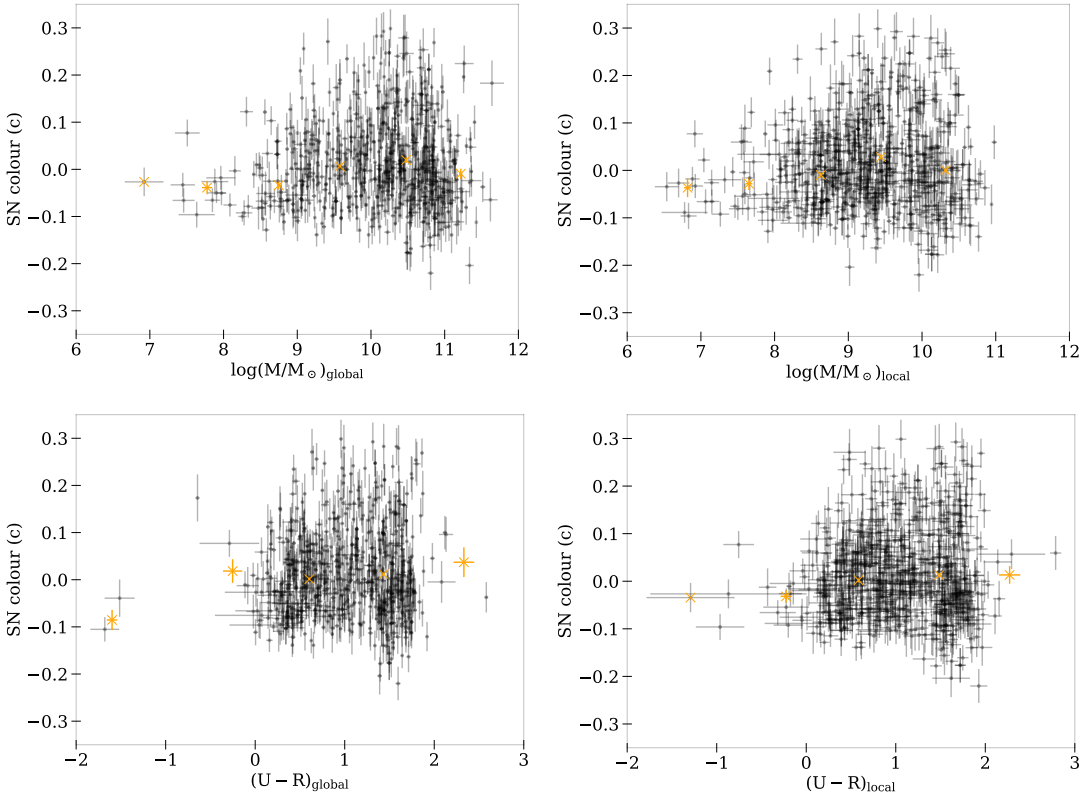

FIGURE 5.2: SN c as a function of both global and local environmental properties: M_{stellar} (upper panels) and rest-frame $U - R$ (lower panels). The orange points show the binned weighted mean colours.

5.1.2 Environmental Properties and c

I then study the relationships between SN Ia colour and the SN Ia environmental properties M_{stellar} and rest-frame $U - R$ colour, both globally for the entire host galaxy, and for the local 4 kpc radius regions around each SN location. Once again, I bin the data and, as illustrated in Figure 5.2, I find trends in environmental properties with c, with more massive, redder galaxies and environmental regions hosting redder SNe Ia, consistent with prior (but weak) observed trends (Sullivan et al., 2010; Childress et al., 2013; Kelsey et al., 2021). As in Chapter 3, I observe an absence of red SNe Ia in low-mass galaxies and, to a lesser extent, in bluer $U - R$ regions. These correspond with the bin mean split plots presented in Figure 4.10, but with a finer binning to allow for greater clarity of the underlying trends with environmental properties and c.

5.1.3 Splitting the Sample based on c

Motivated by the intriguing results found when splitting by c in the DES3YR analysis, in which I found that the redder objects ($c > 0$) have larger steps than the bluer objects,

I repeat the same analysis for this DES5YR sample. I split the SN Ia sample into two based on the SN colour ($c \leq 0$ and $c > 0$), and analyse the relations between Hubble residual and environmental property for each subsample, for both global and local host galaxy properties. In order to be consistent with the $\log(M_{\text{stellar}}/M_{\odot})_{\text{global}} = 10$ division point used by Brout & Scolnic (2021) (which highly motivated the latter part of this DES5YR analysis), I present the step values calculated at the 'literature' division points motivated in Chapter 4. As a reminder:

- $\log(M_{\text{stellar}}/M_{\odot})_{\text{global}} = 10.0$
- $\log(M_{\text{stellar}}/M_{\odot})_{\text{local}} = 9.0$
- $(U-R)_{\text{global}} = 1.0$
- $(U-R)_{\text{local}} = 0.95$

The resulting steps for local and global M_{stellar} and rest-frame $U-R$ are displayed in Figure 5.3, with numerical values given in Table 5.1.

In all cases, the step size is larger in red SNe Ia than in blue SNe Ia, but to varying levels of significance. There is a 2.6σ difference between Hubble residual step sizes for global M_{stellar}, as also seen in Chapter 3. This indicates that this host parameter may have the strongest relationship with c, pointing to the link between host galaxy mass and dust. The differences are not significant ($\simeq 1\sigma$) for the other environmental properties, indicating a weaker link between those properties and SN c. This is different to what was found in Chapter 3, where I found that all environmental property steps had differences of $> 2\sigma$ when split into subsamples by c. As can be seen, the $U-R$ steps for red SNe are large (~ 0.08 mag; 4σ), however there are $> 3\sigma$ $U-R$ steps for blue SNe, causing the difference to only be $\sim 1\sigma$. $U-R$ seems to be more consistent across the different SNe c values.

I repeat the analysis by splitting the sample by environment at the values that gave the largest steps. For these alternative split locations all differences between step sizes increased by at least 0.6σ, with the difference in global M_{stellar} step increasing to approximately 4σ. I also note that, based on the findings of Dixon (2021), by neglecting correlated covariates, the step sizes and significances we report are likely to be underestimated, and the true difference between subsamples may be larger.

As in Chapter 3, and Brout & Scolnic (2021), the r.m.s. values, presented in Table 5.2, for SNe Ia with $c < 0$ are considerably smaller (~ 0.05 mag) than those for SNe Ia with $c > 0$, with the smallest values found for $c < 0$ in low stellar mass or blue environments. This lends more weight to the argument posed in Chapter 3 that SNe Ia in the lower mass, higher star-forming, bluer regions are a more homogeneous sample that may be better to use in cosmology.

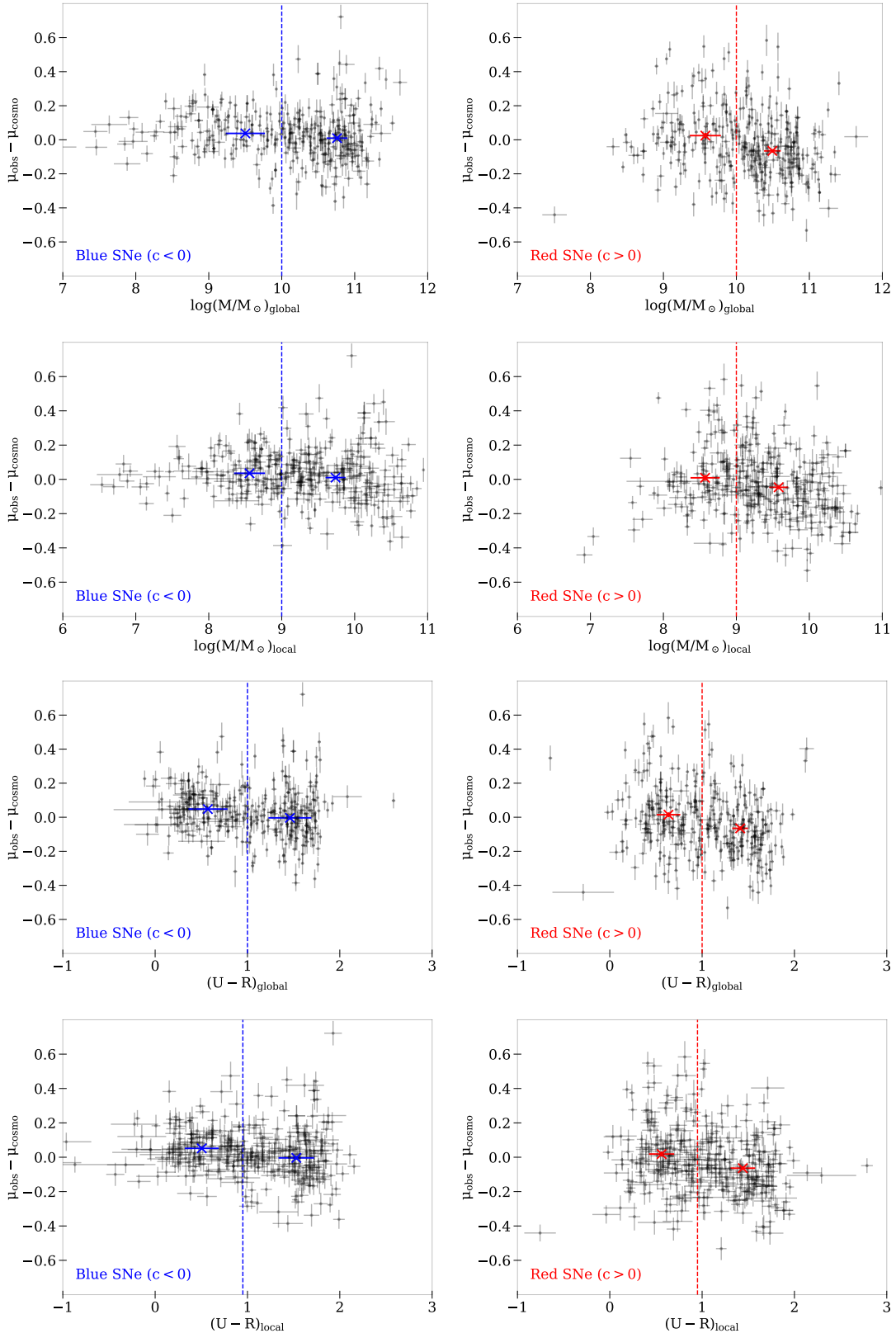

FIGURE 5.3: Hubble residuals as a function of environmental properties for subsamples split by c. The dashed lines represent the split point for each sample indicated in Table 5.1, defined as our location of the step, corresponding with the cross bin mean markers. Numerical values for these steps are displayed in Table 5.1 with r.m.s. values in Table 5.2.

TABLE 5.1: Subsample data when splitting the sample based on c.

Property		$c < 0$		$c > 0$		
Name	Step Location	mag	σ	mag	σ	Difference (σ)[1]
Number of Supernovae		336		341		
Global Mass	10.00	0.028 ± 0.014	2.0	0.090 ± 0.019	4.6	2.6
Local Mass	9.00	0.025 ± 0.014	1.8	0.055 ± 0.021	2.6	1.2
Global U-R	1.00	0.052 ± 0.014	3.7	0.080 ± 0.019	4.3	1.2
Local U-R	0.95	0.056 ± 0.014	4.0	0.082 ± 0.019	4.4	1.1

[1] Significance is quadrature sum.

TABLE 5.2: Subsample r.m.s. when splitting the sample based on c.

Property		$c < 0$		$c > 0$	
Name	Step Location	r.m.s. left	r.m.s. right	r.m.s. left	r.m.s. right
Global Mass	10.00	0.134 ± 0.017	0.156 ± 0.015	0.200 ± 0.024	0.185 ± 0.018
Local Mass	9.00	0.115 ± 0.014	0.166 ± 0.017	0.195 ± 0.027	0.189 ± 0.018
Global U-R	1.00	0.131 ± 0.015	0.161 ± 0.017	0.193 ± 0.021	0.189 ± 0.020
Local U-R	0.95	0.128 ± 0.015	0.161 ± 0.017	0.201 ± 0.023	0.182 ± 0.019

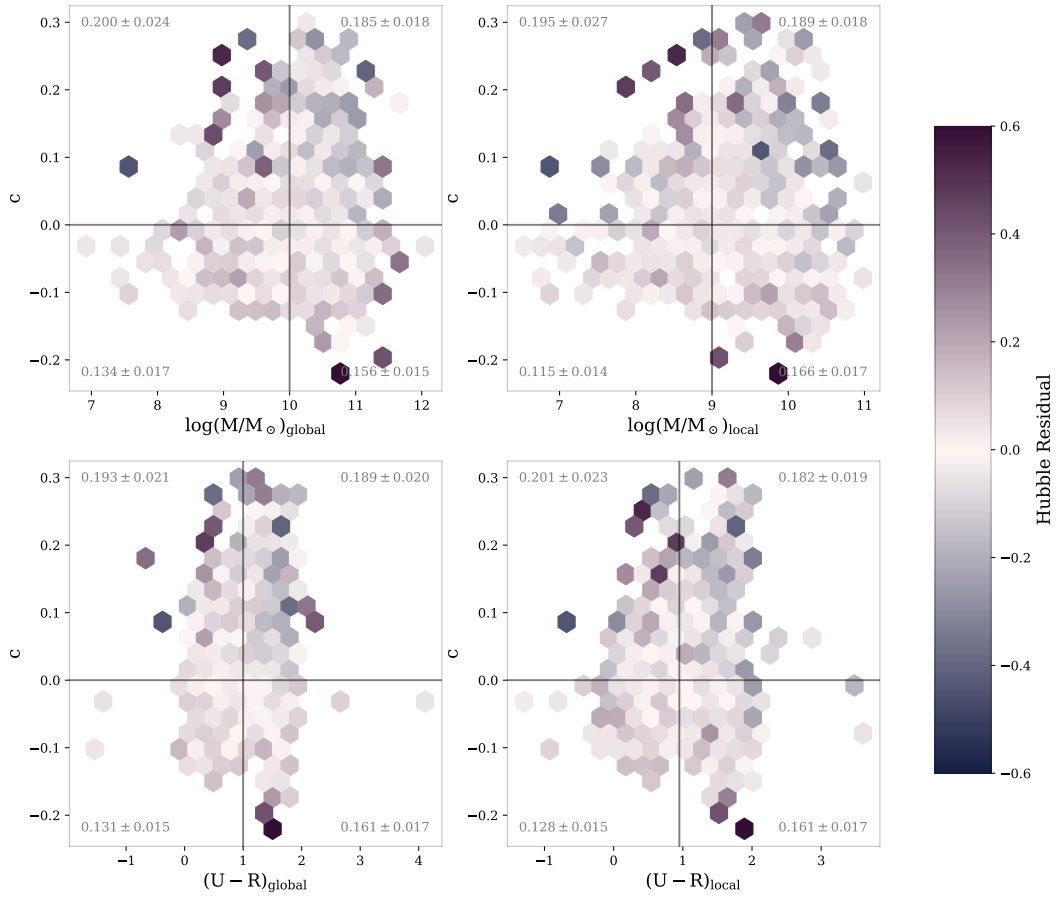

FIGURE 5.4: Hexbinned heatmaps, showing the relationships between rest-frame $U - R$ or M_{stellar} and c as a function of mean Hubble residual. Vertical and horizontal lines show the splits into low and high environmental property, and blue ($c \leq 0$) and red ($c > 0$) colour SNe. The numbers in each quadrant are the r.m.s. values for the SN Ia Hubble residual scatter for events in that quadrant (also in Table 5.2). Shown for both global (right panels) and local (left panels) M_{stellar} (upper panels) and rest-frame $U - R$ galaxy colour (lower panels)

I show these relationships in a different form in Figure 5.4, which is hexbinned heatmaps in the parameter space of environmental property and SN c, with bins shaded according to the mean Hubble residual of events in that bin. These plots show that the most homogeneous SN Ia sample, that additionally has the most consistently close to zero Hubble residual, is in the lower left quadrants, therefore indicating negative c (i.e., blue SNe) and low environmental properties (low M_{stellar}, blue $U - R$ regions).

5.1.3.1 Comparing c subsamples to DES3YR

In Chapter 3 I found that, for DES3YR, all environmental property steps had differences of $> 2\sigma$ between red and blue SNe when split into subsamples by c, whereas using the

TABLE 5.3: Bootstrap analysis - subsample data when splitting the sample based on c.

Property Name	Step Location	$c < 0$ mag[1]	$c > 0$ mag	Difference (σ)[2]
Number of Supernovae		81 ± 6	83 ± 6	
Global Mass	10.00	0.027 ± 0.027	0.089 ± 0.038	1.34
Local Mass	9.00	0.025 ± 0.025	0.056 ± 0.041	0.66
Global U-R	1.00	0.051 ± 0.027	0.079 ± 0.035	0.65
Local U-R	0.95	0.055 ± 0.025	0.081 ± 0.036	0.60

[1] Uncertainties are standard deviation of all bootstrap iterations, and thus are not the same as those from Table 5.1.
[2] Significance is quadrature sum.

DES5YR sample the differences were only significant for the global M_{stellar}. To understand if these changes in step size difference between blue and red SNe between the two samples are just a statistical effect, I performed a bootstrap analysis. In this analysis, I randomly selected a sample of 164 objects from DES5YR to match the sample size of DES3YR, split the sample into red and blue, and measured their environmental property Hubble residual steps for each subsample. This random selection and measurement was repeated 1000 times, and from these iterations the mean and standard deviation were calculated, which are defined as the step size and uncertainty. Thus these uncertainties are not the same as for the main analysis, and instead encompass the range of values obtained from the bootstrap analysis. The steps and associated significance of the difference between red and blue subsamples are presented in Table 5.3.

As can be seen, the values seen here are very similar to those for the main DES5YR analysis, and the only one with a $> 1\sigma$ difference between red and blue is the global M_{stellar}. Ignoring the large uncertainties due to the bootstrap method, the magnitudes of the steps are very consistent with the step sizes in Table 5.1. This indicates that the changes seen between DES3YR and DES5YR are not statistical effects, and are more likely due to differences between the distributions of properties in a spectroscopically-confirmed and photometrically-confirmed sample.

An additional possibility is that the changing step sizes are due to contamination from core-collapse SNe in DES5YR. However, predictions from detailed simulations suggest core-collapse contamination varying from 5.8 to 9.3 per cent, with an average of 7.0 per cent with r.m.s. of 1.1 per cent in the DES5YR sample (Vincenzi et al., 2021). With such a low, well constrained contamination level, it is unlikely core-collapse SNe contamination is the cause of the differences between the step sizes between DES3YR and DES5YR.

5.1.4 Comparison to Brout & Scolnic (2021)

Brout & Scolnic (2021) suggest that the dominant component of SN Ia intrinsic scatter is caused by variation in the extinction factor R_V distribution as a function of host galaxy M_{stellar}. They found that the Hubble residual trends with host M_{stellar} were modelled well by considering the SNe c distribution to be a two-component combination consisting of an intrinsic Gaussian distribution, and an extrinsic exponential dust distribution. This extrinsic dust distribution is host galaxy M_{stellar} dependent, with a mean $R_V = 2.75$ in low mass host galaxies and mean $R_V = 1.5$ in high mass hosts. This means that there are different colour-luminosity relationships either side of the mass step division point. They suggest that the mass step is therefore primarily caused by a difference in dust properties for SNe Ia with different c. This is consistent with the finding in Kelsey et al. (2021) that it is physics that affects the SN colour that is driving the Hubble residual host galaxy correlations. To compare my analysis with Brout & Scolnic (2021), I extend the study of SN c for different host properties, by comparing the Hubble residuals with a finer binning of SN colour, rather than simply red ($c > 0$) or blue ($c < 0$). This follows Brout & Scolnic (2021) Fig. 6.

5.1.4.1 M_{stellar}

First, I present the results with host galaxy M_{stellar} (Figure 5.5). Overplotted is the SN Ia sample used in Brout & Scolnic (2021) (a mostly independent publicly available, spectroscopically classified, photometric light-curve sample consisting of a combination of data from the Foundation, PS1, SNLS, SDSS, CSP, CfA surveys[1], and DES3YR) with a redshift cut of $z < 0.6$ applied for consistency with my analysis. The two data sets – DES5YR and Brout & Scolnic (2021) – generally follow similar trends, and thus I expect that the predictions of the Brout & Scolnic (2021) model will also adequately model the sample. Figure 5.5(a), as in Brout & Scolnic (2021) Fig. 6, shows there is little difference between the r.m.s. values for samples in high and low M_{stellar} for the bluer SNe, but this increases for the red SNe, also mirrored in the larger step sizes in the red bins. This increase in r.m.s. scatter and host M_{stellar} step size towards the redder (right hand) end of the plot suggests that the overall M_{stellar} step is driven by the red SNe.

I attempt to fit a variety of lines with minimal χ^2 to the low and high M_{stellar} data points, generating simple functions for the observed M_{stellar} - c dependent Hubble residual relationships, so that the effect of these trends can be removed from the Hubble residuals and remaining environmental property relationships uncovered. Similarly low χ^2

[1]Foundation: Foley et al. (2018), Pan-STARRS1 (PS1): Rest et al. (2014); Scolnic et al. (2018), SuperNova Legacy Survey (SNLS): Betoule et al. (2014), Sloan Digital Sky Survey (SDSS): Sako et al. (2011), Carnegie Supernova Project (CSP): Stritzinger et al. (2010), Harvard-Smithsonian Center for Astrophysics (CfA3+4): Hicken et al. (2009b,a, 2012).

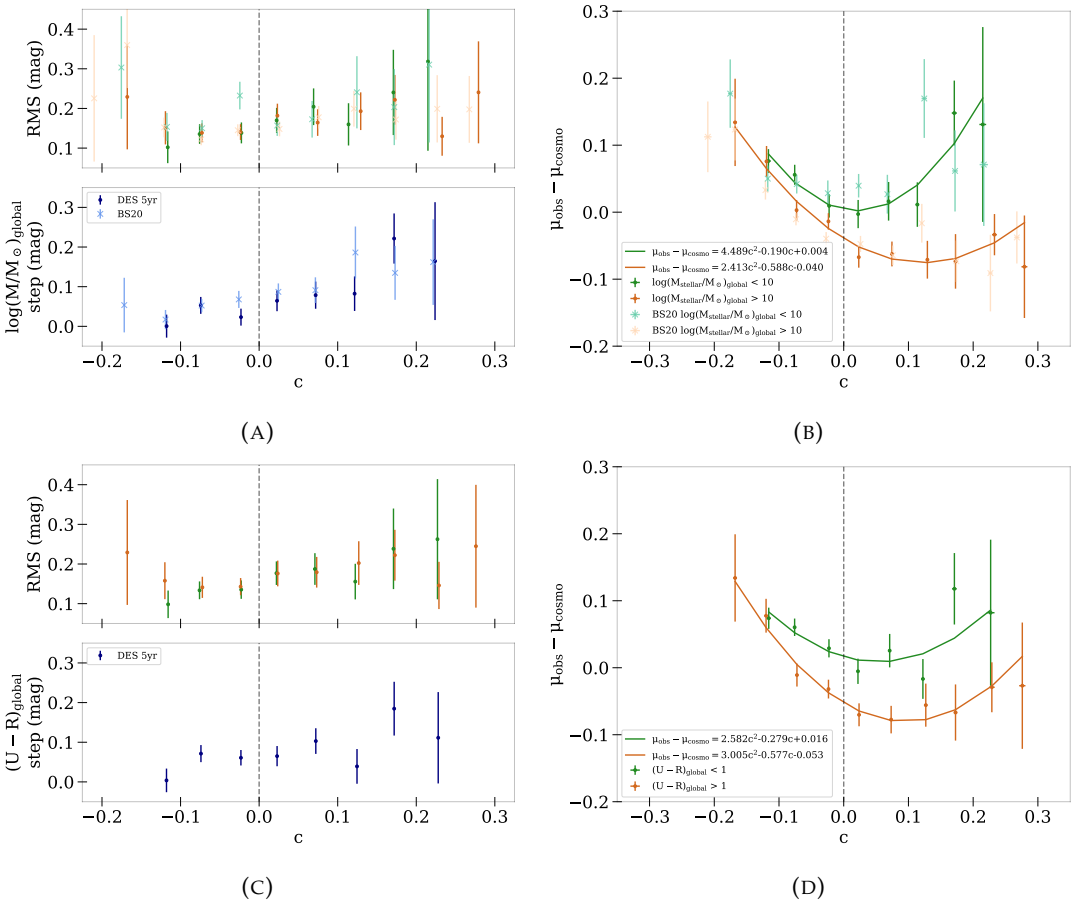

FIGURE 5.5: **a)** and **c)** (Upper panels) Hubble diagram r.m.s. in bins of SALT2 colour c, for SNe Ia in galaxies with high and low M_{stellar} (a), or with high and low rest-frame $U-R$ colour (c). Colour scheme corresponds with (b) and (d). (Lower panels) Calculated values for the size of the environmental property step as a function of c. **b)** and **d)** Binned Hubble residuals as a function of c split by host galaxy M_{stellar} (b) and host galaxy rest-frame $U-R$ (d). The overplotted quadratic fits minimise the χ^2. Data used in BS20 shown for M_{stellar} in (a) and (b) in transparent colours.

values were found when fitting quadratic curves and when fitting two separate linear relations for positive and negative c, for both low and high M_{stellar}. These also resulted in similar remaining relationships once their trends were removed from the data. However, I chose to proceed with the quadratic fits, due to the fact that they are smooth, continuous functions. There is no clear reason why the relationship with c would change dramatically at any particular value, intuitively it is more likely to be a continuous relationship, meaning that combining linear functions for different c bins may not be as realistic. As illustrated in Figure 5.5(b), these quadratic fits generate simple functions for the M_{stellar} - c dependent Hubble residual relationships. By subtracting these curves from the Hubble residual of each SN in my sample, I am able to correct for these observed c - dependent M_{stellar} trends. This simple approximation of the Brout & Scolnic (2021) dust model removes the global host galaxy mass step from my data (0.000 ± 0.012 mag; 0.0σ), however I find significant remaining rest-frame $U-R$ steps

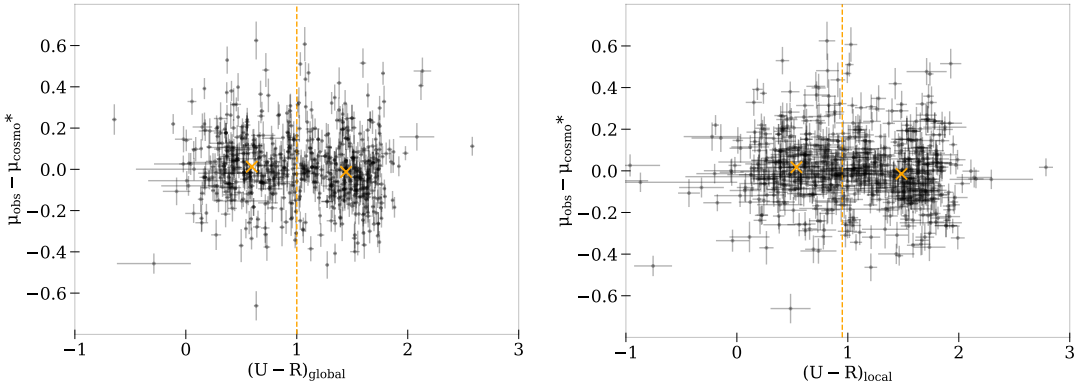

(A) Global $U - R$ (B) Local $U - R$

FIGURE 5.6: Hubble residual plots as a function of global (a) and local (b) rest-frame $U - R$, once the global $M_{stellar}$ - c dependent Hubble residual relationship shown in Figure 5.5b has been removed (as indicted by *). The dashed lines represent the sample split points of $U - R_{global} = 1$ and $U - R_{local} = 0.95$, used as the location of the '$U - R$ step' corresponding with the cross bin mean markers. Numerical values for these steps are displayed in Table 5.4.

of 0.025 ± 0.011 mag; 2.3σ for global and 0.032 ± 0.011 mag; 2.9σ for local when the c - dependent $M_{stellar}$ relation is removed, as can be seen in Figure 5.6. This indicates that the dust model is not the full picture. Either it does not fully explain the complex relationship between SN luminosities and their host properties; or the current dust model needs adjusting.

5.1.4.2 $U - R$

I repeated the above analysis, but starting with and fitting for the relationship between global rest-frame $U - R$ and c, instead of fitting for the global $M_{stellar}$ - c dependent Hubble residual relationship. I split into 'low' and 'high' by splitting at $U - R = 1$, as motivated by Chapter 3. Again, quadratic functions fit the data best through a χ^2 minimisation, which I subtracted from the Hubble residual for each SN to correct for $U - R$ - c dependent Hubble residual relationships, as shown in panels (c) and (d) of Figure 5.5.

This approximation removed the global $U - R$ step from the data, and found remaining mass steps of only 0.015 ± 0.012 mag $= 1.3\sigma$ for global $M_{stellar}$ and 0.011 ± 0.011 mag $= 1.0\sigma$ for local $M_{stellar}$. These are smaller than the remaining $U - R$ steps once the global c-$M_{stellar}$ relation was removed, suggesting that a $U - R$ correction encompasses more of the overall Hubble residual vs host environment relationship than $M_{stellar}$ does; as seen in Kelsey et al. (2021).

TABLE 5.4: Magnitudes and significances of remaining environmental property steps when fitting for relationships between c and environmental properties.

		Fitting For: Global Mass	Local Mass	Global U-R	Local U-R
Remaining Step In:	Global Mass	0.000 ± 0.012 0.0σ	0.039 ± 0.012 3.3σ	0.015 ± 0.012 1.3σ	0.014 ± 0.012 1.2σ
	Local Mass	0.015 ± 0.011 1.3σ	0.003 ± 0.012 0.4σ	0.011 ± 0.011 1.0σ	0.004 ± 0.011 0.4σ
	Global U-R	0.025 ± 0.011 2.3σ	0.047 ± 0.011 4.1σ	0.001 ± 0.011 0.1σ	0.006 ± 0.011 0.5σ
	Local U-R	0.032 ± 0.011 2.9σ	0.047 ± 0.011 4.1σ	0.015 ± 0.011 1.3σ	0.003 ± 0.011 0.2σ

All steps given in mag.
Step split points as described in Section 5.1.3.

5.1.4.3 Meaning

In order to fully test the combinations of M_{stellar} and $U - R$, I looped through all possible combinations of local and global host galaxy environments, fitting c dependent quadratic functions to one environmental property, and calculating the remaining step magnitude in the others, as shown in Table 5.4. From this table, it can be seen that significant local and global $U - R$ steps remain when fitting for either global or local host mass, and less significant steps remain when the reverse is done; adding to the suggestion that a $U - R$ correction encompasses more of the overall Hubble residual relationship than M_{stellar} does. In this table, uncertainties are statistical only, and are likely dominated by uncertainties in the quadratic fitting.

The $> 3\sigma$ steps that remain in both local and global $U - R$ and in global M_{stellar} when fitting for local mass are particularly interesting. Considerable remaining steps remain once the trend with c has been removed, suggesting that local mass may not be removing any trends or perhaps is less correlated with the other parameters than expected, however this disagrees with the trends shown in Figure 3.2 and Figure 4.4 that local and global mass are correlated (albeit with scatter). As from Table 5.1 I found only a 1.2σ difference in local mass step size for blue and red supernovae, this suggests that local mass is not correlated with c, and thus may not be linked to dust in the same way as suggested by Brout & Scolnic (2021) for global mass. Further investigation of this finding is needed in future study, and may require better resolved local properties than those available using DES. This may help to determine the location of dust in the host galaxy, either contained in the local circumstellar region around a SNe, or more dispersed throughout the global host galaxy.

Additionally, when fitting for a c - dependent global $U-R$ step, there remains a 0.015 ± 0.011 mag $= 1.3\sigma$ local $U-R$ step. Whist the significance of this is low, it provides an indication of the differences between local and global properties.

It is also interesting that the quadratic fits do not completely remove the relationships with local mass, and both global and local $U-R$, all having small ($< 0.5\sigma$) 'remaining' steps when their c-dependent relationship is fitted for. Whilst these values are small, they may suggest that there is less of a relationship between these parameters and c, agreeing with the findings in Section 5.1.3.

Intriguingly, a local $U-R$ step of 2.9σ (Figure 5.6b) remains when fitting for the global c-$M_{\rm stellar}$ relation. This is similar to the finding of Roman et al. (2018) of a significant (5σ) remaining $U-V$ step when correcting first for the overall global mass step in their analysis, suggesting that additional information can be provided by local properties when combined with global properties. Local U-R is linked to stellar population age (see Section 2.6.2), and so this result indicates that it is a combination of a c dependent host $M_{\rm stellar}$ relation (acting as a proxy for dust, following Brout & Scolnic, 2021) and local $U-R$ (a measure of age) that may fully explain the remaining SNe Ia dispersion, as has been postulated by hierarchical modelling in Rose et al. (2021a).

5.1.5 An Aside on x_1

In addition to intrinsic colour c, the brightness of SNe Ia is corrected by their stretch (x_1). Based on my findings in Chapter 3, I focused this analysis on c as this is where I found the greatest difference in Hubble residuals. However, as a sanity check, I repeated the analysis using x_1 instead of c and found no significant difference between step sizes for subsamples split on x_1, similar to what I found in Chapter 3. As can be seen in Figure 5.7 and Table 5.5, the largest difference in step size in x_1 subsamples is 1.1σ for global $M_{\rm stellar}$, so whilst it is only small, it is perhaps indicative of the known $x_1 - M_{\rm stellar}$ relation (Smith et al., 2020b). All other differences are to $\leq 0.2\sigma$. Additionally, as shown in Table 5.6, I see no clear difference between r.m.s. values for the subsamples split on x_1, a clear contrast to the findings for subsamples split on c.

5.2 Discussion

Similarly to Smith et al. (2020b); Brout & Scolnic (2021) and Chapter 3 , I find a significant difference between global $M_{\rm stellar}$ step sizes when splitting into subsamples based on SN c. The data agrees well with the dust explanation of Brout & Scolnic (2021) and thus it is likely that the $M_{\rm stellar}$ Hubble residual step differences for c subsamples are due to the role of dust.

TABLE 5.5: Subsample data when splitting the sample based on x_1.

Property		$x_1 < 0$		$x_1 > 0$		
Name	Step Location	mag	σ	mag	σ	Difference (σ)[1]
Number of Supernovae		361		316		
Keeping α and β fixed ($\alpha = 0.172 \pm 0.007$, $\beta = 3.07 \pm 0.07$)						
Global Mass	10.00	0.068 ± 0.019	3.6	0.040 ± 0.017	2.4	1.1
Local Mass	9.00	0.036 ± 0.019	1.9	0.042 ± 0.017	2.5	0.2
Global U-R	1.00	0.063 ± 0.017	3.8	0.060 ± 0.017	3.4	0.1
Local U-R	0.95	0.064 ± 0.018	3.6	0.065 ± 0.017	3.9	0.0

[1] Significance is quadrature sum.

TABLE 5.6: Subsample r.m.s. when splitting the sample based on x_1.

Property		$x_1 < 0$		$x_1 > 0$	
Name	Step Location	r.m.s. left	r.m.s. right	r.m.s. left	r.m.s. right
Keeping α and β fixed ($\alpha = 0.172 \pm 0.007$, $\beta = 3.07 \pm 0.07$)					
Global Mass	10.00	0.172 ± 0.024	0.172 ± 0.015	0.170 ± 0.019	0.168 ± 0.020
Local Mass	9.00	0.157 ± 0.023	0.177 ± 0.015	0.155 ± 0.018	0.180 ± 0.020
Global U-R	1.00	0.166 ± 0.020	0.176 ± 0.017	0.165 ± 0.017	0.017 ± 0.022
Local U-R	0.95	0.169 ± 0.022	0.174 ± 0.016	0.170 ± 0.018	0.168 ± 0.021

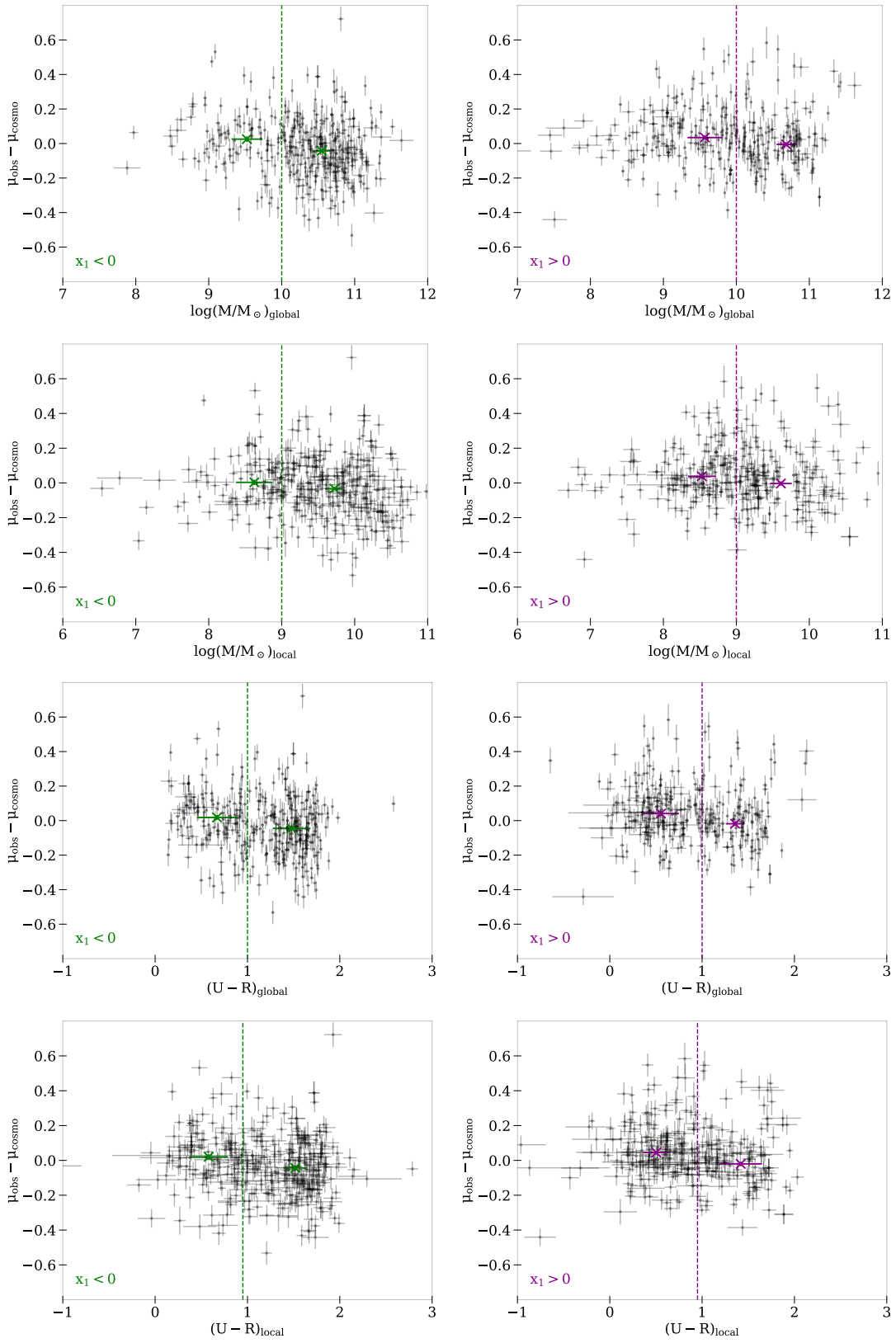

FIGURE 5.7: Hubble residuals as a function of environmental properties for subsamples split by x_1. The dashed lines represent the split point for each sample indicated in Table 5.5, defined as our location of the step, corresponding with the cross bin mean markers. Numerical values for these steps are displayed in Table 5.5 with r.m.s. values in Table 5.6.

However, with the larger sample afforded by the DES5YR photometric sample, I see a different result to my previous work in Chapter 3 with regards to $U-R$ steps when splitting based on c. In Chapter 3, I found $\sim 3\sigma$ differences in step sizes in $U-R$ between red and blue SNe, as opposed to the $\sim 1\sigma$ differences seen with this DES5YR sample. This suggests that environmental $U-R$ is not strongly correlated with SN c, and thus will not follow the same relationship with dust as M_{stellar}.

By fitting for c-dependent global host M_{stellar} Hubble residual relationships in an approximation of the Brout & Scolnic (2021) dust model, I am able to effectively remove the mass step from my data. However, I still found a significant (2.9σ) remaining local $U-R$ step, indicating that, whilst dust modelling may explain the mass step (Brout & Scolnic, 2021), it does not fully explain the SN luminosity dispersion.

5.2.1 Why Not Both?

Much discussion over the years has been dedicated to deciding whether the underlying cause of the remaining SNe Ia dispersion is due to mass, dust or age effects. These are difficult to disentangle, and are correlated. M_{stellar} correlates with star formation rate, metallicity (Tremonti et al., 2004) and age (Gallazzi et al., 2005; Kang et al., 2016); age correlates with morphology, star formation rate and the amount of dust; the amount of dust correlates with M_{stellar} (Garn & Best, 2010b). There are complicated 'twisting' relations between mass, metallicity and star formation rate (Yates et al., 2012), and between mass, metallicity and dust extinction (Zahid et al., 2013). These are all additionally dependent on the star-formation history of the individual host galaxies, potential galaxy mergers, AGN activity etc.

All of these parameters are intertwined, yet are not the same. Intuitively, it does not make sense that correcting for just one of them will account for the effects of all of the others. This analysis implies that a combination of a mass and an age correction, as suggested by Rose et al. (2019, 2021a); Rigault et al. (2020) is needed to better improve the standardisation of SNe Ia.

5.2.2 Impact on Cosmology

Based on this analysis, my suggestion for future cosmology is that, in an ideal situation, one should correct for both a global c-dependent M_{stellar} effect (Brout & Scolnic, 2021; Popovic et al., 2021) to account for the role of dust and for local age, perhaps by using local $U-R$ (Kelsey et al., 2021) or local sSFR as proxies (Rigault et al., 2020). To reduce biases, these should be simultaneously fit with the historic light-curve standardisation parameters (Rose et al., 2021a; Dixon, 2021).

However, this is difficult to do, therefore given the homogeneity (as shown in Table 5.2, Figure 5.4, and in Section 3.3.4) of blue ($c < 0$) supernovae in low mass or locally blue environments, it may be simplest and of most immediate value to just use these SNe in cosmology (Kelsey et al., 2021; Gonzalez-Gaitan et al., 2020). This is not a new suggestion, and there is a wealth of information pointing to the benefits of such a cut. As discussed in Section 3.4, this has previously been suggested by the findings of Rigault et al. (2013); Childress et al. (2014); Kelly et al. (2015); Henne et al. (2017); Kim et al. (2018) with respect to using only SNe Ia from actively star-forming galaxies or local regions, and the additional suggestion of Kim et al. (2018) to use low-mass, star-forming galaxies. In terms of supernova properties, Wang et al. (2009); Foley & Kasen (2011); Siebert et al. (2020) all find a reduction in scatter using low-velocity, blue supernovae, which is complemented by a smaller bias correction for blue supernovae found by Kessler & Scolnic (2017).

By combining all of this knowledge from previous analyses, and the confirmations from Kelsey et al. (2021), Gonzalez-Gaitan et al. (2020) and the analysis of this chapter, we should utilise a subset of blue ($c < 0$) supernovae in low mass/blue/star-forming environments to provide the most homogeneous sample for future cosmology.

5.3 Summary

By expanding the findings of my previous analysis into the relationship between SNIa host environment and c in DES3YR (Chapter 3, published as Kelsey et al., 2021) to a larger sample consisting of SNIa from DES5YR, I have gained further understanding of this relationship, enabling me to provide more weight to the suggestion that it is physics affecting the supernova colour which is the key cause of the remaining luminosity dispersion, and that the most homogeneous sample for use in cosmology comes from the blue supernovae.

When I split my data into two subsamples for $c < 0$ and $c > 0$, I find that the largest, and most statistically significant, difference in Hubble residual 'step' between the two subsamples is for those associated with global M_{stellar}, agreeing with the findings of Chapter 3. Surprisingly, although the step size is consistently larger for red SNe Ia than for blue SNe Ia, with this larger sample I only find differences of $\sim 1\sigma$ for all other environmental properties, in contrast to what I found with DES3YR. This finding indicates that global M_{stellar} has the strongest relationship with SN c, suggestive of the link between host galaxy M_{stellar} and dust.

When measuring the r.m.s. scatter for the subsamples, I observe the lowest r.m.s. scatter, and therefore highest homogeneity for blue SNe Ia in low mass or blue environments, as in Chapter 3 and Gonzalez-Gaitan et al. (2020). This finding adds more weight to the argument that a subsample consisting of such supernovae may provide

the best results for use in future cosmological analyses. Such a sample would likely require no or minimal additional corrections for host galaxy properties.

I then turned splitting my sample by environmental property and fitting a two-component c-dependent Hubble residual, in a simple approximation of the Brout & Scolnic (2021) dust model (i.e. 'high' and 'low' for each environmental property follows a different c-Hubble residual law). When I do this for global M_{stellar} I remove the mass step from the data, suggesting that there is a strong relationship between M_{stellar}, c and dust. However, despite removing the mass step from the data, a statistically significant (2.9σ) step in local $U - R$ remains, suggesting that the dust modelling alone does not fully explain the dispersion in SN luminosity. This implies that combining corrections based on a c-dependent M_{stellar} relation and a relation with $U - R$, a tracer of sSFR and stellar age, in a similar way to that suggested by Rigault et al. (2020); Rose et al. (2021a) may be the best way forward to truly understand the dispersion in SNe Ia luminosity.

This analysis and my findings have important cosmological implications, which should be taken into account in the next generation of cosmological analyses. On one hand, my findings for the homogeneity of blue SNe in low mass or blue environments provides more weight to the argument that they are the best subsample to use for precision cosmology, so it may simply be easiest to just use those. On the other hand, to gain insight into the true astrophysical cause of the SNe Ia dispersion, combining corrections based on a c-dependent host galaxy M_{stellar} and another relationship based on $U - R$ or other age proxies may provide the answers for the true relationships between SNe Ia and their environments.

Chapter 6

Local Environments of Supernova Siblings

An additional investigation that can be done using the DES5YR data is to look into the differences in local environments of SNe located within the same host galaxy, and explore how these local differences may impact SN properties.

6.1 Supernova Siblings

With the ever-growing size of supernova surveys, the likelihood of finding two or more SNe Ia within the same host galaxy is increasing. Such SNe have been termed 'siblings' (Brown, 2014), and they provide a novel data set to study the effects of environmental properties. If the known correlations between global host galaxy properties, such as the well-studied mass step, are the answer for the remaining dispersion in SNe Ia luminosity, one would expect that sibling SNe Ia would have similar properties and Hubble residuals given that they share the same host galaxy. However, if their properties, such as c and x_1, and Hubble residuals are different, it would suggest that global parameters are not the full story.

Supernova siblings are also useful in the context of constraining distances by providing multiple independent measurements to the host galaxy, and by comparison of their relative absolute brightness. As the SNe are within the same galaxy, any additional uncertainty on distance due to peculiar velocities can be avoided.

Until recently, only relatively few SNe Ia siblings had been discovered and analysed in detail, for example: 4 SNe Ia within NGC 1316 (Fornax A) (Stritzinger et al., 2010), 2 SNe Ia within NGC 1404 (Gall et al., 2018; Ashall et al., 2018), and AT2019lcj and SN 2020aeqj from the ZTF survey (Biswas et al., 2021). However, studies using large surveys such as that using DES data (Scolnic et al., 2020), or using new data alongside a

compilation of literature data (Burns et al., 2020), have increased this number allowing for more robust statistical analysis of the properties of SN Ia siblings. It is of note that finding multiple SNe Ia siblings using a large survey, such as DES, allows for all the siblings to be calibrated consistently and for survey selection effects to be taken into account in the same way; an advantage over combining historical observations from multiple surveys.

By studying 8 galaxies that each contained a sibling pair of SNe Ia from DES5YR, Scolnic et al. (2020) found no better agreement between SNe properties in the same galaxy as from any random pair of galaxies, concluding that at least half of the intrinsic scatter in residuals is not from global host properties. They also find that a SN pair with the most differing distance modulus values have SNe located on opposite sides of the galaxy. So the question is: what about their local environments? This is what I intend to answer in this chapter.

6.2 DES Siblings

In this chapter, I use the sample of siblings from Scolnic et al. (2020), and the SN properties quoted within that analysis. By searching for galaxies that host two SNe Ia within the DES5YR sample, Scolnic et al. (2020) found 73 potential galaxies where each SNe Ia was clearly not an AGN or image artifact. By applying the SNN (Möller & de Boissière, 2020) and PSNID (Sako et al., 2011) classifiers and requiring that each SN meets a probability threshold of being a SNe Ia of 0.8, this was reduced to 7 sibling pairs, a total of 14 SNe Ia.

Within DES-SN, candidate detections within 1″ are assigned to the same object, meaning that some very close siblings may have been missed. To take this into account, Scolnic et al. (2020) used the classifiers to check for SNe Ia that appeared in multiple years of the survey, but were located within 1″ of another candidate, finding no additional SNe Ia. However, one event (DES16C3nd) was manually identified over the duration of DES-SN as actually consisting of two SNe within 1″ within the same season of less than 200 days. Both of these SNe have been classified as likely SNe Ia, so were added to the sibling sample. This brings the final DES5YR sibling sample to 8 sibling pairs, 16 SNe Ia. This number was found to be consistent with the expected rate of SNe Ia within the same galaxy in the DES5YR survey. A summary of the sibling candidates is presented in Table 6.1.

6.2.1 SNe Properties

Scolnic et al. (2020) fit the light curves of each SNe using SALT2 (Guy et al., 2010) and SNANA (Kessler et al., 2009), with host galaxy redshifts from OzDES, in the same way

TABLE 6.1: DES5YR siblings sample. Adapted from Scolnic et al. (2020).

z[a]	Host Location[b]	SN_1	SN_1 Location	SN_1 MJD[c]	SN_2	SN_2 Location	SN_2 MJD
0.228	40.8636 -01.6024	DES13S2dlj	40.8637 -01.6017	56541	DES14S2pkz	40.8641 -01.6036	57004
0.349	53.2948 -27.9576	DES14C3zym	53.2948 -27.9573	57002	DES15C3edd	53.2945 -27.9578	57286
0.384	54.4053 -28.3102	DES14C2iku	54.4045 -28.3102	56955	DES17C2jjb	54.4052 -28.3102	58146
0.506	41.7614 -01.3781	DES15S2okk	41.7612 -01.3781	57393	DES17S2alm	41.7616 -01.3781	58005
0.524	55.1459 -28.6279	DES15C2mky	55.1451 -28.6281	57348	DES16C2cqh	55.1459 -28.6279	57689
0.561	06.8201 -42.5739	DES13E1wu	06.8200 -42.5739	56550	DES14E1uti	06.8201 -42.5732	57046
0.648	52.2183 -27.5744	$DES16C3nd_0$[d]	52.2183 -27.5744	57635	$DES16C3nd_1$	52.2183 -27.5744	57753
0.648	35.4094 -05.7659	DES15X2mlr	35.4103 -05.7656	57345	DES15X2nku	35.4088 -05.7656	57363

[a] Redshift of host galaxy. Uncertainties < 0.001.

[b] Locations in degrees.

[c] Modified Julian Date (MJD) of peak brightness.

[d] SNe were given the same id as they are within $1''$ of each other. These are designated with the subscripts 0 and 1 to identify the individual SNe.

as outlined in Section 2.4. This provided the SNe properties, including the light-curve stretch (x_1) and colour (c). Following the Tripp equation (Equation 1.6) and using $\alpha = 0.14$ and $\beta = 3.1$ from Brout et al. (2019a), these were converted to distance modulii. No intrinsic scatter term is added into the μ uncertainty. They do not apply any restrictions on x_1 and c values, meaning that whilst some of these SNe appear in the DES5YR sample analysed in Chapter 4, some do not pass the strict JLA-like SALT2 selection requirements and so do not appear there. I present the x_1, c and Hubble residuals for each SN sibling in Table 6.2.

6.2.2 Local Environment Properties

As the locations and redshifts of the sibling pairs are provided within Scolnic et al. (2020), and I have the seeing-optimised stacked images from the full DES-SN survey, I can measure their local environment properties using the method outlined in Section 2.5.2. However, I replace the standard 'minus-year' (MY) seeing-optimised stacked images outlined in Section 2.2 with 'minus-two-year' stacks. Thus for each sibling pair, environmental photometry is obtained from coadditions free from SN light from each sibling in the pair, e.g. 'MY1+2' (MYX+Y) for the DES13S2dlj and DES14S2pkz pair. There are two pairs in the sample which have SNe from the same season (DES16C3nd$_0$ and DES16C3nd$_1$, DES15X2mlr and DES15X2nku), so for these the standard MY seeing-optimised stacks were used.

Whilst I could simply use the 4 kpc aperture size used in my main analysis for all SNe siblings in this sample, smaller apertures may provide better differentiation between local regions in the same galaxy. For this reason, I iterate over all apertures between 2 kpc and 4 kpc in steps of 0.25 kpc, in the same way as Section 4.3.1, and identify the minimum aperture size to use for each pair based on the redshift of the sibling host galaxy and the seeing of the stacked images, following Section 2.5.2.

As in the rest of the chapters, I follow the method in Section 2.6 to obtain the local environmental properties from the photometry, presenting the local M_{stellar} and $U - R$ values for each SN sibling in Table 6.3.

6.3 Results

By looking at the SN properties in Table 6.2, as discussed in Scolnic et al. (2020), there is a noticeable difference in values for the sibling pairs. In particular, Scolnic et al. (2020) note that the difference in distance moduli is most marked for a pair with SNe located on opposite sides of the galaxy (DES15X2mlr and DES15X2nku), and for a pair where one SNe is at the galactic center and the other is not (DES13E1wu and DES14E1uti).

TABLE 6.2: DES5YR siblings SN properties.

SN		z[a]	x_1[b]		c		Hubble Residual	
SN_1	SN_2		SN_1	SN_2	SN_1	SN_2	SN_1	SN_2
DES13S2dlj	DES14S2pkz	0.228	0.300±0.230	-0.407±0.140	0.186±0.030	0.080±0.020	0.14±0.06	-0.11±0.06
DES14C3zym	DES15C3edd	0.349	-1.560±0.150	-1.370±0.160	-0.070±0.030	-0.050±0.030	0.05±0.07	0.14±0.07
DES14C2iku	DES17C2jjb	0.384	-2.670±1.020	-0.742±0.300	0.410±0.106	-0.010±0.030	0.32±0.23	-0.05±0.08
DES15S2okk	DES17S2alm	0.506	0.089±0.650	1.220±0.620	-0.040±0.030	-0.050±0.040	-0.27±0.12	0.26±0.15
DES15C2mky	DES16C2cqh	0.524	0.820±0.340	-0.847±0.810	-0.080±0.030	0.020±0.020	-0.06±0.10	0.29±0.17
DES13E1wu	DES14E1uti	0.561	-0.832±0.430	3.010±2.170	-0.090±0.040	-0.010±0.060	-0.27±0.13	0.28±0.30
$DES16C3nd_0$	$DES16C3nd_1$	0.648	-1.080±0.290	-0.452±0.280	0.010±0.040	0.040±0.030	-0.28±0.10	-0.44±0.09
DES15X2mlr	DES15X2nku	0.648	-0.720±0.530	1.620±1.050	-0.080±0.050	0.020±0.060	-0.28±0.17	0.17±0.22

[a] Redshift of host galaxy. Uncertainties < 0.001.
[b] SN properties from Scolnic et al. (2020).

TABLE 6.3: DES5YR siblings local environment properties.

SN		z[a]	Aperture	Mass		U-R	
SN_1	SN_2		Radius[b]	SN_1	SN_2	SN_1	SN_2
DES13S2dlj	DES14S2pkz	0.228	2.25	9.329±0.052	8.569±0.076	1.225±0.067	1.478±0.115
DES14C3zym	DES15C3edd	0.349	2.75	9.036±0.072	8.624±0.065	0.938±0.155	3.100±7.446
DES14C2iku	DES17C2jjb	0.384	3.00	8.639±0.204	9.366±0.125	2.014±0.288	1.658±0.093
DES15S2okk	DES17S2alm	0.506	3.50	9.564±0.072	10.201±0.074	0.756±0.098	1.414±0.103
DES15C2mky	DES16C2cqh	0.524	3.50	9.020±0.142	10.194±0.129	1.424±0.310	1.437±0.232
DES13E1wu	DES14E1uti	0.561	4.00	10.560±0.050	9.486±0.865	2.158±0.257	2.649±0.800
$DES16C3nd_0$	$DES16C3nd_1$	0.648	4.00	9.642±0.145	9.652±0.147	1.374±0.206	1.384±0.207
DES15X2mlr	DES15X2nku	0.648	4.00	8.275±0.165	8.836±0.174	0.876±0.276	1.315±0.278

[a] Redshift of host galaxy. Uncertainties < 0.001.
[b] Aperture size dictated by stacked image quality, and host galaxy redshift of the individual sibling pairs.

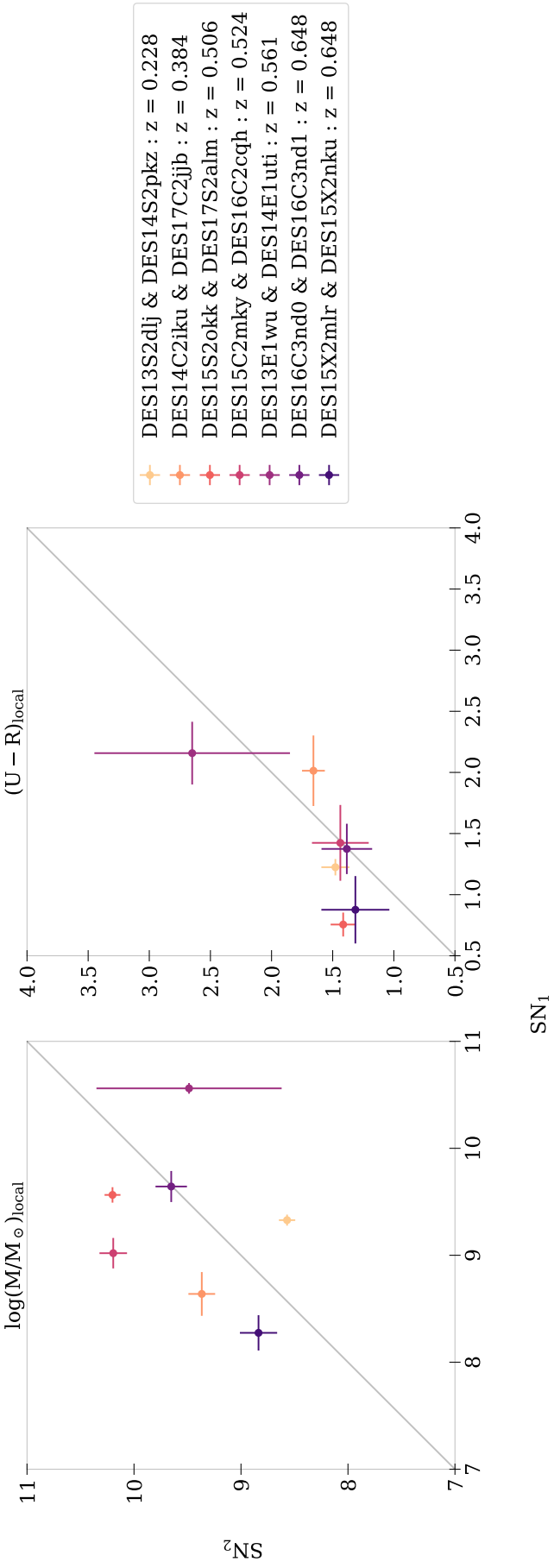

FIGURE 6.1: Comparison of local environmental properties (M_{stellar} and $U - R$) for the sibling pairs. The SN chosen for each axis is arbitrary and can be swapped, and the solid grey line indicates the 1:1 line where properties are equal.

This suggests that their local environments may be different, which can be seen in my measurements of the local properties in Table 6.3. This is illustrated in Figure 6.1, where it is clear to see that the majority of SN do not sit on the 1:1 line corresponding with matching properties with their sibling. The most similar pair is DES16C3nd$_0$ and DES16C3nd$_1$, which was expected as they are the SNe manually identified as separate events due to being within $1''$ of each other, thus they are contained within the same local aperture. As each sibling was treated independently in the method to obtain local properties, the Monte Carlo SED mangling process found slightly different results at the second decimal place level, but this is well contained within the measurement uncertainties.

I note that in the figures and the rest of this analysis that I have removed the sibling pair that contains DES15C3edd. As can be seen in Table 6.3, this object has a particularly large uncertainty in local $U - R$ meaning that it does not pass my $\sigma_{(U-R)} < 1$ quality requirement as outlined in previous chapters. For clarity, I do however present the data for this pair in the tables throughout this chapter. If I include this pair in the figures, they do follow the same trends as the rest of the siblings, but the uncertainties dominate the figures and later correlation analysis.

Now that I have established the SN and local environment properties for each SN sibling pair, I can move on to explore how these compare.

6.3.1 Comparing Sibling SN Properties with their Local Environments

For each SN and local environmental property, I compare the absolute differences and significance of these differences between the two SNe in each sibling pair and see if there are any correlations between the differences in the various properties. From Scolnic et al. (2020), only one of the sibling pairs (DES15X2mlr and DES15X2nku) are contained within a low global mass (< 10) galaxy, meaning that any trends in the relationships between SN and local environment properties are independent of the mass step. From analysis of the DES3YR sample in Chapter 3, high mass (and therefore redder, passive, dustier) galaxies have higher Hubble residual r.m.s. scatter than low mass, bluer galaxies, suggesting that they are a less homogeneous sample. This could be due to differences in progenitors, age, metallicity, dust content - things that could be revealed in the study of local environment properties.

The differences and corresponding σ are presented in Table 6.4. As can be seen, the differences in SN properties are subtle, only on the order of $1 - 2\sigma$, but for precision cosmology understanding the cause of this difference could be vital. Looking at the local environment properties, the differences are considerably more significant, in particular for the local mass. The same aperture sizes were used for each sibling in the pair, so the difference in local mass is in effect due to differences in stellar density in the

individual regions - e.g. the edge of a spiral arm will be very different to the galactic center. The local $U-R$ on the other hand seems more consistent, with only one pair having differences $> 2\sigma$, perhaps suggesting that environmental colour is generally more consistent across the galaxy. This agrees with the local $U-R \simeq$ global $U-R$ suggestion from prior chapters and Roman et al. (2018, for $U-V$). It is particularly interesting to compare the differences in the two environmental properties for each pair, as the differences do not seem to be following the same trends. For example, the sibling pair with the largest difference in local M_{stellar} does not have the largest difference in local $U-R$. This may suggest that one cannot simply correct for just one environmental property, and a combination of properties may need to be taken into account for precision cosmology to more fully understand environmental effects. This agrees with the suggestion in Chapter 5, and of Rose et al. (2021a).

6.3.1.1 Hubble Residuals

I first turn to comparing the difference in local environmental properties with the difference in Hubble residuals for the sibling pairs. As can be seen in the top panels of Figure 6.2, by eye there is a clear positive correlation between Hubble residual difference and local $U-R$ difference, and a lower correlation with local M_{stellar}. These trends are robust whether using absolute or relative differences, or significances of the differences. For clarity here, and consistency with Scolnic et al. (2020), I plot and quote absolute difference values. By colouring the markers by host galaxy redshift, it is clear to see that there is no trend with redshift.

To get a better estimate of the correlations between the differences, I consider the Pearson correlation coefficients (r). Due to the uncertainties in both the x and y axes, I use a Monte Carlo technique to take into account these uncertainties for the correlations. With 10000 iterations for each SN and local environment property, I randomly select a value for that local environment property and Hubble residual that is within the uncertainties for each property for that SN. For each iteration I then calculate the associated r value before taking the mean and standard deviation of all the values found to get an average r value and uncertainty for the data. For the local mass I thus obtain $r_{m;hr} = 0.35 \pm 0.28$ and for the local $U-R$, $r_{U-R;hr} = 0.44 \pm 0.32$; these values are also displayed in the corresponding figures. These r values suggest tentative correlations between the Hubble residual and local properties, i.e. siblings with the largest difference in local mass or local $U-R$ have the largest difference in Hubble residual. This indicates that SNe in the same galaxy are not as similar as perhaps it was thought they were, given that this analysis is independent of the global galaxy properties, and so highlights the need for local corrections in cosmology. Simply correcting for global host parameters may not encompass the relationships seen here, as each sibling in a pair would be corrected in the same way.

TABLE 6.4: Differences between SN and local environmental properties for the sibling pairs.

SN Properties							
SN		Hubble Residual		x_1		c	
SN_1	SN_2	Difference	$\sigma_{difference}$	Difference	$\sigma_{difference}$	Difference	$\sigma_{difference}$
DES13S2dlj	DES14S2pkz	0.250±0.085	2.95	0.707±0.269	2.63	0.106±0.036	2.94
DES14C3zym	DES15C3edd	0.090±0.099	0.91	0.190±0.219	0.87	0.020±0.042	0.47
DES14C2iku	DES17C2jjb	0.370±0.244	1.52	1.928±1.063	1.81	0.420±0.110	3.81
DES15S2okk	DES17S2alm	0.530±0.192	2.76	1.131±0.898	1.26	0.010±0.050	0.20
DES15C2mky	DES16C2cqh	0.350±0.197	1.77	1.667±0.878	1.90	0.100±0.036	2.77
DES13E1wu	DES14E1uti	0.550±0.327	1.68	3.842±2.212	1.74	0.080±0.072	1.11
$DES16C3nd_0$	$DES16C3nd_1$	0.160±0.135	1.19	0.628±0.403	1.56	0.030±0.050	0.60
DES15X2mlr	DES15X2nku	0.450±0.278	1.62	2.340±1.176	1.99	0.100±0.078	1.28

Local Environment Properties					
SN		Local Mass		Local U-R	
SN_1	SN_2	Difference	$\sigma_{difference}$	Difference	$\sigma_{difference}$
DES13S2dlj	DES14S2pkz	0.759±0.092	8.25	0.253±0.132	1.91
DES14C3zym	DES15C3edd	0.411±0.096	4.25	2.162±7.45	0.29
DES14C2iku	DES17C2jjb	0.728±0.240	3.04	0.356±0.303	1.18
DES15S2okk	DES17S2alm	0.637±0.104	6.15	0.659±0.141	4.64
DES15C2mky	DES16C2cqh	1.174±0.192	6.12	0.014±0.387	0.035
DES13E1wu	DES14E1uti	1.075±0.867	1.24	0.491±0.840	0.59
$DES16C3nd_0$	$DES16C3nd_1$	0.009±0.207	0.04	0.010±0.292	0.04
DES15X2mlr	DES15X2nku	0.561±0.240	2.34	0.438±0.392	1.12

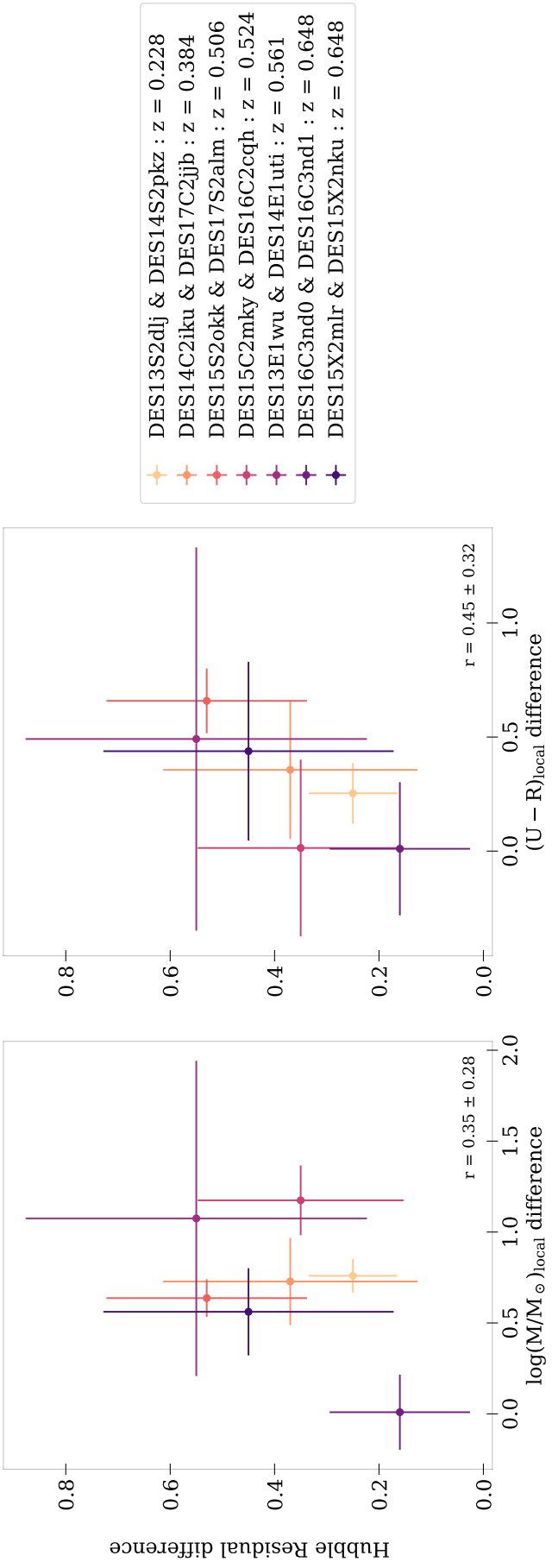

FIGURE 6.2: Comparison of local environmental properties (M_{stellar} and $U-R$) with Hubble residuals. Differences refer to absolute differences between SN_1 and SN_2, error bars are calculated in quadrature. Colours correspond to the sibling pair and host galaxy redshift. As outlined in Section 6.2.1, the error bars do not include intrinsic dispersion.

6.3.1.2 x_1

I repeat the analysis but using x_1 in place of Hubble residual, once again estimating r values using the Monte Carlo technique. From Figure 6.3 again by eye there is a clear correlation between x_1 and the properties, which correspond numerically to $r_{m;x_1} = 0.40 \pm 0.30$ for the local mass and $r_{U-R;x_1} = 0.23 \pm 0.41$ for the local $U - R$. With better constraints, I expect that this value would increase for $U - R$ as it is heavily dominated by the large uncertainties, particularly for the DES13E1wu and DES14E1uti pair.

There is a known correlation between global M_{stellar} and SN x_1 (Smith et al., 2020b), so the trend seen here with the differences in local mass may simply be capturing that trend. However, local mass gives a good understanding of the stellar density in the region around each SN, so may act as a proxy for stellar age. Similarly, given that rest-frame $U - R$ covers the largest wavelength range covered by the DES-SN *griz* photometry, it covers both the old stars and passive galaxies at the red end, and the younger, hotter, more star-forming at the blue end, providing a good indication of the age. Thus the plots could be interpreted that the siblings with the largest difference in age have the largest difference in x_1. This matches well with the observed relation between stellar age and x_1 (Rigault et al., 2013, 2020; Rose et al., 2019; Nicolas et al., 2021).

6.3.1.3 c

Once again, the analysis is repeated for c. Somewhat surprisingly, particularly given the focus of the previous chapters on the relationship between c and environmental properties, there is no clear correlation here for the differences between the sibling pairs, shown in Figure 6.4. For local mass difference, I obtain $r_{m;c} = 0.17 \pm 0.17$ and $r_{U-R;c} = -0.01 \pm 0.24$ for the local $U - R$.

The trend seems to be dependent on the potentially outlying sibling pair consisting of DES14C2iku and DES17C2jjb. Interestingly, from Scolnic et al. (2020), when the sibling data was classified using PSNID, this pair returned redshifts that were $\Delta z > 0.1$ different from one another, and different from their host galaxy redshift, questioning their validity as siblings. In addition, DES14C2iku has $c > 0.3$, which would mean it would be cut from a typical cosmological analysis. However, the pair passed the Scolnic et al. (2020) classification criteria, had large uncertainties, and removing them would not change the conclusion of that analysis. This is a problem with such a small set of siblings in our analysis: is this pair truly an outlier? Or if the sample was larger, would there be more pairs that occupy this parameter space, and would this alter potential trends?

If I remove this sibling pair and calculate the r values again, I obtain $r_{m;c} = 0.41 \pm 0.27$ for the local mass and $r_{U-R;c} = -0.18 \pm 0.33$ for the local $U - R$, with clearer

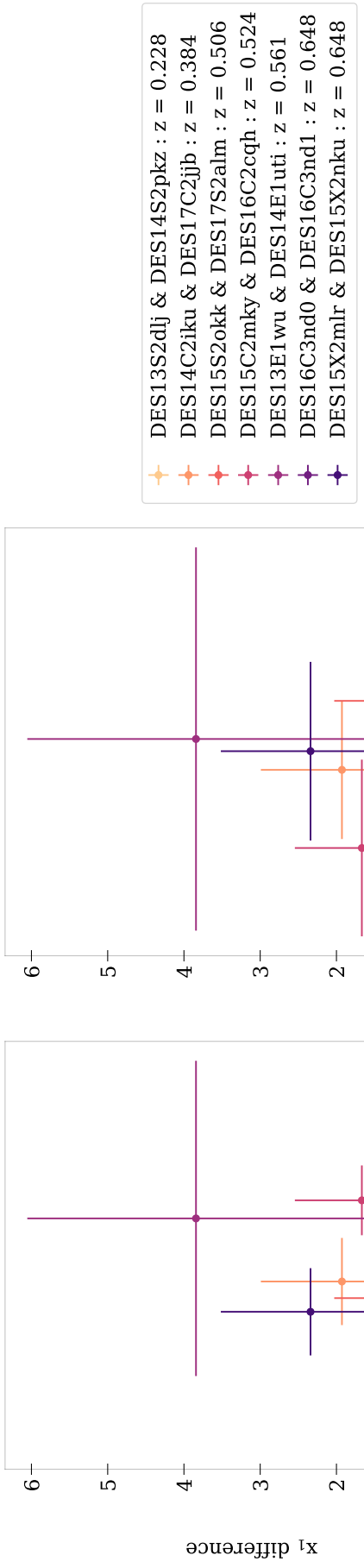

FIGURE 6.3: Comparison of local environmental properties (M_{stellar} and $U - R$) with x_1. Differences refer to absolute differences between SN_1 and SN_2, error bars are calculated in quadrature. Colours correspond to the sibling pair and host galaxy redshift.

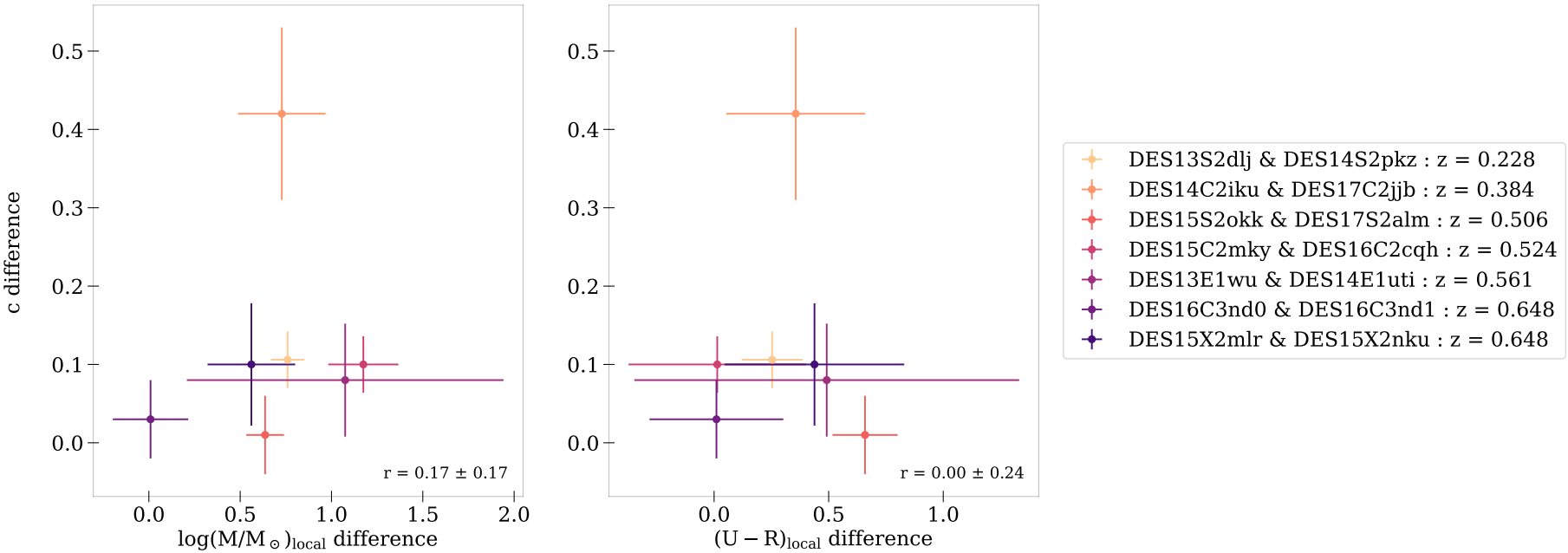

FIGURE 6.4: Comparison of local environmental properties (M_{stellar} and $U - R$) with c. Differences refer to absolute differences between SN_1 and SN_2, error bars are calculated in quadrature. Colours correspond to the sibling pair and host galaxy redshift.

correlations displayed in Figure 6.5. This change is quite large for local mass (and now is on the same order as the correlation with x_1 and local M_{stellar}), and points to a correlation with c. SNe Ia in the same host galaxies with the most differing local M_{stellar} regions have the largest difference in c. As c is known to be connected with dust, this is likely indicative of differing dust properties or amounts at different locations within the SNe host galaxies. For $U - R$ things are less clear, with the correlations being dominated by the size of the uncertainties. As this sibling pair is not an outlier in the parameter space of Hubble residual or x_1, removing it does not have a dramatic effect on the r values there.

6.4 Interpretation and Conclusion

From this brief analysis of the local properties of SNe Ia siblings and how they compare to the SN properties, it is clear that they are a vital tool in understanding the remaining dispersion in SNe Ia luminosities.

From this analysis, I have found that when looking at the differences between local environment properties compared to the difference in SN properties for the eight sibling pairs in DES5YR, all correlations are positive - i.e. the larger the difference in local environment properties between SNe Ia in the same galaxy, the larger the difference in their SN properties of Hubble residual, x_1 and c. However, I note that the uncertainties on these measurements are very large. Throughout this sibling analysis, the errors on the difference are simply the errors of the individual siblings combined in quadrature, and there are likely correlations and covariances that have not been taken into account in this simple analysis, particularly given the limited sample size. Furthermore, with a larger sample of siblings I expect that the measurements of these tentative correlations will be more robust.

For the Hubble residual comparisons in particular, given the sibling analysis is independent of the global galaxy properties, such analysis as this can help to determine if using host M_{stellar} alone is enough to account for environmental effects on SNe Ia. My finding that siblings with the largest difference in both local M_{stellar} and $U - R$ have the largest difference in Hubble residual highlights the need for additional local corrections for cosmology, as using global properties alone would mean siblings are corrected for in the same way.

Looking to x_1, my findings match well with known relationships between stellar age and x_1, due to both local M_{stellar} giving an indication of the stellar density and thus acting as a proxy for stellar age, and the local $U - R$ probing both the old stars at the red end of the spectrum and the younger at the blue, again providing a suggestion of stellar age. From Scolnic et al. (2020), I know that all bar one of the sibling pairs are in

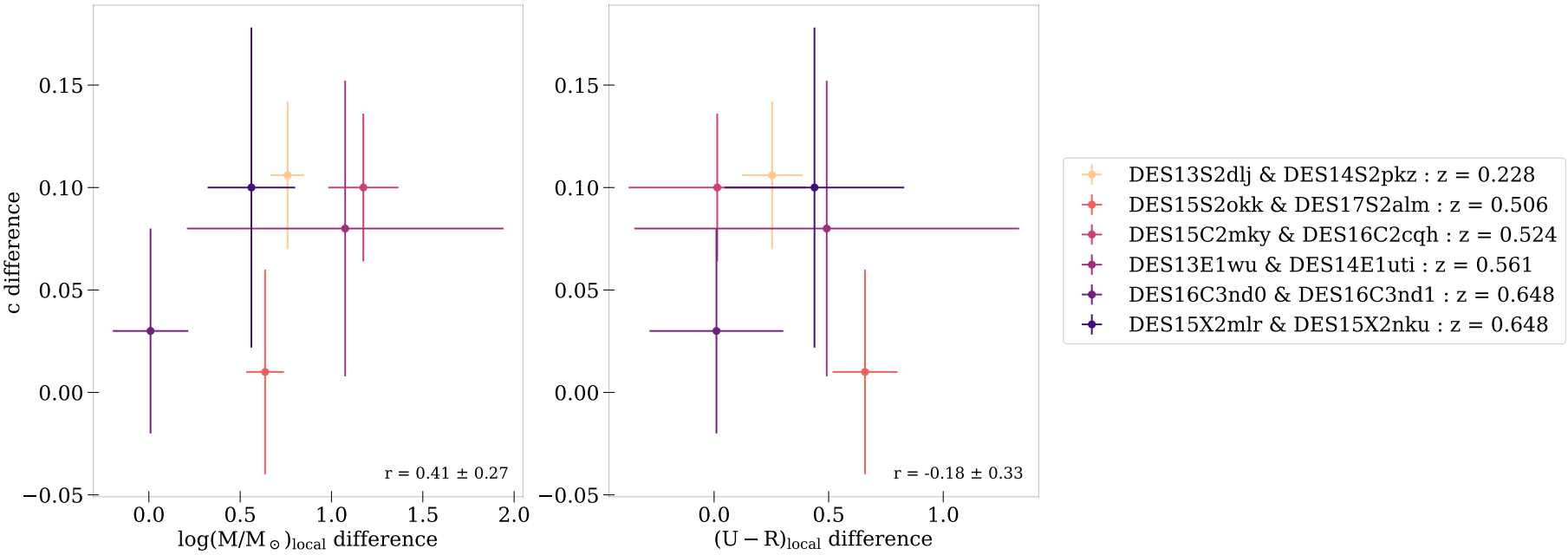

FIGURE 6.5: Comparison of local environmental properties (M_{stellar} and $U - R$) with c, removing the outlier sibling pair: DES14C2iku and DES17C2jjb. Differences refer to absolute differences between SN_1 and SN_2, error bars are calculated in quadrature. Colours correspond to the sibling pair and host galaxy redshift.

high mass (> 10) galaxies, so this x_1-age relation is suggestive of more massive, typically older, passive galaxies having regions of more recent star formation with younger stellar ages. This could cause such a galaxy to host SNe Ia with a range of different x_1 values.

Moving to c, the results were a little surprising as correlations are weaker than for the other parameters, which I interpret as likely due to the potential outlying pair containing a SNe with a high (> 0.3) value for c that would be removed from cosmological analyses. When I remove this sibling pair, the correlation with local M_{stellar} increases, whilst with $U - R$ remains more consistent. With the knowledge from previous chapters and current analysis in the field, this points to the connection between M_{stellar} and dust properties, and suggests that this is not just a global effect for the host galaxies, but one that may change on the local scale.

In addition to these correlations with SN properties, I found that sibling SNe with the largest differences in local M_{stellar} did not also have the largest differences in local $U - R$. This is intriguing as it indicates that the two parameters are relatively independent and so multiple environmental effects may need to be corrected for when SNe Ia are used in cosmology, agreeing with Chapter 5 and Rose et al. (2021a).

As we enter the new era of large high-z surveys, more SNe siblings will be found, with a prediction of ~ 800 pairs in LSST from Scolnic et al. (2020). Other surveys such as ZTF (which currently has a few SN Ia siblings Graham (in prep, see also (Biswas et al., 2021))) and the Young Supernova Experiment (YSE; Jones et al., 2019) will also find further siblings, thus enabling a more detailed and robust analysis of their SN and environmental properties. These studies will add greatly to the ongoing discussion on how best to correct SNe Ia for use in cosmology, and aid in understanding the effects of dust and stellar age, and the differences between global and local host galaxy properties.

Chapter 7

Conclusion

"Blue! Blue! Blue!"
— Patrick Rothfuss, *The Name of the Wind*

In this thesis, I have analysed the effect of environments on type Ia supernovae from the Dark Energy Survey, exploring how these environments impact the properties of the supernovae themselves, and their subsequent standardisation for use in cosmology. By building upon the analysis of global host galaxy properties, I analysed properties within a local aperture around each supernova location to understand how these properties differ. I studied these environmental properties in the DES3YR spectroscopically-confirmed and DES5YR photometrically-confirmed SNe Ia samples, additionally focusing on the intriguing differences found for SNe of different colours. As an example of an additional use of local environment analysis, I investigated the local properties of SNe Ia hosted within the same galaxy. In this final, concluding chapter, I summarise my results, discuss the impact of my analysis and look to the future of such analyses, and make my final remarks.

7.1 Summary of Results

First, I begin by summarising the key results of this thesis.

7.1.1 Environmental Effects in DES3YR

In Chapter 3, I measured the global and local host properties of the DES3YR spectroscopically-confirmed SNe Ia sample, using photometry from the supernova-free stacked images with SED-fitting to obtain the M_{stellar} and rest-frame $U - R$ for the host galaxies and

local apertures at each SN position. These properties were then compared to their light-curve properties and luminosities.

By comparing environmental properties with Hubble residuals, and analysing relationships between them, I was able to compare my findings to the well-studied 'mass step', obtaining steps for local and global M_{stellar} and $U - R$. I found that all the measured steps are significant at $> 3\sigma$, whether using local or global measures, or using M_{stellar} or $U - R$ colour, as is also the case when considering other rest-frame colours and sSFR. I also found that local M_{stellar} steps are larger than global M_{stellar} steps by up to 0.03 mag, which suggests that they may recover more of the remaining dispersion in SNe Ia magnitudes. Both global and local $U - R$ steps were similar in magnitude and larger than the global mass step, suggesting that $U - R$ may be a better probe of the environment than M_{stellar}.

By splitting the sample based on the SN light-curve stretch (x_1) and optical colour (c), I found that the redder objects ($c > 0$) had larger steps in Hubble residual for both M_{stellar} and $U - R$, for both global and local, of ~ 0.14 mag, suggesting that they drive the step size. I also divided my sample by environmental properties and refitted the nuisance parameters α and β, finding mild tension ($\sim 2\sigma$ difference) in α and β across the division point in which smaller β values were observed in higher mass, redder regions (or galaxies). I also found smaller α for low mass, bluer regions, suggesting that the most cosmologically-uniform sample is in actively star-forming, lower-mass galaxies.

Furthermore, through the analysis of the r.m.s. scatter in Hubble residuals, I found that SNe Ia in redder environments had a higher r.m.s. than SNe in bluer environments, with a particularly low r.m.s. scatter for SNe Ia in bluer environments when $c < 0$. This suggests that blue SNe Ia in blue environments present the most homogeneous sample for use in cosmology.

7.1.2 Environmental Effects in DES5YR

In Chapter 4, I repeated my analysis for DES3YR but using a preliminary DES5YR sample of photometrically-confirmed SNe Ia. For this sample, I found that DES5YR has higher global host galaxy M_{stellar} distributions compared to DES3YR, meaning that the median global and local M_{stellar} values for the sample shift to ~ 0.2 dex larger. As redder SNe Ia preferentially explode in more massive galaxies, there is an increase in the number of $c > 0$ (red) SNe in DES5YR.

As in DES3YR, all measured M_{stellar} and rest-frame $U - R$ Hubble residual steps are significant at $> 3\sigma$, with the majority significant at $> 5\sigma$. Unlike DES3YR, the steps for local M_{stellar} are slightly smaller ($< 1\sigma$) than for global M_{stellar}, but this is likely to be due to the large number of SNe in high global M_{stellar} galaxies. As with DES3YR, local and

global $U - R$ steps are similar. This was robust when altering the size of local apertures and adding more restrictive redshift cuts. Trends in r.m.s values are consistent with DES3YR, with the most homogeneous sample in lower mass, bluer regions.

7.1.3 Concerning Colour

In Chapter 5, I split the DES5YR sample into two subsamples for $c < 0$ and $c > 0$, and found that the most statistically significant difference in Hubble residual step between the two subsamples is for global M_{stellar}, consistent with that for DES3YR in Chapter 3. However in contrast to DES3YR, although the step is consistently larger for red SNe Ia than for blue SNe Ia, I only find differences of $\sim 1\sigma$ for all other environmental properties, suggesting that global M_{stellar} has the strongest relationship with SN c. As in DES3YR, I measure the lowest r.m.s. scatter in Hubble residual for blue SNe Ia in low mass or blue environments.

By splitting my sample by environmental property and fitting a two-component c-dependent Hubble residual (i.e. 'high' and 'low' for each environmental property follows a different c-Hubble residual law; a simple approximation of Brout & Scolnic (2021) dust modelling), I was able to remove steps from the data and recover remaining underlying relationships. By doing this for global M_{stellar} I remove the mass step, however a statistically significant (2.9σ) step in local $U - R$ remains, suggesting that dust modelling alone does not fully explain the dispersion in SN luminosity. Combining corrections based on a c-dependent M_{stellar} relation and a relation with $U - R$, a tracer of sSFR and stellar age, may be needed to account for the dispersion in SNe Ia luminosity.

7.1.4 Local Environments of Supernova Siblings

As an additional use case for my local photometry, in Chapter 6 I investigated the local properties of SNe Ia siblings in DES. Siblings have the same host galaxy cosmological corrections, and thus they provide an excellent sample to investigate the benefits of local corrections.

When looking at the differences between local environmental properties compared to the difference in SN properties for each pair of siblings, all correlations were positive: the larger the difference in local environment properties between SNe Ia in the same galaxy, the larger their differences in Hubble residual, x_1 and c. However, the sample size is small so uncertainties dominate.

My findings highlight the need for additional local corrections for the best standardisation in cosmology. The correlations with x_1 match well with known relationships with stellar age given both local M_{stellar} and $U - R$ are linked to this property. As the large

majority of the pairs are in high mass galaxies, this relation suggests that more massive, older, passive galaxies have regions of more recent star formation with younger stellar ages, causing it to host SNe Ia with a range of different x_1, local M_{stellar} and $U-R$ values. Correlations with c were weaker, but suggestive of a link between M_{stellar} and c, echoing the findings of previous chapters.

7.2 Impact

The analysis undertaken in this thesis has added to the ongoing discussion about the effect of environment on SNe Ia cosmology, and helped to uncover new insights that will aid the future direction of such analyses. As a main astrophysical systematic in modern SN cosmology, environmental effects are vital to take into account and to understand as we progress to higher precision cosmology. To illustrate my key findings with regards to the Hubble residual steps, I present in Figure 7.1 the steps for M_{stellar} and rest-frame $U-R$ colour from this thesis, both globally and locally, compared to literature values[1].

My results are consistent with literature findings, and the small error bars highlight the quality of the DES3YR and DES5YR samples. Additionally the nature of DES5YR, with the size, redshift coverage, and photometric classification, means that it acts as a testing-ground for the next generation of large scale SNe surveys. Hence my results provide for an excellent comparison for what we may expect from these future surveys.

Of particular importance is my work investigating differences when splitting on SN x_1 and c. I uncovered direct observational evidence that SNe Ia in redder (and presumably more passive or dustier) galaxies have a higher r.m.s. scatter in their Hubble residuals, suggesting that SNe Ia in bluer galaxies provide a more homogeneous sample. I also found that redder SNe ($c > 0$) exhibit larger environmental steps, whilst the bluer SNe were more homogeneous. My findings confirm that the most cosmologically-uniform sample are blue supernovae found in actively star-forming, lower-mass galaxies. This finding has significant cosmological implications, especially as we enter an era of large surveys and are no longer limited by sample statistics. This finding will impact future cosmological studies, as the homogeneity of blue SNe in low mass or blue environments suggests that it may be most convenient to only use those for precision cosmology. However, to understand the astrophysical cause of the remaining dispersion in SNe Ia luminosities, my work indicates that combining corrections may help to provide the answers.

[1] Kelly et al. (2010); Lampeitl et al. (2010); Sullivan et al. (2010); D'Andrea et al. (2011); Gupta et al. (2011); Childress et al. (2013); Rigault et al. (2013); Betoule et al. (2014); Pan et al. (2014); Scolnic et al. (2014); Jones et al. (2015); Rigault et al. (2015); Campbell et al. (2016); Wolf et al. (2016); Uddin et al. (2017); Jones et al. (2018a,b); Kim et al. (2018); Roman et al. (2018); Scolnic et al. (2018); Brout et al. (2019b); Kim et al. (2019); Rose et al. (2019); Ponder et al. (2020); Rigault et al. (2020); Smith et al. (2020b); Uddin et al. (2020); Johansson et al. (2021); Thorp et al. (2021)

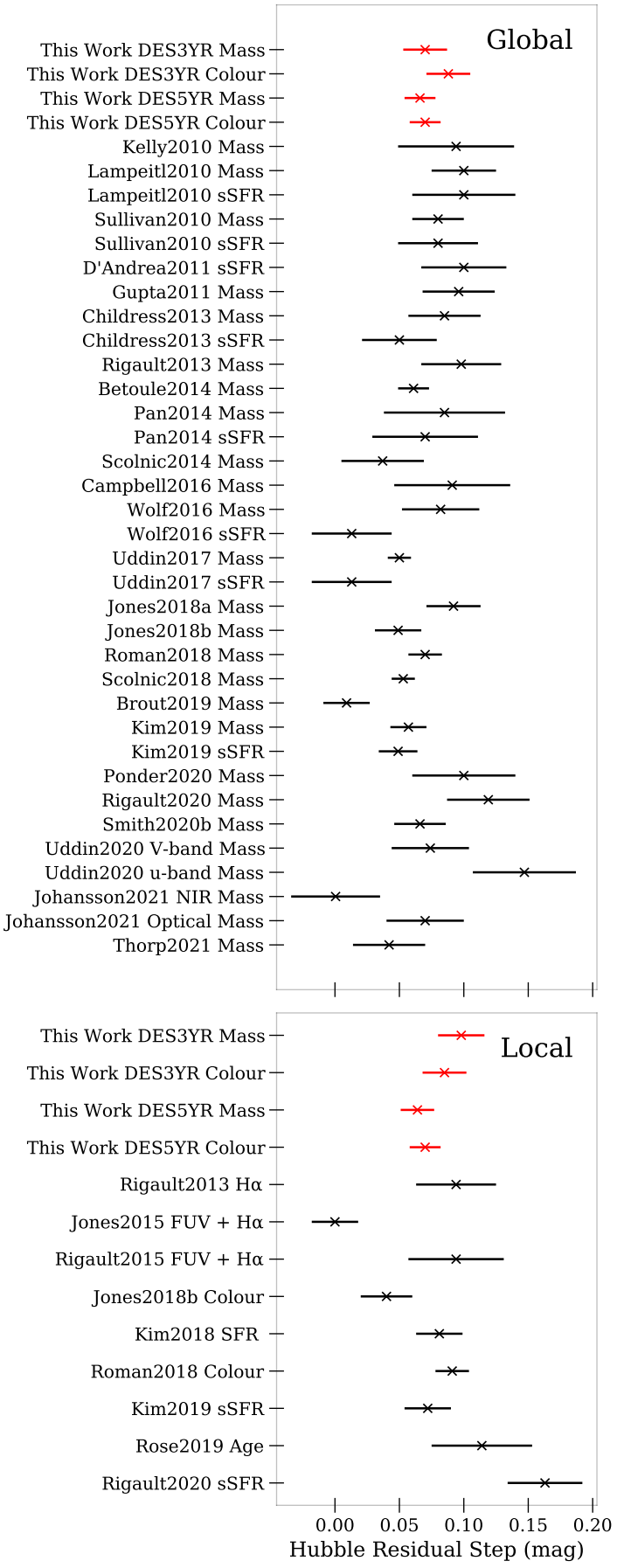

FIGURE 7.1: Comparison of Hubble Residual differences in this thesis and literature analyses. If literature studies used multiple light-curve fitters, I present here the step measured using SALT2 for consistency.

7.3 Future Perspectives

Despite the progress in the field of SNe host galaxy studies, there are still open questions and considerable unknowns to be addressed as we move forward in the next generation of large supernova surveys. Whilst DES has fantastic redshift coverage and photometric calibration, it will be dwarfed by the number of SNe Ia found by LSST on the Vera C. Rubin Observatory (Ivezić et al., 2019), and the Nancy Grace Roman Space Telescope (Hounsell et al., 2018). As an example, LSST is expected to find $\sim 50,000$ SNe Ia per year to a redshift of $z = 0.8$, with Roman finding $\sim 10,000$ but to higher redshifts ($z > 2$) (Rose et al., 2021b). Given the number of SNe Ia detected, obtaining spectroscopy for each of their host galaxies will be difficult, meaning that photometric measurements of their environmental properties, such as that undertaken in this thesis, will be increasingly important. The greater sample size of these surveys will enable further study of the relationships between environmental properties and SN properties, to understand how best to standardise SNe Ia for use in cosmology. Such surveys will also aid in further understanding the impact that SNe Ia environmental properties have on measurements of H_0, providing information that may help resolve the Hubble Tension (Rigault et al., 2015, 2020).

Upcoming analyses are also primed to observe in a wide range of wavelengths, including in the NIR. Studying SNe Ia and their galactic environments at this wavelength allows for constraints on dust, and may help to disentangle the complicated relationship between dust and intrinsic colour (Ponder et al., 2020; Uddin et al., 2020; Mandel et al., 2020; Brout & Scolnic, 2021).

The larger sample size afforded by the next generation of surveys will allow for further analysis through splitting the sample by SN property to investigate in more depth the finding that bluer SNe (and particularly those in low mass, bluer environments) are more homogeneous and thus better standard candles (Foley & Kasen, 2011; Gonzalez-Gaitan et al., 2020; Brout & Scolnic, 2021; Kelsey et al., 2021, Chapter 3). In particular, this will also enable further study of the tentative finding of a two-component colour-luminosity (dust) relation when split on SNe properties (Brout & Scolnic, 2021; Gonzalez-Gaitan et al., 2020, Chapter 5). This will provide further evidence of the underlying cause of the observed SNe Ia intrinsic scatter, and elucidate if it is due to dust, age, a combination of the two, or something else entirely.

In addition, with the next generation of surveys, SNe Ia siblings will be more frequently found, with an estimation of $\sim$ 800 sibling pairs in LSST (Scolnic et al., 2020). This will allow for more rigorous analysis of their local properties compared to global host galaxy parameters. This would be an intriguing avenue of study, and something that I would be keen to remain involved in, enabling the improvement of systematics and a greater understanding of the potential causes of the remaining dispersion. As SNe Ia in the same host galaxy have the same global parameters, SNe Ia siblings can determine

if using host M_{stellar} alone is enough to account for environmental effects on SNe Ia, or if local properties, or a combination of the two, gives better standardisation.

Linked to this, in future analyses, it would also be beneficial to investigate further applying multiple environmental corrections to SNe Ia luminosities. As studied in detail in Rose et al. (2021a), and inferred through the analysis in Chapter 5, combining corrections based on a c-dependent global M_{stellar} relation and local age (or a proxy of age), may improve the standardisation of SNe Ia for use in cosmology. It would be of interest to understand whether making such a correction, or simply restricting SNe Ia cosmological studies to only include the blue SNe Ia located in low mass, blue environments gives the best standardisation.

7.4 Closing Remarks

As key cosmological probes, SNe Ia are of vital importance for our understanding of the evolution of the universe. Alongside this, the nature of their own stellar evolution into powerful explosions means that they are objects of fascinating astrophysical study. The observed relationships between their SN and host environment properties only adds to this intrigue, as the findings both affect cosmology and add to our knowledge of the astrophysical causes of these transients. Studying environmental properties allows for a range of important analyses, including the investigation of SNe Ia progenitors, the impact of dust, and providing improved standardisation techniques for the next generation of modern cosmological surveys. SNe Ia and their environments will remain major topics of astrophysical and cosmological research for many years to come.

Appendix A

Seeing-optimised Image Stack Parameters

TABLE A.1: Seeing-optimised image stack parameters.

Field[1]	Band[2]	MY[3]	N_{exp}[4]	$t_{\mathrm{exp;tot}}$[5]	m_{lim}[6]
SN-E1	g	1	7	0.34	26.25
SN-E1	g	2	3	0.15	25.06
SN-E1	g	3	6	0.29	26.24
SN-E1	g	4	5	0.24	26.17
SN-E1	g	5	7	0.34	26.25
SN-E1	r	1	22	0.92	25.86
SN-E1	r	2	14	0.58	25.71
SN-E1	r	3	19	0.79	25.83
SN-E1	r	4	15	0.62	25.91
SN-E1	r	5	18	0.75	25.78
SN-E1	i	1	33	1.83	25.85
SN-E1	i	2	23	1.28	25.75
SN-E1	i	3	24	1.33	25.84
SN-E1	i	4	25	1.39	25.61
SN-E1	i	5	27	1.50	25.81
SN-E1	z	1	83	4.61	25.80
SN-E1	z	2	54	3.00	25.55
SN-E1	z	3	65	3.61	25.85
SN-E1	z	4	61	3.39	25.80
SN-E1	z	5	69	3.83	25.79
SN-E2	g	1	11	0.53	26.37

Continued on next page

Table A.1 – continued from previous page

Field[1]	Band[2]	MY[3]	N_{exp}[4]	$t_{\mathrm{exp;tot}}$[5]	m_{lim}[6]
SN-E2	g	2	7	0.34	26.19
SN-E2	g	3	8	0.39	26.20
SN-E2	g	4	8	0.39	26.29
SN-E2	g	5	10	0.49	26.37
SN-E2	r	1	24	1.00	26.11
SN-E2	r	2	14	0.58	26.13
SN-E2	r	3	20	0.83	25.78
SN-E2	r	4	19	0.79	26.11
SN-E2	r	5	19	0.79	26.01
SN-E2	i	1	39	2.17	25.86
SN-E2	i	2	26	1.44	25.89
SN-E2	i	3	29	1.61	25.78
SN-E2	i	4	31	1.72	25.88
SN-E2	i	5	31	1.72	25.93
SN-E2	z	1	92	5.11	25.96
SN-E2	z	2	63	3.50	25.79
SN-E2	z	3	72	4.00	25.95
SN-E2	z	4	69	3.83	25.87
SN-E2	z	5	72	4.00	25.88
SN-S1	g	1	9	0.44	26.33
SN-S1	g	2	7	0.34	26.19
SN-S1	g	3	7	0.34	26.28
SN-S1	g	4	6	0.29	26.31
SN-S1	g	5	7	0.34	26.20
SN-S1	r	1	22	0.92	26.15
SN-S1	r	2	19	0.79	26.17
SN-S1	r	3	17	0.71	26.12
SN-S1	r	4	16	0.67	26.17
SN-S1	r	5	14	0.58	26.00
SN-S1	i	1	34	1.89	25.80
SN-S1	i	2	25	1.39	25.95
SN-S1	i	3	27	1.50	25.88
SN-S1	i	4	26	1.44	25.67
SN-S1	i	5	24	1.33	25.70
SN-S1	z	1	69	3.83	25.68
SN-S1	z	2	52	2.89	25.56
SN-S1	z	3	55	3.06	25.70

Continued on next page

Table A.1 – continued from previous page

Field[1]	Band[2]	MY[3]	N_{exp}[4]	$t_{\mathrm{exp;tot}}$[5]	m_{lim}[6]
SN-S1	z	4	49	2.72	25.65
SN-S1	z	5	51	2.83	25.57
SN-S2	g	1	9	0.44	25.83
SN-S2	g	2	7	0.34	25.87
SN-S2	g	3	7	0.34	25.88
SN-S2	g	4	7	0.34	25.95
SN-S2	g	5	6	0.29	25.79
SN-S2	r	1	19	0.79	25.76
SN-S2	r	2	12	0.50	25.86
SN-S2	r	3	15	0.62	25.87
SN-S2	r	4	16	0.67	25.92
SN-S2	r	5	14	0.58	25.78
SN-S2	i	1	30	1.67	25.44
SN-S2	i	2	21	1.17	25.60
SN-S2	i	3	25	1.39	25.60
SN-S2	i	4	23	1.28	25.19
SN-S2	i	5	21	1.17	25.40
SN-S2	z	1	66	3.67	25.53
SN-S2	z	2	45	2.50	25.28
SN-S2	z	3	55	3.06	25.67
SN-S2	z	4	50	2.78	25.56
SN-S2	z	5	48	2.67	25.55
SN-C1	g	1	14	0.68	26.21
SN-C1	g	2	12	0.58	26.28
SN-C1	g	3	9	0.44	26.34
SN-C1	g	4	12	0.58	26.05
SN-C1	g	5	9	0.44	26.10
SN-C1	r	1	27	1.12	26.13
SN-C1	r	2	20	0.83	26.10
SN-C1	r	3	21	0.88	26.19
SN-C1	r	4	22	0.92	25.84
SN-C1	r	5	18	0.75	26.01
SN-C1	i	1	39	2.17	26.12
SN-C1	i	2	27	1.50	25.85
SN-C1	i	3	31	1.72	26.22
SN-C1	i	4	34	1.89	26.10
SN-C1	i	5	25	1.39	26.00

Continued on next page

Table A.1 – continued from previous page

Field[1]	Band[2]	MY[3]	N_{exp}[4]	$t_{\mathrm{exp;tot}}$[5]	m_{lim}[6]
SN-C1	z	1	100	5.56	25.90
SN-C1	z	2	68	3.78	25.73
SN-C1	z	3	84	4.67	25.90
SN-C1	z	4	80	4.44	25.90
SN-C1	z	5	68	3.78	25.91
SN-C2	g	1	17	0.83	26.10
SN-C2	g	2	12	0.58	26.23
SN-C2	g	3	12	0.58	26.09
SN-C2	g	4	13	0.63	26.05
SN-C2	g	5	14	0.68	26.11
SN-C2	r	1	32	1.33	25.98
SN-C2	r	2	25	1.04	26.00
SN-C2	r	3	24	1.00	25.86
SN-C2	r	4	25	1.04	25.87
SN-C2	r	5	22	0.92	25.92
SN-C2	i	1	46	2.56	25.75
SN-C2	i	2	33	1.83	25.69
SN-C2	i	3	37	2.06	25.62
SN-C2	i	4	37	2.06	25.64
SN-C2	i	5	31	1.72	25.61
SN-C2	z	1	101	5.61	25.76
SN-C2	z	2	71	3.94	25.73
SN-C2	z	3	83	4.61	25.79
SN-C2	z	4	81	4.50	25.73
SN-C2	z	5	72	4.00	25.75
SN-C3	g	1	52	2.89	26.82
SN-C3	g	2	35	1.94	26.84
SN-C3	g	3	42	2.33	26.80
SN-C3	g	4	41	2.28	26.31
SN-C3	g	5	38	2.11	26.66
SN-C3	r	1	87	9.67	26.74
SN-C3	r	2	69	7.67	26.86
SN-C3	r	3	65	7.22	26.85
SN-C3	r	4	70	7.78	26.23
SN-C3	r	5	57	6.33	26.70
SN-C3	i	1	215	21.50	26.69
SN-C3	i	2	153	15.30	26.47

Continued on next page

Table A.1 – continued from previous page

Field[1]	Band[2]	MY[3]	N_{exp}[4]	$t_{\mathrm{exp;tot}}$[5]	m_{lim}[6]
SN-C3	i	3	184	18.40	26.67
SN-C3	i	4	163	16.30	26.48
SN-C3	i	5	161	16.10	26.62
SN-C3	z	1	567	51.98	26.13
SN-C3	z	2	448	41.07	26.04
SN-C3	z	3	433	39.69	25.86
SN-C3	z	4	431	39.51	26.08
SN-C3	z	5	389	35.66	26.07
SN-X1	g	1	9	0.44	25.59
SN-X1	g	2	6	0.29	25.62
SN-X1	g	3	7	0.34	25.85
SN-X1	g	4	8	0.39	25.76
SN-X1	g	5	6	0.29	26.26
SN-X1	r	1	17	0.71	25.84
SN-X1	r	2	11	0.46	25.85
SN-X1	r	3	13	0.54	25.94
SN-X1	r	4	13	0.54	25.45
SN-X1	r	5	14	0.58	25.60
SN-X1	i	1	26	1.44	25.69
SN-X1	i	2	18	1.00	25.51
SN-X1	i	3	22	1.22	25.82
SN-X1	i	4	19	1.06	25.68
SN-X1	i	5	19	1.06	25.64
SN-X1	z	1	65	3.61	25.53
SN-X1	z	2	47	2.61	25.64
SN-X1	z	3	53	2.94	25.52
SN-X1	z	4	47	2.61	25.93
SN-X1	z	5	48	2.67	25.58
SN-X2	g	1	7	0.34	25.98
SN-X2	g	2	6	0.29	25.98
SN-X2	g	3	4	0.19	26.04
SN-X2	g	4	6	0.29	25.87
SN-X2	g	5	5	0.24	26.31
SN-X2	r	1	19	0.79	26.15
SN-X2	r	2	17	0.71	25.85
SN-X2	r	3	14	0.58	26.14
SN-X2	r	4	17	0.71	26.03

Continued on next page

Table A.1 – continued from previous page

Field[1]	Band[2]	MY[3]	N_{exp}[4]	$t_{exp;tot}$[5]	m_{lim}[6]
SN-X2	r	5	13	0.54	25.88
SN-X2	i	1	31	1.72	25.72
SN-X2	i	2	26	1.44	25.64
SN-X2	i	3	24	1.33	25.86
SN-X2	i	4	27	1.50	25.80
SN-X2	i	5	20	1.11	25.58
SN-X2	z	1	88	4.89	25.44
SN-X2	z	2	68	3.78	25.94
SN-X2	z	3	72	4.00	25.49
SN-X2	z	4	70	3.89	25.23
SN-X2	z	5	62	3.44	25.30
SN-X3	g	1	15	0.83	26.23
SN-X3	g	2	11	0.61	26.12
SN-X3	g	3	12	0.67	26.17
SN-X3	g	4	10	0.56	26.14
SN-X3	g	5	12	0.67	26.04
SN-X3	r	1	59	6.56	26.46
SN-X3	r	2	43	4.78	26.54
SN-X3	r	3	46	5.11	26.61
SN-X3	r	4	45	5.00	26.31
SN-X3	r	5	43	4.78	26.41
SN-X3	i	1	141	14.10	26.05
SN-X3	i	2	100	10.00	25.83
SN-X3	i	3	119	11.90	25.99
SN-X3	i	4	112	11.20	26.06
SN-X3	i	5	92	9.20	26.05
SN-X3	z	1	441	40.42	25.62
SN-X3	z	2	325	29.79	25.76
SN-X3	z	3	366	33.55	25.77
SN-X3	z	4	345	31.62	25.75
SN-X3	z	5	311	28.51	25.71

[1] SN field.

[2] Filter band.

[3] 'Minus Year' missing season, subtracted to remove contamination from SN light.

[4] Number of single exposures in each coadd.

[5] Total exposure time given in hours.

[6] Limiting magnitude determined from the sky background.

Appendix B

Environmental Properties for DES3YR

The below table contains the SNID, SALT2 c and x_1 parameters, Hubble residual, and the global and local M_{stellar} and $U - R$ measurements for the DES3YR sample used in this analysis, and published in Kelsey et al. (2021).

As the DES5YR sample used in this analysis is preliminary, and the final version has not yet been published by the collaboration, individual SNID properties and cosmological values for that sample are not detailed here.

TABLE B.1: SNe and environment properties of the DES3YR sample.

SNID	Global Mass	Global U-R	Local Mass	Local U-R	x_1	c	Hubble Residual
1248677	9.608±0.015	0.532±0.014	8.145±0.122	0.275±0.113	1.002±0.114	-0.111±0.022	0.038±0.029
1250017	8.824±0.045	0.584±0.051	8.223±0.050	0.399±0.055	0.952±0.155	-0.092±0.026	0.050±0.023
1253039	9.432±0.065	0.813±0.053	8.132±0.192	0.852±0.174	0.351±0.270	-0.097±0.028	0.060±0.042
1253101	8.607±0.076	0.757±0.113	7.959±0.126	0.078±0.136	1.434±0.377	0.014±0.033	-0.038±0.043
1253920	9.467±0.017	1.524±0.019	9.284±0.047	1.427±0.085	-0.733±0.138	-0.084±0.028	-0.115±0.024
1255502	10.734±0.013	1.487±0.023	9.314±0.087	1.044±0.149	1.110±0.298	-0.060±0.046	-0.162±0.033
1257366	10.752±0.042	1.230±0.086	9.506±0.023	0.898±0.066	-0.190±0.485	0.116±0.041	0.079±0.039
1257695	9.716±0.026	0.530±0.028	8.403±0.063	0.448±0.087	0.346±0.093	-0.116±0.025	0.035±0.022
1258906	8.971±0.024	0.474±0.024	8.555±0.044	0.607±0.048	-0.016±0.314	0.003±0.036	0.053±0.038
1258940	10.821±0.025	1.197±0.015	8.670±0.055	0.793±0.049	-0.109±0.391	-0.106±0.037	0.091±0.044
1259412	10.417±0.012	0.815±0.014	8.938±0.045	0.579±0.046	0.849±0.148	-0.040±0.027	-0.008±0.030
1261579	11.193±0.017	1.656±0.014	8.887±0.037	1.394±0.053	-0.167±0.118	-0.006±0.023	-0.199±0.029
1263369	10.448±0.012	1.075±0.014	9.452±0.030	1.114±0.036	0.164±0.271	-0.089±0.031	0.027±0.033
1263715	8.715±0.051	0.462±0.041	8.436±0.078	0.477±0.066	0.414±0.280	-0.060±0.032	0.012±0.032
1275946	7.967±0.081	0.892±0.167	7.387±0.118	0.163±0.131	1.670±0.172	-0.059±0.027	0.095±0.028
1279500	9.705±0.009	0.948±0.017	8.950±0.054	1.082±0.086	0.688±0.167	-0.027±0.025	0.097±0.028
1280217	8.354±0.091	0.437±0.096	7.724±0.051	0.369±0.137	1.960±0.608	0.087±0.035	0.006±0.048
1281668	9.960±0.012	0.843±0.015	9.091±0.050	0.797±0.038	0.132±0.276	-0.112±0.031	0.072±0.035
1281886	9.407±0.017	0.998±0.038	9.175±0.043	0.898±0.057	1.187±0.426	-0.040±0.041	0.110±0.046
1282736	10.514±0.029	1.206±0.014	9.596±0.039	1.236±0.061	-0.774±0.426	0.094±0.044	-0.155±0.046

Continued on next page

Table B.1 – continued from previous page

SNID	Global Mass	Global U-R	Local Mass	Local U-R	x_1	c	Hubble Residual
1282757	10.159±0.017	0.623±0.018	8.503±0.063	0.518±0.068	2.753±0.227	-0.093±0.029	0.014±0.031
1283373	10.423±0.060	1.704±0.032	9.993±0.101	1.691±0.060	-1.070±0.262	-0.047±0.033	0.127±0.029
1283878	11.242±0.014	1.715±0.014	10.504±0.072	1.841±0.061	-0.833±0.482	-0.014±0.049	0.004±0.047
1283936	9.617±0.029	0.759±0.018	9.182±0.047	0.766±0.045	0.044±0.611	0.188±0.059	0.095±0.058
1284587	10.506±0.015	1.275±0.029	9.338±0.043	1.160±0.138	-0.388±0.435	0.292±0.060	0.194±0.048
1285317	8.529±0.064	-0.085±0.123	8.101±0.048	-0.415±0.101	0.037±0.556	-0.062±0.042	-0.046±0.058
1286398	10.416±0.037	1.336±0.038	10.052±0.120	1.775±0.118	-1.837±0.225	-0.042±0.043	0.101±0.032
1287626	8.224±0.066	0.458±0.110	7.480±0.036	0.833±0.288	0.040±0.423	-0.001±0.031	-0.207±0.037
1289288	10.612±0.011	1.298±0.015	10.213±0.032	1.263±0.039	-1.097±0.517	0.093±0.045	-0.140±0.046
1289555	9.042±0.039	0.249±0.060	8.546±0.041	0.080±0.081	0.356±0.520	-0.129±0.045	0.010±0.064
1289600	9.474±0.019	0.457±0.017	8.667±0.046	0.249±0.035	1.286±0.273	0.043±0.028	0.257±0.038
1289656	8.551±0.103	0.237±0.253	7.815±0.097	0.308±0.114	-0.033±0.574	-0.038±0.050	0.010±0.066
1289664	7.910±0.171	0.534±0.243	7.193±0.095	-0.164±0.121	-1.079±0.187	-0.035±0.028	-0.116±0.030
1290816	8.775±0.021	0.687±0.036	8.155±0.091	0.515±0.109	1.370±0.256	0.010±0.027	0.221±0.027
1291080	8.705±0.090	0.984±0.164	8.471±0.074	1.292±0.259	-1.568±0.683	0.016±0.047	-0.155±0.065
1291090	9.410±0.047	0.291±0.029	8.974±0.068	0.446±0.050	1.239±0.231	-0.082±0.032	0.055±0.033
1291794	10.604±0.044	1.359±0.014	9.436±0.039	1.260±0.055	0.133±0.485	-0.005±0.038	-0.079±0.046
1292145	9.140±0.061	0.746±0.067	8.648±0.083	0.618±0.100	0.711±0.685	0.117±0.060	0.186±0.080
1292332	10.192±0.046	1.722±0.026	10.024±0.099	1.693±0.061	0.272±0.247	-0.107±0.035	-0.035±0.035
1292336	9.116±0.013	1.044±0.028	8.918±0.030	0.880±0.055	-0.149±0.242	0.053±0.033	-0.015±0.031
1292560	8.604±0.028	0.407±0.040	8.242±0.091	0.458±0.112	0.307±0.160	-0.115±0.028	0.081±0.027

Continued on next page

Table B.1 – continued from previous page

SNID	Global Mass	Global U-R	Local Mass	Local U-R	x_1	c	Hubble Residual
1293319	9.103±0.026	0.621±0.025	8.177±0.063	0.911±0.122	1.750±0.285	-0.001±0.031	-0.011±0.033
1293758	10.743±0.024	1.268±0.045	9.050±0.064	0.956±0.184	-1.312±0.178	-0.026±0.039	-0.010±0.031
1294014	9.202±0.018	0.198±0.014	8.312±0.043	0.329±0.056	0.521±0.394	-0.052±0.042	-0.043±0.044
1294743	10.292±0.012	0.981±0.014	9.441±0.062	1.061±0.064	-0.388±0.399	0.209±0.039	-0.125±0.038
1295027	10.057±0.014	0.904±0.016	9.369±0.078	0.892±0.077	-0.156±0.508	-0.031±0.049	-0.013±0.053
1296321	9.300±0.015	0.710±0.028	8.986±0.057	0.590±0.082	0.474±0.204	0.084±0.028	0.263±0.025
1296657	9.465±0.029	0.228±0.030	9.103±0.059	0.075±0.061	0.882±0.385	0.019±0.043	0.050±0.030
1297026	10.854±0.013	1.772±0.016	11.002±0.039	2.602±0.060	-0.713±0.209	-0.042±0.031	0.053±0.030
1297465	9.987±0.009	0.907±0.016	8.761±0.038	0.882±0.081	1.164±0.136	0.042±0.027	0.211±0.029
1298281	9.220±0.042	1.552±0.050	8.698±0.071	1.507±0.123	-1.560±0.229	0.056±0.031	-0.055±0.030
1298893	10.784±0.070	1.640±0.035	9.821±0.046	1.582±0.054	-2.238±0.784	-0.028±0.120	-0.065±0.097
1299643	9.561±0.022	1.106±0.030	9.020±0.035	1.042±0.049	0.686±0.263	-0.090±0.029	0.058±0.036
1299775	10.716±0.012	1.713±0.021	10.463±0.040	1.929±0.063	-0.413±0.196	0.185±0.037	-0.136±0.029
1299785	10.122±0.017	0.816±0.014	8.436±0.051	0.581±0.064	0.003±0.422	0.050±0.041	-0.075±0.043
1300516	9.978±0.026	1.722±0.056	9.604±0.048	1.381±0.061	0.908±0.290	0.159±0.034	-0.302±0.038
1300912	9.566±0.019	0.578±0.016	8.789±0.053	0.639±0.060	-0.478±0.147	0.045±0.026	0.000±0.031
1301933	9.729±0.013	0.835±0.015	6.878±0.340	0.308±0.575	-0.217±0.090	-0.128±0.022	0.083±0.031
1302058	9.849±0.011	1.066±0.018	9.421±0.046	1.004±0.085	0.378±0.130	-0.001±0.027	-0.299±0.024
1302187	10.984±0.012	1.430±0.017	11.021±0.036	2.788±0.061	-0.885±0.340	0.041±0.038	-0.126±0.035
1302523	10.314±0.012	1.047±0.015	9.297±0.031	1.166±0.050	0.232±0.271	-0.022±0.028	-0.010±0.036
1302648	10.251±0.071	1.600±0.034	10.031±0.093	1.642±0.060	-0.715±0.225	0.114±0.030	-0.204±0.029

Continued on next page

Table B.1 – continued from previous page

SNID	Global Mass	Global U-R	Local Mass	Local U-R	x_1	c	Hubble Residual
1303279	10.739±0.017	1.360±0.020	10.758±0.105	2.161±0.090	1.141±0.357	-0.063±0.033	0.049±0.027
1303496	10.422±0.012	1.443±0.019	9.974±0.045	1.533±0.054	-0.309±0.364	0.068±0.033	-0.141±0.027
1303883	10.684±0.026	1.591±0.016	9.619±0.048	1.388±0.047	0.588±0.219	-0.037±0.031	0.063±0.032
1303952	11.263±0.050	1.385±0.029	9.057±0.060	1.621±0.411	0.582±0.580	-0.193±0.044	0.399±0.066
1304442	9.280±0.019	0.343±0.026	8.985±0.045	0.602±0.109	0.259±0.302	-0.071±0.036	0.116±0.031
1304678	11.171±0.013	1.620±0.018	10.864±0.064	2.145±0.070	-1.434±0.648	-0.046±0.089	0.073±0.088
1305504	11.253±0.011	1.651±0.017	9.009±0.043	1.612±0.134	-0.437±0.164	-0.084±0.025	0.081±0.039
1305626	9.251±0.011	0.887±0.020	9.018±0.061	0.933±0.060	-0.296±0.101	-0.108±0.023	0.055±0.028
1306029	9.562±0.017	0.487±0.017	7.912±0.110	0.849±0.295	0.984±0.541	0.029±0.037	0.136±0.050
1306073	10.469±0.031	1.579±0.015	10.522±0.073	1.884±0.074	-1.305±0.201	-0.037±0.030	-0.009±0.033
1306141	9.740±0.015	0.608±0.015	8.554±0.067	0.650±0.085	-0.134±0.222	-0.072±0.028	-0.099±0.032
1306360	10.843±0.028	1.365±0.017	9.697±0.049	1.414±0.058	-0.652±0.725	0.004±0.051	-0.042±0.069
1306390	10.380±0.042	1.535±0.018	10.073±0.081	1.602±0.047	0.043±1.041	0.167±0.066	-0.047±0.094
1306537	9.787±0.037	1.374±0.050	8.871±0.079	1.144±0.096	1.231±0.511	-0.077±0.036	0.111±0.049
1306626	8.772±0.035	0.208±0.035	8.464±0.036	0.327±0.044	0.224±0.367	-0.078±0.030	0.006±0.041
1306785	11.104±0.055	2.106±0.043	9.843±0.148	1.525±0.185	-1.220±1.256	-0.014±0.061	-0.447±0.121
1306980	10.319±0.018	1.016±0.022	9.581±0.045	1.063±0.078	-1.139±0.816	0.050±0.066	-0.370±0.104
1306991	10.932±0.026	1.698±0.016	10.518±0.053	1.831±0.071	-0.402±0.736	-0.048±0.059	-0.145±0.064
1307277	10.354±0.013	1.261±0.015	9.954±0.057	1.254±0.068	-0.392±0.835	0.058±0.058	-0.077±0.072
1307830	10.695±0.009	1.814±0.014	9.214±0.040	1.736±0.031	-1.841±0.207	-0.085±0.030	0.152±0.034
1308326	9.573±0.019	0.436±0.015	8.460±0.042	0.425±0.053	0.452±0.208	-0.118±0.027	0.077±0.031

Continued on next page

Table B.1 – continued from previous page

SNID	Global Mass	Global U-R	Local Mass	Local U-R	x_1	c	Hubble Residual
1308582	10.750±0.033	1.736±0.013	10.349±0.018	1.670±0.042	-0.426±0.343	-0.067±0.035	-0.130±0.037
1308884	10.377±0.017	0.808±0.040	9.007±0.029	0.946±0.150	-1.426±0.080	0.072±0.029	0.000±0.019
1309288	10.918±0.019	1.350±0.016	10.762±0.047	1.833±0.065	0.487±0.443	-0.101±0.046	-0.017±0.043
1309492	9.337±0.017	0.791±0.017	8.974±0.025	0.952±0.056	0.184±0.090	-0.084±0.022	-0.068±0.029
1312274	10.484±0.019	1.716±0.028	9.835±0.047	1.721±0.064	-1.444±0.526	-0.093±0.040	0.026±0.050
1313594	10.121±0.016	1.222±0.018	9.086±0.065	1.036±0.089	0.498±0.163	-0.102±0.028	0.046±0.030
1314897	10.894±0.011	1.378±0.014	9.551±0.067	1.272±0.063	0.892±0.305	0.017±0.032	-0.143±0.037
1315192	10.433±0.011	1.174±0.017	9.031±0.024	0.972±0.042	1.023±0.350	0.082±0.034	-0.107±0.029
1315259	11.361±0.013	1.442±0.018	9.035±0.045	1.294±0.083	-0.491±0.174	0.039±0.029	0.013±0.027
1315296	9.596±0.017	0.396±0.014	9.110±0.040	0.416±0.061	1.579±0.698	0.055±0.045	0.388±0.054
1316385	10.160±0.013	1.284±0.022	9.890±0.057	1.380±0.118	1.323±0.255	0.004±0.032	-0.134±0.024
1316431	6.559±0.325	-0.168±0.449	6.830±0.077	-0.532±0.222	1.265±0.130	-0.080±0.026	0.048±0.026
1316437	9.311±0.018	0.169±0.023	7.643±0.068	-0.048±0.255	0.068±0.623	0.030±0.044	0.036±0.057
1316465	9.104±0.016	0.591±0.017	8.131±0.041	0.306±0.055	0.401±0.105	-0.022±0.023	-0.020±0.028
1317164	11.134±0.024	2.369±0.024	9.944±0.080	1.721±0.098	-2.297±0.215	0.114±0.046	0.184±0.039
1317277	10.072±0.062	1.707±0.035	10.021±0.100	1.715±0.056	-1.406±0.318	0.040±0.035	-0.093±0.033
1317286	7.501±0.132	0.071±0.239	7.108±0.121	-0.269±0.195	0.734±0.159	-0.086±0.026	-0.025±0.037
1317666	10.009±0.013	1.168±0.021	9.243±0.050	1.282±0.134	-0.130±0.110	0.084±0.029	0.077±0.022
1319366	9.529±0.017	0.615±0.027	8.726±0.063	0.485±0.071	1.454±0.217	-0.019±0.028	-0.013±0.030
1319821	10.251±0.014	0.682±0.015	8.751±0.046	0.820±0.066	-0.483±0.224	-0.083±0.032	0.075±0.033
1322229	9.643±0.019	0.678±0.020	9.022±0.057	0.603±0.140	1.148±0.574	0.009±0.033	-0.055±0.050

Continued on next page

Table B.1 – continued from previous page

SNID	Global Mass	Global U-R	Local Mass	Local U-R	x_1	c	Hubble Residual
1322979	8.087±0.082	0.056±0.608	7.501±0.071	-0.064±0.237	0.056±0.224	-0.090±0.024	0.072±0.043
1324542	9.000±0.152	0.694±0.113	7.667±0.110	-0.162±0.254	0.341±0.621	-0.065±0.042	0.226±0.059
1327978	11.070±0.043	1.712±0.025	10.637±0.115	1.832±0.061	0.046±0.585	0.063±0.047	-0.078±0.045
1328066	9.977±0.036	1.439±0.027	9.693±0.110	1.449±0.077	0.726±0.455	-0.127±0.038	0.151±0.050
1328105	11.111±0.013	1.113±0.015	9.309±0.055	0.949±0.067	0.092±0.432	-0.048±0.035	-0.124±0.045
1329312	10.851±0.013	1.480±0.014	10.076±0.070	1.848±0.059	-1.395±0.345	-0.054±0.035	0.012±0.038
1329615	10.994±0.024	1.656±0.015	9.797±0.103	1.523±0.072	-0.473±0.563	-0.011±0.040	-0.014±0.050
1330031	9.071±0.029	0.997±0.051	8.755±0.028	0.905±0.063	0.022±0.107	-0.128±0.036	0.000±0.026
1330426	7.862±0.103	0.750±0.236	7.192±0.095	0.272±0.219	1.283±0.121	-0.097±0.026	0.073±0.029
1331123	11.127±0.053	1.782±0.026	9.088±0.055	1.473±0.060	-1.644±0.208	-0.014±0.031	0.034±0.030
1333246	10.792±0.019	1.183±0.018	10.214±0.051	1.320±0.074	1.798±0.901	0.142±0.067	0.079±0.087
1334084	9.973±0.010	0.971±0.021	9.776±0.028	0.832±0.059	-0.739±0.378	0.092±0.050	-0.079±0.040
1334087	10.961±0.097	1.714±0.040	9.451±0.095	1.638±0.056	0.624±0.374	-0.009±0.048	-0.288±0.050
1334302	10.671±0.014	1.544±0.019	9.817±0.043	1.330±0.069	-1.044±0.525	-0.024±0.039	-0.136±0.051
1334423	9.303±0.018	0.178±0.015	8.848±0.040	0.334±0.051	0.911±0.390	0.010±0.032	0.098±0.037
1334448	11.145±0.038	2.180±0.039	10.399±0.126	1.937±0.103	-2.783±0.812	-0.112±0.063	-0.139±0.093
1334597	9.076±0.069	1.335±0.078	8.748±0.071	1.340±0.095	0.582±0.102	-0.048±0.026	-0.047±0.030
1334620	10.150±0.010	1.104±0.018	9.730±0.033	1.096±0.044	-0.482±0.324	0.220±0.035	-0.144±0.031
1334644	11.375±0.013	1.814±0.016	9.355±0.142	1.831±0.078	-1.728±0.347	-0.049±0.036	-0.067±0.038
1334645	10.404±0.028	1.408±0.018	9.032±0.047	1.313±0.069	-0.843±0.179	-0.032±0.028	-0.078±0.027
1335694	10.273±0.023	0.361±0.020	7.056±0.124	-0.162±0.120	0.932±0.230	-0.027±0.031	-0.043±0.032

Continued on next page

Table B.1 – continued from previous page

SNID	Global Mass	Global U-R	Local Mass	Local U-R	x_1	c	Hubble Residual
1335717	9.652±0.013	0.704±0.016	8.662±0.026	0.761±0.033	-0.093±0.123	0.051±0.027	0.129±0.030
1336008	9.773±0.013	0.967±0.020	9.233±0.043	1.042±0.078	0.670±0.322	-0.062±0.028	-0.101±0.040
1336009	9.350±0.019	0.804±0.023	8.676±0.057	0.763±0.052	-0.422±0.347	0.146±0.036	0.028±0.040
1336453	9.193±0.030	0.344±0.041	8.865±0.060	0.468±0.085	0.976±0.139	-0.062±0.027	0.053±0.024
1336480	9.992±0.011	0.776±0.016	9.181±0.051	0.674±0.050	-0.130±0.302	0.002±0.036	0.177±0.035
1336687	8.603±0.028	0.215±0.040	8.157±0.087	0.123±0.081	0.404±0.163	0.089±0.028	0.031±0.026
1337117	8.678±0.080	0.736±0.155	7.898±0.196	0.381±0.127	0.523±0.324	-0.087±0.032	-0.233±0.050
1337228	9.768±0.052	0.896±0.044	8.907±0.058	0.557±0.096	-0.713±0.766	-0.068±0.074	0.128±0.098
1337272	8.500±0.095	0.333±0.117	8.017±0.091	-0.015±0.099	-0.966±0.571	-0.077±0.048	0.004±0.060
1337649	8.741±0.025	0.678±0.061	8.496±0.052	0.747±0.092	1.067±0.189	0.051±0.028	0.022±0.031
1337687	8.267±0.050	0.194±0.050	8.220±0.044	0.427±0.050	0.876±0.153	-0.112±0.024	0.094±0.031
1337703	10.681±0.033	1.667±0.021	10.179±0.073	1.682±0.076	-1.038±0.462	-0.105±0.045	-0.268±0.062
1337838	7.987±0.188	0.595±0.268	6.921±0.099	0.120±0.193	1.002±0.203	-0.033±0.026	0.021±0.031
1338128	8.984±0.029	0.434±0.019	8.869±0.049	0.489±0.049	-0.686±0.332	-0.009±0.033	0.079±0.035
1338170	10.168±0.023	1.388±0.015	9.507±0.071	1.399±0.058	-0.081±0.585	0.051±0.045	-0.083±0.051
1338278	10.082±0.027	0.896±0.030	9.285±0.082	0.658±0.086	1.709±0.806	0.006±0.050	0.075±0.075
1338430	10.973±0.035	1.491±0.019	9.347±0.085	1.481±0.091	0.529±0.485	-0.072±0.040	-0.079±0.053
1338471	10.268±0.015	1.029±0.021	9.310±0.079	1.065±0.076	-0.918±1.212	-0.040±0.060	0.200±0.110
1338675	9.308±0.016	0.486±0.015	8.898±0.050	0.423±0.054	0.015±0.190	0.026±0.026	0.073±0.030
1339002	10.686±0.044	1.515±0.017	10.144±0.038	1.676±0.050	-1.253±0.388	0.112±0.045	-0.207±0.046
1339149	9.803±0.030	0.496±0.025	8.272±0.058	0.212±0.089	-0.268±0.504	0.023±0.041	-0.211±0.051

Continued on next page

Table B.1 – continued from previous page

SNID	Global Mass	Global U-R	Local Mass	Local U-R	x_1	c	Hubble Residual
1339392	10.320±0.032	1.627±0.033	10.341±0.061	1.600±0.059	-0.416±0.620	-0.028±0.056	-0.315±0.048
1339450	11.174±0.056	1.211±0.025	9.726±0.056	1.143±0.114	-1.175±1.074	0.080±0.066	-0.195±0.112
1340454	10.065±0.014	0.990±0.016	8.967±0.063	0.714±0.061	1.421±0.481	0.121±0.039	-0.166±0.046
1341370	8.738±0.052	0.608±0.080	7.656±0.135	0.204±0.166	1.126±0.569	0.021±0.037	0.121±0.045
1341894	10.142±0.015	1.048±0.016	9.303±0.063	0.673±0.069	-0.226±0.368	-0.045±0.035	0.034±0.037
1342255	9.791±0.010	0.997±0.016	8.227±0.053	1.001±0.125	0.251±0.298	-0.083±0.027	0.001±0.027
1343208	10.578±0.041	1.411±0.016	9.810±0.059	1.335±0.049	-0.086±0.366	-0.012±0.030	-0.060±0.044
1343337	9.676±0.019	0.613±0.015	8.945±0.044	0.683±0.047	0.775±0.675	0.163±0.041	-0.092±0.043
1343401	11.036±0.016	1.649±0.014	9.998±0.127	1.686±0.076	0.752±0.777	-0.058±0.038	-0.092±0.047
1343533	10.728±0.035	1.491±0.014	10.331±0.092	1.547±0.064	-0.890±1.149	-0.006±0.067	0.139±0.076
1343759	9.393±0.015	0.354±0.021	8.193±0.052	0.380±0.061	0.684±0.348	-0.092±0.024	0.053±0.041
1344692	11.081±0.125	1.711±0.016	10.063±0.105	1.924±0.071	-1.803±1.800	0.170±0.089	-0.085±0.090
1345553	10.177±0.030	1.505±0.031	9.403±0.053	0.995±0.067	0.287±0.522	-0.143±0.031	0.184±0.037
1345594	11.175±0.041	1.553±0.015	10.672±0.110	1.893±0.049	-0.006±1.141	-0.144±0.050	0.090±0.059
1346137	9.921±0.015	0.627±0.015	9.576±0.044	0.673±0.045	0.825±0.620	0.025±0.042	0.004±0.045
1346387	9.075±0.081	1.260±0.138	8.204±0.052	1.082±0.083	-2.111±0.333	-0.027±0.027	0.065±0.034
1346956	6.936±0.250	0.008±0.316	6.744±0.147	-0.751±0.786	0.902±0.370	-0.065±0.033	-0.055±0.036
1346966	9.490±0.019	0.431±0.015	8.597±0.057	0.753±0.050	0.619±0.394	-0.100±0.032	-0.035±0.032

References

Abbot, T., Annis, J., DePoy, D., et al. 2009, Dark Energy Camera Specifications and Technical Requirements, https://www.noao.edu/meetings/decam/media/DECam_Technical_specifications.pdf, ,

Abbott, T. M. C., Abdalla, F. B., Allam, S., et al. 2018, ApJS, 239, 18

Abbott, T. M. C., Allam, S., Andersen, P., et al. 2019, ApJ, 872, L30

Akaike, H. 1974, IEEE Transactions on Automatic Control, 19, 716

Aldering, G., Adam, G., Antilogus, P., et al. 2002, in Society of Photo-Optical Instrumentation Engineers (SPIE) Conference Series, Vol. 4836, Proc. SPIE, ed. J. A. Tyson & S. Wolff, 61–72

Anderson, J. P., James, P. A., Förster, F., et al. 2015, MNRAS, 448, 732

Arnett, W. D. 1979, ApJ, 230, L37

—. 1982, ApJ, 253, 785

Ashall, C., Mazzali, P. A., Stritzinger, M. D., et al. 2018, MNRAS, 477, 153

Astier, P., Guy, J., Regnault, N., et al. 2006, A&A, 447, 31

Baade, W., & Zwicky, F. 1934, Proceedings of the National Academy of Science, 20, 254

Baldry, I. K., & Glazebrook, K. 2003, ApJ, 593, 258

Bernstein, J. P., Kessler, R., Kuhlmann, S., et al. 2012, ApJ, 753, 152

Bertin, E. 2010, SWarp: Resampling and Co-adding FITS Images Together, https://ui.adsabs.harvard.edu/abs/2010ascl.soft10068B, , , ascl:1010.068

Bertin, E., & Arnouts, S. 1996, A&AS, 117, 393

Betoule, M., Kessler, R., Guy, J., et al. 2014, A&A, 568, A22

Binney, J., & Merrifield, M. 1998, Galactic Astronomy

Biswas, R., Goobar, A., Dhawan, S., et al. 2021, arXiv e-prints, arXiv:2103.16978

Blondin, S., & Tonry, J. L. 2007, ApJ, 666, 1024

Bonnett, C., Troxel, M. A., Hartley, W., et al. 2016, Phys. Rev. D, 94, 042005

Bradley, L., Sipocz, B., Robitaille, T., et al. 2019, astropy/photutils: v0.6, v.v0.6, Zenodo, doi:10.5281/zenodo.2533376

Branch, D., & van den Bergh, S. 1993, AJ, 105, 2231

Bravo, E., & Badenes, C. 2011, MNRAS, 414, 1592

Bravo, E., Domínguez, I., Badenes, C., Piersanti, L., & Straniero, O. 2010, ApJ, 711, L66

Briday, M., Rigault, M., Graziani, R., et al. 2021, arXiv e-prints, arXiv:2109.02456

Brout, D., & Scolnic, D. 2021, ApJ, 909, 26

Brout, D., Sako, M., Scolnic, D., et al. 2019a, ApJ, 874, 106

Brout, D., Scolnic, D., Kessler, R., et al. 2019b, ApJ, 874, 150

Brown, P. 2014, in Proceedings of Swift: 10 Years of Discovery (SWIFT 10, 125

Bruzual, G., & Charlot, S. 2003, MNRAS, 344, 1000

Burns, C. R., Ashall, C., Contreras, C., et al. 2020, ApJ, 895, 118

Campbell, H., Fraser, M., & Gilmore, G. 2016, MNRAS, 457, 3470

Chabrier, G. 2003, PASP, 115, 763

Chandrasekhar, S. 1931, ApJ, 74, 81

Childress, M., Aldering, G., Antilogus, P., et al. 2013, ApJ, 770, 108

Childress, M. J., Wolf, C., & Zahid, H. J. 2014, MNRAS, 445, 1898

Childress, M. J., Lidman, C., Davis, T. M., et al. 2017, MNRAS, 472, 273

Churazov, E., Sunyaev, R., Isern, J., et al. 2014, Nature, 512, 406

Conley, A., Sullivan, M., Hsiao, E. Y., et al. 2008, ApJ, 681, 482

Conroy, C. 2013, ARA&A, 51, 393

Dai, M., Kuhlmann, S., Wang, Y., & Kovacs, E. 2018, MNRAS, 477, 4142

D'Andrea, C. B., Gupta, R. R., Sako, M., et al. 2011, ApJ, 743, 172

Dark Energy Survey Collaboration, Abbott, T., Abdalla, F. B., et al. 2016, MNRAS, 460, 1270

Diehl, R., Siegert, T., Hillebrandt, W., et al. 2014, Science, 345, 1162

Dixon, S. 2021, PASP, 133, 054501

Einstein, A. 1915, Sitzungsberichte der Königlich Preußischen Akademie der Wissenschaften (Berlin), 844

Filippenko, A. V. 1989, PASP, 101, 588

—. 1997, ARA&A, 35, 309

Fioc, M., & Rocca-Volmerange, B. 1997, A&A, 500, 507

—. 2019, A&A, 623, A143

Firth, R. E., Sullivan, M., Gal-Yam, A., et al. 2015, MNRAS, 446, 3895

Fitzpatrick, E. L. 1999, PASP, 111, 63

Flaugher, B., Diehl, H. T., Honscheid, K., et al. 2015, AJ, 150, 150

Foley, R. J., & Kasen, D. 2011, ApJ, 729, 55

Foley, R. J., Scolnic, D., Rest, A., et al. 2018, MNRAS, 475, 193

Freedman, W. L., & Madore, B. F. 2010, ARA&A, 48, 673

Friedmann, A. 1922, Zeitschrift fur Physik, 10, 377

Galbany, L., Anderson, J. P., Sánchez, S. F., et al. 2018, ApJ, 855, 107

Gall, C., Stritzinger, M. D., Ashall, C., et al. 2018, A&A, 611, A58

Gallazzi, A., Charlot, S., Brinchmann, J., White, S. D. M., & Tremonti, C. A. 2005, MNRAS, 362, 41

Garn, T., & Best, P. N. 2010a, MNRAS, 409, 421

—. 2010b, MNRAS, 409, 421

Garnavich, P. 2017, in Handbook of Supernovae, ed. A. W. Alsabti & P. Murdin, 2605

Goldstein, D. A., D'Andrea, C. B., Fischer, J. A., et al. 2015, AJ, 150, 82

Gonzalez-Gaitan, S., de Jaeger, T., Galbany, L., et al. 2020, arXiv e-prints, arXiv:2009.13230

Graham, M. in prep

Green, D. A. 2017, in Handbook of Supernovae, ed. A. W. Alsabti & P. Murdin, 37

Gruen, D., Seitz, S., & Bernstein, G. M. 2014, PASP, 126, 158

Grylls, P. J., Shankar, F., Leja, J., et al. 2020, MNRAS, 491, 634

Gupta, R. R., D'Andrea, C. B., Sako, M., et al. 2011, ApJ, 740, 92

Gupta, R. R., Kuhlmann, S., Kovacs, E., et al. 2016, AJ, 152, 154

Gutiérrez, C. P., Anderson, J. P., Hamuy, M., et al. 2017, ApJ, 850, 89

Guy, J., Astier, P., Baumont, S., et al. 2007, A&A, 466, 11

Guy, J., Sullivan, M., Conley, A., et al. 2010, A&A, 523, A7

Hamuy, M., Phillips, M. M., Suntzeff, N. B., et al. 1996, AJ, 112, 2391

Henne, V., Pruzhinskaya, M. V., Rosnet, P., et al. 2017, New Astronomy, 51, 43

Hicken, M., Wood-Vasey, W. M., Blondin, S., et al. 2009a, ApJ, 700, 1097

Hicken, M., Challis, P., Jha, S., et al. 2009b, ApJ, 700, 331

Hicken, M., Challis, P., Kirshner, R. P., et al. 2012, ApJS, 200, 12

Hoeflich, P., Khokhlov, A., Wheeler, J. C., et al. 1996, ApJ, 472, L81

Hounsell, R., & Sako, M. in prep

Hounsell, R., Scolnic, D., Foley, R. J., et al. 2018, ApJ, 867, 23

Howell, D. A., Sullivan, M., Perrett, K., et al. 2005, ApJ, 634, 1190

Howell, D. A., Sullivan, M., Brown, E. F., et al. 2009, ApJ, 691, 661

Hsiao, E. Y., Conley, A., Howell, D. A., et al. 2007, ApJ, 663, 1187

Hubble, E. 1929, Proceedings of the National Academy of Sciences, 15, 168

Iben, I., J., & Tutukov, A. V. 1984, ApJS, 54, 335

Inserra, C. 2019, Nature Astronomy, 3, 697

Ivezić, Ž., Kahn, S. M., Tyson, J. A., et al. 2019, ApJ, 873, 111

Jha, S., Riess, A. G., & Kirshner, R. P. 2007, ApJ, 659, 122

Jha, S. W., Maguire, K., & Sullivan, M. 2019, Nature Astronomy, 3, 706

Johansson, J., Thomas, D., Pforr, J., et al. 2013, MNRAS, 435, 1680

Johansson, J., Cenko, S. B., Fox, O. D., et al. 2021, arXiv e-prints, arXiv:2105.06236

Jones, D. O., Riess, A. G., & Scolnic, D. M. 2015, ApJ, 812, 31

Jones, D. O., Scolnic, D. M., Riess, A. G., et al. 2017, ApJ, 843, 6

Jones, D. O., French, K. D., Agnello, A., et al. 2019, Transient Name Server AstroNote, 148, 1

Jones, D. O., Scolnic, D. M., Riess, A. G., et al. 2018a, ApJ, 857, 51

Jones, D. O., Riess, A. G., Scolnic, D. M., et al. 2018b, ApJ, 867, 108

Kang, Y., Kim, Y.-L., Lim, D., Chung, C., & Lee, Y.-W. 2016, ApJS, 223, 7

Kasen, D., Röpke, F. K., & Woosley, S. E. 2009, Nature, 460, 869

Kasen, D., & Woosley, S. E. 2007, ApJ, 656, 661

Kauffmann, G., Heckman, T. M., White, S. D. M., et al. 2003, MNRAS, 341, 54

Kelly, P. L., Filippenko, A. V., Burke, D. L., et al. 2015, Science, 347, 1459

Kelly, P. L., Hicken, M., Burke, D. L., Mandel, K. S., & Kirshner, R. P. 2010, ApJ, 715, 743

Kelsey, L., Sullivan, M., Smith, M., et al. 2021, MNRAS, 501, 4861

Kessler, R., & Scolnic, D. 2017, ApJ, 836, 56

Kessler, R., Bernstein, J. P., Cinabro, D., et al. 2009, PASP, 121, 1028

Kessler, R., Marriner, J., Childress, M., et al. 2015, AJ, 150, 172

Kessler, R., Brout, D., D'Andrea, C. B., et al. 2019, MNRAS, 485, 1171

Kim, Y.-L., Kang, Y., & Lee, Y.-W. 2019, Journal of Korean Astronomical Society, 52, 181

Kim, Y.-L., Smith, M., Sullivan, M., & Lee, Y.-W. 2018, ApJ, 854, 24

Kron, R. G. 1980, ApJS, 43, 305

Kroupa, P. 2001, MNRAS, 322, 231

Lampeitl, H., Smith, M., Nichol, R. C., et al. 2010, ApJ, 722, 566

Leavitt, H. S., & Pickering, E. C. 1912, Harvard College Observatory Circular, 173, 1

Lemaître, G. 1927, Annales de la Société; Scientifique de Bruxelles, 47, 49

Lidman, C., Tucker, B. E., Davis, T. M., et al. 2020, MNRAS, 496, 19

Lintott, C. J., Schawinski, K., Slosar, A., et al. 2008, MNRAS, 389, 1179

Liu, Y.-Q., Modjaz, M., Bianco, F. B., & Graur, O. 2016, ApJ, 827, 90

Livio, M., & Mazzali, P. 2018, Phys. Rep., 736, 1

Maguire, K. 2017, in Handbook of Supernovae, ed. A. W. Alsabti & P. Murdin, 293

Mandel, K. S., Thorp, S., Narayan, G., Friedman, A. S., & Avelino, A. 2020, arXiv e-prints, arXiv:2008.07538

Maoz, D., Mannucci, F., & Nelemans, G. 2014, Annual Review of Astronomy and Astrophysics, 52, 107

Maraston, C. 2005, MNRAS, 362, 799

Milne, P. A., Brown, P. J., Roming, P. W. A., Bufano, F., & Gehrels, N. 2013, ApJ, 779, 23

Minkowski, R. 1941, PASP, 53, 224

Modjaz, M., Liu, Y. Q., Bianco, F. B., & Graur, O. 2016, ApJ, 832, 108

Möller, A., & de Boissière, T. 2020, MNRAS, 491, 4277

Morganson, E., Gruendl, R. A., Menanteau, F., et al. 2018, PASP, 130, 074501

Neill, J. D., Sullivan, M., Howell, D. A., et al. 2009, ApJ, 707, 1449

Neilsen, Eric H., J., Annis, J. T., Diehl, H. T., et al. 2019, arXiv e-prints, arXiv:1912.06254

Neilsen, Eric H., J., Bernstein, G., Gruendl, R., & Kent, S. 2016, FERMILAB-TM-2610-AE-CD, doi:10.2172/1250877

Nicolas, N., Rigault, M., Copin, Y., et al. 2021, A&A, 649, A74

Pan, Y. C., Sullivan, M., Maguire, K., et al. 2014, MNRAS, 438, 1391

Pereira, R., Thomas, R. C., Aldering, G., et al. 2013, A&A, 554, A27

Perlmutter, S., Gabi, S., Goldhaber, G., et al. 1997, ApJ, 483, 565

Perlmutter, S., Aldering, G., Goldhaber, G., et al. 1999, ApJ, 517, 565

Phillips, M. M. 1993, ApJ, 413, L105

Planck Collaboration, Aghanim, N., Akrami, Y., et al. 2020, A&A, 641, A6

Ponder, K. A., Wood-Vasey, W. M., Weyant, A., et al. 2020, arXiv e-prints, arXiv:2006.13803

Popovic, B., Brout, D., Kessler, R., Scolnic, D., & Lu, L. 2021, arXiv e-prints, arXiv:2102.01776

Popper, D. M. 1937, PASP, 49, 283

Quimby, R. M., De Cia, A., Gal-Yam, A., et al. 2018, ApJ, 855, 2

Rana, N. C., & Basu, S. 1992, A&A, 265, 499

Rest, A., Scolnic, D., Foley, R. J., et al. 2014, ApJ, 795, 44

Riess, A. G., Casertano, S., Yuan, W., Macri, L. M., & Scolnic, D. 2019, ApJ, 876, 85

Riess, A. G., Press, W. H., & Kirshner, R. P. 1996, ApJ, 473, 88

Riess, A. G., Filippenko, A. V., Challis, P., et al. 1998, AJ, 116, 1009

Rigault, M., Copin, Y., Aldering, G., et al. 2013, A&A, 560, A66

Rigault, M., Aldering, G., Kowalski, M., et al. 2015, ApJ, 802, 20

Rigault, M., Brinnel, V., Aldering, G., et al. 2020, A&A, 644, A176

Roman, M., Hardin, D., Betoule, M., et al. 2018, A&A, 615, A68

Röpke, F. K., & Hillebrandt, W. 2004, A&A, 420, L1

Rose, B. M., Garnavich, P. M., & Berg, M. A. 2019, ApJ, 874, 32

Rose, B. M., Rubin, D., Strolger, L., & Garnavich, P. M. 2021a, ApJ, 909, 28

Rose, B. M., Aldering, G., Dai, M., et al. 2021b, arXiv e-prints, arXiv:2104.01199

Sako, M., Bassett, B., Connolly, B., et al. 2011, ApJ, 738, 162

Sako, M., Bassett, B., Becker, A. C., et al. 2018, PASP, 130, 064002

Salpeter, E. E. 1955, ApJ, 121, 161

Schlafly, E. F., Meisner, A. M., Stutz, A. M., et al. 2016, ApJ, 821, 78

Schlegel, D. J., Finkbeiner, D. P., & Davis, M. 1998, ApJ, 500, 525

Schmidt, B. P., Suntzeff, N. B., Phillips, M. M., et al. 1998, ApJ, 507, 46

Scolnic, D., Rest, A., Riess, A., et al. 2014, ApJ, 795, 45

Scolnic, D., Smith, M., Massiah, A., et al. 2020, ApJ, 896, L13

Scolnic, D. M., Jones, D. O., Rest, A., et al. 2018, ApJ, 859, 101

Siebert, M. R., Foley, R. J., Jones, D. O., & Davis, K. W. 2020, MNRAS, 493, 5713

Silk, J. 2011, in IAU Symposium, Vol. 277, Tracing the Ancestry of Galaxies, ed. C. Carignan, F. Combes, & K. C. Freeman, 273–281

Silk, J. 2013, ApJ, 772, 112

Silverman, J. M., Foley, R. J., Filippenko, A. V., et al. 2012, MNRAS, 425, 1789

Slipher, V. M. 1913, Lowell Observatory Bulletin, 1, 56

—. 1915, Popular Astronomy, 23, 21

—. 1917, Proceedings of the American Philosophical Society, 56, 403

—. 1921, Popular Astronomy, 29, 128

Smith, M., D'Andrea, C. B., Sullivan, M., et al. 2020a, AJ, 160, 267

Smith, M., Sullivan, M., Wiseman, P., et al. 2020b, MNRAS, 494, 4426

Speagle, J. S., Steinhardt, C. L., Capak, P. L., & Silverman, J. D. 2014, ApJS, 214, 15

Stephenson, F. R. 2017, in Handbook of Supernovae, ed. A. W. Alsabti & P. Murdin, 49

Stritzinger, M., Burns, C. R., Phillips, M. M., et al. 2010, AJ, 140, 2036

Stritzinger, M. D., Phillips, M. M., Boldt, L. N., et al. 2011, AJ, 142, 156

Stritzinger, M. D., Shappee, B. J., Piro, A. L., et al. 2018, ApJ, 864, L35

Sugiura, N. 1978, Communications in Statistics - Theory and Methods, 7, 13

Sullivan, M., Le Borgne, D., Pritchet, C. J., et al. 2006, ApJ, 648, 868

Sullivan, M., Conley, A., Howell, D. A., et al. 2010, MNRAS, 406, 782

Sullivan, M., Guy, J., Conley, A., et al. 2011, ApJ, 737, 102

Taylor, G., Lidman, C., Tucker, B. E., et al. 2021, MNRAS, 504, 4111

Taylor, P., Federrath, C., & Kobayashi, C. 2017, MNRAS, 469, 4249

Thorp, S., Mandel, K. S., Jones, D. O., Ward, S. M., & Narayan, G. 2021, arXiv e-prints, arXiv:2102.05678

Timmes, F. X., Brown, E. F., & Truran, J. W. 2003, ApJ, 590, L83

Tortora, C., Napolitano, N. R., Cardone, V. F., et al. 2010, MNRAS, 407, 144

Trayford, J. W., Theuns, T., Bower, R. G., et al. 2016, MNRAS, 460, 3925

Tremonti, C. A., Heckman, T. M., Kauffmann, G., et al. 2004, ApJ, 613, 898

Tripp, R. 1998, A&A, 331, 815

Turatto, M. 2003, in Supernovae and Gamma-Ray Bursters, ed. K. Weiler, Vol. 598, 21–36

Uddin, S. A., Mould, J., Lidman, C., Ruhlmann-Kleider, V., & Zhang, B. R. 2017, ApJ, 848, 56

Uddin, S. A., Burns, C. R., Phillips, M. M., et al. 2020, ApJ, 901, 143

Vincenzi, M., Sullivan, M., Firth, R. E., et al. 2019, MNRAS, 489, 5802

Vincenzi, M., Sullivan, M., Graur, O., et al. 2021, MNRAS, 505, 2819

Wang, X., Filippenko, A. V., Ganeshalingam, M., et al. 2009, ApJ, 699, L139

Wechsler, R. H., & Tinker, J. L. 2018, ARA&A, 56, 435

Whelan, J., & Iben, Icko, J. 1973, ApJ, 186, 1007

Williamson, M., Modjaz, M., & Bianco, F. B. 2019, ApJ, 880, L22

Winkler, C., Courvoisier, T. J. L., Di Cocco, G., et al. 2003a, A&A, 411, L1

Winkler, P. F., Gupta, G., & Long, K. S. 2003b, ApJ, 585, 324

Wiseman, P., Smith, M., Childress, M., et al. 2020, MNRAS, 495, 4040

Wiseman, P., Sullivan, M., Smith, M., et al. 2021, arXiv e-prints, arXiv:2105.11954

Wolf, R. C., D'Andrea, C. B., Gupta, R. R., et al. 2016, ApJ, 821, 115

Woosley, S. E., & Weaver, T. A. 1994, ApJ, 423, 371

Yates, R. M., Kauffmann, G., & Guo, Q. 2012, MNRAS, 422, 215

Yuan, F., Lidman, C., Davis, T. M., et al. 2015, MNRAS, 452, 3047

Zahid, H. J., Yates, R. M., Kewley, L. J., & Kudritzki, R. P. 2013, ApJ, 763, 92